Heat transfer in active volcanoes: models of crater lake systems

Thesis

HEAT TRANSFER IN ACTIVE VOLCANOES: MODELS OF CRATER LAKE SYSTEMS

A thesis presented for the degree of

Doctor of Philosophy

by

DAVID STACEY STEVENSON

B.Sc. (Hons) Liverpool 1988

Department of Earth Sciences,
The Open University.

February 1992

Frontispiece

Acknowledgements

Geoff Brown, Hazel Rymer and Phiroze Kapadia initiated this project, and commented on earlier versions of this text. In the U.K., Geoff Brown, Steve Blake, Clive Oppenheimer, Claude Jaupart, Stephen Hallinan, Andrea Borgia, Joe Cann, Ros Strens, Grant Bigg, John Murray and Roy Keam offered useful advice and helpful discussions. In Costa Rica, Gerardo Soto, Jorgé Barquero, Mario Fernandez, Hector Flores, Steve Hallinan, Clive Oppenheimer, Hazel Rymer, Geoff Brown, the Earthwatch team, ICE employees, and Poás national park rangers provided field assistance. The Land-Rover deserves a mention for surviving some tough driving. In New Zealand, Trevor Hunt and Laura generously put me up in Taupo, the DSIR let me use the observatory in Whakapapa (pronounced fuck-a-papa) village, and Christine and David Robinson gave me a bed in Wellington. Peter Otway, Steve Sherburn, Dave Keen, Tony Hurst, Ray Dibble, John Latter all helped logistically and scientifically, and I had useful chats with Bruce Christenson and Werner Giggenbach. At the O.U., Dentinho negotiated MacDraw predicaments, Jon Maynard produced a smart congratulations card, Clive Oppenheimer often produced quite extra-ordinary food despite his love of wank pasties. Edgar provided hours of carefree motoring before finally succumbing to Thatcher's Britain, and my best mate Fiona McGibbon sat there looking gone out and helped assemble this gobsmacking goosgog of a thesis.

NERC and the DSS funded the project.

EX12

HIGHER DEGREES OFFICE

LIBRARY AUTHORISATION FORM

STUDENT: DAVID S. STEVENSON SERIAL NO:_____

DEGREE: PH. D.

TITLE OF THESIS: HEAT TRANSFER IN ACTIVE VOLCANOES :
MODELS OF CRATER LAKE SYSTEMS

I confirm that I am willing that my thesis be made available to readers and maybe photocopied, subject to the discretion of the Librarian.

SIGNED: D. Stevenson DATE: 29th octobe 1992

Abstract

Heat transfer in active volcanoes was investigated in this thesis. A general model of a crater lake system was developed that takes inputs of lake temperature, volume, chemical content, and meteorological conditions, and outputs the mass, energy, and chemical flows to and from the lake. The model was applied to lakes at Poás (Costa Rica) and Ruapehu (New Zealand), yielding volcanic power outputs of ~10^2-10^3 MW, and heat fluxes of ~10^2-10^4 W m^{-2}. Heat is added to the lakes by hot brine and steam, derived from lake seepage and magmatic gas.

The heat source is magma crystallising, cooling, and degassing. Background heat inputs are maintained by hydrothermal infiltration of magma, releasing latent and specific heat. Infiltration of the conductive boundary layer surrounding magma was modelled. The permeability created by contractive cooling was equated with the permeability required for two-phase convection to transport heat away from the boundary. Infiltration rates of ~1-100 m a^{-1} (metres/year), into conductive layers ~30-0.3 m thick, creating permeabilities of ~10^{-10}-10^{-14} m^2, will provide the required heat flux. Cracking temperatures of magma depend upon infiltration rate, ranging from hydrothermal system temperatures at slow rates, to magma temperatures at the fastest rates. Predicted maximum rates are ~300 m a^{-1} for near-surface magma, and ~800 m a^{-1} for magma at ~1-3 km depth.

Measured SO_2 fluxes at Poás, and calculated influxes of HCl to both lakes imply that degassed magma volumes (~0.004-0.08 km^3 a^{-1}) are much larger than likely intrusions. A new model was developed of small, vesiculating intrusions that circulate magma due to the density increase associated with gas loss. Dense, degassed magma descends, whilst buoyant, volatile-rich magma rises from a deep source. Pipe-like intrusions of radius ~5 m, tapping magma volumes >~0.05 km^3, can produce the gas fluxes needed. Intrusions of this type probably occurred in 1980/81 and 1986 at Poás, and in 1968, 1971, 1975, 1977, 1981 and 1985 at Ruapehu, and were followed by intermittent eruptions and degassing. This degassing mechanism probably occurs at many volcanoes where high gas fluxes are observed, but no evidence exists for large,

shallow intrusions. A model of compressible fluid flow in a rough fumarole conduit, with conductive heat loss to the surroundings, allows fumarole temperatures to be used to estimate the depth of their magma source. This also indicates shallow magma was emplaced at Poás in 1980/81 and 1986.

In summary, heat transfer is achieved by a combination of intermittent gas release from minor shallow intrusions, together with infiltration of deeper magma. Infiltration is one mechanism for providing fractures allowing the release of gas from shallow intrusions, and circulation probably ceases due to freezing caused by infiltration.

Contents

List of figures

List of Tables

List of Plates

CHAPTER 1

Introduction

1.1 The problem

The problem addressed by this thesis can be stated immediately: how does heat get out of an active volcano ? Possible answers to this question are shown diagrammatically in fig. 1.1. Taking the source of volcanic heat to be crystallising, cooling and possibly vesiculating magma, heat can be lost by: (i) conduction alone; (ii) conduction feeding hydrothermal convection; (iii) advection of gas; and (iv) advection of magma. This thesis concentrates on conduction, hydrothermal convection and magma degassing, rather than eruption of magma. This is because these are thought to be the major heat transfer processes operating within the volcanoes considered in this study.

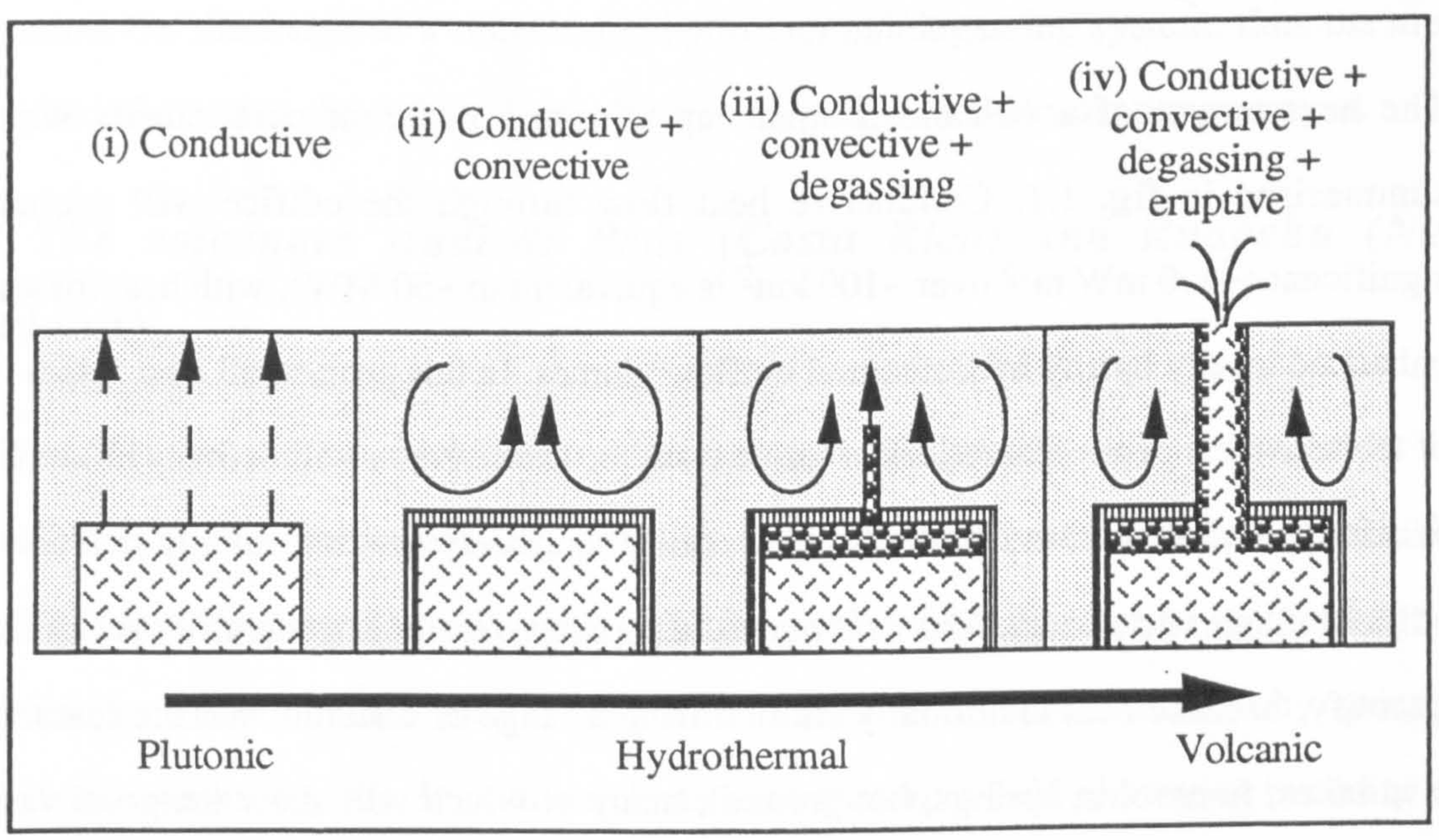

Fig. 1.1 *Cartoon of heat transfer mechanisms from magma bodies to the earth's surface: (i) conduction through the overlying rock; (ii) conduction through a thin boundary layer feeding hydrothermal convection in permeable country rock; (iii) additional heat transfer by advection of magmatic gas; (iv)heat transfer by magmatic eruption.*

The approach taken is firstly to develop a method for quantifying the heat output of an active volcano using crater lake calorimetry (e.g. Shepherd and Sigurdsson, 1978; Hurst and Dibble, 1981). This method is then applied to two volcanoes, using an 11 year data set from Poás in Costa Rica, and 25 years of data from Ruapehu in New Zealand. The calculated heat fluxes are used to constrain possible heat transfer processes within these volcanoes. Physical models involving conduction and advection of heat at the boundary between hot magma and cool country rock, convection and crystallisation within the magma, and convection of fluid within the hydrothermal system are developed. Advection of heat by magma degassing is considered initially as a separate process, and then integrated into a general model of the magmatic-hydrothermal system. Finally, conclusions are drawn regarding the possible processes operating within Poás and Ruapehu, and generalised models of heat transfer mechanisms within active, but non-erupting volcanoes of this type are stated.

1.2 Quantifying the heat output of an active volcano: crater lake calorimetry

The heat output of a volcano is made up of many different components which are summarised in fig. 1.1. Conductive heat flow through the edifice will probably be significant (~500 mW m^{-2} over ~100 km^2 is equivalent to ~50 MW), with heat losses being enhanced locally by any hydrothermal outflow plumes. In this project, all heat losses outside of the active crater are ignored. Heat losses from the active crater will define a minimum heat loss for the whole volcano, and will reflect fairly accurately losses from any shallow (upper edifice) magmatic system. The heat output of an active crater is generally very difficult to quantify, because heat is normally emitted from a range of different surface features (e.g. lava lakes, fumaroles, springs, hot ground), many of which will show temporal variation, and require awkward and extensive monitoring. However, this problem is largely overcome at volcanoes where the main active vent is filled by a water lake, as the water will absorb heat from the variety of sources, generally homogenise the temperature, then emit the heat approximately uniformly from its surface, through evaporation, sensible heat, and radiation. Using formulae from the literature (e.g. Henderson-Sellers, 1986; and see chapter 2), measurements of the lake temperature, surface area, and ambient weather conditions can be

used to estimate surface mass and energy losses. With additional data on lake chemistry, these losses may be incorporated into a model of mass, energy and chemical flows within a crater lake system, which is developed in chapter 2. Lake chemistry data allows minimum values for seepage to be found, and helps to characterise the hydrothermal fluids flowing into the lake by constraining their chemistry. This generalised model produces values for the average power input to a lake over a time interval between lake temperature measurements.

In the model, heat is supplied to the lake by inflowing hot hydrothermal fluid, with a possible range in composition from superheated steam to hot brine. For conduction through the lake bed to be important, a very thin and/or areally extensive boundary layer between material at high temperature and the lake is required. This may occur if lava is erupted onto the lake floor (e.g. at Soufrière, St.Vincent, in 1971-2 (Shepherd and Sigurdsson, 1978)); but a deeper magma source is thought to be more typical at most crater lakes, thus lake-floor conduction is ignored. The crater lake model produces values for fluid flow rates into and out of a lake, and chemical contents of each flow. The fluid flowing into the lake from below represents the discharge of a magma-fed hydrothermal/degassing system, thus the model provides information about the sub-lake system as well as the volcanic power output.

1.3 The volcanoes studied: Poás (Costa Rica) and Ruapehu (New Zealand)

Poás and Ruapehu are andesitic arc volcanoes, and both usually have a hot, acidic lake partially filling their active summit craters, covering their main vents. Both have exhibited periods of frequent phreatic activity that typically involve repeated ejection of lake water and sediment to a few hundred metres height for weeks to months, followed by quiescent periods of months to years. In addition, Poás has a fumarole field of varying intensity on a recently erupted (1952) pyroclastic cone adjacent to the lake. Ruapehu has produced numerous recent (e.g. 1971, 1975, 1982) phreato-magmatic eruptions, and because of the perched location of the lake, many of the eruptions produced damaging lahars (Houghton et al., 1987). The fumaroles at Poás reached temperatures of ~1000 °C in 1981 (Barquero, 1983), and generated fluxes of ~700 t d^{-1} (tonnes/day) SO_2 in 1982 (Casadevall et al.,

1984a), indicating the presence of near-surface degassing magma. Lake temperatures generally fall in the range 20 - 60 °C at both volcanoes, typically losing heat at rates of between 100 and 1000 MW.

Iterative application of the lake model to the crater lakes of Poás and Ruapehu is used in chapter 4 to constrain the composition and enthalpy of the incoming fluid. A brine/steam mixture, rather than simple steam influx, is required at both lakes, on the basis of the conservation of metal ions. This suggests that a major sub-lake process is the recycling of lake seepage, some of which percolates downwards towards the magma source, is vaporised and returned as steam, whilst some is heated, but not vaporised, and returned as hot brine. Additional heat is sometimes supplied by the direct addition of magmatic gas to the lake.

1.4 Heat transfer processes

Having quantified the heat output of the two volcanoes studied, methods of transferring the energy from magma bodies are investigated. The boundary between hot magmatic material and cool country rock is at the centre of this study. Heat will be transferred across this boundary by conduction, and, in some cases, by advection of gas. Beneath the boundary, crystallisation and perhaps convection of magma will occur; above the boundary, convection of hydrothermal fluid will occur within the permeable country rock. The calculated volcanic power outputs from Poás and Ruapehu suggest heat fluxes of ~10^2-10^4 W m^{-2} must be occurring through the roofs of underlying magma bodies, and through the hydrothermal system.

1.4.1 Conduction

Wherever a temperature gradient exists, heat will diffuse into the cooler material by conduction. The conductive heat flux (Q_{cond}) will be given by:

$$Q_{cond} = k \nabla T$$

where k is the thermal conductivity and T is the temperature. Conduction is thought to dominate heat transfer at the magma/country rock boundary. The thickness and temperature

drop across the boundary control the heat flux. Thicknesses of ~0.1-10 m are required to conduct the calculated fluxes at Poás and Ruapehu, if the boundary remains fixed.

1.4.2 Convection

Wherever the critical Rayleigh number is exceeded in a fluid, heat will be transferred by displacement of cold material by hot material, and vice-versa, i.e. convection. The Rayleigh number in a fluid of density ρ, coefficient of thermal expansion α, thermal diffusivity κ, and dynamic viscosity μ, experiencing a temperature drop ΔT over a height h, is given by:

$$Ra = \frac{\rho\, g\, \alpha\, \Delta T\, h^3}{\kappa\, \mu}$$

where g is the acceleration due to gravity. Convection within magma chambers is much debated, with views ranging from those of Marsh (1989) who suggested that convection only occurs in super-heated magmas, to those of Worster et al. (1990) who suggested that turbulent convection occurs very easily within mafic magma bodies. The consensus view appears to be that convection does occur in most low viscosity, mafic magmas, but becomes increasing more difficult as viscosity increases (Tait et al., 1989). However, even if it is feasible, convecting andesitic magma alone will not provide sufficient heat at Poás or Ruapehu to account for the calculated losses; another source of heat is required.

1.4.3 Crystallisation

Crystallisation will occur in all non-superheated magmas that are cooling. Crystallisation releases latent heat to the crystal surroundings. The location of crystallisation within magma chambers is also disputed, but essentially some occurs on the floor, and some at the roof (e.g. Worster et al., 1990). Crystallisation at the roof will release latent heat directly to the base of the conducting boundary. However, crystallisation beneath a conducting layer with a fixed upper surface will thicken the boundary, reducing the conducted heat flux. A mechanism of maintaining a thin boundary layer is required.

1.4.4 Advection of magmatic heat into the hydrothermal system

Lister (1974) proposed that the cooling of magma by a hydrothermal system would induce penetrative fracturing of the outer part of the conductive boundary layer. As heat was extracted, the fractures would infiltrate further into the layer, allowing hydrothermal fluids direct access to hot rock. Viewed from the reference frame of the boundary layer, this penetration represents advection of magma into the hydrothermal system. This mechanism provides a concentrated source of energy, and maintains a thin boundary layer above a crystallising magma. Infiltration velocities of ~1-100 m a^{-1} would provide the heat fluxes observed at Poás and Ruapehu.

1.4.5 Two phase hydrothermal fluid convection

Heat from the magma must traverse a hydrothermal system to reach the overlying lake. Two-phase convection involving up-flowing steam and down-flowing water is much more efficient than single phase convection, due to the large density difference between steam and water, and the large latent heat of water. The one-dimensional model of two-phase convection developed by Hardee (1982) is used to relate heat flux and permeability within the hydrothermal system. In addition, Hardee (1980) produced a model of conduction through a migrating boundary layer, and related the migration velocity to the heat flux in the hydrothermal system, and hence to the permeability.

The theory of Lister (1974, 1983) produces values for the permeability created by the cracking process, as a function of infiltration velocity, and cracking temperature. The theories of Lister and Hardee can therefore be combined to produce a relationship between cracking temperature and infiltration velocity.

1.4.6 Advection of gas

On the basis of observed high temperature fumaroles at Poás, and periods of chloride-rich fluid inputs to both lakes, magmatic degassing occurs, at least intermittently, at Poás and Ruapehu. Magma emplaced at shallow depths will probably be super-saturated in volatiles, and thus will tend to vesiculate. Escape of gas from a magma represents an advective heat

loss, and will occur given a pathway for the gas, and a driving pressure gradient. Magmatic gas usually consists mainly of water; thus using the enthalpy of water at 1000 °C (~4 MJ kg^{-1}), steam flows of ~25-250 kg s^{-1} will provide 10^2 to 10^3 MW. Taking the water content of the magma to be 2-4 wt.%, then magma degassing rates of ~600-12000 kg s^{-1} would be needed to provide all of the energy.

These degassing rates are higher than the expected rate of emplacement of magma as shallow intrusions at the volcanoes, based on geophysical evidence (Otway, 1979; Brown et al., 1991), and are much greater than time-averaged erupted volumes at Ruapehu. This suggests that convection of magma to shallow depths is required, in order to supply sufficient gas-rich magma without large-scale deformation. A model of recirculating magma flow within a conduit, where vesiculation and gas loss occurs at the top of the conduit, and flow is induced by the density difference between volatile rich and degassed magma, is developed in chapter 6. This provides a mechanism for degassing deep magma reservoirs, and is probably applicable to many degassing volcanoes.

CHAPTER 2

A new mass, energy and chemical balance model for crater lakes

2.1 Introduction

In this chapter, a model is presented that uses some of the measured characteristics of crater lakes to constrain the mass and energy flows within these systems. The lake is considered as a totally separate system from the volcano as a whole, and a number of simplifications are made. The main assumption is that spot measurements of lake temperature and chemical content are representative of the lake as a whole, i.e. the lake is well mixed. This is thought to be usually, although not always, the case (e.g. see chapter 3).

Significant mass flows into and out of the lake are: (i) steam and brine from lake floor vents; and (ii) precipitation and runoff/meltflow (generally called rainfall/meltflow to avoid confusion with chemical precipitation, but including snowfall etc.); (iii) evaporation; and (iv) seepage and overflow. An equation balancing these mass flows with any change in the lake mass can be written (see section 2.2).

Similarly, the energy flows can be listed: (i) steam and brine adding heat through lake floor vents; (ii) evaporation cooling the lake's surface; (iii) seepage and overflow removing hot lake-water; (iv) sensible heat loss from the surface; and (v) radiation emitted from the lake surface. Again, a simple equation balancing these flows with any change in the stored energy content of the lake can be stated (see section 2.3). These two equations define the mass and energy balance model, and can be applied simultaneously to find two unknowns, if the other flows are known or can be estimated.

Major chemical flows are associated with: (i) the influx of (volatile-rich) steam and/or (metal-rich) brine from lake floor vents; and (ii) the seepage and overflow of lake brine. Differential equations relating steam/brine and overflow/seepage mass flows to changes in lake chemical

concentrations are stated. These can be used to constrain the overflow/seepage, and the chemical content of the incoming steam/brine mixture (see section 2.4). In turn, the chemical content of the steam/brine mixture is used to constrain its enthalpy (and hence the proportions of brine and steam) (see chapter 4).

In most cases, the major energy loss from a hot lake will be evaporation from its surface. Several theoretical and semi-empirical models have been developed for the calculation of surface losses from thermally loaded water bodies. Four of these models are reviewed in section 2.5, three of which have previously been used in crater lake studies: (i) Weisman and Brutsaert (1973), used by Hurst and Dibble (1981), Brown et al. (1989), and Hurst et al. (1991); (ii) Ryan et al. (1974), used by Brown et al. (1991); (iii) Sill (1983), not previously used; and (iv) Adams et al. (1990), used by Rowe et al. (1991a). The effects on surface losses of varying meteorological conditions are considered, as are the errors associated with the assumption of 'average' weather conditions. Many of the differences in final results between discrete crater lake studies simply reflect the use of different surface loss models, or different 'average' meteorological conditions.

Where appropriate in the following sections, the mass and energy balance model presented here is compared to previous work, and differences discussed. The application of the model, and the subsequent results are considered in future chapters.

2.2 Mass Balance

The mass balance is described diagrammatically in figure 2.1. The mass inflows and outflows to and from the lake, over the periods of time between lake measurements are considered. The masses are converted to average mass flow rates (M, in kg s^{-1}) for each time interval. Mass is added to the lake by steam/brine (at a rate $M_{st/br}$), and rainfall/meltflow (rate M_{rm}). Meltflow is important at crater lakes surrounded by glaciers (e.g. Ruapehu). Mass is lost through evaporation from the surface of the lake (rate M_{ev}), and seepage/overflow (rate M_{os}). Thus the rate of change of lake mass (ΔM) is given by (fig. 2.1):

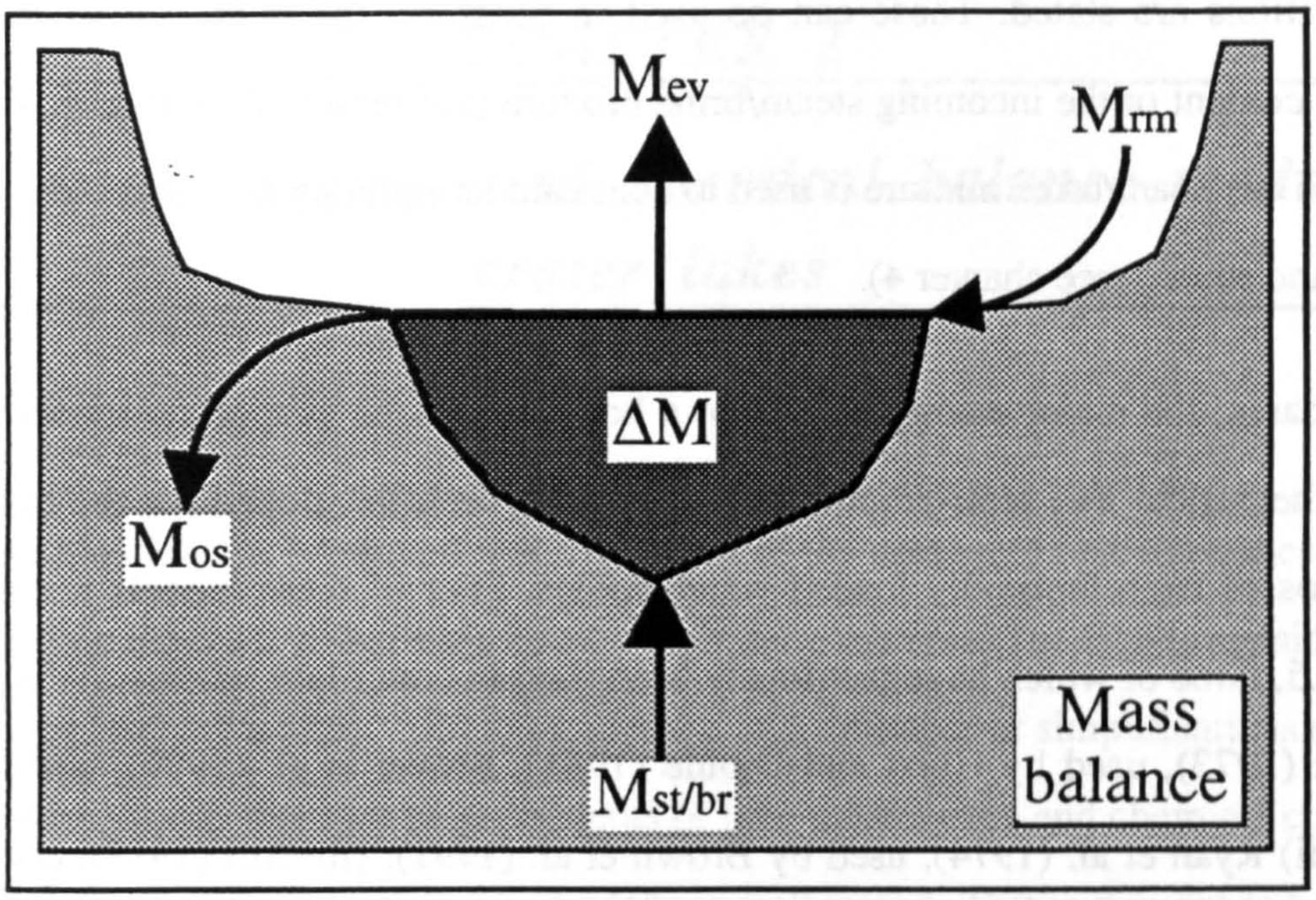

Figure 2.1 *Cartoon depicting the mass flows into and out of a heated crater lake. See text for definitions of the symbols.*

$$\Delta M = M_{st/br} + M_{rm} - M_{ev} - M_{os} \qquad (2.1).$$

If the bathymetry of the lake is constrained, then lake level measurements can be converted to give estimates of changes in lake surface area and volume between observations (and hence ΔM). If rainfall data exist for the summit region of the volcano (e.g. at Poás), then these data can be converted to minimum rainfall input rates to the lake ($M_{rm(min)}$) by estimating a 'minimum' catchment area (see chapter 4). A minimum estimate of overflow/seepage ($M_{os(min)}$) can be derived from lake chemistry data (see section 2.4), by assuming no new input of ions between measurements, and that ions are only lost through overflow/seepage. The evaporative mass loss (M_{ev}) can be estimated from the surface loss models discussed in section 2.5.1, using lake surface area, lake temperature, and ambient weather conditions. The steam/brine input rate is unknown; M_{rm} and M_{os} have minimum values.

2.3 Energy Balance

The energy balance is described diagrammatically in figure 2.2. Each mass flow has an energy content or enthalpy, H (units J kg^{-1}). Enthalpy is defined on a relative scale as:

$$H(T) = H(0) + \int_0^T c_p(T)\ dT$$

where c_p is the specific heat capacity. Quoted values of enthalpies are usually relative to water at 0 °C; with values for steam given by Rogers and Mayhew (1980), and values for brines by Mayrath and Wood (1982); typical values are given in table 2.1. Energy is added to the lake solely by steam/brine, at a rate $E_{st/br}$, which is the product of mass flow of steam/brine and its enthalpy ($E_{st/br} = M_{st/br} . H_{st/br}$). All energy rates have units of Watts ($W \equiv J\ s^{-1}$). Energy is lost from the lake by evaporation at the lake's surface at a rate E_{ev} (as above: $E_{ev} = M_{ev} . H_{ev}$). The overflow/seepage of hot lake water also results in an energy loss E_{os} ($E_{os} = M_{os} . H_{os}$). Additional lake surface energy losses not associated with mass flows are sensible heat (E_{sh}) and radiation (E_{ra}). Sensible heat loss is due to conductive heat transfer from hot lakewater to cold air. The air heats up and becomes lighter than overlying colder air, leading to convection. This loss, and the other surface losses are considered in detail in section 2.5.

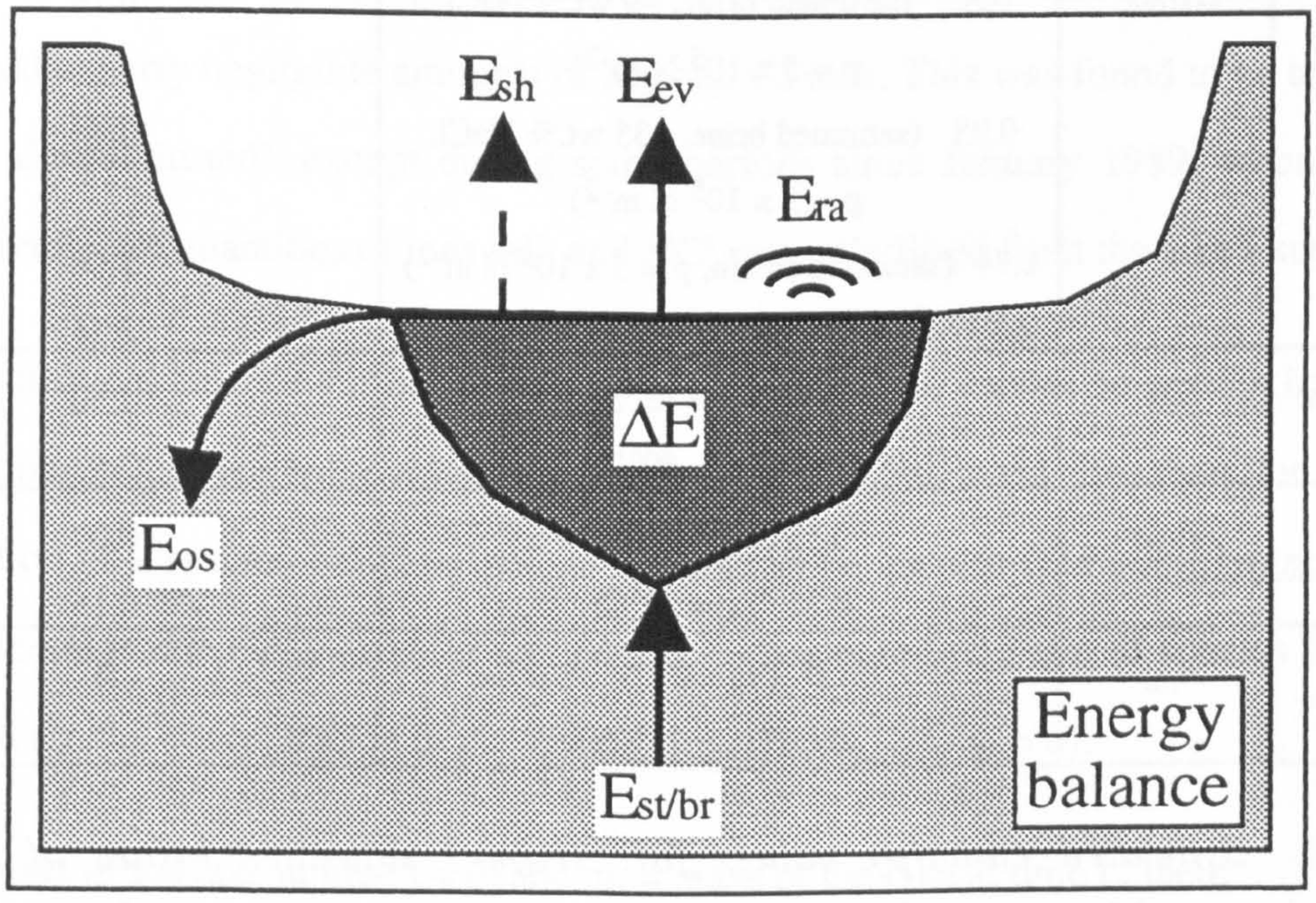

Figure 2.2 *Cartoon depicting the energy flows into and out of a heated crater lake. See text for definitions of the symbols.*

Quoted enthalpy values of water/steam (e.g. Rogers and Mayhew, 1980) are relative to water at 0°C; in this model all enthalpies are defined relative to water at ambient air temperatures (T_a). This adjustment of quoted enthalpy values is small (see table 2.1). Rainfall/meltflow is assumed to be at ambient air temperatures, thus its enthalpy is zero ($H_{rm} = 0$ J kg^{-1}); it therefore carries no energy. Thus the rate of change of energy stored in the lake (ΔE) is given by (fig. 2.2):

$$\Delta E = E_{st/br} - E_{ev} - E_{sh} - E_{ra} - E_{os} \qquad (2.2).$$

Using ΔM in conjunction with lake temperature measurements, and the specific heat capacity of lakewater, yields ΔE. If weather conditions (average windspeed, air temperature and humidity) and surface areas are known, then surface losses (E_{ev}, E_{sh}, E_{ra}) can be estimated from lake temperatures (see section 2.4).

Flow	Symbol	Enthalpy / MJ kg^{-1}	Corrected enthalpy (T_a=15°C)
Steam/ brine	$H_{st/br}$	0.8 (saturated brine, ~9 wt.% NaCl, p = 5 x 10^5 N m^{-2})	0.74
		0.95 (saturated brine, ~35 wt.% NaCl, p = 5 x 10^5 N m^{-2})	0.89
		2.74 (saturated steam, p = 5 x 10^5 N m^{-2})	2.68
		2.80 (saturated steam, p = 3 x 10^6 N m^{-2})	2.74
Evaporation	H_{ev}	2.56 (T_w = 30°C)	2.50
		2.59 (T_w = 50°C)	2.53
Overflow/ seepage	H_{os}	0.13 (T_w = 30°C)	0.07
		0.21 (T_w = 50°C)	0.15
Rainfall/ meltflow	H_{rm}	0 (T_a = 0°C)	0
		0.06 (T_a = 15°C)	

Table 2.1 *Estimated enthalpy values for: $H_{st/br}$ - saturated brines of two NaCl concentrations, and for saturated steam at two pressures, corresponding to ~50m and ~300m of hydrostatic pressure; H_{ev} and H_{os} - for water vapour and liquid at two temperatures; and H_{rm} for two ambient temperatures. The final column shows the corrected enthalpies for T_a = 15°C. From Rogers and Mayhew (1980) and Mayrath and Wood (1982).*

Thus equations (2.1) and (2.2) represent two simultaneous equations with two clear unknowns: $M_{st/br}$ and $H_{st/br}$; and two terms with minimum values: M_{rm} and M_{os}. Assuming values for $H_{st/br}$ and catchment area (A_{catch}) (see chapter 4), values for the unknown mass flows can be found for each time interval between measurement of lake characteristics, by iteratively increasing M_{os}, until the model produces a value of M_{rm} consistent with the assumed catchment area. The values of $H_{st/br}$ and A_{catch} are then adjusted, and the model re-run (see section 2.4).

2.4 Chemical Balance

The chemical balance is described diagramatically in fig. 2.3. Regular measurements are made of the concentrations of a number of chemical species in the lakes of Poás and Ruapehu. In this discussion, only magnesium and chloride ions will be considered in detail. Neither of these species is thought to be precipitated by reactions occurring within Ruapehu crater lake (Giggenbach, 1974), and the same will be assumed for Poás. Each mass flow will have a chemical content, [X] (units kg kg^{-1} of fluid), of species X. Rainfall/meltflow and evaporation are assumed to carry negligible amounts of Mg and Cl ions. This was found to be true at Poás (Rowe et al., submitted), except during some periods since January 1989, when acid rain carrying significant quantities of ions fell, and HCl was volatilised from the lake's surface.

A simple chemical balance similar to equations (2.1) and (2.2) cannot be written because the concentrations in the lake will evolve over the time period considered. However, the change in concentration of a species between measurements can be used to find a *minimum* value for overflow/seepage rate ($M_{os(min)}$) for that period, by assuming *no input* of species X over the time period (i.e.the concentration in the steam/brine is zero, $[X]_{st/br} = 0$):

Let m_o = mass of the lake at time t = 0, and m_t = mass of the lake at time t , then:

$$m_t = m_o + \Delta M\, t$$

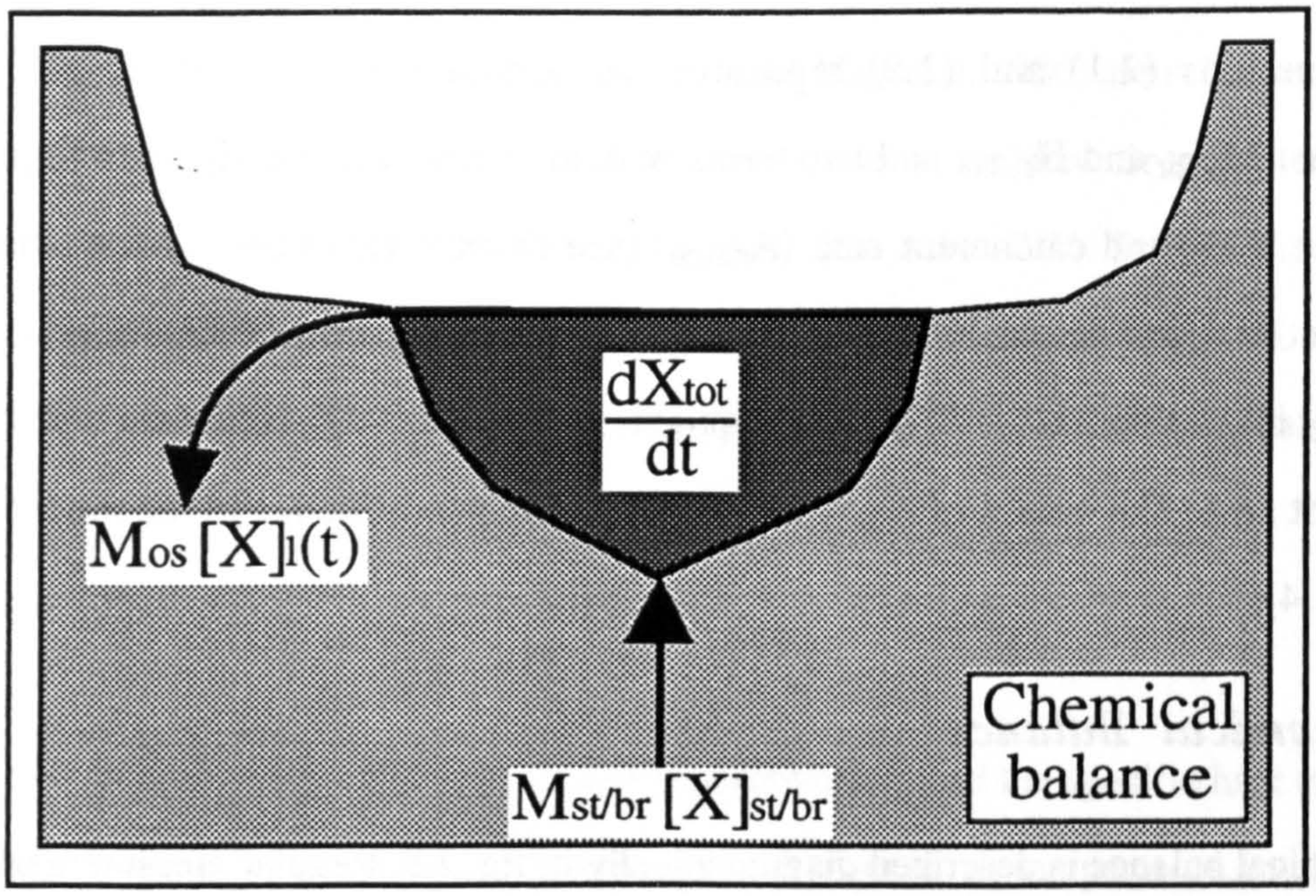

Figure 2.3 *Cartoon depicting the chemical flows into and out of a crater lake. See text for definitions of the symbols.*

Let X_o = the total mass of species X dissolved in the lake at time t = 0, and X_t = the total mass of species X dissolved in the lake at time t. It follows (fig. 2.3):

$$\frac{dX}{dt} = -M_{os(min)}\left(\frac{X_t}{m_t}\right) = -M_{os(min)}\left(\frac{X_t}{m_o + \Delta M\ t}\right) \qquad (2.3),$$

Integrating between 0 and t, we have:

$$\ln\left(\frac{X_t}{X_o}\right) = -\left(\frac{M_{os(min)}}{\Delta M}\right)\ln\left(\frac{m_t}{m_o}\right),$$

which gives:

$$M_{os(min)} = \Delta M\left(\frac{\ln\left(\frac{X_t}{X_o}\right)}{\ln\left(\frac{m_o}{m_t}\right)}\right) \qquad (2.4).$$

This minimum value is used initially as an input to the mass and energy balance model. Also input are assumed values for catchment area (A_{catch}) and steam/brine enthalpy ($H_{st/br}$) - these values are adjusted manually after considering model outputs (see below and chapters 3 and 4),

and the model re-run. The catchment area is used in conjunction with rainfall figures (at Poás) or estimates (at Ruapehu) to give a 'minimum' acceptable rainfall/meltflow rate ($M_{rm(min)}$) for a given period. If the output value of rainfall/meltflow ($M_{rm(mod)}$) for a given period is below $M_{rm(min)}$, then the M_{os} value input is increased (increasing M_{os} increases M_{rm}) iteratively until $M_{rm(mod)}$ exceeds $M_{rm(min)}$. If M_{os} has to be increased above the $M_{os(min)}$ value, this simply means that the assumption of zero influx of chemical species was wrong. Once a final value for M_{os} (for the assumed values of A_{catch} and $H_{st/br}$) has been found, the chemical measurements can then be used to find the required influx of chemicals. The concentration of a chemical species in the incoming steam/brine ($[X]_{st/br}$) can be found over each time period, assuming a steady influx rate. This can be found by rewriting equation (2.3) with an extra term:

$$\frac{dX}{dt} = -M_{os}\,[X]_t + k_1 \quad (2.5)$$

where $k_1 = M_{st/br}\,[X]_{st/br}$. Writing $X_t = [X]_t\, m_t$, differentiating this product gives:

$$m_t \frac{d[X]}{dt} + [X]_t\,\Delta M = -M_{os}\,[X]_t + k_1$$

Integrating between 0 and t, yields:

$$\left(\frac{-1}{M_{os} + \Delta M}\right) \ln\left(\frac{k_1 - (M_{os} + \Delta M)\,[X]_t}{k_1 - (M_{os} + \Delta M)\,[X]_o}\right) = \frac{1}{\Delta M} \ln\left(\frac{m_t}{m_o}\right),$$

Eliminating the logs gives:

$$\frac{k_1 - (M_{os} + \Delta M)\,[X]_t}{k_1 - (M_{os} + \Delta M)\,[X]_o} = \left(\frac{m_o}{m_t}\right)^{\left(\frac{M_{os} + \Delta M}{\Delta M}\right)},$$

re-arranging, and substituting $k_1 = M_{st/br}\,[X]_{st/br}$, gives:

$$[X]_{st/br} = \left(\frac{M_{os} + \Delta M}{M_{st/br}}\right)\left([X]_t - [X]_o \left(\frac{m_o}{m_t}\right)^{\left(\frac{M_{os} + \Delta M}{\Delta M}\right)}\right)\left(1 - \left(\frac{m_o}{m_t}\right)^{\left(\frac{M_{os} + \Delta M}{\Delta M}\right)}\right)^{-1}$$

(2.6a),

or, when $\Delta M = 0$, the original equation simplifies to:

$$m_t \frac{d[X]}{dt} = -M_{os}\,[X]_t + k_1$$

and again, integrating with the same limits as above, yields:

$$\frac{-1}{M_{os}} \ln\left(\frac{k_1 - M_{os}\,[X]_t}{k_1 - M_{os}\,[X]_o}\right) = \frac{t}{m_o} \quad ,$$

re-arranging, and substituting $k_1 = M_{st/br}\,[X]_{st/br}$, gives:

$$[X]_{st/br} = \frac{M_{os}}{M_{st/br}}\left([X]_t - [X]_o \exp\left(\frac{-M_{os}\,t}{m_o}\right)\right)\left(1 - \exp\left(\frac{-M_{os}\,t}{m_o}\right)\right)^{-1} \qquad (2.6b).$$

The value of $[X]_{st/br}$ can be used to constrain the value of $H_{st/br}$, if the concentration of X in the brine and steam is assumed. Metal ions (Mg is used here) cannot be carried in significant quantities by steam, thus only the brine content need be assumed. This is estimated using the lake-water content as a lower bound (see chapter 4).

The catchment area can be constrained by looking at the final outputs of M_{rm} (i.e. once M_{os} has reached its final value for the given inputs), for different assumed 'minimum' values of A_{catch}. During some time periods, when the chemistry of the lake decreased rapidly, large values of $M_{os(min)}$ are input, which produce outputs of $M_{rm(mod)}$ that are already above the minimum values, thus an iterative increase in M_{os} is not required. Presumably, A_{catch} remains approximately constant with time, thus the best estimate of A_{catch} will be when the assumed input value of A_{catch} produces values of $M_{rm(min)}$ that just match the highest output(s) of $M_{rm(mod)}$ produced using $M_{os} = M_{os(min)}$. This procedure is followed in chapter 4.

2.5 Surface Losses

Energy losses from the lake's surface are: evaporation, sensible heat, and radiation (see review by Henderson-Sellers, 1986). Evaporation is usually the largest loss, and is the only one that also removes mass; it has also provoked the most interest in the literature, with numerous different equations quoted for its calculation. In the following three sections, the three losses are considered in detail, with an aim to assessing how useful previous crater lake models were,

and to identify the most realistic equations to use in future work.

2.5.1. Evaporation

Evaporation is the process whereby molecules of liquid at the lake's surface obtain enough energy to overcome inter-molecular binding forces, become a vapour and rise into the atmosphere. The lake therefore loses the energy required for the phase transition (the latent heat of vaporization, $L_w(T)$, which is a weak function of temperature), and also the energy contained in the initial liquid (its enthalpy, $H_l(T)$). This second term is usually much smaller than the first, and is generally ignored in 'normal' lake modelling, because lake temperatures are near ambient. However, for volcanic lakes at elevated temperatures, it needs to be taken into account. This can simply be done by using the enthalpy of the vapour, $H_{ev}(T)$, which is equivalent to the sum of the latent heat of vaporization and the liquid enthalpy. Thus at a given temperature, the following is evaluated:

$$H_{ev} = H_l + L_w \qquad (2.7).$$

Quoted water and vapour enthalpies refer to a base enthalpy equal to zero for water at 0°C (Rogers and Mayhew, 1980). The base enthalpy in the model presented here is defined as zero for water at the ambient air temperature for a specific location. Quoted enthalpies are therefore adjusted by the necessary amount (see table 2.1).

Many attempts have been made to calculate the evaporative losses from a water body. Dalton (1802) was the first to recognise that evaporation increased with (i) higher water temperature, (ii) higher windspeeds, and (iii) lower background humidity. These properties were eventually stated as an equation by Stelling (1882):

$$\Phi = (A + B\,u)\,(e_w - e_a) \qquad (2.8a),$$

where Φ is the rate of evaporation, as height of water per unit time; A and B are empirical constants, u is the mean windspeed, e_w is the saturation vapour pressure in air at the temperature of the water surface (T_w), and e_a is the ambient air vapour pressure. In stating this

equation, Stelling (1882) also observed that evaporation occurred even at zero windspeed - hence the constant A. This equation proved very successful for predicting evaporation, with many attempts made to optimize the values of A and B for different conditions, and it is still widely used today (e.g. Harbeck, 1962). The equation can be restated as an evaporative energy flux (ϕ_e, units W m^{-2}) in terms of the vapour concentration in air at a given temperature (q):

$$\phi_e = H_{ev} (A' + B' u) (q_w - q_a) \qquad (2.8b),$$

where q_w is the saturation vapour concentration in air at temperature T_w, and q_a is the vapour concentration in ambient air. Constants A' and B' tend to be site specific, and require long periods of monitoring to find their values before equation (2.8b) can be used predictively. It is shown in the following surface loss models, which seek to explain some of the physics of evaporation, that A' and B' are actually dependent on the average meteorological conditions at a given site. Four surface loss models will now be considered in detail.

2.5.1.1 Weisman and Brutsaert (1973)

Weisman and Brutsaert (1973) (hereafter WB) have produced a theoretical evaporation model for a warm lake under unstable atmospheric conditions. The WB model was specifically designed for use over: (i) deep lakes during autumn (i.e. when they are still significantly warmer than air); and (ii) bodies of water subject to thermal pollution. This approach should, therefore, be applicable to crater lakes, and has been used in mass/energy balance models of the crater lakes of Ruapehu (Hurst and Dibble (1981), and Hurst et al.(1991)) and Poás volcanoes (Brown et al., 1989).

WB considered what happens when a neutrally stratified (i.e. stable) air mass, with a wind profile decreasing downwards, encounters the unstable situation occurring over a relatively warm water body. Instability over the warm water occurs for two reasons: (i) warm air (heated by the lake) is less dense than cold air, and (ii) water vapour has a lower density than air (p.40, Eskinazi, 1975). The instability is usually great enough to lead to turbulent convection of air and water vapour, producing an upwards flux of particles. WB applied two-dimensional

conservation of momentum, sensible heat, and water vapour to an air mass above a warm lake, subject to a combination of a lateral advection (due to wind) and vertical advection. WB produced the following equation for the evaporative flux (ϕ_{ewb}):

$$\phi_{ewb} = H_{ev}\, W\, u_f\, (q_w - q_a) \qquad (2.9);$$

where u_f is the friction velocity (see below), and W is the dimensionless average vertical particle flux. This particle flux was calculated by WB via. a number of steps. Firstly, two dimensionless parameters χ and φ were evaluated:

$$\chi = \frac{k\, g\, Z_0}{u_f^2}\left(\frac{T_a - T_w}{T_a}\right) \qquad (2.10a)$$

$$\varphi = 0.61\,\frac{k\, g\, Z_0}{u_f^2}\,(q_a - q_w) \qquad (2.10b),$$

where k is the von Kármán constant (a universal constant, see Brutsaert, 1982, p.58), g is the acceleration due to gravity, and Z_0 is the surface roughness length of the water surface. The surface roughness length is a function of the mean height and shape of the roughness obstacles; values for water are typically 0.01-0.06 cm, with an average value of 0.02 cm (Brutsaert, 1982). The WB model is quite strongly dependent upon the value assumed for Z_0, and one of the approximations of the model is that roughness length is assumed continuous across the land/water boundary. Values of χ and φ can then be used to look up values of a and n in tables 2.2 and 2.3, which feature in the equation for W:

$$W = a\left(\frac{X_0}{Z_0}\right)^{-n} \qquad (2.11),$$

where X_0 is the fetch (i.e. a representative size dimension of the water body).

The friction velocity, u_f, is not a parameter that can be directly measured. It can be found indirectly by measuring windspeed at a given height, and assuming a roughness length and a wind profile. The most commonly used (e.g. Hurst and Dibble, 1981) wind profile is a logarithmic one:

			-χ		
-φ	0.1	0.05	0.01	0.0001	0
0.01			0.121	0.112	0.122
0.003	0.150	0.140	0.120	0.135	0.166
0.001			0.112	0.152	0.167
0			0.120	0.167	0.210

Table 2.2 *Values of a in equation (2.11), from WB.*

			-χ		
−φ	0.1	0.05	0.01	0.0001	0
0.01			0.036	0.042	0.045
0.003	0.025	0.034	0.046	0.081	0.089
0.001			0.042	0.082	0.093
0			0.045	0.093	0.112

Table 2.3 *Values of n in equation (2.11), from WB.*

$$u_z = \frac{u_f}{k} \ln\left(\frac{z}{Z_0}\right) \qquad (2.12),$$

where u_z is the windspeed at height z. Weisman (1975), however, suggested that a logarithmic wind profile is unsuitable for unstable conditions. He suggested that a power law profile as recommended by Brutsaert and Yeh (1970) be used instead:

$$u_z = C\, u_f \left(\frac{z}{Z_0}\right)^m \qquad (2.13),$$

where C and m vary with the degree of instablity, with quoted values of C=7.38 and m=0.11. Since the situation above crater lakes is almost always going to be unstable, this is the wind profile used here.

Outputs from the WB model of evaporative flux (ϕ_{ewb}) over a range of windspeeds, water temperatures, values of surface roughness and fetch are shown in figures 2.4 and 2.5. The plots do not always extend to zero windspeed (or high surface temperatures) because values of χ and φ are outside the range quoted in tables 2.2 and 2.3, making it impossible to calculate W. Figure 2.4 shows approximately exponential increases of evaporative flux (ϕ_{ewb}) with surface temperature (T_w). Figure 2.5 shows approximately linear increases in ϕ_{ewb} with windspeed; however, the linearity breaks down at high water temperatures ($T_w > \sim 30°C$). At a surface temperature of 50°C the WB model suggests very little increase in ϕ_{ewb} between windspeeds of ~2.5 and ~3.5 m s^{-1} ($Z_0 = 0.02$cm), and an actual decrease in ϕ_{ewb} between 3.25 and 4 m s^{-1} ($Z_0 = 0.04$cm). Results from the WB model are strongly dependent upon the surface roughness length (Z_0); an increase in Z_0 from 0.02cm to 0.04cm increases ϕ_{ewb} by ~10-40%. Results are also weakly dependent upon fetch (X_0); a decrease in X_0 from 500m to 250m produces an increase in ϕ_{ewb} of ~5-10%. A comparison with the other models is given in section 2.5.1.5.

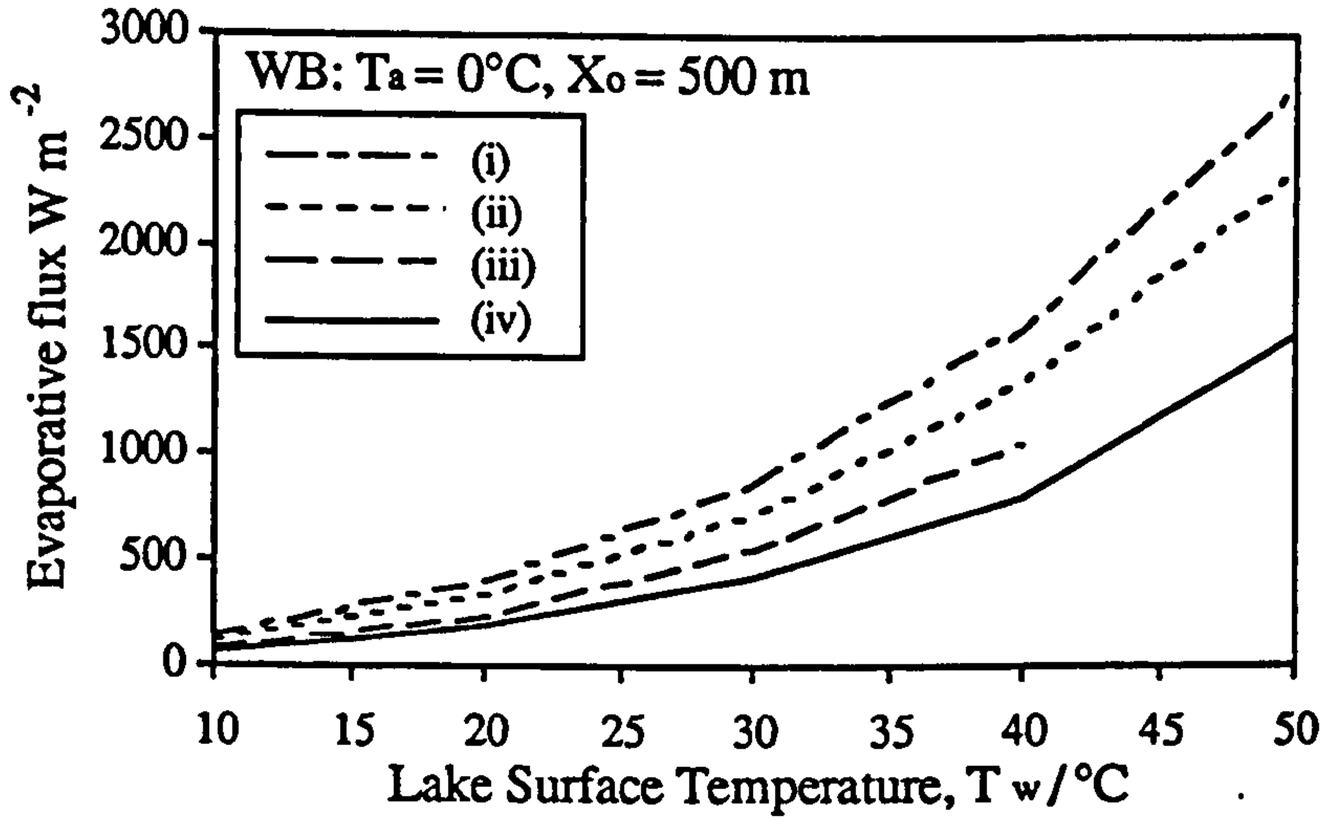

Figure 2.4 *Evaporative fluxes produced by the WB model, for two windspeeds, two surface roughnesses, and over a range of surface temperatures. (i) $u_2 = 5$ m s^{-1}, $Z_0 = 0.04$ cm, (ii) $u_2 = 5$ m s^{-1}, $Z_0 = 0.02$ cm, (iii) $u_2 = 2.5$ m s^{-1}, $Z_0 = 0.04$ cm, (iv) $u_2 = 2.5$ m s^{-1}, $Z_0 = 0.02$ cm. Ambient temperature (T_a) 0°C, humidity (ψ) 100%, and fetch (X_0) 500 m.*

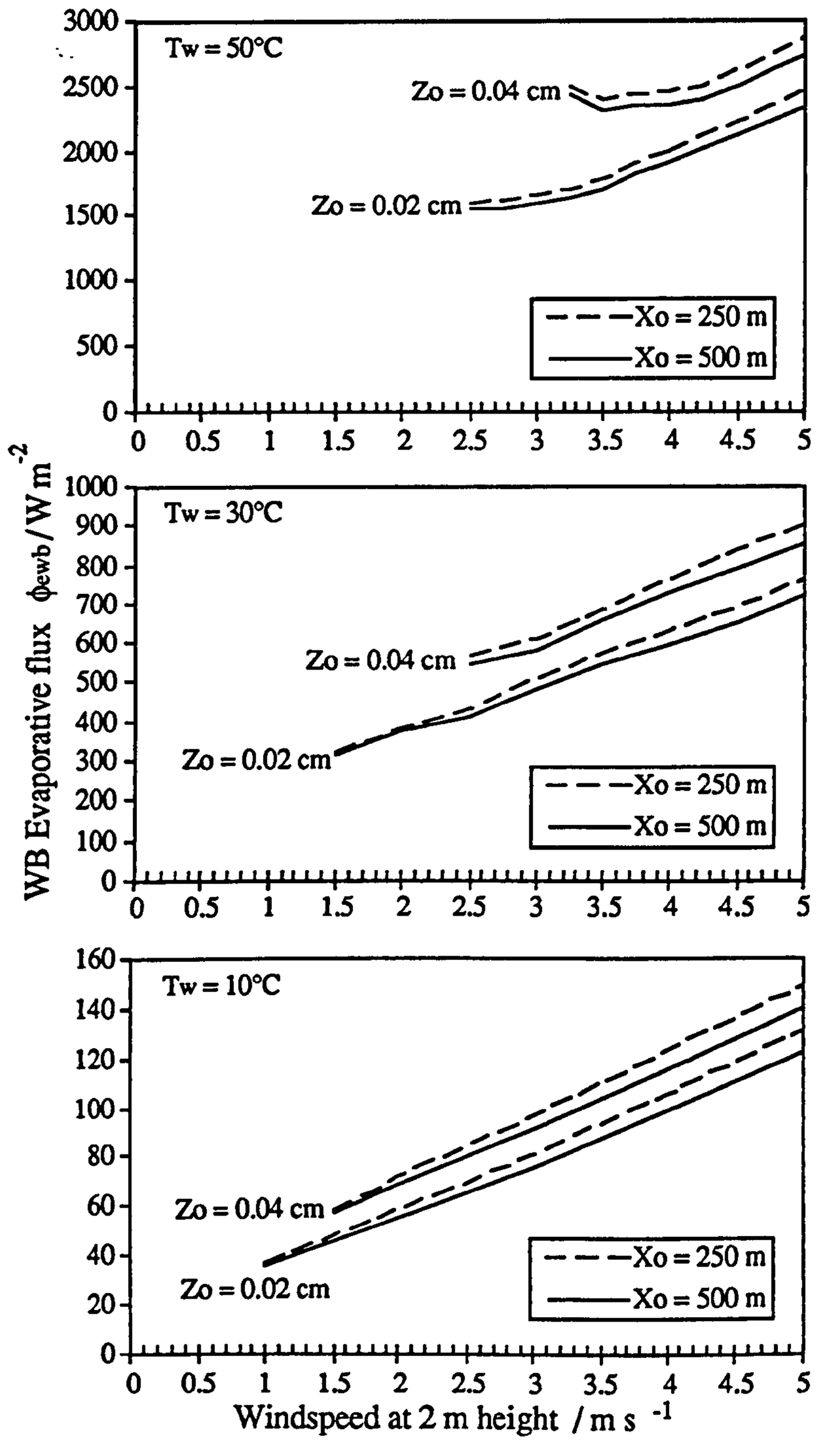

Figure 2.5 *Evaporative fluxes produced by the WB model, for three surface temperatures (10, 30, 50 °C), over a range of windspeeds (0 - 5 m s^{-1}), for two roughness lengths (0.02, 0.04 cm), and two fetches (250, 500 m). T_a = 0 °C, and ψ = 100 %.*

2.5.1.2 Ryan et al. (1974)

Ryan et al. (1974) (hereafter RY) have produced an evaporation model based on heat losses from power station cooling ponds. These are bodies of water used by the electricity industry for cooling waste water, before it is re-used or returned to the environment. Typical surface temperatures are up to 30°C above ambient, areas are 5×10^6 - 10^7 m^2, whilst depths are only a few metres (Jirka et al., 1978). These ponds are therefore comparable to crater lakes in temperature and surface area, if not in depth. The RY model was used by Brown et al. (1991) to estimate losses from Poás crater lake.

In the RY model, evaporation was separated into two components: one due to free convection in the air above the lake, and the second due to forced convection (wind); these correspond to A and B in equation (2.8). The free convection component was calculated on a theoretical basis (see below), and then tested against laboratory evaporation data, measured from heated tanks of water under zero windspeed conditions. The theoretical model was found to have a good fit (~±10%) with the data. The forced convection term was then found empirically, by using observed evaporation data from (outdoor) cooling ponds together with measured average windspeeds. Increases in evaporation above the free convective value were assumed to be due to wind (i.e. forced convection). A curve was fitted to the observed data in order to assess the relationship between forced convection and windspeed, assuming that the free convection term remained unaffected by the wind.

(i) Free Convective Evaporation

Free convection of vapour in the air above the lake occurs because hot water vapour molecules, lost from the lake's surface, are lighter than surrounding air. The convection induced by the density instability introduces dryer air into the region directly above the lake surface, thus encouraging evaporation. The loss is modelled by comparing it with the well studied situation of free convection of (dry) air above a hot plate (Kraichnan, 1962). Convection of air also occurs above a hot water body - this has already been termed the sensible heat loss (ϕ_{sh}). The

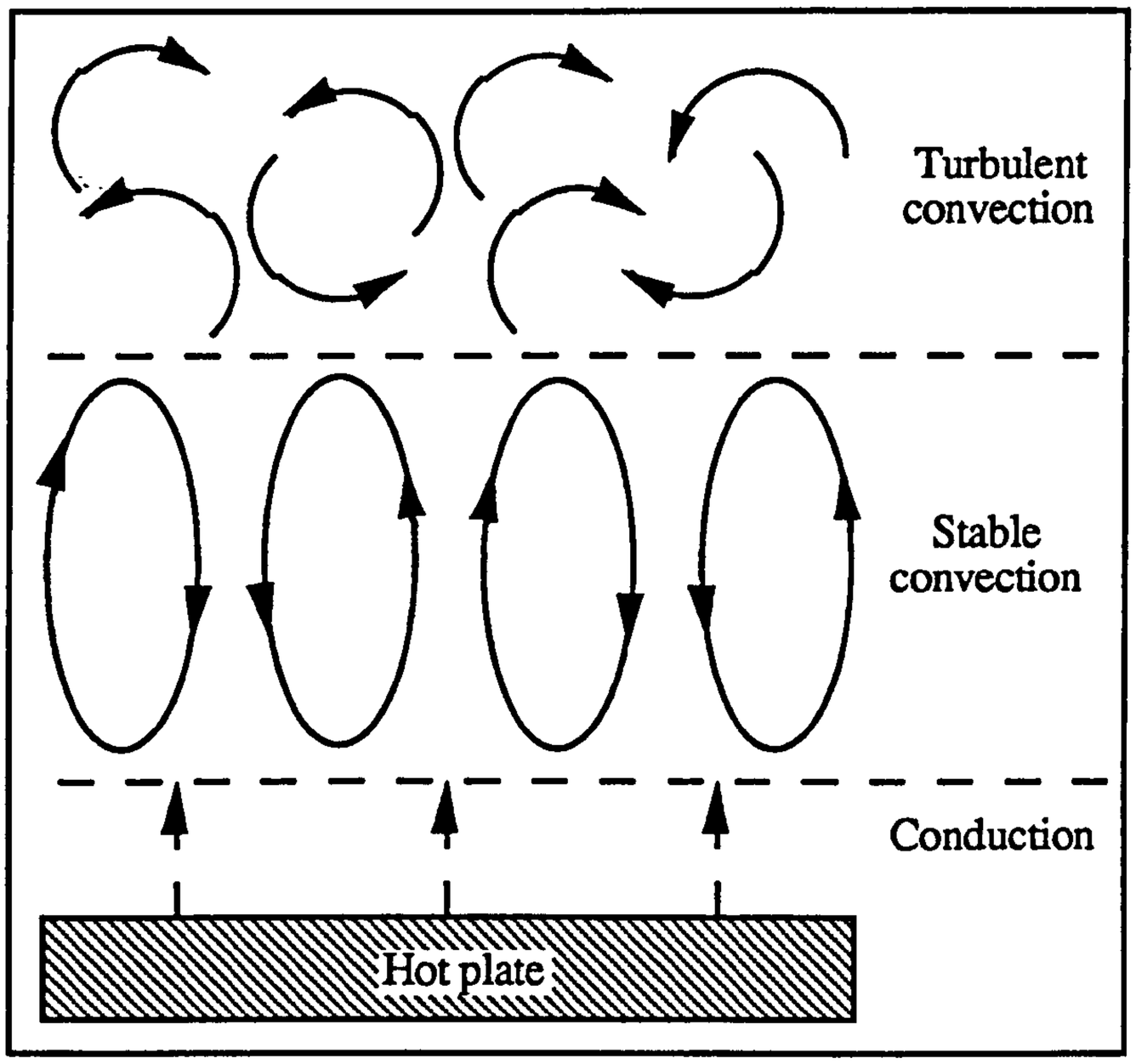

Figure 2.6 *Conduction and free convection of air above a heated surface, which leads to the free convective sensible heat loss ($\phi_{sh(free)}$).*

following equations explain the theory behind the free convective component of the sensible heat loss, and the relationship between this and the free convective evaporative loss. The relation will be returned to when the sensible heat loss is considered.

Above a hot plate, three main regions will develop (Kraichnan, 1962), as illustrated in fig. 2.6. These layers produce a relationship between the free convective sensible heat flux ($\phi_{sh(free)}$) and the temperature contrast between the plate and the air ($\Delta T = T_s - T_a$), stated as (Jaluria, 1987):

$$Nu = 0.14\ (Ra)^{1/3} \qquad Ra > 2 \times 10^8 \qquad (2.14a),$$

where Nu is the Nusselt number (the ratio between total heat transfer and that by conduction alone), and Ra is the Rayleigh number:

$$Nu = \frac{\phi_{sh(free)}\, l}{\rho\ \alpha\ C_p\ \Delta T} \qquad (2.14b),$$

$$Ra = \frac{l^3 \beta g \Delta T}{\nu \alpha} \qquad (2.14c),$$

where l is the height of the system, and ρ, α, C_p, β, and ν are the density, thermal diffusivity, specific heat capacity, coefficient of thermal expansion, and kinematic viscosity of air respectively (see Table 2.4 for values). Combining equations (2.14a-c), the resulting expression for the free convective sensible heat flux is:

$$\phi_{sh(free)} = 0.14 \rho C_p \Delta T \left(\frac{g \beta \alpha^2 \Delta T}{\nu}\right)^{1/3} \qquad (2.15).$$

This is the heat flux due to convection of air molecules above a heated plate (or water body). The expression can be rewritten in terms of a bulk heat transfer coefficient (k_h):

$$\phi_{sh(free)} = k_h \rho C_p \Delta T \qquad (2.16),$$

$$\text{where:} \qquad k_h = 0.14 \left(\frac{g \beta \alpha^2 \Delta T}{\nu}\right)^{1/3}$$

What we require is the heat flux due to the evaporation and subsequent free convection of water molecules in air above a hot water surface ($\phi_{e(free)}$). This can be written in terms of the humidity difference between ambient air and air directly above the water surface ($\Delta q = q_w - q_a$), the water vapour enthalpy (H_{ev}), and a bulk mass transfer coefficient (k_m):

$$\phi_{e(free)} = k_m \Delta q H_{ev} \qquad (2.17),$$

Equations (2.16) and (2.17) are now related by assuming the two coefficients to be equal, i.e. $k_m = k_h$. This was found to be true for numerous cases by Monin and Yaglom (1971) and Brutsaert (1982). The free convective evaporative heat flux is therefore given by:

$$\phi_{e(free)} = \lambda' (\Delta T)^{1/3} \Delta q H_{ev} \qquad (2.18),$$

$$\text{where } \lambda' \text{ is a constant, } = 0.14 \left(\frac{g \beta \alpha^2}{\nu}\right)^{1/3} \quad \text{(see table 2.4 for values),}$$

At this stage, RY converted vapour concentrations (q) to vapour pressures (e) by the ideal gas approximation:

$$q = \frac{M_{H_2O}\, e}{R\ T} \qquad (2.19a),$$

where M_{H_2O} is the molecular weight of water and R is the universal gas constant (see table 2.4 for values). The value of T used should be the temperature of the air packet considered, e.g. the vapour concentration in the air (at temperature T_w) directly above the water surface (q_w) is given by:

$$q_w = \frac{M_{H_2O}\, e_w}{R\ T_w} \qquad (2.19b).$$

However, T is stated in RY to be the mean absolute air temperature; the value used seems to be 288K. RY also incorporated a vapour enthalpy (quoted as a latent heat of vaporization (L), but actually equal to 2.55×10^6 J kg^{-1}) in their equivalent 'constant', λ:

$$\phi_{e(free)} = \lambda\, (\Delta T)^{1/3}\, (e_w - e_a) \qquad (2.20),$$

$$\lambda = 0.14 \left(\frac{L\, M_{H_2O}}{R\ T}\right)\left(\frac{g\ \beta\ \alpha^2}{\nu}\right)^{1/3} \qquad \text{(see table 2.4 for values).}$$

These approximations are unnecessary, and equation 2.20 is less useful than equation 2.18, because it incorporates approximations that increase errors with higher water surface temperatures, mainly due to the assumption of the constant value of T in the equation for λ.

One further refinement of the equation is required however, because the convecting fluid is now moist air, which has a lower density than dry air, and therefore increased buoyancy. RY overcame this problem by using virtual temperatures (T_v), where:

$$T_v = \frac{T}{\left(1 - \frac{0.378\ e}{P}\right)} \qquad (2.21);$$

e is the water vapour pressure in air at temperature T, and P is the atmospheric pressure. The

virtual temperature of moist air is the temperature of dry air at the same density. Thus RY concluded that the free convective evaporative flux could be written:

$$\phi_{ery(free)} = \lambda\,(\Delta T_v)^{1/3}\,(e_w - e_a) \qquad (2.22),$$

where $\Delta T_v = T_{wv} - T_{av}$. However, using the arguments outlined above, the free convective evaporative flux can be more accurately written as:

$$\phi_{e(free)} = \lambda'\,H_{ev}\,(\Delta T_v)^{1/3}\,\Delta q \quad (2.23).$$

Equation (2.22) was found by RY to have a good fit with laboratory evaporation data at zero windspeed over various bodies of water, with ΔT_v up to ~30°C, and surface areas up to 84 m^2. If the physical basis of the model is correct, then equation (2.22) should overpredict at higher temperatures, because λ will be too large, due to the value of T used being too small. Equation (2.23) should be a better fit at higher temperatures, and both of the equations should produce similar results at $\Delta T_v < 30$°C.

Symbol	Meaning	h = 0 m T_a = 288 K	h = 2500 m T_a = 273 K	Units
α	Thermal Diffusivity	2.03×10^{-5}	2.48×10^{-5}	$m^2\,s^{-1}$
β	Coefficient of thermal expansion	3.47×10^{-3}	3.66×10^{-3}	K^{-1}
ν	Kinematic viscosity	1.46×10^{-5}	1.79×10^{-5}	$m^2\,s^{-1}$
ρ	Density	1.225	0.957	$kg\,m^{-3}$
g	Acceleration due to gravity	9.81	9.80	$m\,s^{-2}$
M_{H_2O}	Molecular weight of H_2O	0.018	0.018	$kg\,mol^{-1}$
R	Universal gas constant	8.31	8.31	$J\,mol^{-1}\,K^{-1}$
C_p	Specific heat capacity at constant pressure	1005	1004	$J\,kg^{-1}\,K^{-1}$
λ	Constant in equation 2.20	0.027	0.029	$m\,s^{-1}\,(K)^{-1/3}$
λ'	Constant in equation 2.18	0.0014	0.0015	$m\,s^{-1}\,(K)^{-1/3}$
b_0	Constant in equation 2.24	0.0017	0.0018	None

Table 2.4 *Physical properties of air, at two altitudes (h) and two ambient temperatures, and resulting 'constants'. From Rogers and Mayhew (1980), and Kakaç et al. (1987).*

(ii) Forced Convective Evaporation

RY proceeded by simply adding a forced convection term to equation (2.22) empirically. This was done by using observed evaporation data from cooling ponds at known windspeeds. Increases in evaporation above the free convective value were found to be directly proportional to increases in windspeed; thus a simple constant (b_o) multiplied by windspeed (u) term was added to equation (2.22), giving:

$$\phi_{ery(total)} = (\lambda\,(\Delta T_v)^{1/3} + b_o\,u_2)\,(e_w - e_2) \qquad (2.24),$$

where a subscript of 2 defines conditions at 2m height. RY acknowledged that the constant b_o may be weakly dependent on lake area, but that this effect is small enough to be swamped by other errors. Equation (2.24) was tested against two other data sets, and found to have reasonable agreement for values of $\phi_{ery(total)}$ up to ~600 W m^{-2}. Thus this equation is probably valid for values of $\Delta T_v < 30°C$, and $\phi_{ery(total)} < 600$ W m^{-2}. Beyond these limits, the model is theoretically more questionable in its free convection approximation, and untested overall.

Plots of $\phi_{ery(total)}$ for various values of water temperature and windspeed are shown in figures

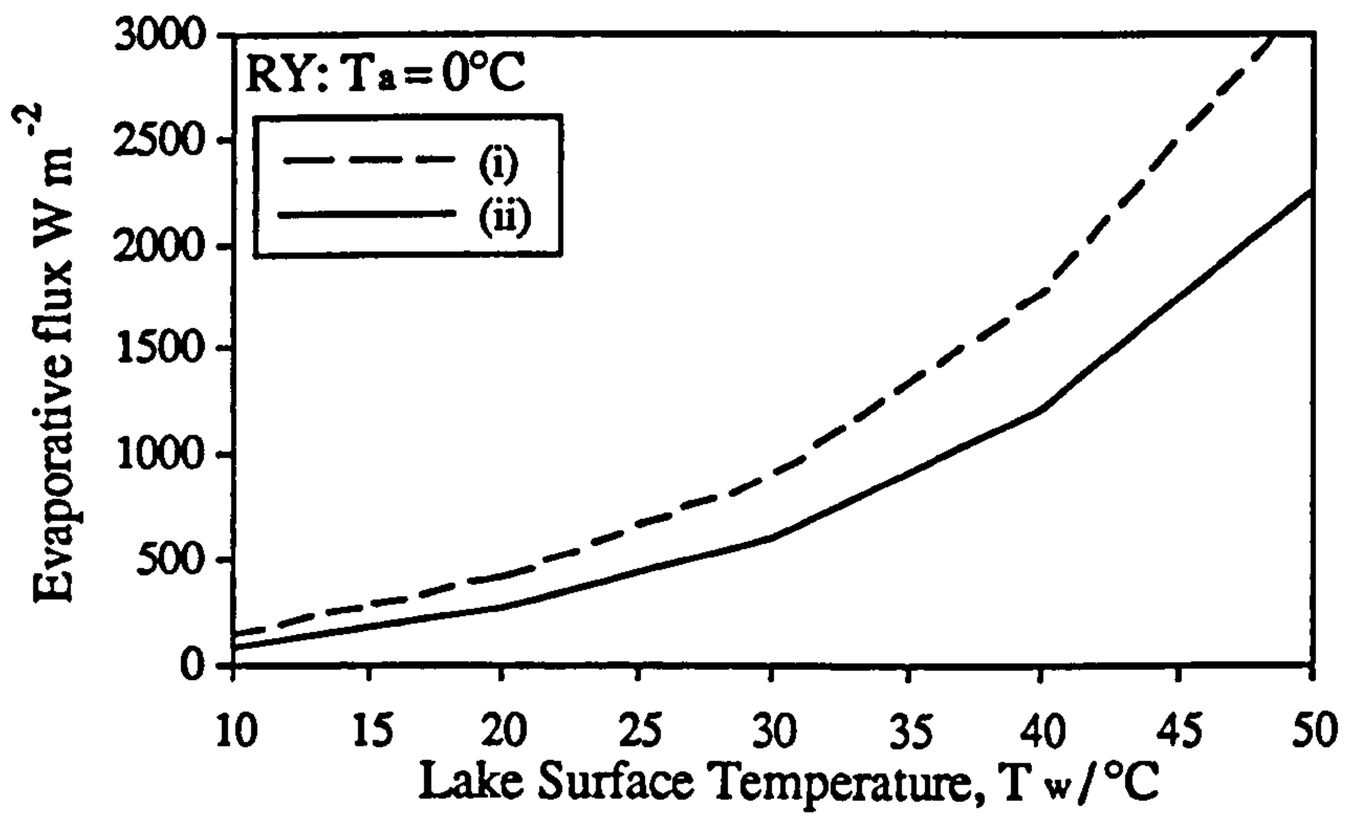

***Figure 2.7** Evaporative fluxes ($\phi_{ery(total)}$) produced by the RY model, for two windspeeds and over a range of surface temperatures. (i) $u_2 = 5$ m s^{-1}, (ii) $u_2 = 2.5$ m s^{-1}. Ambient temperature (T_a) 0°C, humidity 100%.*

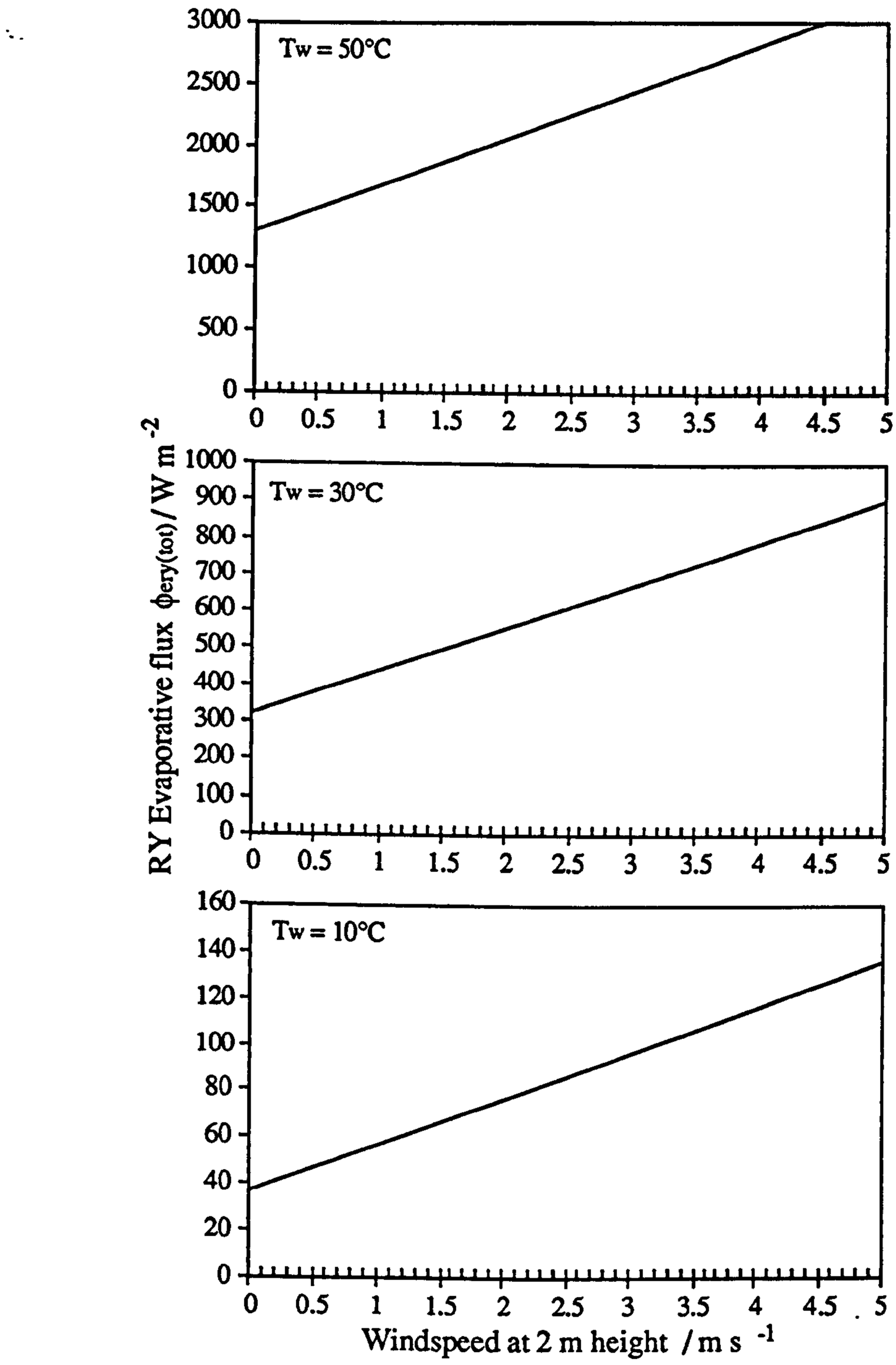

Figure 2.8 *Evaporative fluxes produced by the RY model, for three surface temperatures (10, 30, 50 °C), and over a range of windspeeds. Ambient temperature 0 °C, humidity 100 %.*

2.7 and 2.8. $\phi_{ery(total)}$ increases exponentially with surface temperature, and linearly with windspeed. The effects of different surface roughness lengths and fetches are not considered by RY. A comparison with the other models is given in section 2.5.1.5.

2.5.1.3 Sill (1983)

Another model which attempts to unify existing evaporation equations, for a broad range of conditions (i.e. 'normal' to heated lakes) was developed by Sill (1983) (hereafter SI). The initial evaporation equation (2.8b) was restated as:

$$\phi_{esi} = H_{ev} (Da_{fr} + Da_{fo}) u_z \Delta q \qquad (2.8c),$$

where Da_{fr} is the free convection Dalton number, and Da_{fo} is the forced convection Dalton number. The two Dalton numbers can be written as:

$$Da_{fr} = \frac{\lambda' (\Delta T_v)^{1/3}}{u_z} \qquad (2.25),$$

$$Da_{fo} = Cd_z \quad \text{(for 'rough' surfaces)} \quad (2.26),$$

where Cd_z is the drag coefficient at height z. At zero windspeed, Cd_z is equal to zero, thus substitution of equation (2.25) into equation (2.8c) yields equation (2.23). Brutsaert (1982) gives the following equation for Cd_z over water at ten metres height:

$$Cd_{10} = a (Z_{0+})^b \qquad (2.27),$$

where a and b are empirical constants: a = 0.0012 and b = 0.15; and Z_{0+} is the roughness Reynolds number, a dimensionless form of the roughness length (Z_0), normalised using the friction velocity (u_f) and the kinematic viscosity (ν), given by (Brutsaert, 1982):

$$Z_{0+} = \frac{u_f Z_0}{\nu} \qquad (2.28).$$

SI went on to consider whether it was reasonable to simply sum the forced and free convective terms. This was the procedure followed in the past (e.g. RY), for which there was no

theoretical justification. He found that at relatively high windspeeds, or relatively low water temperatures, the lateral movement of air (forced convection) seemed to disrupt the free convection cells, reducing the free convection mechanism of evaporation. This implied that equation (2.8c) would overestimate losses in these situations. To overcome this problem, SI suggested a two part evaporation formula:

$$\phi_{esi} = H_{ev}\ (1 + C_r)\ Cd_z\ u_z\ \Delta q \qquad \text{(for } C_r \geq 1.37\text{)} \qquad \text{(2.29a)},$$

$$\phi_{esi} = H_{ev}\ (1 + 0.73\ C_r{}^2)\ Cd_z\ u_z\ \Delta q \qquad \text{(for } C_r \leq 1.37\text{)} \qquad \text{(2.29b)},$$

where C_r was defined as the ratio between free and forced evaporation:

$$C_r = \frac{Da_{fr}}{Da_{fo}} = \frac{\lambda'\ (\Delta T_v)^{1/3}}{u_z\ Cd_z} \qquad \text{(2.30)}.$$

Equation (2.29b) is used when windspeeds reach the level at which they start to disrupt the free convection cells. Equations (2.29) were tested rigourously by SI, using data from six large U.S. lakes (including Lake Hefner, Lake Colarado City, and Lake Mead), and also one small (60 m by 60 m) pond. SI considers that the formulae are applicable to a wide range of conditions, including thermally loaded lakes.

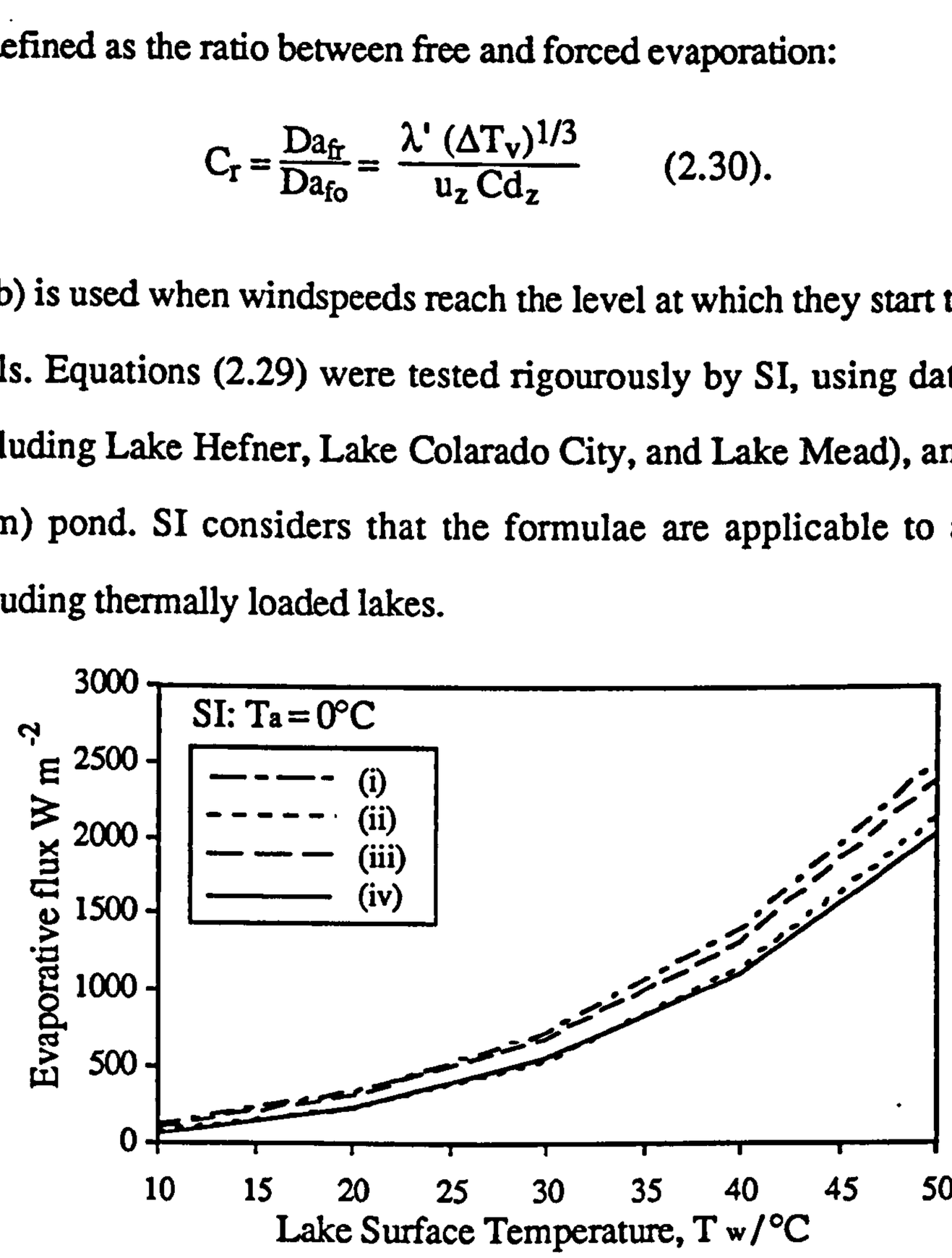

Figure 2.9. *Evaporative fluxes produced by the SI model (ϕ_{esi}) for two windspeeds, two surface roughnesses, and over a range of surface temperatures. (i) $u_2 = 5\ m\ s^{-1}$, $Z_0 = 0.04\ cm$, (ii) $u_2 = 2.5\ m\ s^{-1}$, $Z_0 = 0.04\ cm$, (iii) $u_2 = 5\ m\ s^{-1}$, $Z_0 = 0.02\ cm$, (iv) $u_2 = 2.5\ m\ s^{-1}$, $Z_0 = 0.02\ cm$. $T_a = 0°C$, $\psi = 100\%$, and altitude 2500m.*

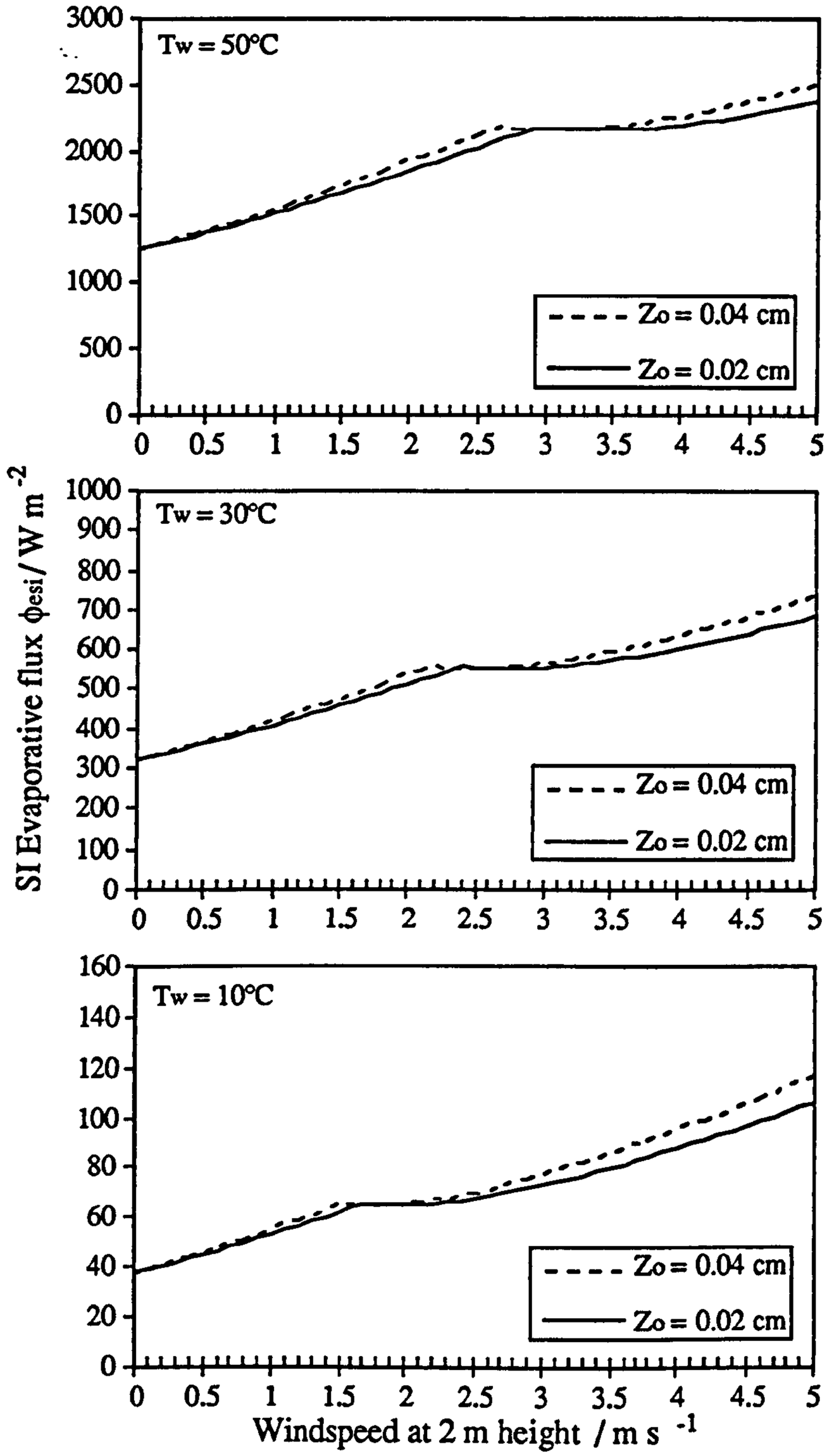

Figure 2.10 *Evaporative fluxes produced by the SI model, for three surface temperatures (10, 30, 50 °C), over a range of windspeeds (0 - 5 m s^{-1}), and for two roughness lengths (0.02, 0.04 cm). Ambient temperature 0 °C, humidity 100 %, altitude 2500 m.*

Plots of ϕ_{esi} for a variety of surface temperatures, windspeeds and surface roughness lengths are shown in figures 2.9 and 2.10. ϕ_{esi} exponentially increases with surface temperature (fig. 2.9), and also with windspeed (fig. 2.10), although there is a step in all of the curves where the formula swaps over from equation (2.29a) (lower windspeed) to equation (2.29b) (higher windspeed). This step indicates the windspeed where forced convection disrupts the free convection cells; it occurs at higher windspeeds for higher surface temperatures because the free convection cells are more stable at higher values of T_w. The model is weakly dependent on roughness length; an increase in Z_0 from 0.02cm to 0.04cm increases ϕ_{esi} by ~0-10%. A comparison with the other models is given in section 2.5.1.5.

2.5.1.4 Adams et al. (1990)

Adams et al. (1990) (hereafter AD), have produced another different model for evaporation from heated lakes, once again using data from power station cooling ponds. Extensive measurements were made at two ponds: (i) East Mesa, California, which has an area of 3×10^3 m^2, a typical value for ΔT_v (virtual temperature difference between the lake and ambient air) of ~18°C, and a typical value for u_2 (windspeed at 2m height) of ~2.2 m s^{-1}; and (ii) Savannah River plant, South Carolina, area 4×10^4 m^2, $\Delta T_v \approx 67$°C, and $u_2 \approx 1.8$ m s^{-1}.

AD follow RY and again split the evaporation into free and forced convection components. The free convection term is calculated from the same basis as the RY model, but with a number of refinements. The correct adjustment for the conversion from vapour concentrations (q) to vapour pressures (e) (as pointed out in section 2.5.1.2) is used, given by AD as:

$$q_w - q_a = \frac{T_a (e_w - e_a) - (T_w - T_a) e_a}{T_w T_a} \qquad (2.31)$$

where temperatures are in K. The latent heat of vaporisation (L_w, in J kg^{-1}) is considered a function of temperature, given by (Wunderlich, 1972) as (T_w in °C):

$$L_w = 2500000 - 2390\, T_w \qquad (2.32).$$

However, the enthalpy of the liquid (see equation 2.7) is not included in the loss.

A further correction is suggested if the measured values of water temperature are from the bulk part of the lake (T_{bulk}), as opposed to the actual surface layer (T_w). The temperature drop across the top few millimetres of the ponds at both sites was measured, with values of between 0.1 and 3.7 °C (average 1.3°C). This produced an average overestimation in Δe of ~7.5% (AD). AD suggested that the use of surface temperatures, or the application of a correction to bulk temperatures, should be used in the calculation of ϕ_{ev}.

For the forced convection term, AD went back to a formula suggested by Harbeck (1962):

$$\phi_{e(forced)} = 3.2\ (Ar)^{-0.05}\ u_2\ (e_s - e_2) \quad (2.33),$$

where Ar is the lake surface area (m^2). This relation was derived by Harbeck (1962) following the study of a number of natural (unheated) lakes (where forced convection dominates), of area 10^3 -10^8 m^2.

In the combination of free and forced convection components, AD pointed out that the simple addition of free and forced terms (e.g. RY) overpredicts evaporation by 15-25%. Instead, AD

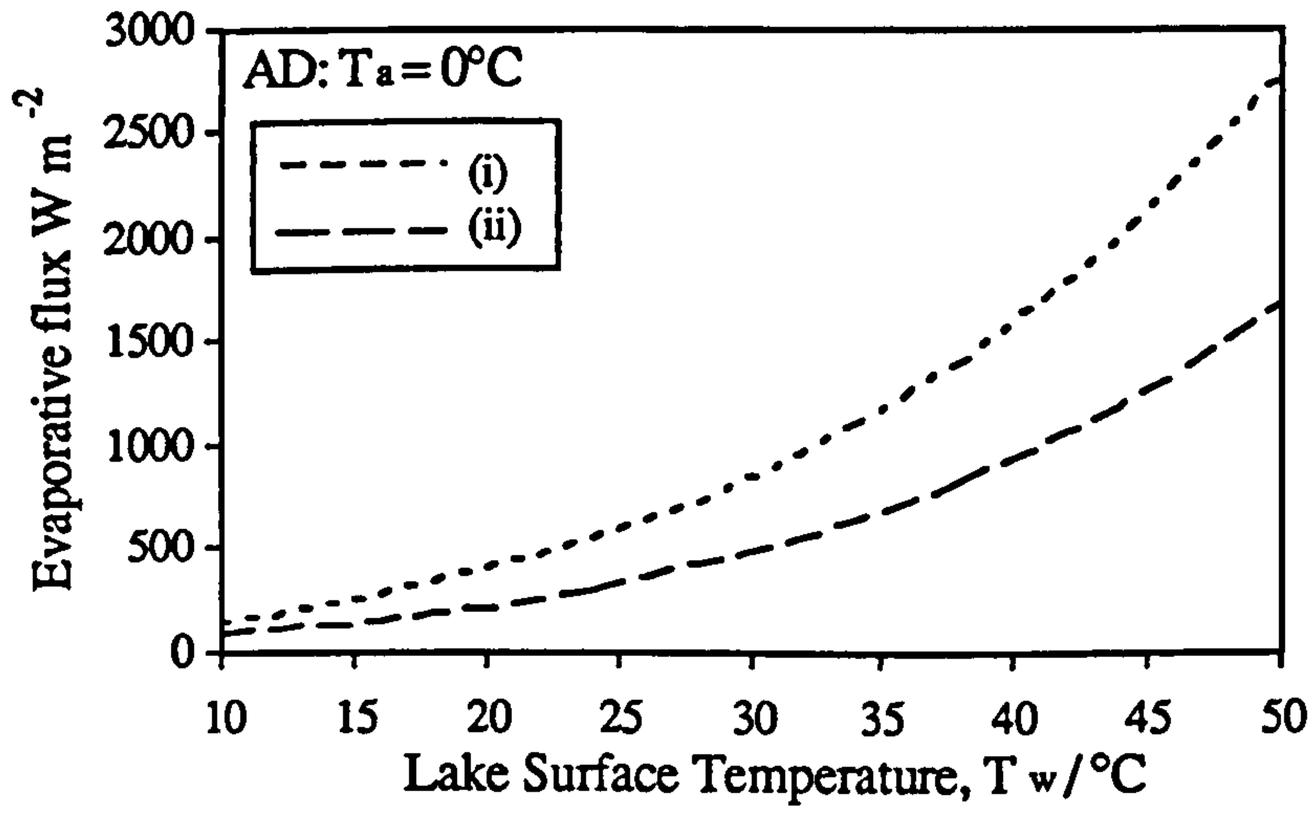

Figure 2.11 *Evaporative fluxes produced by the AD model, for two windspeeds: (i) 5 m s^{-1} and (ii) 2.5 m s^{-1}, and over a range of surface temperatures. Ambient temperature 0°C, humidity 100%, and area 20 hectares.*

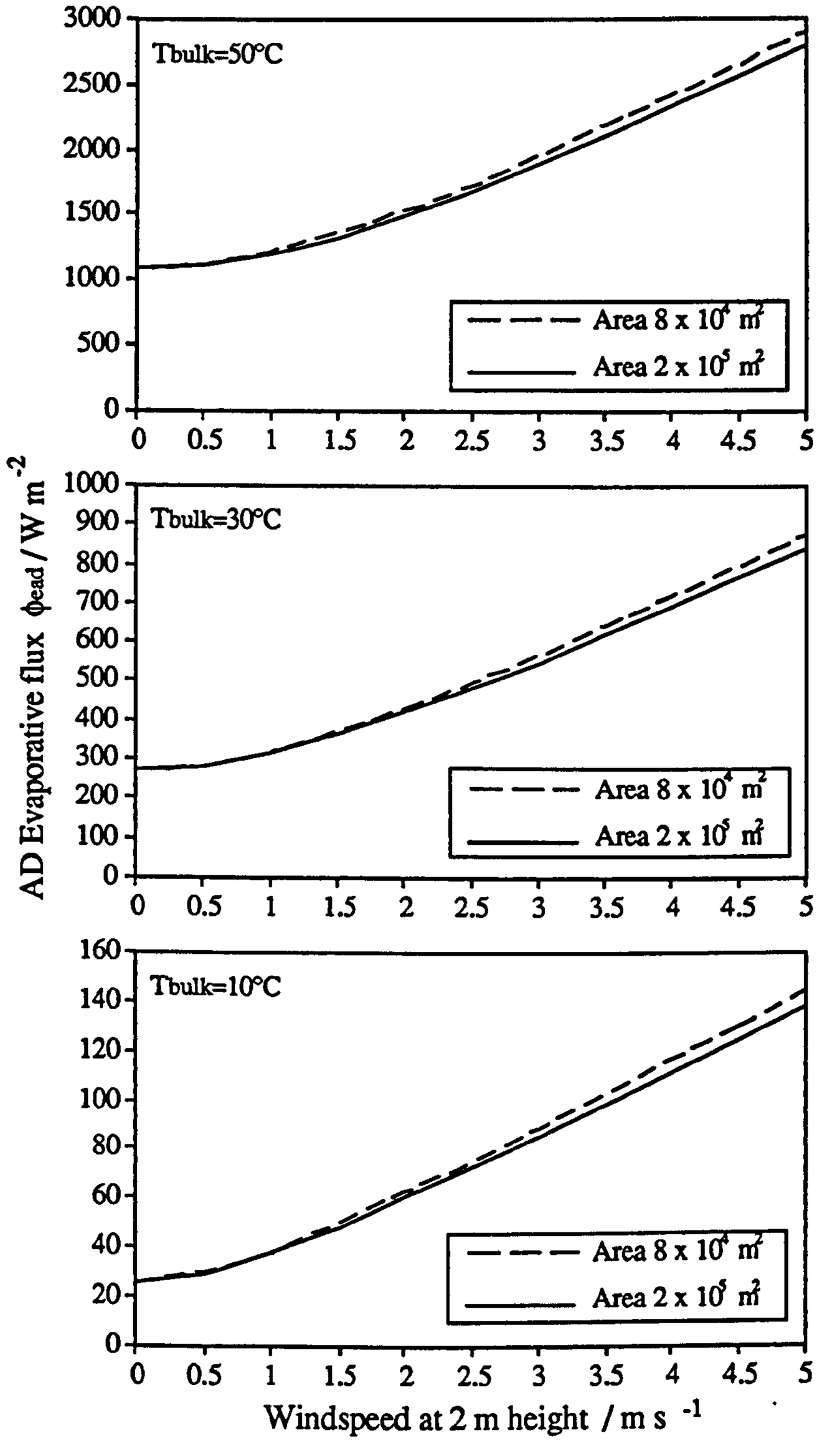

Figure 2.12 *Evaporative fluxes produced by the AD model, for three bulk temperatures (10, 30, 50 °C), two lake areas (8 x 10^4 m^2 and 2 x 10^5 m^2), and over a range of windspeeds (0 - 5 m s^{-1}). T_a = 0 °C, ψ = 100 %.*

suggested a vector addition of the two components, taking the square root of the sum of the squares:

$$\phi_{ead} = \sqrt{\phi_{e(free)}^2 + \phi_{e(forced)}^2} \qquad (2.34),$$

where $\phi_{e(free)}$ is effectively given by equation 2.23, and $\phi_{e(forced)}$ given by equation 2.33. This was found to give good fits to observed data, both new and old.

Plots of ϕ_{ead} for a range of T_{bulk} (10-50°C) (assuming for simplicity that T_w is 2°C less than T_{bulk}) and windspeed (0-5 m s^{-1}) are shown in figures 2.11 and 2.12. ϕ_{ead} increases exponentially with with T_w (fig. 2.11), and approximately linearly with windspeed (fig.2.12), except for low values ($u_2 < 1$ m s^{-1}), where the increase is exponential. Area has a minor effect, with smaller areas giving slightly higher losses per unit area. A comparison with the other models is given in the following section.

2.5.1.5 Comparison and Assessment of Evaporation Models

The four evaporation models are compared graphically in figures 2.13 and 2.14. Figure 2.13 shows one example of each model over a range of water temperatures (10-50°C), for two windspeeds (2.5 and 5 m s^{-1}). All four models show similar exponential increases in evaporation with surface temperature, mainly because of their direct dependence on e_w (or q_w). The RY model consistently predicts the highest values, typically ~15-20% more than the average of all of the models. The WB model generally predicts the lowest values, ~15-20% less than the average of the models. The SI and AD models generally predict values between those of the WB and RY models.

Figure 2.14 shows one example of each model over a range of windspeeds (0-5 m s^{-1}) for three water temperatures (10, 30, 50°C). As with fig. 2.13, all of the models show similar trends, (although the exact shape of each curve differs) and, again, there is a spread of 30-40% in evaporation values, with the WB model generally the lower bound, and the RY model the upper bound.

It should be reiterated that the WB model is purely theoretical, whereas the RY, SI and AD models are all semi-empirical. With only a small increase (<0.01cm) in surface roughness length (Z_0), the WB model shows increases in evaporative flux (see figs. 2.4, 2.5), shifting values into the middle of the spread of results from the other models. It is encouraging that a theoretical model predicts broadly similar results as the semi-empirical models.

The spread of 30-40% between the models reflects the spread in measured values of evaporation (e.g. see RY, SI, AD). The different empirical equations suggested for forced convection reflect the biases (or perhaps the limited data sets) of each author. The model of SI

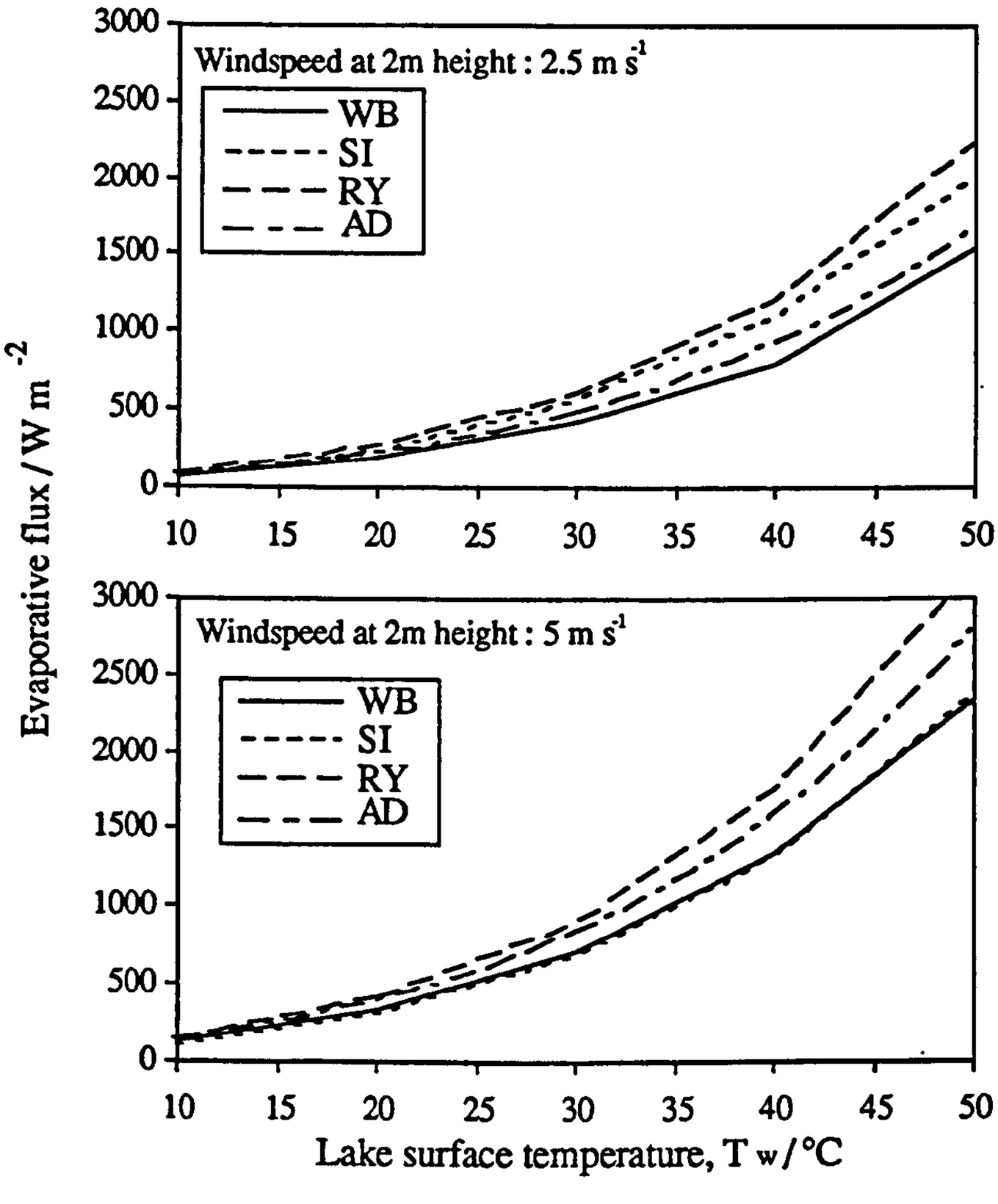

Figure 2.13 *Comparison of the four evaporative models: WB, RY, SI, and AD. WB and SI fluxes are for Z_0 = 0.02 cm, WB is for X_0 = 500 m, and AD is for area 2 x 10^5 m^2. Comparison is shown for the same two windspeeds (2.5 and 5 m s^{-1}) as in figs. 2.4, 2.7, 2.9, and 2.11. T_a = 0 °C, ψ = 100 %, and altitude 2500 m.*

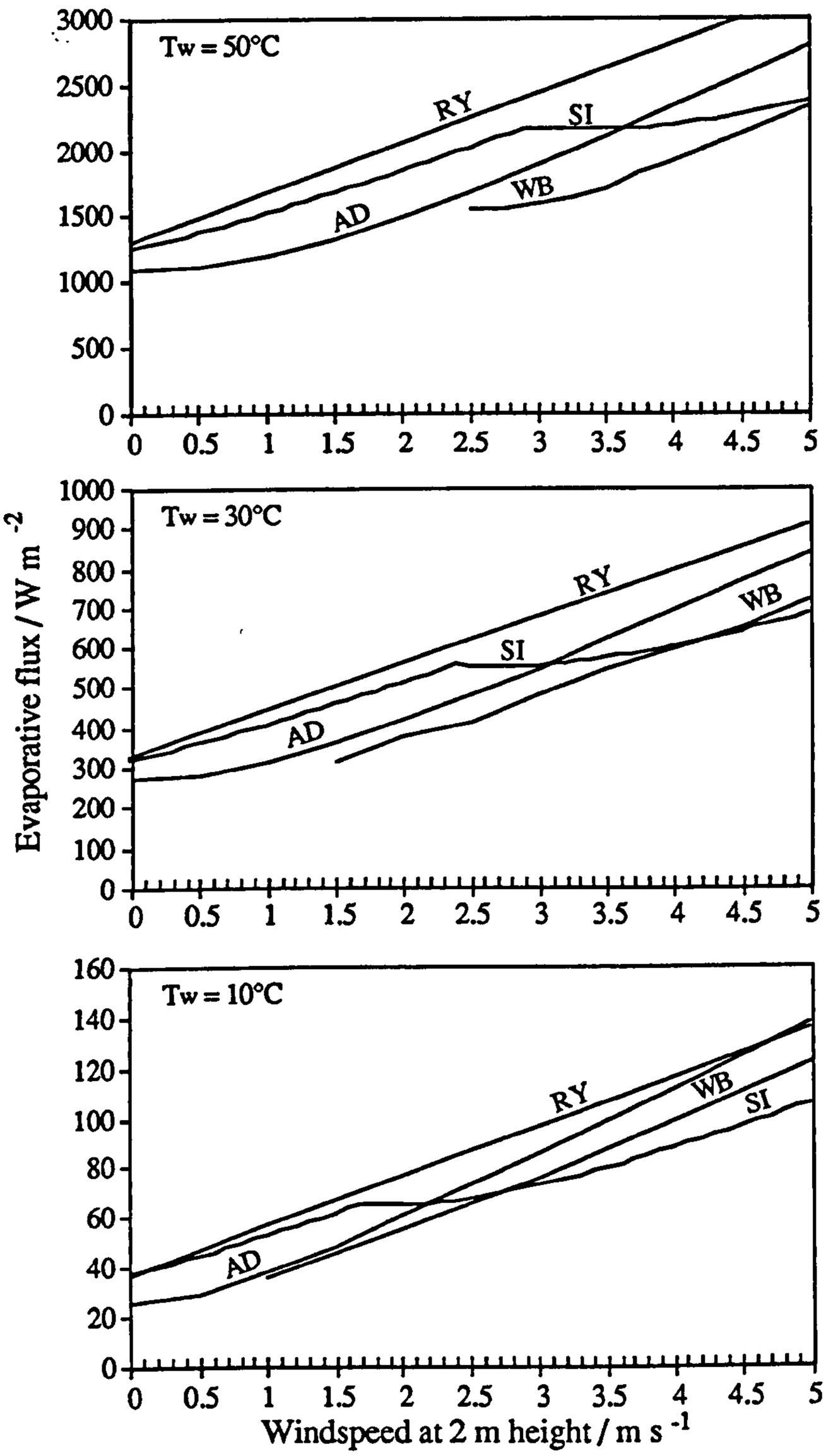

Figure 2.14 *Comparison of the evaporation models, for the same conditions as fig. 2.13.*

is the only one to consider the possibility of interaction between free and forced convection. The RY model assumes simple addition of free and forced convection terms, and the AD model vector addition. SI considered the broadest range of situations, whereas AD only considered in detail two heated lakes, with a maximum 'typical' windspeed (u_2) of 2.2 m s^{-1}. It is therefore maybe not suprising that the data of AD did not reveal the discontinuity present in the SI model (fig. 2.14). The WB model also predicts a similar 'kink' at high surface temperatures/surface roughnesses (fig. 2.5).

For these reasons, it is thought that the model of SI is the nearest to the truth, and the most useful for modelling crater lake evaporative losses. The choice of roughness length (Z_0) is not critical in the SI model; thus the typical value for water surfaces (0.02 cm, Brutsaert, 1982) will be used. An uncertainty of ±15% for a given value of surface temperature and windspeed will also be assumed. In future, Sill's evaporative flux (ϕ_{esi}) will be referred to as simply the evaporative flux (ϕ_{ev}).

2.5.2 Sensible Heat

This form of heat loss has already been described, and used as an analogy to calculate the evaporative losses (see section 2.5.1.2, fig 2.6). Molecules of air, directly above the water surface, are heated by conduction in a thin boundary layer. This heating leads to a lowering of air density, and rapidly to convection. Equation (2.15) states the free convective sensible heat flux above a hot body, and equation (2.23) the free convective evaporative flux above a hot, wet body; the ratio between the two can be written:

$$\frac{\phi_{sh(free)}}{\phi_{e(free)}} = \frac{\rho\, C_p}{H_{ev}} \left(\frac{\Delta T}{\Delta q}\right) \left(\frac{\Delta T}{\Delta T_v}\right)^{1/3} \qquad (2.35),$$

All existing surface loss models assume that this ratio holds for cases that also involve forced convection, thus it follows:

$$\phi_{sh} = \frac{\phi_{ev}\, \rho\, C_p}{H_{ev}} \left(\frac{\Delta T}{\Delta q}\right) \left(\frac{\Delta T}{\Delta T_v}\right)^{1/3} \qquad (2.36).$$

This is the equation used in this study. Previous models (RY, Rowe et al., 1991) have used the simplified equation given by Bowen (1926):

$$\phi_{sh} = \frac{\phi_{ev}\ 0.61\ \Delta T}{\Delta e} \qquad (2.37),$$

where $\Delta e = e_s - e_a$. This equation only holds at sea level, or one atmosphere pressure. The pressure dependent version of this equation is more accurately written:

$$\phi_{sh} = \frac{\phi_{ev}\ 0.61 \times 10^{-5}\ P\ \Delta T}{\Delta e} \qquad (2.38),$$

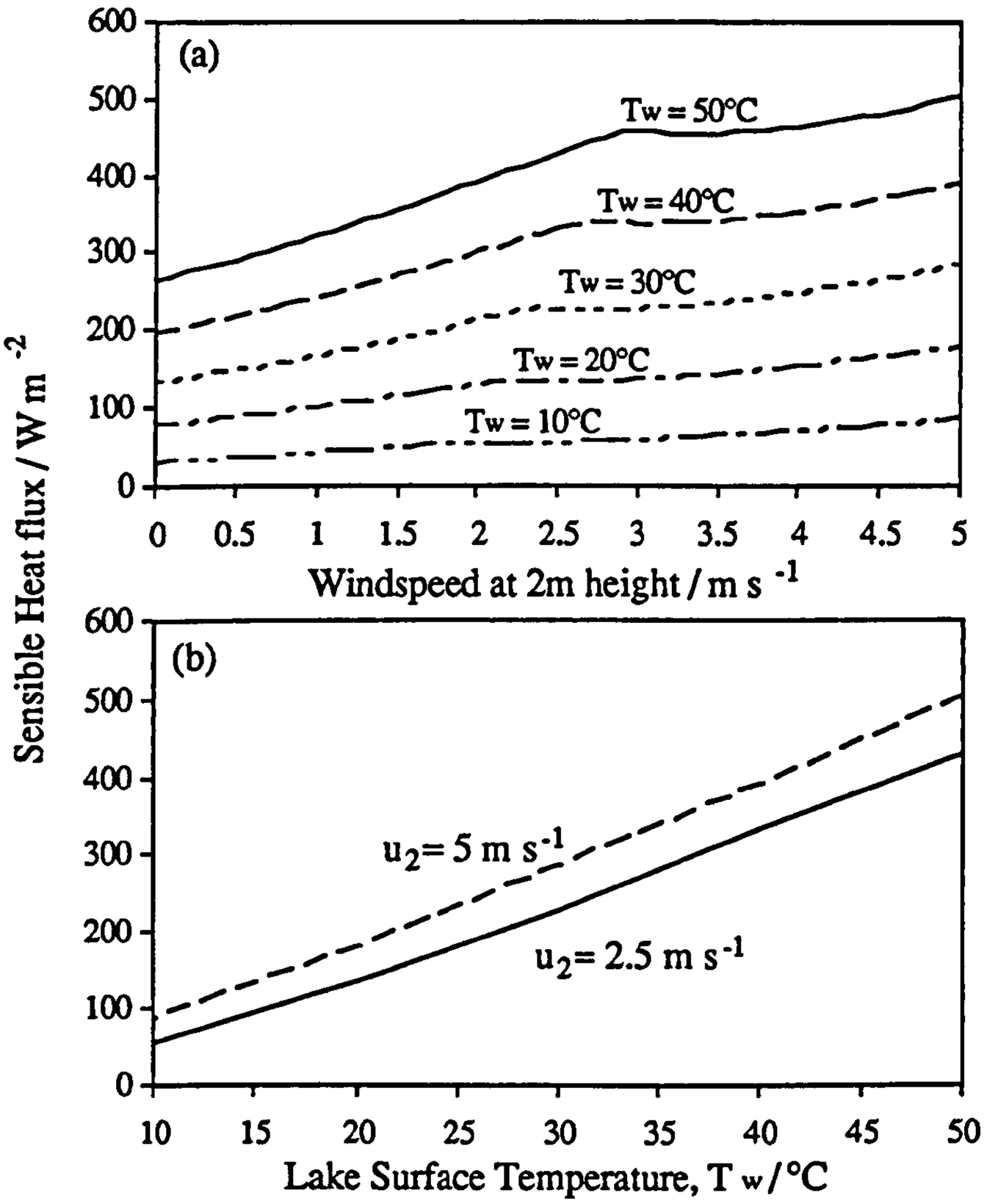

Figure 2.15 *Sensible heat fluxes calculated using equation (2.37): (a) for five water temperatures, and a range of windspeeds; and (b) for two windspeeds, and a range of water temperatures. Calculated using the SI evaporation model, using Z_0 = 0.02 cm, T_a = 0 °C, ψ = 100 %, and altitude 2500 m.*

where P is atmospheric pressure (in N m^{-2}). However, even this version of the equation includes the approximation met earlier (see section 2.5.1.2), of converting vapour concentrations (q) to vapour pressures (e). Thus equation (2.36) is considered the most useful, and illustrates that the sensible heat loss is directly proportional to air density (ρ), and therefore decreases with altitude. Hurst et al. (1991), in their model of Crater Lake, Ruapehu, suprisingly ignored the sensible heat loss completely.

Plots of ϕ_{sh} (from equation (2.36)) over a range of windspeeds and surface temperatures are shown in fig 2.15. Sensible heat losses vary from being about half the evaporative losses at low surface temperatures, to around 20% of evaporative losses at T_s = 50°C. Unlike evaporative losses, they increase approximately linearly (as opposed to exponentially) with surface temperature.

2.5.3 Net Radiation

Net radiation is usually the least important surface energy term associated with hot water lakes, however, it does become important when lake temperatures approach ambient air temperatures. The lake will gain some energy from shortwave solar radiation, and also from longwave atmospheric radiation. Energy will be lost through longwave back radiation leaving the surface of the lake. These three terms can be approximated.

2.5.3.1 Incoming Radiation

(i) Shortwave radiation

Shortwave radiation at the top of the atmosphere ($\phi_{s\infty}$) varies with latitude and date, but its value is reasonably well known (e.g. Eskinazi, 1975). However, passage through the atmosphere significantly reduces its value, mainly because of reflection/absorption by clouds, but also by atmospheric scatter, reflection back into space, and molecular absorption (all these occur in even a cloudless atmosphere). Under clear skies, shortwave radiation reaching the surface of the lake will have been reduced by 20-30% (Henderson-Sellers, 1986), and by more

under cloudy conditions. In this study, an average reduction of 50% is assumed. The shortwave albedo (A_S) also varies with weather conditions (see fig.4, Henderson-Sellers, 1986), but on average, has a value of ~0.1. The incoming shortwave radiation (ϕ_S) is thus approximated as:

$$\phi_S \approx (0.5)\,(1 - 0.1)\,\phi_{S\infty} = 0.45\,\phi_{S\infty} \qquad (2.39).$$

(ii) Longwave radiation

Incoming longwave radiation comes from emissions within the atmosphere, mainly from CO_2, water vapour and liquid water in clouds. Emission and reabsorbtion take place throughout the atmosphere, so it is reasonable to assume that the radiation that reaches the lake has an emission temperature equal to that of the air adjacent to the surface, T_a. Using the Stefan-Boltzmann Law, the incoming longwave radiation is given by:

$$\phi_l = \varepsilon_a\,\sigma\,T_a^4 \qquad (2.40),$$

where σ is the Stefan-Boltzmann constant (5.67×10^{-8} W m^{-2} K^{-4}), and ε_a is the effective atmospheric emissivity, which again is dependent upon atmospheric conditions, in particular, cloud cover. Typical values of ε_a are 0.7-0.9 (see fig.9, Henderson-Sellers, 1986), and in this work an average value of 0.8 is used. The longwave albedo (A_l) has a value of ~0.03, and thus is small enough to be ignored in this study.

2.5.3.2 Outgoing Radiation

Outgoing longwave back-radiation is the only well constrained radiative term, and can be calculated in a similar way to the incoming longwave term:

$$\phi_{br} = \varepsilon_w\,\sigma\,T_w^4 \qquad (2.41),$$

where ε_w is the emissivity of the water surface (assumed a constant, found to be 0.972 by Davies et al., 1971).

2.5.3.3 Summary of Radiative terms

The radiative budget of a lake is therefore quite complex, and when it is an important component it requires detailed information on a number of meteorological variables, particularly to calculate the shortwave radiation. Ultimately, the best way around this problem is to instal a radiometer, actually to measure the incoming radiation. This method is usually invoked, at least initially, in reservoir and lake studies where radiation is the major heat transfer process in operation.

In volcanically heated lakes, however, radiative fluxes are usually found to be the least important, with evaporation and sensible heat dominating at high surface temperatures. This allows the relatively simple approximations stated above to be used in calculating the net radiation, without producing significant errors. The formula used in this work for net radiative flux (ϕ_{ra}) is an amalgamation of equations (2.39), (2.40) and (2.41):

$$\phi_{ra} = \phi_{br} - \phi_l - \phi_s = \sigma\,(0.972\,T_w^4 - 0.8\,T_a^4) - 0.45\,\phi_{s\infty} \qquad (2.42).$$

A plot of ϕ_{ra} against T_w is shown in figure 2.16. It can be seen that ϕ_{ra} is typically half the value of ϕ_{sh}, and ~10% of the value of ϕ_{ev}.

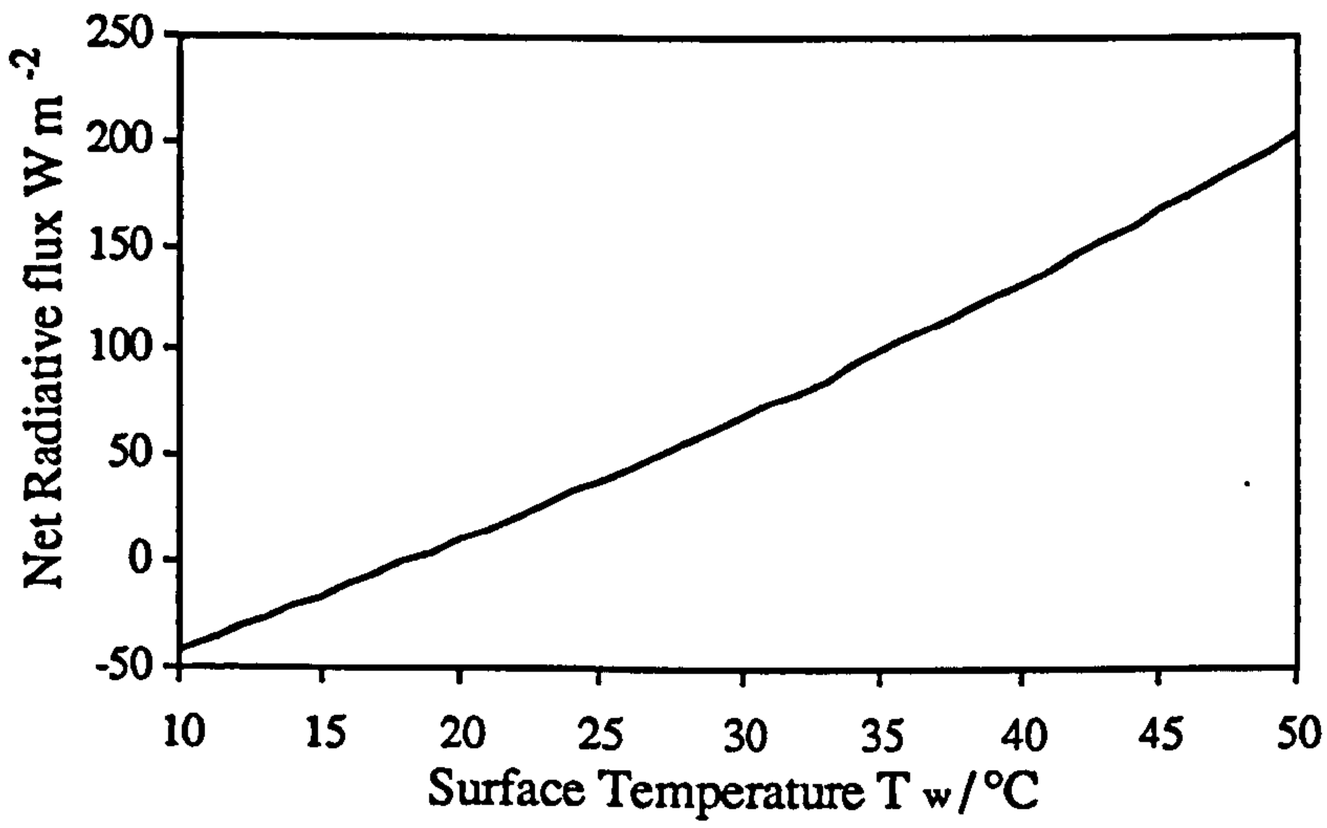

Fig 2.16 *Net radiative flux (ϕ_{ra}) calculated using equation (2.42) for a range of water temperatures. $T_a = 0$°C, $\phi_{s\infty} = 320\ W\ m^{-2}$.*

2.5.4 Summary of Surface Losses.

Combined plots of evaporative, sensible heat and net radiative fluxes, together with total heat fluxes, are shown for a range of lake temperatures and windspeeds in figures 2.17 and 2.18. Evaporation is usually by far the largest component, followed by the sensible heat , then the net radiation. Table 2.5 gives values for each flux, relative to the total flux ($\phi_{tot} = \phi_{ev} + \phi_{sh} + \phi_{ra}$), for a range of situations.

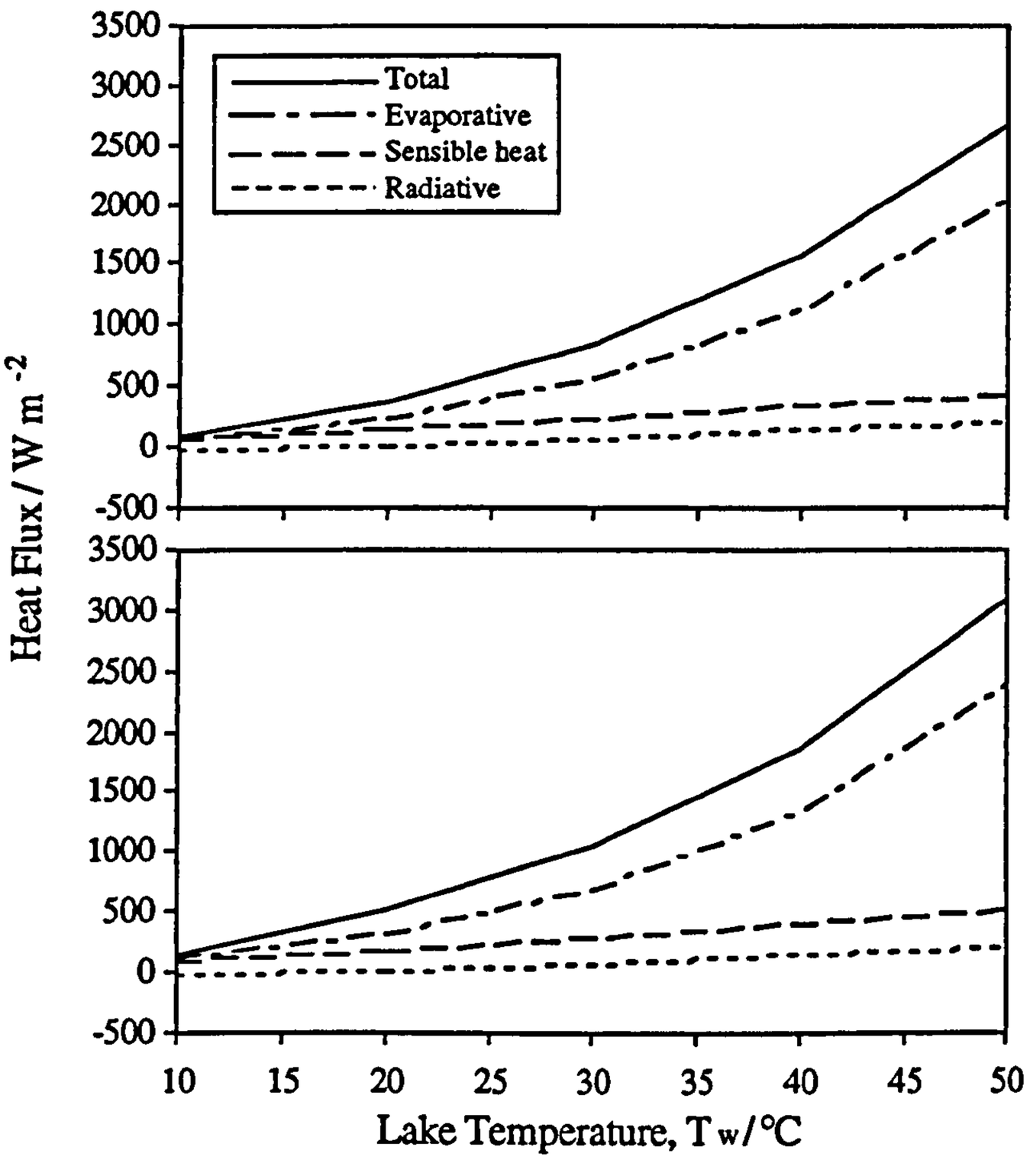

Figure 2.18 *Summary diagrams of surface losses, over a range of surface temperatures, for two windspeeds (upper diagram $u_2 = 2.5$ m s^{-1}; lower diagram $u_2 = 5$ m s^{-1}). Same conditions as for fig. 2.15.*

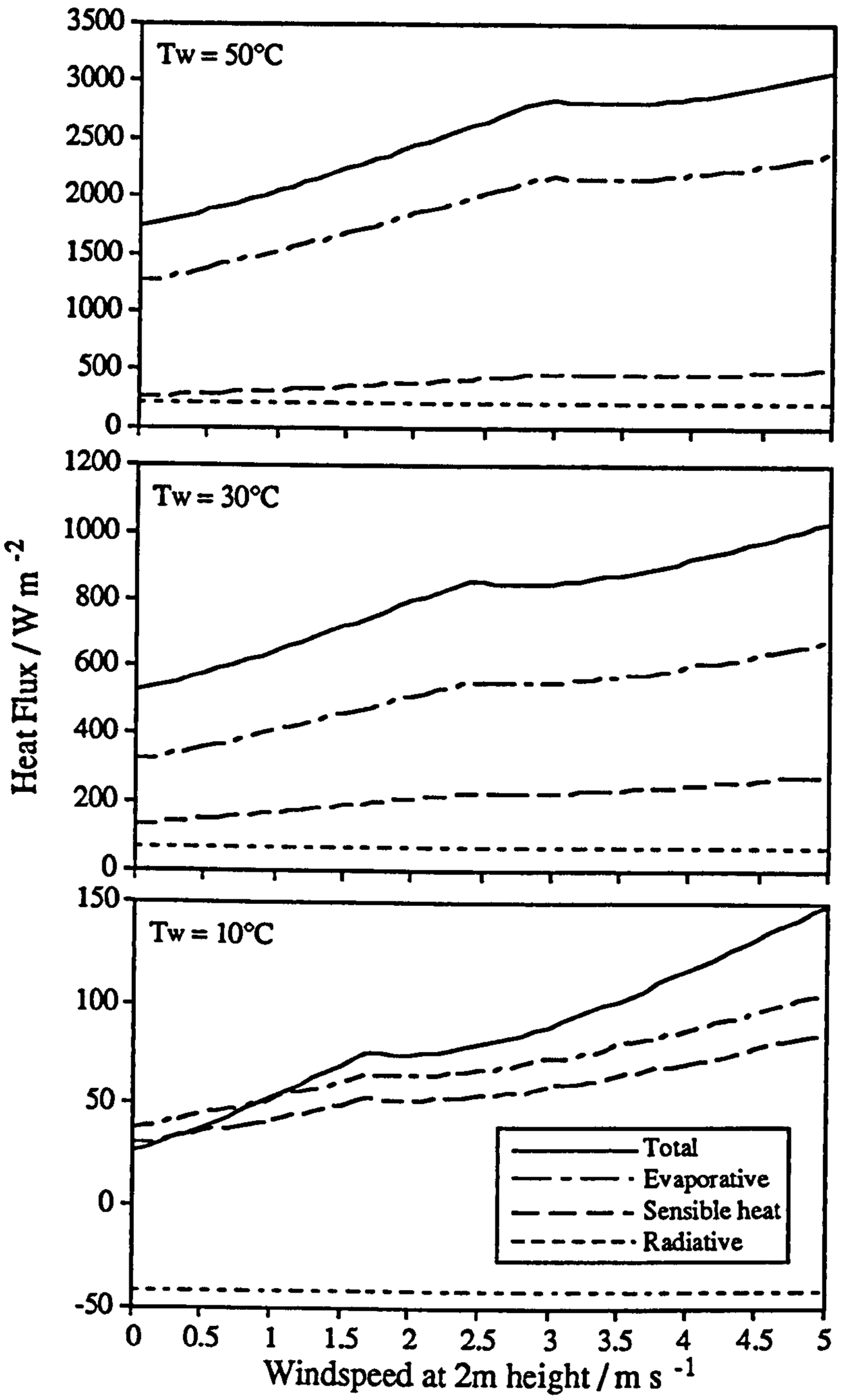

Figure 2.17 *Summary diagrams of surface losses, over a range of windspeeds, and for three surface temperatures. Same conditions as for fig. 2.15.*

T_w / °C	u_2 / m s^{-1}	ϕ_{ev} / ϕ_{tot}	ϕ_{sh} / ϕ_{tot}	ϕ_{ra} / ϕ_{tot}
50	2.5	0.76	0.16	0.08
	5	0.77	0.16	0.07
30	2.5	0.65	0.27	0.08
	5	0.66	0.27	0.07

Table 2.5 *Contribution of evaporation, sensible heat and net radiative loss at water temperatures of 30 and 50°C, and for two windspeeds: 2.5 and 5 m s^{-1}. Assuming T_a = 0°C, 100 % humidity, altitude 2500m, and Z_0 = 0.02 cm.*

2.6 Summary of the Mass, Energy and Chemical Balance Model

Equations 2.1 and 2.2 define the mass and energy balance model. The rate of change of lake mass, ΔM, over the time interval Δt, is found by using:

$$\Delta M = \frac{m_2 - m_1}{\Delta t} \qquad (2.43),$$

where m_1 and m_2 are the lake masses at times t_1 and t_2, and $\Delta t = t_2 - t_1$. The lake masses are calculated using a geometric approximation of the lake shape (see chapters 3 and 4). If chemical data exist, a *minimum* value for the overflow/seepage rate is calculated using equation (2.4). A minimum value for the rainfall/meltflow rate is either found using rainfall data (q_{rain}, kg m^{-2}), and an estimated catchment area (A_{catch}):

$$M_{rm(min)} = \frac{q_{rain}\, A_{catch}}{\Delta t} \qquad (2.44),$$

or is simply estimated. The evaporation rate is calculated using equations (2.29a) and (2.29b) for the evaporative flux, a lake area (A), and a vapour enthalpy (table 2.1):

$$M_{ev} = \frac{\phi_{ev}\, A}{H_{ev}} \quad (2.45).$$

Thus equation (2.1) has one clear unknown: $M_{st/br}$; and two parameters with minimum values: M_{rm} and M_{os}.

The change in stored energy in the lake (ΔE) can be found using:

$$\therefore \quad \Delta E = \frac{m_2 H_2 - m_1 H_1}{\Delta t} \qquad (2.46),$$

where H_1 and H_2 are the enthalpy of lake-water at times t_1 and t_2. The evaporative energy flow is given by $E_{ev} = M_{ev} H_{ev}$. Similarly, the energy loss through overflow/seepage is given by $E_{os(min)} = M_{os(min)} H_{os}$, where $H_{os} = (H_1 + H_2) / 2$. The sensible heat and net radiation terms are given by $E_{sh} = \phi_{sh} A$ and $E_{ra} = \phi_{ra} A$, respectively. Thus, for an estimated value of $H_{st/br}$ (see chapter 4), and using $M_{os(min)}$, unknowns $M_{st/br}$ and M_{rm} can be evaluated from equations (2.2) and (2.1):

$$M_{st/br} = \frac{\Delta E + E_{ev} + E_{os(min)} + E_{ra} + E_{sh}}{H_{st/br}} \qquad (2.47)$$

$$M_{rm(mod)} = \Delta M + M_{ev} + M_{os(min)} - M_{st/br} \qquad (2.48)$$

2.6.1 Application of the model

The application of the model is summarised in fig. 2.19. This flow diagram describes the procedure followed for the interval of time (Δt) between each measurement of lake temperature (T_w). Surface losses (M_{ev}, E_{ev}, E_{sh}, and E_{ra}) are calculated using ψ, u_2, T_a, T_w, h, and the lake shape. Rates of change of lake mass and energy (ΔM and ΔE) are found using T_w, ΔT_w, h, Δh, and the lake shape. A minimum value for overflow/seepage ($M_{os(min)}$) is found using h,the lake shape, [X], and Δ[X] (using X = Mg and Cl, and preferring whichever returns the highest value for $M_{os(min)}$) in equation (2.4). This also allows evaluation of $E_{os(min)}$. At this stage, $M_{st/br}$ can be found using equation (2.47), *assuming* a value for $H_{st/br}$. $H_{st/br}$ has a possible range from hot brine (~0.8 MJ kg^{-1}) to saturated steam at lake bottom pressures (~5 bar for a full lake at Poás, and up to ~30 bar for a full lake at Ruapehu) (~2.75 MJ kg^{-1}), and possibly higher, to superheated steam (maximum ~3.8 MJ kg^{-1}). Having calculated a value for $M_{st/br}$, the model output of rainfall/meltflow ($M_{rm(mod)}$) can be found using equation (2.48). Clearly, M_{rm} must be positive, and it should be greater than a minimum value ($M_{rm(min)}$), that

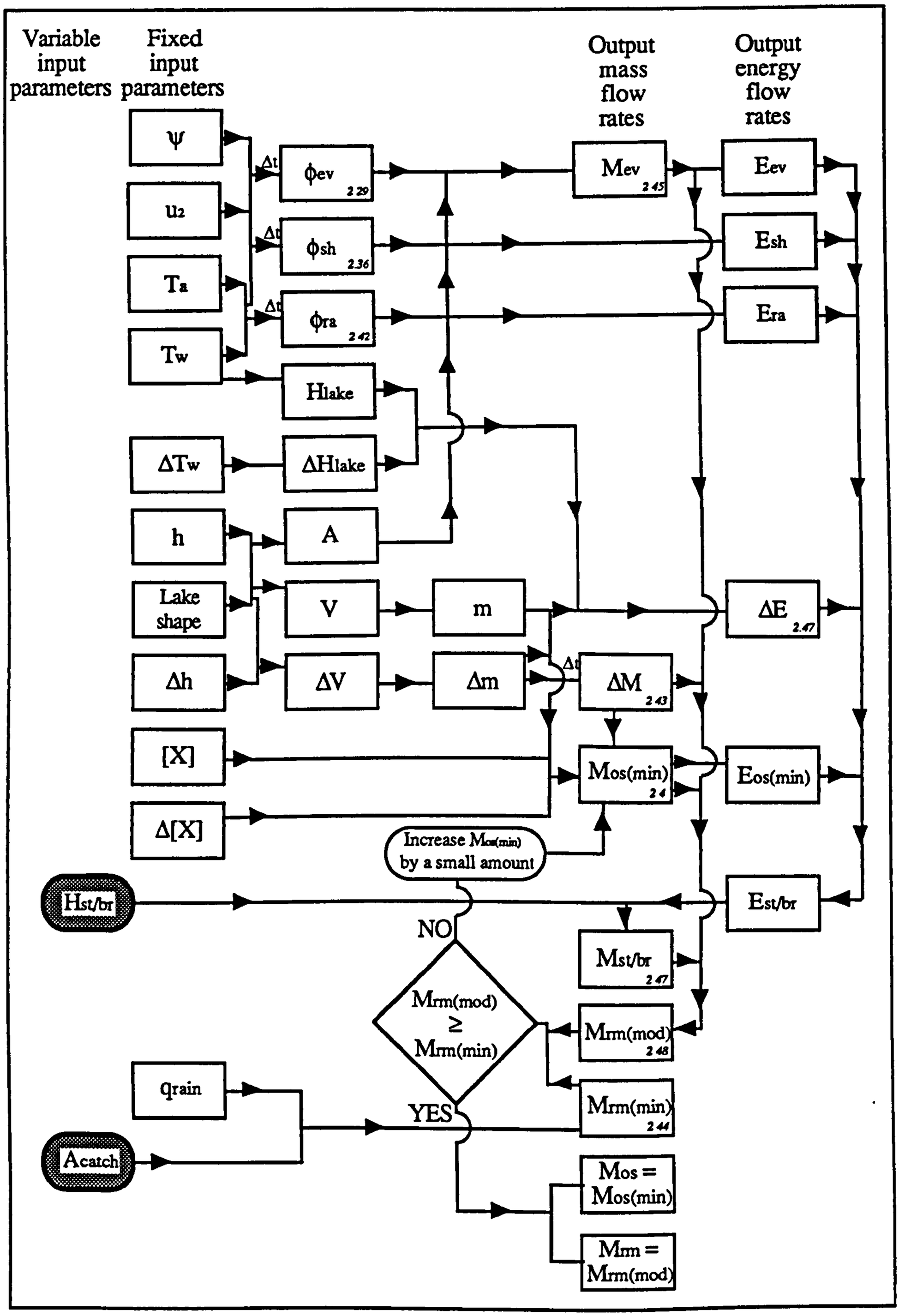
Variable input parameters
Fixed input parameters
Output mass flow rates
Output energy flow rates
ψ
u2
Ta
Tw
Hlake
ΔTw
ΔHlake
h
A
Lake shape
V
m
Δh
ΔV
Δm
[X]
Δ[X]
Δt
ϕev 2.29
ϕsh 2.36
ϕra 2.42
Mev 2.45
ΔM 2.43
ΔE 2.47
Mos(min) 2.4
Eev
Esh
Era
Eos(min)
Est/br
Mst/br 2.47
Mrm(mod) 2.48
Mrm(min) 2.44
Increase Mos(min) by a small amount
Hst/br
NO
Mrm(mod) ≥ Mrm(min)
YES
qrain
Acatch
Mos = Mos(min)
Mrm = Mrm(mod)

Figure 2.19 *(opposite) Flow diagram, showing input parameters on the left, and output mass and energy flows on the right. Each output depends upon a number of input parameters. The diagram illustrates how the overflow/seepage rate is iteratively increased, until the rainfall/meltflow value output by the model exceeds the minimum value suggested by the chosen catchment area. The enthalpy of the steam/brine, and the catchment area are varied (within possible values), depending upon model outputs (see text, and chapter 4) and the model re-run. A Δ signifies the change in a parameter over the time interval (Δt) between measurements. Relevant equations are numbered in the bottom right-hand corner of some boxes.*

can be calculated using equation (2.44), rainfall data (q_{rain}) and an *assumed* minimum catchment area (A_{catch}). This constraint on the value of M_{rm} is used to iteratively increase the overflow/seepage rate from its minimum value, until a rainfall/meltflow value above the suggested minimum is produced. This process is repeated for each time interval between lake temperature measurements.

2.6.2 Errors

The primary input parameters to the model are listed in table 2.6, with their typical uncertainties. The individual mass and energy flow input terms are calculated from these input parameters. Each input mass/energy flow is therefore dependant on one or more of the primary input parameters. Thus each primary input parameter error will produce an error in the input mass/energy flows. Typical contributions of each primary error on each mass/energy flow input are shown in table 2.7, together with the root mean square of the errors, a gauge of the overall error associated with that flow. The magnitude of many of these errors is dependant upon the state of the lake, e.g. the error in lake volume arising from a measurement of lake level will increase as the lake volume decreases. The errors quoted are for the conditions specified, which are typical. An example of the method followed in calculating the errors is given below.

Parameter	Typical value ± uncertainty
Lake temperature (T_w)	(50) ± 2 °C
[Lake (overflow/seepage) enthalpy (H_{os})]	[± 4 %]
[Evaporated vapour enthalpy (H_{ev})]	[± 0.1 %]
Ambient temperature (T_a)	(10) ± 10 °C
Windspeed (u_2)	(2.5) ± 1 m s^{-1}
Lake area (when full) (A_{full})	(3×10^5) ± 5 %
Lake level (h)	(100) ± 0.2 m [± 0.2 %]
[Change in lake level (Δh)]	[2 m: ± 14 % (see text)]
[Lake area (A)]	[± 0.4 %]
[Change in area (ΔA)]	[± 14 % (see text)]
[Lake volume (V)]	[± 0.6 %]
[Change in volume (ΔV)]	[± 14 % (see text)]
Humidity (ψ)	(70 %) ± 30 %
Rainfall catchment area (A_{catch})	(6×10^5) ± 30 %
Chemical measurements ([x])	(2×10^{-3} kg kg^{-1}) ± 10 %
Steam/brine enthalpy ($H_{st/br}$)	see chapter 4

Table 2.6 *Primary input parameters for the mass, energy and chemical balance model, and their typical values and uncertainties. These typical values are used as a guide to assess errors on the inputs to the mass/energy balance model, in table 2.7.*

The rate of change of lake mass depends upon the change in lake level, and the shape of the lake basin - typically defined as a cone plus a truncated cone (see chapter 4). Thus a ±0.2 % uncertainty in lake level (h) corresponds to a ±0.6 % uncertainty in lake volume (and hence mass). However, the error in ΔM will depend upon whether the change in lake mass is large compared to the errors in lake mass (Topping, 1972):

$$\Delta M_{error} = 0.006 \frac{\sqrt{m_1^2 + m_2^2}}{m_1 - m_2} \qquad (2.49)$$

For example, consider a cone-shaped lake of depth 100 (±0.2) m. The volume of the lake will have an error of ±0.6 %. If the depth changes to 98 (±0.2) m, then the new volume will have an error of approximately ±0.6 %. The error on the change in mass (given by equation 2.49)

	ΔM	M_{ev}	$M_{rm(min)}$	$M_{os(min)}$	ΔE	E_{ev}	$E_{os(min)}$	E_{sh}	E_{ra}
T_w	-	± 10 %	-	-	± 7 %	± 10 %	± 4 %	± 6 %	± 10 %
T_a	-	± 8 %	-	-	-	± 8 %	-	± 30 %	± 30 %
u_2	-	± 13 %	-	-	-	± 13 %	-	± 12 %	-
A_{full}	-	± 5 %	-	-	-	± 5 %	-	± 5 %	± 5 %
h	± 14 %	± 0.4 %	-	± 14 %	± 14 %	± 0.4 %	± 14 %	± 0.4 %	± 0.4 %
ψ	-	± 4 %	-	-	-	± 4 %	-	-	-
A_{catch}	-	-	± 30 %	-	-	-	-	-	-
[x]	-	-	-	± 1 %	-	-	± 1 %	-	-
Evap. model	-	± 15 %	-	-	-	± 15 %	-	± 15 %	-
RMS	±14 %	± 26 %	± 30 %	± 14 %	±16 %	± 26 %	± 15 %	± 38 %	± 34 %

Table 2.7 *Typical errors in the mass and energy balance inputs associated with each of the primary input parameters, and the root mean square (RMS) of the errors on each term. Values are for T_w = 50 (±2) °C, u_2 = 2.5 (±1) m s^{-1}, T_a = 10 (±10) °C, ψ = 70 (±30)%, a cone-shaped lake of radius 200 m, and depth 100 (± 0.2) m, undergoing a change in level of 2 m (see table 2.6 and text), and a change chemical content [X] from 2 x 10^{-3} kg kg^{-1} to 10^{-3} kg kg^{-1}.*

however, will be ±14 %. The smaller the change in level, the larger the error - however, small changes in lake volume don't effect the mass/energy balance significantly, thus the large error is not propagated.

The typical errors on input parameters feed through to the outputs of the model. Referring to equations (2.47) and (2.48), and using the root mean square (RMS) errors from table 2.7, the errors on outputs $M_{st/br}$ and M_{rm} can be estimated. Of the terms in the numerator of equation (2.47), E_{ev} and $E_{os(min)}$ will usually dominate, suggesting a typical error of ~±30 % in $M_{st/br}$. Feeding this into equation (2.48) and noting that ΔM will usually be much smaller than the other terms suggests an RMS error of ~±40 % in M_{rm}. These values disregard uncertainties in

the steam/brine enthalpy, which are discussed in chapter 4, and are larger.

CHAPTER 3

Historical activity and a review of recent work at Poás and Ruapehu

3.1 Poás volcano, Costa Rica

Poás volcano is located approximately 30 km NW of San José, within the Cordillera Central of Costa Rica, a volcanic arc of Quaternary age (fig. 3.1). Volcanism is associated with subduction of the Cocos plate north eastward beneath the Caribbean plate, at a rate of ~9 cm yr^{-1} (Seyfried et al., 1991). Carr (1984) estimated the average arc-trench gap for the Cordillera Central to be ~165 km, the depth to the Benioff zone to be ~75 km, and hence the dip of the subducted plate to be ~30°. Poás has a maximum elevation of ~2700 m, rising ~1300 m above the surrounding country, a basal diameter of ~20 km, and a volume of ~140 km^3. The underlying rocks are a massive volcanic pile of welded and non-welded ignimbrites and lava flows (Williams, 1952). Saenz (1982) has dated an ignimbrite outcropping at the base of Poás at 0.98 Ma, indicating that Poás is younger than this age. The volcano has gentle slopes (~10-15°) and a broad (~5 km wide) summit consisting of two large, nested calderas (Rymer, 1985; Brown et. al, 1987; Prosser and Carr, 1987), the larger roughly circular, ~9 km in diameter, the other elliptical with dimensions ~5 km N-S, and ~3 km E-W (fig. 3.2). Within these calderas are three smaller north-trending features (fig. 3.2): to the north, the partly eroded Von Frantzius Cone; to the south, the younger, less eroded Botos Cone, which contains a shallow (~15 m deep) fresh water lake, ~500 m in diameter (Rymer, 1985); and in the centre, the main crater, site of all historic activity.

The active crater (plate 3.1; fig. 3.3) has dimensions ~1100 m N-S by ~800 m E-W, and a depth (from crater rim to floor) varying between ~150-250 m. On the eastern side of the crater there is a ledge, approximately half-way between the rim and the floor, that is probably a remnant of a previous crater floor. The present sites of activity are located towards the northern part of the crater floor, where there is a pit crater (~50 m deep and ~300 m diameter), and on its southern margin, the remnant of a basaltic-andesite pyroclastic cone, both formed during the most recent cycle of magmatic activity in 1952-54 (see below). A

lake formed within the pit crater between 1954 and 1964, and has been present, to a greater or lesser extent, since then. This lake, and the pyroclastic cone adjacent to the lake have been the site of all historical activity, with numerous phreatic eruptions and geysers occurring within the lake, and fumaroles fluctuating in flux and temperature on the cone.

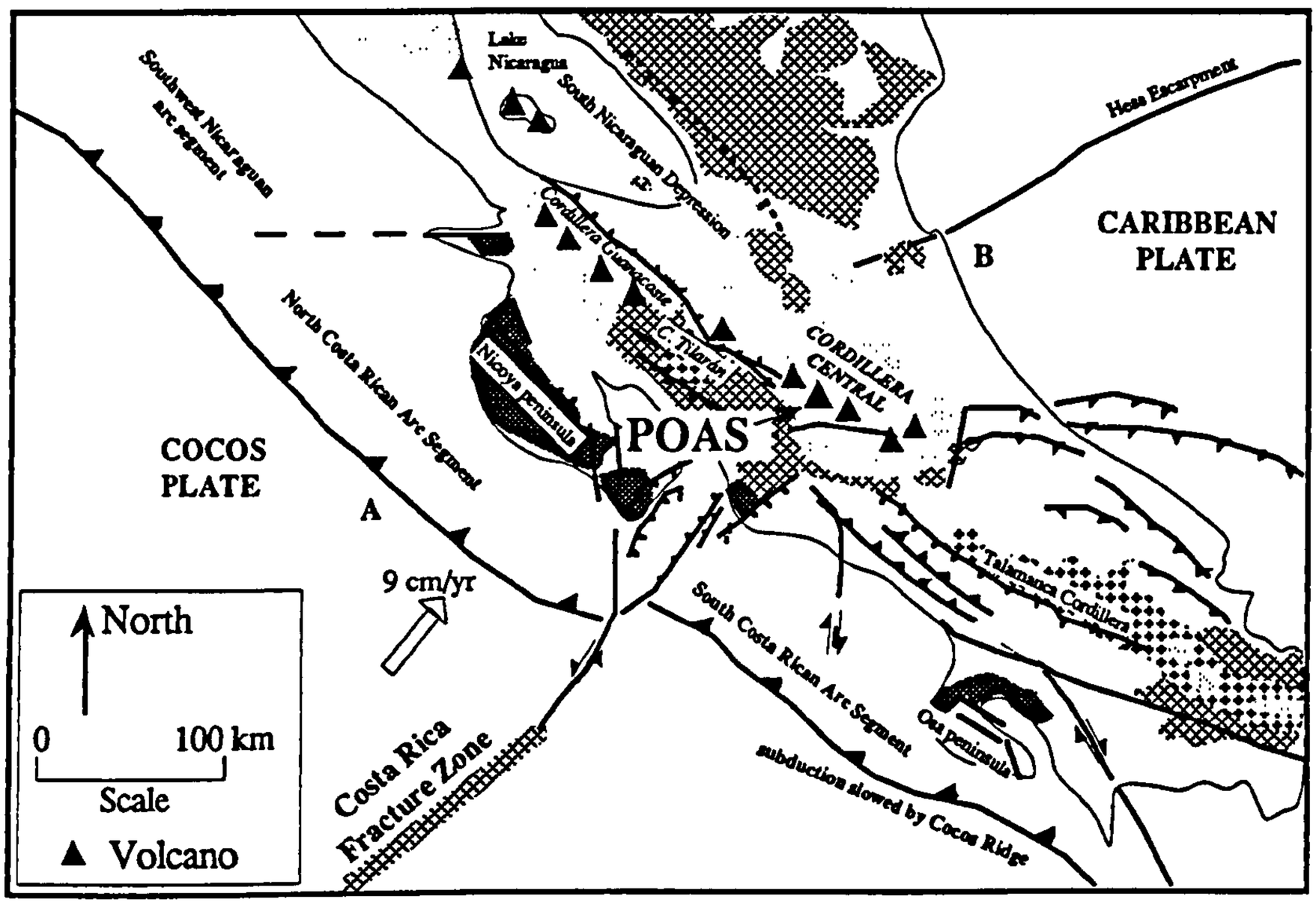

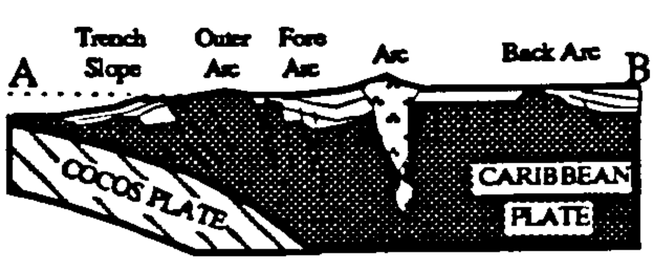

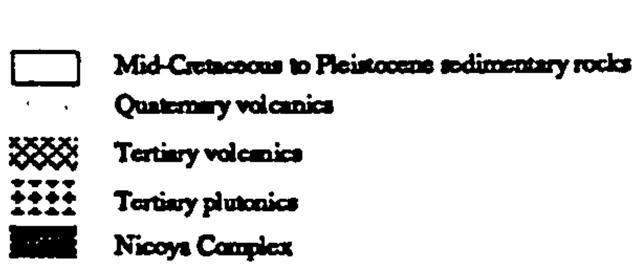

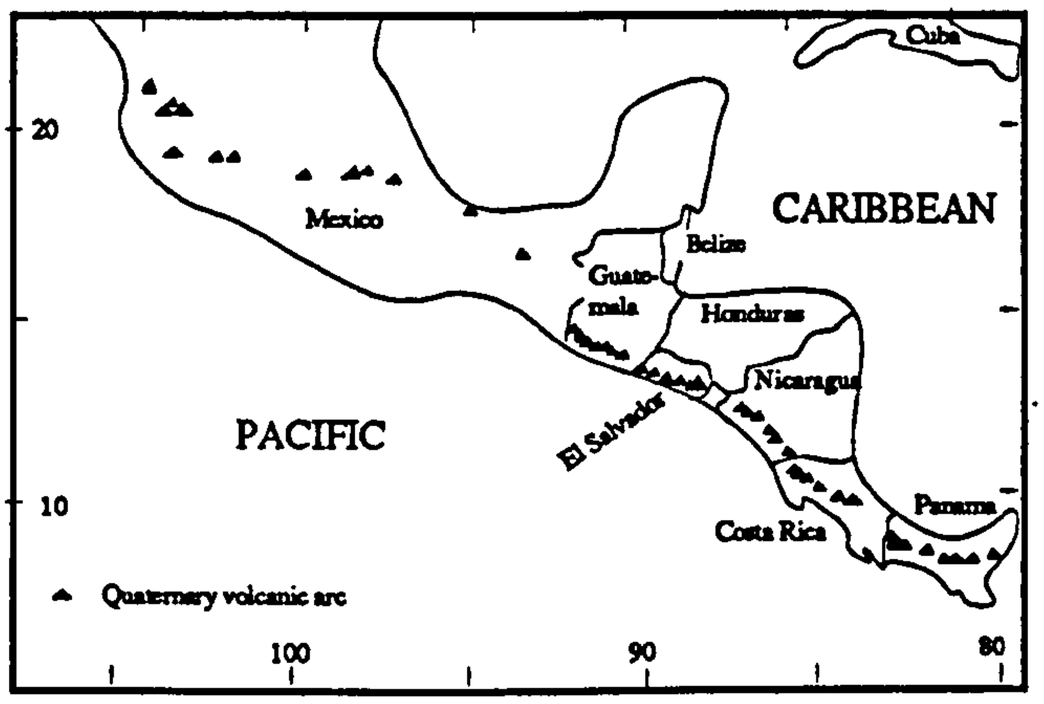

Figure 3.1 *Location of Poás volcano, Costa Rica, within the Quaternary Central American arc. Section is marked A-B on the map. Adapted from Seyfried et al. (1991) and Hallinan (1991).*

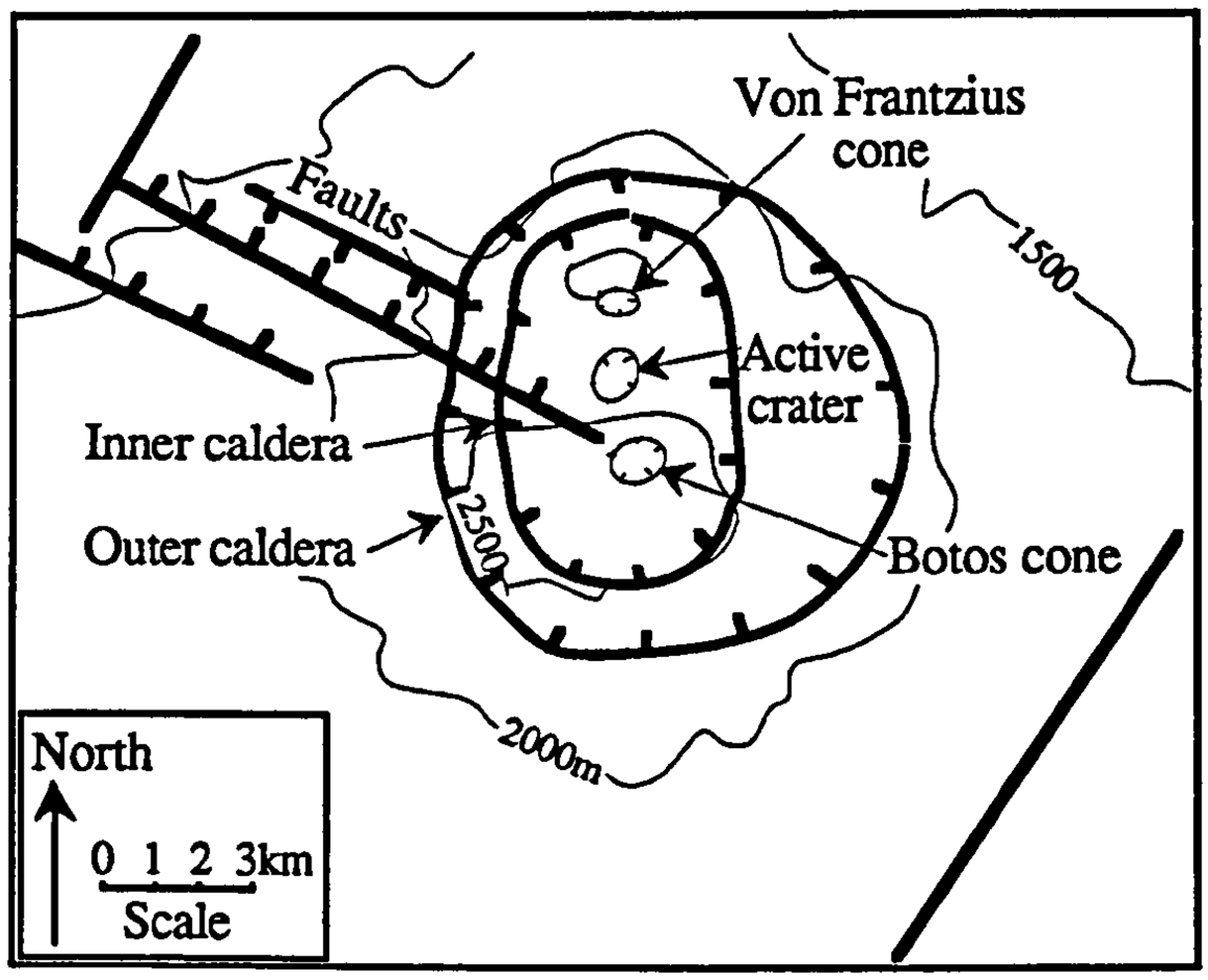

Figure 3.2 *Structure of the summit region at Poás. Adapted from Prosser and Carr (1983).*

3.2 Historical Activity at Poás

Historical activity at Poás is summarised in fig. 3.4. The first observation of activity at Poás is reported for the period 1826-28 (Newhall and Dzurisn, 1988), when earthquakes, and phreatic explosions or geyser-type activity were noted. An explosive ash eruption occurred in 1834, with a column reaching ~2 km above the crater, and ash falling ~40 km to the south. Between 1834 and 1910 a ~100 m diameter crater lake was present, exhibiting occasional geyser activity (Sapper, 1925). A minor ash eruption took place in 1880, and another in 1907. The largest historical eruption occurred on the 25th January, 1910. An ash column rose up to 8 km above the summit, and deposited ~8 x 10^5 m^3 of ash over the summit and surrounding villages (Boza and Mendoza, 1981). Small-scale geyser activity continued following the 1910 eruption.

The most recent phase of magmatic activity commenced at ~7 am on the 9th September, 1952, when a strong earthquake occurred and a 'mushroom-shaped' cloud of ash was erupted (Boza and Mendoza, 1981). Explosive ash eruptions continued through the crater

Plate 3.1 *View of the active crater at Poás, from the eastern crater rim in April 1989. The remnant of the 1952-54 pyroclastic cone is in the centre of the picture, and is the usual site of fumarolic emission. The pit crater to the right (north) of the cone, was also formed during the 1952-54 activity. This crater is emitting gas, and is the site of the crater lake, which had been almost removed when this photograph was taken. Lake sediments, and yellow sulphur deposits can be seen on the former lake floor.*

lake, and on the 17th May, 1953, (perhaps significantly, near the end of the dry season) the lake was observed to be much reduced in size, and a violent explosion produced incandescent scoria. The lake had disappeared five days later, and on the 24th May large eruptions produced further incandescent materials, and an ash/steam column visible from the Central Valley, ~30 km away. By January, 1954, a cinder cone had grown; a small lava flow followed, and then a pit crater formed following explosions. The lava flow, and the NE portion of the cinder cone subsequently collapsed into this pit crater (Krushensky and Escalante, 1967). A new lake formed within this crater between 1954 and 1964.

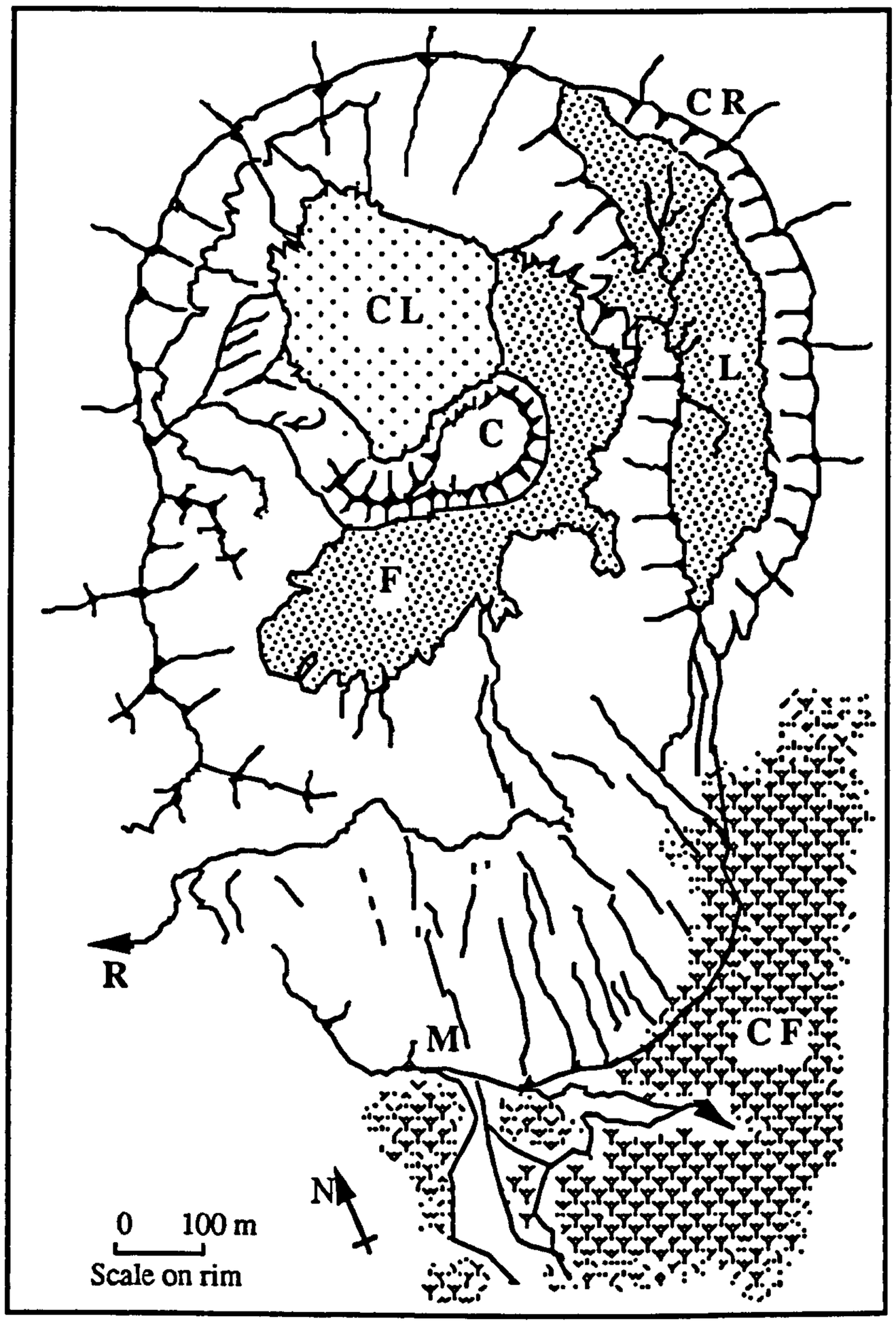

Figure 3.3 *Map of the active crater at Poás, drawn from an aerial photograph. CL is the site of the crater lake; C is the cone; L is the ledge, a flat area intermediate in level between the crater rim and floor; F is the flat crater floor; CR is the crater rim; R is the river valley draining the south-western end of the crater; M is the Mirador (look-out position); CF is cloud forest. The scale is taken from points surveyed on the crater rim (G. Brown, pers. comm.), but is only valid around the crater rim to the east, north, and west. The lake appears too small (by ~10 %) in the aerial photograph, due to foreshortening, and the Mirador area (which is higher than most of the crater rim) too large.*

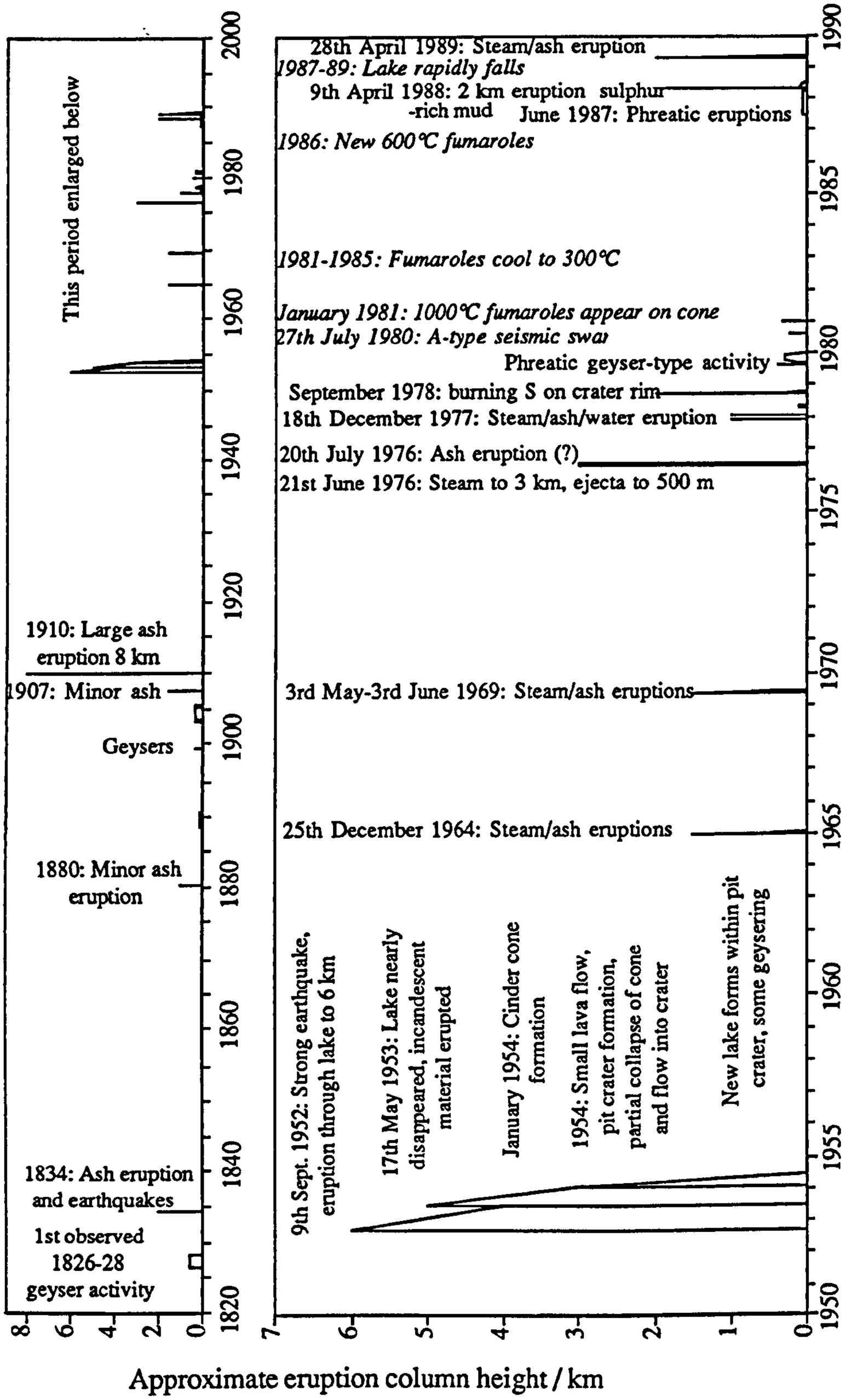

Figure 3.4 *Summary of historical activity at Poás. See text for details.*

Further eruptions occurred at ~5 am on the 25th December, 1964, when steam/ash eruptions were observed from San José (Krushensky and Escalante, 1967). Fog obscured observations for the following three days, however, aerial reconnaissance revealed the upper parts of dark-brown ash clouds on the 26th. The crater was visited on the 28th, and this revealed that the floor and walls were covered in ~2 cm of light-grey mud, up to 15 cm thick in places. Reddish-brown very fine ash covered the mud in some areas and a number of volcanic bombs, up to 25 cm long were 'thickly scattered' over the eastern part of the crater floor. The bombs were all non-juvenile, and made up of weathered red, vesicular andesite lava fragments, encrusted with fused sulphur. Activity on the 28th was restricted to ejection of ash-laden steam clouds from a 'funnel-shaped' depression on the pit floor, rising to no more than 600 m before they were dispersed. The vent was in 'about the same location as geyser activity seen previously'. Activity decreased, and by January the site of the active vent was 'again filled by a boiling mud lake to about the same level as the previous lake'. This lake showed 'the same geyser-like fountaining as before the December 1964 eruptions'.

A further period of heightened activity at Poás during May-June 1969 is documented by the 'Smithsonian Institution, Centre for Short Lived Phenomena' newsletters (No.s 529, 540, 548, 552, and 568): At 0600 on 3rd May 1969, a 'vapour eruption' was observed to ~1500 m over the crater. At 0820 on 13th May, a 'probable ash eruption' was observed, with steam and 'clouds of black smoke'. At 0600 on 15th May, further eruptions were seen to ~1300 m above the crater. On the 19th May, an increase in fumarolic activity was noted, with continuous emission of vapour from the main crater, 'which is full of water', suggesting that the lake was well established at the time. Gases and pyroclastic material were being thrown ~15-25 m above the lake every 6-7 minutes on the 30th of May. At 0615 on 3rd June, 'considerable black smoke' was seen to ~300m.

Another Smithsonian newsletter (No. 2477) reported that on the 21st June, 1976 a steam cloud was observed at 3 km height above Poás, with ejecta thrown 500 m above the crater. A radio report on the 20th July, 1976 stated that Poás 'began to rumble continuously and emit large quantities of ash which darkened the sky and covered thousands of acres of

this, but noted that minor activity may have occurred. Bennett and Raccihini (1978) reported an eruption of ash and bombs in November 1976, which 'spread a mantle of ash for some kilometres west of the crater'. They noted that plumes erupted during geyser activity at Poás were often charged with 'greenish amorphous sulphur particles', and suggested the presence of a lake of molten sulphur beneath the water lake immediately prior to eruptions. Bennett and Raccichini (1978) estimated that several hundred tons of sulphur were lying on the surface within a circle of radius half a mile (800 m) from the lake centre.

The only eruption reported to have occurred during 1977 was on the 18th December, when a 'column of water, ash and mud was ejected, rose more than 1 km above the vent, then fell on the flanks of the volcano, covering a large area with mud' (SEAN2:12, 1977).

Since 1978, when the road leading to the summit was completed, the monitoring of Poás has increased, with regular, approximately monthly visits by Jorgé Barquero (Universidad Nacional de Heredia, Costa Rica), who has made measurements of lake and fumarole temperatures and chemical compositions (see below), and provided reports of observations to the Smithsonian Event Alert Network (SEAN). The following are summaries of reports, collected together in McClelland et al. (1989) for the period 1978-85 (interspersed chronologically with other material):

SEAN 3:11: From the 10th April 1978 and through May, ejection of sulphur-rich grey clouds of ash and mud to a height of 5-100 m occurred, at a rate of ~50 per day, at intervals of ~30 minutes, with ejecta falling within the crater or nearby. The lake level fell by ~0.5 m over the period of activity. The lake cooled as activity ended, but heated up again when explosions recommenced on the 22nd September. Gray ash and mud were thrown 40-300 m above two vents, one in the centre of the lake, the other at its southern margin. Up to 30 explosions per day occurred, with ~45 minute intervals. The lake had fallen by ~3 m in level by the 4th October, and was entirely grey in colour, as opposed to the turquoise green colour observed during prolonged periods of inactivity.

SEAN 4:3: Activity declined in November 1978, with the maximum height of columns reaching only 25 m, and ended in December.

reaching only 25 m, and ended in December.

Francis et al. (1980) reported frequent small eruptions and one large eruption during January 1978, and another large eruption in September 1978, when rangers of the Costa Rican National Park Service reported hearing loud explosions and seeing small, but widespread blue flames around the crater rim (sulphur burns with a blue flame). The level of the lake was also much reduced, with the bottom visible in places. In January 1979, numerous bombs and fresh impact craters were found on the north-eastern flank of the crater, with blocks 0.3 m in diameter found several hundred metres from the rim. The asymmetrical distribution of bombs, craters, and scoriaceous sulphur isopachs indicated a directed blast had occurred, originating from the southern part of the lake or the cone. Three distinct types of blocks were erupted: (1) poorly consolidated mud and clay (lake sediments); (2) fresh, dark basaltic material, which may have represented a juvenile component; and (3) heavily altered, sulphur encrusted blocks. The sulphur on these blocks was clearly molten when they were erupted, and produced stalagmites and stalactites, probably suddenly starting to flow as the sulphur passed through its viscosity minimum (~116°C) during cooling. Some 10-15 tonnes of scoriaceous sulphur was also erupted in late 1978.

SEAN 5:1: A single explosion occurred on the 8th September 1979, and produced a pine-tree shaped eruption column of tephra and water to a height of ~400 m, which fell back into the lake. From 15th - 30th September, up to 10 small phreatic explosions occurred per day, ejecting material to 15-50 m above the lake. During October, geysering reached heights of 150 m, and during November and December, 300 m, decreasing to 100 m in January, and then ceasing.

In 1980, surface activity remained at a normal low level until September (see below), however, at 0700 GMT on the 27th July 1980, intense seismic activity was observed (Casertano et al., 1983, 1985, 1987). The shocks were classified as 'fracture-type micro-earthquakes', (or A-type, Minakami (1969)), with S-P time differences of less than one second, indicating a source within ~4 km of the seismometer, which was located on the SW flank of the active crater. Following this seismic swarm, B-type earthquakes (Minakami,

1969) and harmonic tremor began to increase (Casertano et al., 1987), and it was suggested that hydrofracturing of the magmatic carapace had occurred, with release of magmatic volatiles.

SEAN 6:2 Surface activity resumed at 0950 on the 11th September 1980 with a 250 m high explosion of 'lake water laden with ash, sand, and small blocks rich in mineralised sulphur' from the southern end of the lake.

SEAN 6:5 Another explosion occurred at about dawn on the 26th December, 1980, again from the southern end of the lake, sending ash, small blocks and water to 320 m. In mid-January 1981, Parque Nacional employee Geiner Chacón reported seeing incandescence on the northern wall of the cone. Fumarole temperatures were estimated at 700-800 °C from the colour of the incandescence, a sudden rise from the previous measurements of ~90 °C (~boiling point for the altitude of Poás) (see fig. 3.5).

SEAN 6:8 A maximum fumarole temperature of ~1000 °C was measured on the 28th April, 1981. New fissures grew and rapidly heated on the eastern portion of the cone.

Figure 3.5 *Maximum fumarole temperatures on the pyroclastic cone adjacent to the lake at Poás (Barquero, 1983 and J.Barquero, pers. comm., 1989).*

(see fig 3.5), to ~300 °C in 1985. Lake temperatures (fig 4.1a) increased from ~30 °C in June 1980 to 60 °C by April 1983, accompanying a fall in lake level (see fig 4.1b). Lake temperatures then began to fall gradually, reaching 38 °C by April 1986, and the lake refilled to approximately its maximum level, with a depth of 47 m estimated in January 1985 (Brantley et al., 1987). Another, smaller A-type seismic swarm occurred between February and May 1986 (Fernandez, 1990). In June 1986, lake temperatures began to rise, and new, high temperature (~600 °C) fumaroles appeared on the cone at a site further to the NW. By January 1987, the lake had fallen ~7 m (Brantley et al., 1987), and by June 1987 lake temperatures had reached 70 °C.

SEAN13:6: Phreatic geyser eruptions resumed in June 1987, producing columns of water and sediments to heights of ~30m. Explosions became stronger by early 1988, and on the 9th April, 1988, two explosions ejected a ~2 km plume, depositing sulphur-rich mud onto the crater rim. In late April, small mud eruptions to ~5-100 m occurred every ~3 minutes. Activity was similar in June 1988, when wide terraces of sediment were visible around the lake edge, indicating that the lake level was continuing to fall.

The lake continued to decrease in volume, and increased in temperature to 82 °C by February 1989, when it started to degenerate into separate mudpools. By early 1989, fumarole temperatures over the entire cone had fallen to ~95 °C, and major gas emission had returned to sites on the lake bed. As the lake continued to dry up, mud/sulphur volcanoes built up upon the former sites of upwelling mudpools, and vented sediments and sulphur to heights of ~10 m (plate 3.2; Oppenheimer and Stevenson, 1989). These miniature volcanoes were rapidly (hours to days) built and destroyed, collapsing due to internal erosion, returning to vigorously bubbling mudpools. Some cones developed chimneys of sulphur (plate 3.3). On the 16th March, 1989, the collapse of a sulphur cone revealed a small pool of bubbling molten sulphur (Oppenheimer and Stevenson, 1989), and by the 19th of April, two lakes of

Plate 3.2 *Sulphur cone on the former lake bed, March 1989. The cone was approximately 2 m high, and was formed of mainly sulphur, with some lake sediment. The cone grew on the site of a former vigorously bubbling mud-pool, and was built in a few hours, spraying sulphur particles over a radius up to ~50 m from the cone vent, carpetting the surrounding lake sediments. The cone proceeded to cease erupting, was eroded (like the former cone in background left), and eventually returned to a bubbling mudpool. Similar cones developed chimneys of sulphur (plate 3.3). This site eventually developed into the sulphur lakes (plate 3.4).*

Plate 3.3 *Sulphur cones with chimneys, with weak fumarolic activity from the cone in the background (March 1989).*

Plate 3.4 *Dessicated lake-bed in April 1989, with two sulphur lakes (left foreground), the larger, elliptical one ~28 x 15 m. Vigourous gas emission within the lake remnant (background) is throwing up mud to a few metres height.*

liquid sulphur, one elliptical ~28 x 15 m, the other dumbell-shaped with maximum dimensions ~24 x 11 m, were established (plate 3.4).

Coincident with the formation of the sulphur lakes in April 1989, the remainder of the lake virtually disappeared, and lake-floor activity increased. Phreatic activity built up to six ~10 m high cones of lake sediment material towards the centre of the lake floor (plate 3.5), which emitted lake-floor material to heights of up to ~100 m. The plumes were generally dark and

Plate 3.5 *Erupting sediment cone on the former lake bed in late April 1989. Explosions were continuous, with some ejecting sediments to over 100 m height, and building at least six cones up to 10 m high. Vigorous gas emissions continued over much of the lake floor.*

cypressoid (pine-tree-shaped), but occasionally coloured yellow by sulphur. Activity increased, and on the 25th of April, 1989, a turbulently convecting, dark brown column was erupted to a height of ~300 m (plate 3.6), and deposited sulphur and sediments on the crater rim. The temperature of this eruption column was at least 459 °C, measured by optical

Plate 3.6 *Eruption on the 25thApril, 1989, at ~1200 hrs local time. The source of the eruption is just to the south of the cone in plate 3.5 (visble just to right of column), and just to the north-west of the sulphur lakes in plate 3.4 (shrouded in steam, foreground). The column radiated heat, and an optical pyrometer gave a minimum temperature of 459 °C. The range of brown colourations within the column is probably due to high temperature sulphur, or altered andesite material. The vertical column section is ~100 m, and sulphur and sediment were carried to beyond the crater rim.*

pyrometer. The column also featured a range of yellow and red-brown colourations, presumably due to sulphur in various forms and/or altered andesite material. Activity continued to increase, with columns up to ~1.5-2 km on the 28th April, and ~1-1.5 km on the 1st May, with wind carrying lithic ash and mud westward several kilometres (SEAN14:4). With the onset of the rainy season (May to December) in Costa Rica, the lake began to reform, and activity declined.

By March 1990, the lake level had again fallen, leaving isolated mudpools around a remnant central lake (SEAN15:4). Mud/sulphur cones were built and destroyed, and some vigorous fumaroles around the lake margin ignited, producing temperatures of ~400 °C during March, rising to 793 °C on 18th April. Similar activity to March/April 1989 was observed, with phreatic eruptions of lake sediments reaching heights of >300 m on 29th April. Activity decreased in May, as in 1989, but with mud eruptions to several hundred metres on the 4th and 8th May (SEAN15:5). No further eruptions occurred until the 6th March 1991 (SEAN16:2), when minor eruptions of lake sediments recommenced.

3.3 Summary of recent work at Poás

3.3.1 Geology

Prosser and Carr (1987) described the recent (~10-20 ka) eruptive activity of Poás on the basis of field mapping of the summit region. This period began with caldera formation, followed by cone construction, faulting and flank subsidence, flank fissure eruption, and multiple crater collapses. The chemical composition of recent calc-alkaline basaltic to andesitic lavas show temporal magmatic variation, with three similar felsic (~60-66 wt.% SiO_2) to mafic (~50-55 wt.% SiO_2) sequences, each separated by major structural changes (Prosser and Carr, 1987). The chemistry of the 1954 lava indicates that Poás is near the end of its present cycle. The geochemistry of the lavas suggested three separate sources, one originating from a magma chamber at mid- to sub-crustal depths, another from a deeper, more water-rich magma chamber, and the third a batch of mixed magma, with the first group as one endmember, and a less siliceous magma as the other.

3.3.2 Static gravity surveys

Rymer (1985) and Brown et al. (1987) presented static gravity data from Poás, of a closed positive (~+8 mGal) anomaly of about 1 km diameter, centred on the crater lake, surrounded by a broader negative (~-8 mGal) anomaly, centred on Botos cone, ~3-4 km in diameter. The data was speculatively interpreted as a ~800 m diameter cylindrical solidified magma pipe (density 2.5 - 2.7 Mg m^{-3}) directly beneath the active crater, intruded into low density caldera infill material. Two calderas were suggested: an inner one of diameter ~3 km, centred midway between the active crater and Botos cone, with a thickness of infill (density ~2.3 Mg kg^{-1}) typically a few hundred metres, but up to ~1 km within the Botos cone; and an outer one of diameter ~9 km, centred on approximately the same point, with ~1 km thickness of infill (density ~2.4 Mg kg^{-1}).

3.3.3 Dynamic gravity surveys

Rymer (1985) and Rymer and Brown (1984, 1987, 1989) presented data on gravity changes measured at Poás. Cyclic gravity changes of magnitude 50-120 μGal and period ~30 days from crater rim and flank stations were recorded in April/May 1983 (Rymer and Brown, 1984). These were interpreted in terms of magma movement or vesiculation cycles within the upper parts of a magma conduit (> 500 m depth), possibly tidally induced. A 1 % variation in vesiculation produces a density change of ~0.03 Mg m^{-3}, which, across a cylinder of diameter 1 km is large enough to account for the measured gravity changes. Groundwater variations were ruled out as the cause, because improbably large changes in water table height (~10-20 m) were required. In the absence of data on the height variation of these stations, ground movement could not initally be ruled out as the cause of these gravity changes. However, using an appropriate Bouguer-corrected free air gradient (-216 μGal m^{-1} for a density of 2.2 Mg m^{-3}), changes of 50-120 μGal would correspond to ground deformation of 23-56 cm, improbably large, given that .only a few centimetres of vertical movement has been observed at all except the cone stations since 1987, when the first survey of the required accuracy was done (Rymer and Brown, 1989).

Further data on gravity changes at Poás are presented in Rymer and Brown (1989) and

Brown et al. (1991). Uni-directional, non-cyclic increases in gravity of ~50-200 μGal over the period March 1987 to March 1989 were measured at six stations on the pyroclastic cone and crater floor, accompanied by deflation of up to ~30 cm. All these stations showed a residual gravity increase, after accounting for deflation, of ~50-150 μGal. This was contemporaneous with a period of lake phreatic activity (June 1987-July 1988), a dramatic fall in lake level (~32 m), and the fall in fumarole temperatures on the cone from ~600 °C to ~95 °C. The gravity increases were interpreted as the addition of ~10^8 kg of mass, in the form of 'dendritic stringers' of magma beneath the southern lake/cone area over the period March 1987 to March 1989 (Rymer and Brown, 1989; Brown et al., 1991). Rowe et al. (1991a) suggested that the gravity increases may, alternatively, be accounted for by the filling of cavities with elemental sulphur following the proposed 1986 magma carapace 'hydrofracturing' event (see section 3.3.4) and the associated release of sulphur volatiles. This would require an average sulphur flux from the magma of ~1.6 kg s^{-1} over the two year period (twice the estimated background level, see section 3.3.7), equivalent to an SO_2 flux of ~270 t d^{-1}, assuming 100 % efficiency in the conversion of SO_2 to S. Another possibile explanation of the increase in gravity is the flooding of a vapour zone beneath the cone/southern lake with hydrothermal liquid. Saturating a rock volume of 10^6 m^3, assuming a porosity of 10 %, would add 10^8 kg of mass. This idea is also consistent with the fall in maximum fumarole temperatures to ~95 °C, probably reflecting a change in the fumarolic source from a high temperature vapour region to a liquid-dominated zone with a boiling upper surface.

3.3.4 Seismic Data

Seismic data for the period 1980-89 was summarized by Fernandez (1990) and Rowe et al. (1991a). An A-type seismic swarm occurred on the 27th July 1980, and has been interpreted as 'hydrofracturing of a water-saturated carapace of a magma body at depth due to second boiling' (Casertano et al., 1987). Second boiling is a degassing process which occurs when volatiles (chiefly water) exceed their solubility in the melt, and enter the gas phase (Burnham, 1985, and see chapter 6). Fracturing would have occurred when the build-up of gas pressure exceeded the confining pressure. Following this event, B-type seismicity and

harmonic tremors increased, and five months later fumaroles with temperatures up to ~1000 °C appeared on the cone, clearly of direct magmatic origin.

The source mechanisms of type B events at Poás are thought to be due to the movement of high temperature liquid/gas mixtures through fractures and pore spaces, and the collapse of vapour cavities within the hydrothermal system between the magma body and the crater lake (Morales et al., 1988; Fernandez, 1990). Increases in B-type seismicity or tremors are generally thought to represent a heightened volatile flux from an underlying magma body (McNutt and Harlow, 1983).

Tremor at Poás is thought to be related to the degassing of high temperature fluids through rigid-walled conduits beneath the cone (Morales et al., 1988; Fernandez, 1990). Tremor decreased in intensity as fumarole temperatures fell between 1981-85 (Rowe et al., 1991a).

A second recent period of A-type seismicity from February to May 1986, followed a sharp increase in B-type seismicity in late 1985 (Fernandez, 1990; Rowe et al., 1991a), and again preceded a sudden increase in maximum fumarole temperatures in June 1986 (fig. 3.5). B-type activity increased after mid-1987, coinciding with the onset of phreatic activity in the lake, and the decline in lake level. The sharp decline in B-type activity associated with the disappearance of the lake in 1989 was probably due to the increased ease of gas venting due to the lack of water interrupting the gas flow. Indeed, B-type events increased sharply in May 1989 when the lake reformed, and fell again when the lake disappeared again in 1990 (Rowe et al., 1991a).

3.3.5 Sulphur

Bennett and Raccichini (1977) postulated the existence of a lake of liquid sulphur beneath the crater lake at Poás, based on the observation of greenish scoriaceous sulphur particles deposited from plumes erupted from the lake. They suggested that molten sulphur (density 1.9-2.0 Mg m^{-3}) would accumulate between andesitic material (density 2.5-2.7 Mg m^{-3}) and lake sediments (density 1.0-2.0 Mg m^{-3}). If the sediments gradually compacted and increased in density, approaching the density of liquid sulphur, the stratigraphy could become unstable and overturn, exposing high temperature sulphur to the lake water. Fluid-

coolant interaction could follow, producing an explosive eruption.

Francis et al. (1980) stressed that Poás was the only known site of pyroclastic sulphur eruptions, and described in detail a number of blocks erupted in 1978 that were covered in sulphur. They suggested that sulphur concentrated around fissures and pore spaces in the conduit beneath the active lake bottom fumaroles, and was subsequently sprayed into the air by explosive eruptions. Francis et al. (1980) thought the presence of a lake of liquid sulphur beneath the *entire* water lake, as suggested by Bennett and Raccichini (1978), 'unlikely'.

Oppenheimer and Stevenson (1989) reported the appearance of two lakes of molten sulphur in March 1989, accompanying the disappearance of mudpools surrounding the remnants of the crater lake. This observation confirmed that large quantities of elemental sulphur were present in the lake sediments, and particularly around certain fumarole sites. The appearance of the lakes was preceded by the formation of miniature mud and sulphur volcanoes (Oppenheimer, 1991), which collapsed to reveal the lakes. Some of these cones were constructed of near pure sulphur tephra, thought to be formed by gases venting through a liquid sulphur body, creating a spray of crystallised sulphur , including some accretionary lapilli of sulphur. Sulphur isotope data (Oppenheimer, 1991; J. Maynard, pers. comm.) indicate that the sulphur was isotopically light, probably due to low-temperature (~100 °C) fractionation between hydrogen sulphide and sulphur dioxide, before the deposition of elemental sulphur by the reaction of these gases with water (Giggenbach, 1974). Gases sampled in November, 1990, from a vent near the site of the former sulphur lakes, were found to be largely water and SO_2, interpreted as a re-heated mixture of lake water and deposited sulphur, and not a primary magmatic gas (W. Giggenbach, pers. comm.).

3.3.6 Gas chemistry and flux

Casadevall et al. (1984) reported COSPEC measurements of the SO_2 flux from Poás in February 1982, together with data on fumarole gas chemistry measured in March 1982. An SO_2 flux of 700±180 t d^{-1} was measured, which, combined with the gas chemistry data (table 3.1), yields estimated fluxes of the magmatic gas species (table 3.1).

Species	Volume %	Weight %	Flux (Feb 1982) / kg s^{-1}
H_2O	79.5	54.4	17±5
CO_2	10.5	17.6	5.4±1.4
$SO_2 + H_2S$	14.2	26.4	8.1±2.1
H_2	1.9	0.2	0.06±0.02
HCl	0.66	0.9	0.3±0.1
HF	0.10	0.1	0.03±0.01
$O_2 + N_2 + Ar$	0.39	0.5	0.15±0.05

Table 3.1 Composition, and flux based on COSPEC measurements of SO_2 flux, of gas emission from Poás, 1982 (from Casadevall et al., 1984).

3.3.7 Integrated models of activity at Poás

Brantley et al. (1987) applied a mass, energy and chemical balance to Poás crater lake for the period 1985-1987. A seepage term was required, because the lake chemistry remained steady despite the continuous input of fumarolic chemicals, and the lack of precipitation in the lake (excepting S, Si and Ca). Average mass flow rates were calculated as: rainfall ~60 kg s^{-1}; evaporation ~100 kg s^{-1}; seepage ~40 kg s^{-1}; and fumarolic steam input ~80 kg s^{-1}.

Brown et al. (1989) estimated the total power output of Poás, and suggested that it had increased from ~160 MW in 1985 to ~265 MW in 1988. This modelling was brought a stage further by Brown et al. (1991), who calculated the average monthly power input to the lake for the period 1978-89. The model used was a simplified version of the model presented in chapter 2 - results of this, more rigorous model are presented in chapter 4. On the basis of both the gradual increase in gravity, and the increase in thermal output, minor intrusions of magma were inferred to have occurred between 1987 and 1989. The crystallisation, cooling and degassing of these intrusions, with accompanying vesiculation and enhanced heat transfer from throughout the shallow (~200 m deep) magma feeder system were suggested as the sources of the additional heat output.

Rowe et al. (1991a) suggested from mass and chemical balance considerations that most of

the heat supplied to Poás lake was in the form of hot brine, supplemented by condensation of fumarolic steam. This assertion was based on the conservation of a number of metal ions (Na, Mg, Fe) in lakewater with time. If heat was only supplied by fumarolic steam, which cannot contain significant quantities of metals (Gemmell, 1987), then lake metal ion concentrations should decrease due to losses through seepage, assuming that lake sediments release negligible amounts of metal ions. Brine, however, can contain large quantities of metal ions, and could replenish the lake with ions lost through seepage. Much higher seepage rates (~600 kg s^{-1}) were calculated, indicating rapid recycling of lake water through the underlying lake sediments and pyroclastic deposits. The major differences between the model of Rowe et al. (1991a) and that described in chapter 2 are summarised in section 3.7. Rowe et al. (1991a) estimated a background energy flux of ~300 MW was being supplied to the lake. Assuming this heat originated from crystallisation of magma, this implied a solidification rate of ~0.012 km^3 yr^{-1}, and magmatic volatile releases of ~12 kg s^{-1} H_2O, ~0.8 kg s^{-1} S, ~0.15 kg s^{-1} HCl and ~0.006 kg s^{-1} HF.

Rowe et al. (1991a) suggested fracturing of a magmatic carapace caused the increase in fumarole temperatures in June 1986, which was preceded by A-type seismicity between February and May, 1986. This process was also proposed for the seismicity and increase in fumarolic activity in 1980-81 (Casertano et al., 1987, and see section 3.3.4). Rowe et al. (1991a) believed that below average rainfall over the period 1983-89, and in particular during 1985-87, caused the fall in lake level, which, in conjunction with the increased heat influx to the lake from mid-1986 onwards, contributed to the resumption of phreatic activity in June 1987, and the ultimate loss of the lake in 1989. They also suggested that recycling of acidic brine beneath the lake could dissolve material at a rate of ~1250 m^3 yr^{-1}, and that the rate of formation of native sulphur from ascending gases would be sufficient to fill these voids. This would require a sulphur deposition rate of ~0.08 kg s^{-1}, approximately one tenth of the estimated magmatic volatile flux of sulphur (see above).

3.4 Mount Ruapehu, New Zealand

Currently active volcanism in New Zealand is associated with subduction of the Pacific plate beneath the Australian plate, and occupies a band ~250 km long by ~50 km wide in the

North Island, known as the Taupo Volcanic Zone (TVZ) (figs. 3.6, 3.7) (Cole, 1990). The TVZ comprises an arc and back-arc basin of Miocene to recent age.

Mt. Ruapehu (plate 3.7) is an active andesitic composite volcano of the Tongariro volcanic centre, located at the southern end of the TVZ, approximately 250 km from both Wellington and Auckland. Ruapehu has a maximum elevation of 2797 m, rising ~1500 m above the surrounding country, a basal diameter of ~20 km, and a volume of ~150 km^3. A simple stratigraphy of underlying rocks was given by Latter (1981) as ~0.7 km of sediments, ~0.7 km of weathered greywacke and a basement of schistose greywacke. The oldest dated lava from Ruapehu is 0.23±0.006 Ma (Cole et al., 1986). The permanently glaciated summit region has three craters, two historically inactive, and mainly filled by ice, and the most westerly, active crater, largely filled by a warm, acidic lake, known as Crater Lake (plate 3.8; fig. 3.8).

The active crater has a diameter of ~800 m, and is surrounded by the peaks of Tahurangi (2797 m) to the south, connected by a possible older crater rim to Paretetaitonga (2754 m) to the NW, the 'Dome' (2675 m) to the north, and a well defined crater rim to the east, whose highest point is Pyramid Peak (2649 m) (fig. 3.8). The active crater is surrounded by glaciers, which occupy all the major valleys leading from the summit: the Mangaturuturu Glacier to the west, the Whakapapa Glacier to the north, and the Whangaehu Glacier to the east (fig. 3.8). Crater Lake fills the crater to a maximum height of 2531 m, at which level it overflows the southern crater rim, is diverted eastwards towards the Whangaehu Glacier, and forms the headwaters of the Whangaehu river. Minor activity in the lake usually sends a surge of water down this valley; major activity can create lahars fed by lakewater down all of the valleys. Indeed, the largest historical loss of life associated with Ruapehu occurred on the 24th December, 1953, when a large lahar swept down the Whangaehu valley, destroying

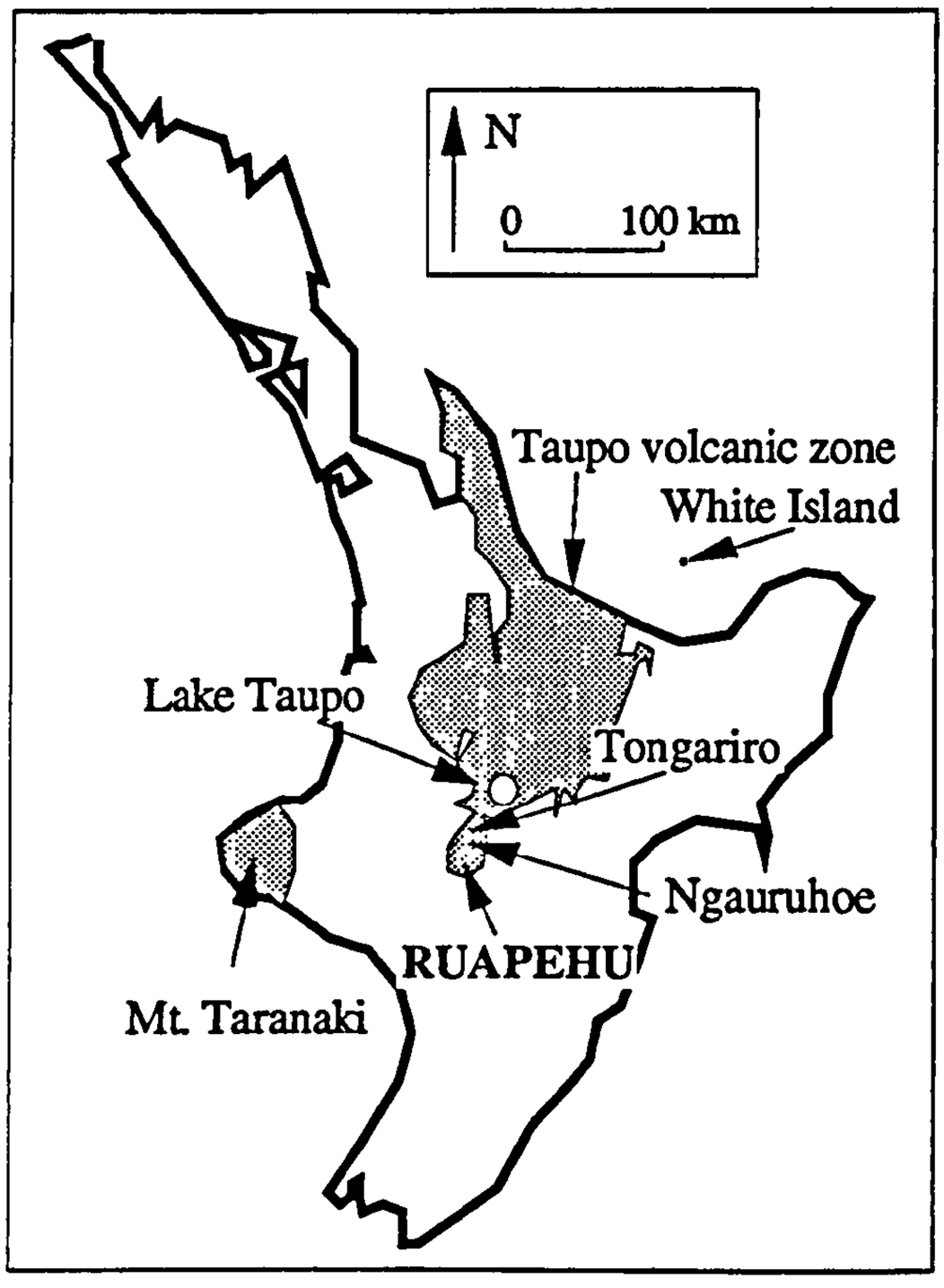

Fig. 3.6 *Location of Ruapehu, within the Taupo volcanic zone of the North Island of New Zealand. Adapted from Cole (1990).*

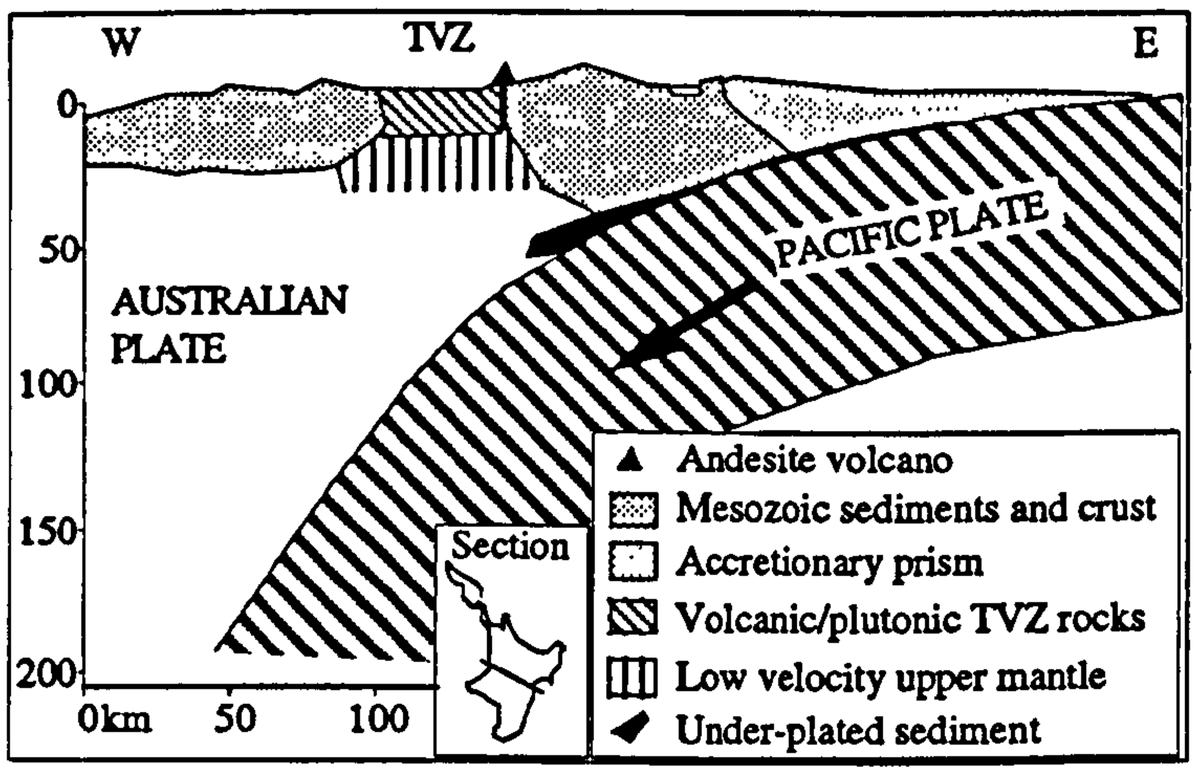

Fig. 3.7 *Schematic cross-section through the North Island of New Zealand, determined from seismology. Adapted from Cole (1990).*

Plate 3.7 *View of Mt. Ruapehu from the north, in March 1990 (summer). Small pockets of snow can be seen near the summit. The plume is not strictly volcanic, although vapour from Crater Lake probably helped to seed the cloud.*

the Tangiwai railway bridge. Minutes later, the Wellington-Auckland express train arrived, and 151 people died. Healy (1954) suggested that ice and debris from the 1945 eruption had created barrier at the lake outlet, allowing the lake level to rise 8 m above its normal level. The sudden collapse of this barrier, apparently not associated with volcanic activity, released ~1.9 x 10^6 m^3 of lake water, causing the lahar. Subsequently the New Zealand railway company have continuously monitored the flow and acidity of the Whangaehu river.

3.5 Historical Activity at Ruapehu

Activity at Ruapehu from 1945 to 1990 is summarised in fig 3.9 and table 3.2. The most significant recent magmatic events occurred in 1861 and 1945 (Gregg, 1960). Between March and July 1945, lava was emplaced under the eastern part of Crater Lake, gradually displacing lake water down the Whangaehu valley. By July, a lava dome with a central vent

Plate 3.8 *View of Crater Lake from near Dome Shelter (see fig. 3.8), in March 1990. The peak in the background is Tahurangi, the highest point of the volcano. The lake was ~40 °C, and was clearly evaporating.*

had completely replaced the lake. This vent was progressively enlarged by explosive ash eruptions, and when the activity ended in November, it was ~100 m wide and ~300 m deep. By 1953 a lake was re-established to its former level. The 1861 eruption is poorly documented, but also seems to have involved the emplacement of a lava dome in this crater.

Phreatomagmatic eruptions, involving the interaction of magma and lake water, have occurred on numerous occasions at Ruapehu. Major events in June 1969 and April 1975 created lahars down four valleys leading from the summit (Nairn et al., 1979). These two events both involved a base surge component, composed mainly of lake water, which draped the summit region in 1969, and the summit and upper flanks in 1975.

Phreatic eruptions through Crater Lake are common (frequency ≈ 1 year) at Ruapehu, and are generally confined to the crater area. They typically involve ejection of steam, lake-water, sediments, and blocks of altered andesitic material, occasionally draped in sulphur. More violent eruptions generally contain a juvenile component.

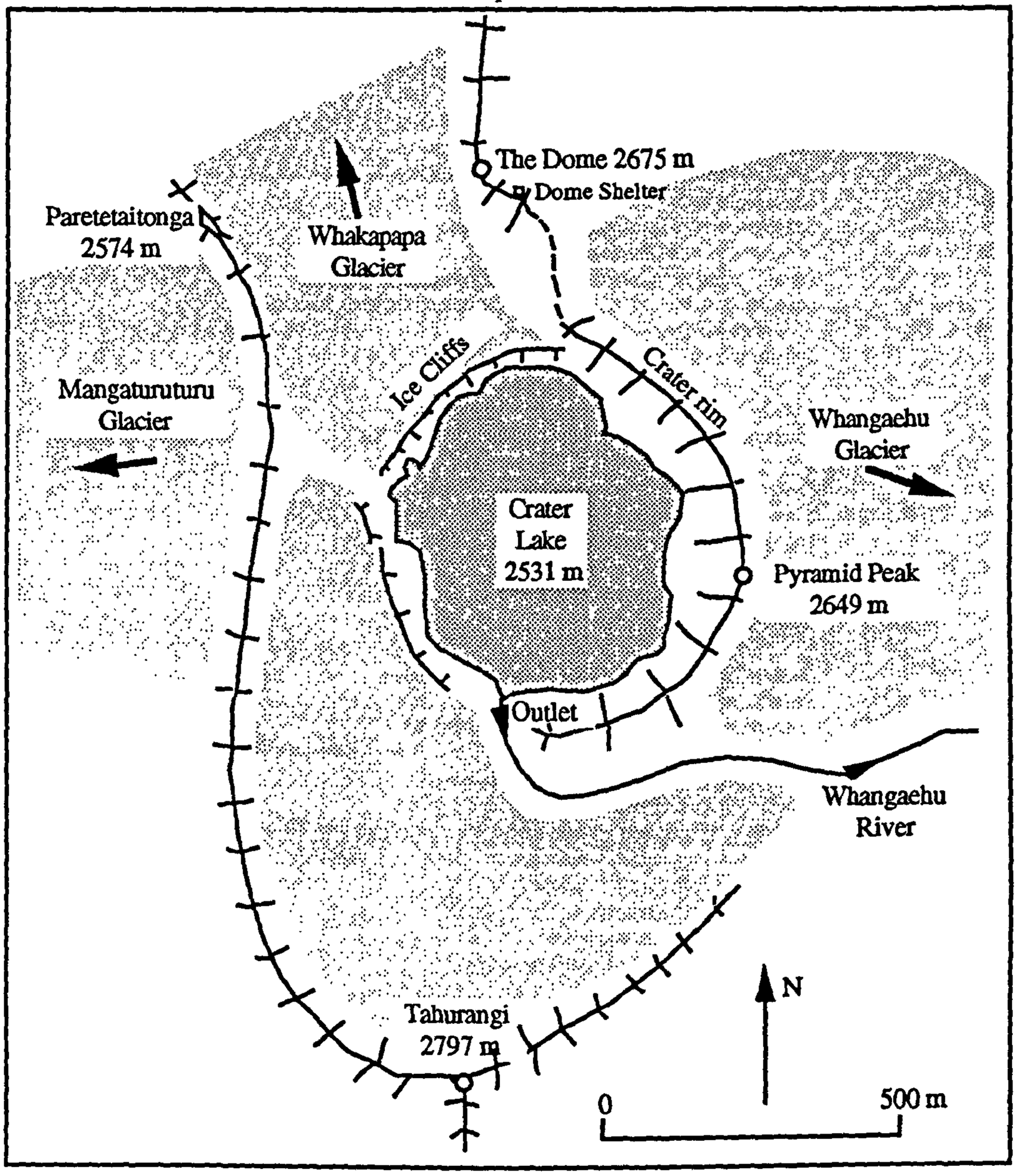

Figure 3.8 *Sketch map of the active crater and surroundings at Mt. Ruapehu. Light stipple indicates ice fields. Adapted from Nairn et al. (1979).*

Since 1977, only relatively minor phreatic and phreatomagmatic eruptions have occurred (n ≤ 2, see table 3.2, fig. 3.9). Hurst et al. (1991) noted that since 1979, it has become common for the lake to gradually cool for long periods (typically 6 months to a year) before suddenly rising in temperature, with minor eruptions and seismicity either initiating activity, or occurring around the peak in lake temperature. During long quiescent periods the lake is blue-green in colour, whereas during heating or activity, when sediments are stirred, the lake turns battleship grey. Since 1985, a clear cyclicity (period ~ 1 year) in heating and cooling phases has been seen, with heating for 2-3 months, followed by cooling (see figs. 4.13 and 4.20).

Date	Description of event	Magnitude (n)
Mar-Nov 1945	Dome emplacement and explosive removal	5
April 1946	Small phreatic/phreatomagmatic eruption	2-3
Sept-Oct 1946	Steam columns observed (?)	1
21 Nov 1946	Small phreatic/phreatomagmatic eruption	2
8 Feb 1947	Small phreatic/phreatomagmatic eruption	2
March 1947	Small phreatic/phreatomagmatic eruption	2
28 April 1947	Small phreatic/phreatomagmatic eruption	2
31 May 1947	Small phreatic/phreatomagmatic eruption	2
Jan-Feb 1948	Steam columns observed (?)	1
26 July 1950	Small phreatic/phreatomagmatic eruption	2
24 Dec 1953	Lahar generated by collapse of ice/debris barrier (see text)	3
8 Oct 1954	Steam columns observed (?)	1
23 Oct 1956	Steam columns observed (?)	1
18 Nov 1956	Small phreatic/phreatomagmatic eruption	2
21 May 1959	Small phreatic/phreatomagmatic eruption	2
1 Jun- 31 Aug 1959	6+ small phreatic/phreatomagmatic eruptions	2
28 April 1964	Steam columns observed (?)	1
1-29 June 1964	Steam columns observed (?)	1
23 March 1966	Steam columns observed (?)	1
Aug 1966	Small phreatomagmatic eruption	2
27 Sept 1966	Small geyser-like events in lake	1
24 Oct 1966	Steam columns observed (?)	1
22-24 Jul 1967	Small geyser-like events in lake	1
4 Oct 1967	Steam eruption (?)	1
7 April 1968	Geyser-like events in lake	1
26 April 1968	Moderate phreatomagmatic eruption	3
23 May-10 Jun 1968	Several small phreatomagmatic eruptions	2
22 June 1969	Major phreatomagmatic eruption. Lahars in 4 main valleys.	4
Sept 1970	Small phreatic/phreatomagmatic eruption	2
3-7 April 1971	Small phreatic/phreatomagmatic eruption	2
8 May 1971	Moderate phreatomagmatic eruption. Lahars down Whangaehu valley.	3
15-16 May 1971	Numerous moderate events. Lahars down Whangaehu valley.	3-4
14 July 1971	Small phreatic/phreatomagmatic eruption. Lahars down Whangaehu valley.	3
Nov 1972	Small phreatic eruption	2
Jan 1973	Small phreatic eruption	1
Oct-Nov 1973	Several very small phreatic eruptions	1
Jan-May 1974	Small phreatic eruptions	1
2-5 Aug 1974	Small phreatic eruptions	1
8 Aug 1974	Steam column observed (?)	1
Sept-Oct 1974	Numerous steam columns (?)	1
24 April 1975	Major phreatomagmatic eruption. Lahars down 4 main valleys	5
27 April 1975	Moderate phreatomagmatic eruption	2-3
Oct 1975	Small phreatomagmatic eruption	2
6 April 1976	Small phreatic eruption	1
Jul-Aug 1977	Several very small phreatic eruptions	1
2 Nov 1977	Moderate phreatomagmatic eruption ~1800 m. Lahar down Whangaehu.	3
Jan 1978	Very small phreatic eruption	1
7 Mar 1978	Small phreatic eruption to ~610 m	2
June 1978	Several small phreatic eruptions	1
Sept 1978	Small phreatomagmatic eruption	2
Jan 1979	Several small phreatomagmatic eruptions	1
June-July 1979	Several small phreatomagmatic eruptions	1
Dec 1979	Small phreatomagmatic eruptions	2
Jan 1980	Small phreatic/phreatomagmatic eruption	1
Feb-April 1980	Several small phreatic/phreatomagmatic eruptions	1-2
Oct 1980	Very small phreatic/phreatomagmatic eruption	2
Oct 1981-Apr 1982	Several small phreatic/phreatomagmatic eruptions	1-2
2 April 1984	Small phreatic eruption	1
May-June 1985	Several very small phreatic eruptions	1
Feb 1986	Very small phreatic eruptions	1
August 1987	Very small phreatic eruptions	1
Mar-May 1988	Very small phreatic eruptions	1
Jan-Feb 1989	Small phreatic eruptions	1
July 1989	Small phreatic eruptions	1
Jan-Feb 1990	Small phreatic eruptions	1

Table 3.2 *Summary of activity at Ruapehu 1945-1990, adapted from Houghton et al. (1987), with additional data from SEAN bulletins. The magnitudes (n) are from Houghton et al. (1987), and based upon the approximate area (A) of extreme risk from ballistic blocks, surges and lahars, where* $A \approx 10^{n+1}$ *to* 10^{n+2} m^2, *and the total range (R) of fall ejecta, where* $R \approx 10^n$ *to* 10^{n+1} m.

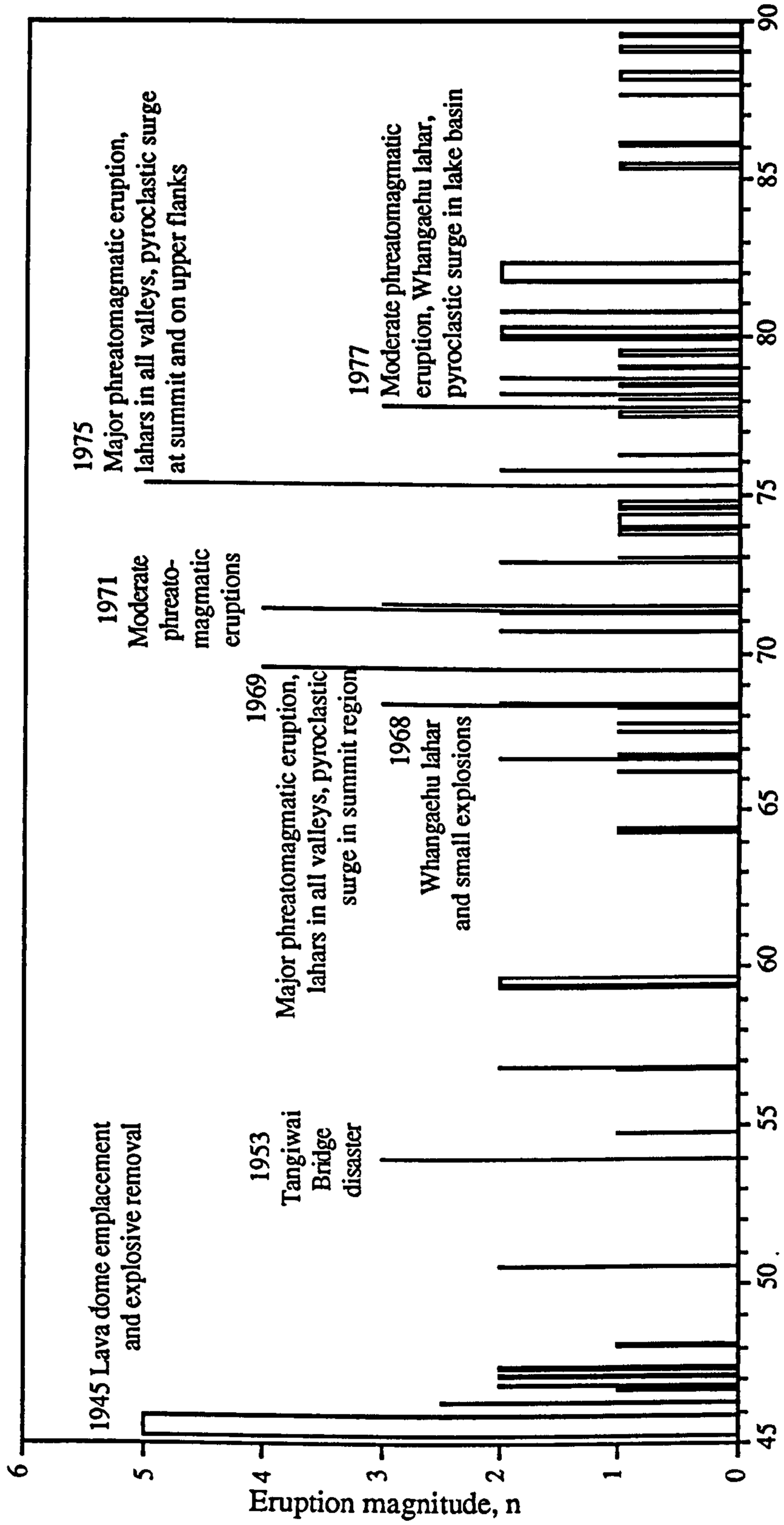

Fig 3.9 *Activity at Ruapehu 1945-90, using data from Houghton et al. (1987), with additional data from SEAN bulletins. See Table 4.1 for explanation of scale.*

3.6 Summary of recent work at Ruapehu

3.6.1 Volcanology and Petrology

Ruapehu has been mapped in detail by Hackett (1985), and the main conclusions are summarised in Cole et al. (1986). The oldest of four formations identified was the Te Herenga (> ~130 ka), exposed mainly on the NW slopes of Ruapehu, which consists of lava flows, autoclastic breccias, plugs and dykes. The Wahianoa formation (~60-120 ka) comprises lava flows, autoclastic breccias and lahars, and is exposed on the SE flanks. The present day highest peaks and main cone of Ruapehu are made from lavas and pyroclastics of the Mangawhero formation (~15-60 ka). The most recent, Whakapapa formation (~15-0 ka) consists of block lavas, autoclastic breccias and pyroclastics erupted from six vents across the massif. Cole et al. (1986) concluded that activity at Ruapehu was a complex alternation of extrusive (lava domes, aa and block flows) and explosive (strombolian, subplinian, vulcanian, phreatic and phreatomagmatic) volcanism.

Lavas erupted from Ruapehu range from basalt to dacite in composition (SiO_2 ~53-64 wt. %), but are mainly plagioclase and plagioclase-pyroxene andesites, containing ~30-40 wt. % phenocrysts, and follow typical calcalkaline geochemical trends. The majority of lavas can be generated from a basaltic parent, by plagioclase, olivine/orthopyroxene, augite and magnetite fractionation, or AFC (assimilation-fractional crystallisation) involving a small component of granitic partial melt developed from the greywacke-gneiss basement.

3.6.2 Seismology

The first attempts at seismic monitoring were made in 1952, with the installation of a seismometer at Whakapapa village, ~9 km from the summits of both Ruapehu and Ngaurahoe (Hurst, 1986). This meter recorded vibrations from the lahar of 1953, and tremor and explosion earthquakes during the vulcanian eruptions of Ngaurahoe in 1952-53. Seismic observations were greatly improved by the installation of a seismometer at Dome Shelter (fig 3.8), ~700 m N of Crater Lake (Dibble, 1972).

Dibble (1972, 1974) found that major eruptions ($n \geq 3$) at Ruapehu were usually preceded

by a period powerful (> 1kW source) seismic tremor, and B-type earthquakes close to Crater Lake, less than 1 km deep. Hours to days of unstable (stop-start) tremor typically followed the earthquakes and preceded eruptions, but only 20 minutes of tremor and B-type earthquakes occurred before the powerful eruption of 22nd June 1969.

Latter (1981) classified earthquakes recorded at Ruapehu into two categories: (1) 'volcanic', generally low frequency (≤ 3 Hz), with emergent onsets, poorly defined phases, and often multiple; and (2) 'volcano-tectonic', high frequency (≥ 3 Hz, except when attenuated along path), with sharp onsets and well defined phases. Type 1 events were thought to have weak, soft (hot) sources, whereas type 2 earthquakes were thought to originate in cool, high-strength material. Shallow, type 2 events were termed 'roof-rock' earthquakes by Latter (1981), and were thought to represent fracturing of the country rock above a magma chamber. 'Roof-rock' earthquakes often preceded type 1 seismicity, tremor, and eruptions.

No simple relationship exists between the size of an earthquake and the magnitude of an eruption (Dibble, 1983). Latter (1981) observed that Ruapehu could be in either a 'closed-vent' or an 'open-vent' state. Small eruptions often followed minor earthquakes during 'open-vent' states, which usually corresponded to periods of high heat flow into the lake. However, during 'closed-vent' states, which often corresponded to low heat flow, moderate earthquakes were often followed by no eruptions. The swap-over between closed and open-vent states generally occurs with a 'vent clearing' eruption, accompanyied by type 1 seismicity (Latter, 1981).

Volcanic tremor is often observed at Ruapehu (Sherburn and Hurst, 1989). 3 Hz tremor usually occurs during periods of increased heat flow into Crater Lake, and has been qualitatively interpreted as the rise of hot volcanic gases encountering an obstruction in the shallow part of the volcanic conduit. Variable amplitude 2 Hz tremor is recorded almost continuously, and often exhibits large variations in energy, which generally do not correlate with activity in the lake. Sherburn and Hurst (1989) suggested that 2 Hz tremor originated in the deeper part of the conduit.

3.6.3 Fluid Geochemistry

Giggenbach (1974) analysed over twenty samples of Crater Lake water collected between December 1970 and February 1973. He found that three chemical indicators - chloride and magnesium concentrations, and pH - were most useful in assessing the processes occuring in and below the lake. Giggenbach and Glover (1975) reached the same conclusion, and suggested that prolonged constancy of the ratio Mg/Cl was a precursor to eruptions, because it indicated a blocking of the volcanic conduit (i.e. a 'closed-vent' state), reducing the input of magmatic HCl to near zero.

Giggenbach (1974) suggested that the origin of all the chemical species within Crater Lake could be split into two broad categories: (i) volatile components, which probably enter the lake in the gaseous phase, and arise from magma degassing; and (ii) metal ions and silica, which are added by interaction between lake water and andesitic material.

The first category probably includes H_2O, CO_2, HCl, HF, HBr, H_2S, SO_2, NH_3, H_3BO_3, H_2, CH_4, and N_2. Of these, CO_2, H_2, CH_4, and N_2 will pass directly through the lake into the atmosphere, whereas the others are soluble enough to become absorbed by lake water. Of the others, many will experience secondary reactions: SO_2 will be oxidised to sulphate, H_2S will be oxidised to elemental sulphur and fluoride will be precipitated as fluorite.

Of the major metal ions, Mg, Li and to some degree Na are the main ones that are not limited by solubility. Giggenbach (1974) suggested that leaching of rocks and debris within the lake basin would introduce few metal ions, and that high temperature interaction between water and hot andesitic material was required. B. Christenson (pers. comm., 1990) suggested that metal ion inputs to the lake could represent a brine input to the lake, with the high temperature interaction occurring between brine and andesite (old and new) in the hydrothermal system beneath the lake. The state of fumarolic fluid entering the lake (steam, brine, or a mixture of the two) is of prime importance in the application of the mass/energy/chemical balance model, and also in the interpretation of its results.

3.6.4 Thermal Modelling

Hurst and Dibble (1981) used measurements of lake temperature, level and lake chloride and magnesium ion concentrations from the period 1966-78 as inputs to a mass/energy balance model similar to that described in chapter 2.

Surface losses were calculated using the Weisman and Brutsaert (1973) equations, using a windspeed of 5 m s^{-1} at 2 m height, and a constant value of W (the dimensionless particle flux) equal to 0.05. Using a constant value of W does not incur large errors.

Outflow was calculated by using the decrease in Mg concentration over a time period. Mg was assumed to be added to the lake only during eruptive periods - for such times the measured outflow at the outlet was used. Seepage through the lake floor was considered insignificant.

The heat source for the lake was assumed to be condensation of steam. Surface losses, together with the change in energy stored within the lake, were used to calculate the required steam input to supply the energy. This steam was assumed to be slightly superheated, with 5-10 % other gases, and assigned an enthalpy of 3.0 MJ kg^{-1}.

The input of cold water was found by calculating the difference between the outputs (evaporation, and outflow or change in volume) and the steam input. A small adjustment was then made in the steam input to account for the energy required to heat this cold water to lake temperatures. Thus enthalpies were defined relative to lake temperatures (i.e. outflow removes no energy; c.f chapter 2).

Hurst and Dibble (1981) found that the power input to the lake had high values during eruptive periods, and occasionally fell to very low values, which they thought indicated the blockage of steam vents, but usually was between 100 and 700 MW. Calculated values of cold water inflow generally showed peaks of ~100 kg s^{-1} in summer (when high meltflow would be expected), falling to zero in winter (when low meltflow would be expected). However, some values of cold inflow were negative, and some summers had little or no inflow, demonstrating a deficiency in the model. The mean annual inflow over nine years

that involved no 'disturbing' eruptions was ~1.1 x 10^6 m^3. This value is less than half the 'minimum' value suggested by using rainfall figures from the Chateau weather station (~9 km N of Crater Lake, and ~1500 m lower) and a catchment area of 8 x 10^5 m^2. Hurst and Dibble (1981) suggested that this discrepancy was due to about half of all cold inflow floating (rainwater is less dense than mineralised lake water) on the surface of the lake to the overflow, essentially bypassing the system (i.e. not removing any Mg, and hence not diluting the lake).

Hurst and Dibble (1981) also estimated the Rayleigh number in Crater Lake, on the basis of temperature and density profiles collected in 1966 (Dibble, 1974) (fig. 3.10). From the temperature gradient in the top 100 m of the lake, a thermal Rayleigh number of 2.5 x 10^{17} was calculated, way above the critical value of ~1000, indicating that vigorous convection should have been occurring. The increase in suspended sediment with depth acts against the reduction in density due to the increase in temperature, reducing the magnitude of the density gradient, and hence reducing the overall Rayleigh number, but only by ~30 %. Thus convection should be occurring, however, this would tend to homogenise the lake, creating an approximately adiabatic temperature gradient, of only a few degrees through the lake, which was not observed. If the temperature profile was more or less steady-state, then the measurements of density must be wrong, possibly due to the loss of some suspended sediment during sampling (Hurst and Dibble, 1981).

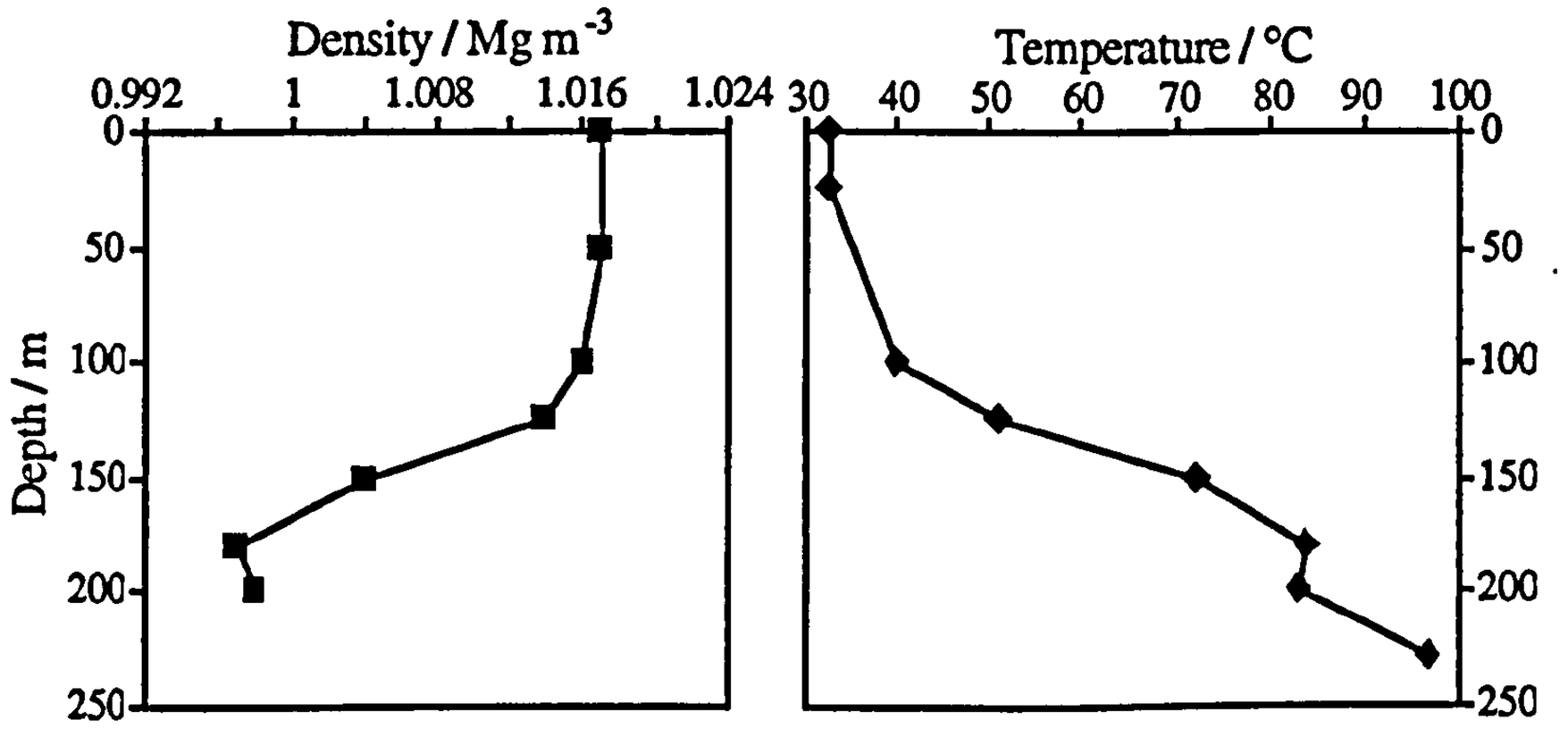

Figure 3.10 *Density and temperature of Crater Lake, Ruapehu, against depth, measured in 1966. From Dibble (1974) and Hurst and Dibble (1981).*

Hurst et al. (1991) extended the period of data considered for Ruapehu to the end of 1989. The mass/energy balance model used was of the same format as Hurst and Dibble (1981), with some minor changes. The windspeed used was deduced by calculating predicted cooling curves for different windspeeds, and comparing them to lake temperature records for periods of time when the heat input to the lake was thought to be near zero. A value of 3 m s^{-1} was found to be the best fit. However, Hurst et al. (1991) omitted a separate term for sensible heat loss, and indicated that the evaporation term now included 'convective heat loss to the air'. It is unclear whether this just referred to free and forced convective evaporation, or to both total evaporative and sensible heat losses.

The enthalpy of the incoming steam was varied in an attempt to increase calculated values of meltflow, some of which were negative. An enthalpy of 6.0 MJ kg^{-1} was required to make the calculated meltflow values not 'significantly negative'. This also produced an average annual meltflow of ~2.3 x 10^6 m^3, the same as the minimum value estimated (see above); however, some summers still had low calculated meltflow inputs.

An enthalpy of 6.0 MJ kg^{-1} is approximately double a reasonable value, and implied that about half of the energy was supplied to the lake without adding mass. This was explained by a two-phase heat pipe mechanism, whereby heat is transferred from a magmatic source by rising vapour condensing at shallow depths, and subsequently sinking back down again (see chapter 5). In this way, a region beneath the lake could become heated. A conductive boundary layer between the heat pipe and the lake was not considered a viable option, because of the very small thickness (< 1 m) required for the layer. Hurst et al. (1991) instead proposed that once a region had been heated, a change occurred in the system, and the heat could be extracted by circulation of lake water into this zone. They suggested that this process could proceed in a cyclic manner, first the heat pipe adding energy to the region, then lake water removing the heat. The cyclicity could be due to a layer of sulphur on the lake floor. Sulphur has a high viscosity at temperatures of around 160-220 °C, but falls at higher temperatures, possibly suddenly allowing the flow of gas. This was put forward as an explanation of the cyclic heating and cooling phases seen at Ruapehu since 1985.

3.7 Critique of the current models of Poás and Ruapehu

The mass, energy and chemical balance model of Rowe et al. (1991a) differs from that presented in chapter 2 in the use of: (i) a different evaporation model (Adams et al., 1990; see chapter 2); (ii) a less rigorous chemical balance (that of Brantley et al. (1987) is used, which assumes linear variation of chemical contents between samples); (iii) a fixed catchment area of 7.1×10^5 m^2 is assumed; and (iv) the likely variation in brine/steam ratio is not rigorously explored. In addition, Rowe et al. (1991a) use only yearly averages of lake temperature, thus they miss short-term changes. The overall model results of Rowe et al. (1991a) are otherwise not significantly different to the results presented in chapter 4. The interpretation of the magmatic and hydrothermal systems beneath the lake are somewhat different, however (see chapters 5, 6 and 7).

The mass, energy and chemical model presented by Hurst et al. (1991) differs widely from that presented in chapter 2: (i) a seepage term is not assumed (only overflow); (ii) only fumarolic *steam* input is considered (no brine); (iii) the evaporation equations of Weisman and Brutsaert (1973) are used; (iv) negative model outputs of rainfall/meltflow are allowed; and (v) a complex heat transfer system is required beneath the lake, that requires half of the heat to be added without adding mass. Factors (i) and (ii) led Hurst et al. (1991) to produce negative rainfall/meltflow values (iv), because the chemical balance became strictly limited. In an attempt to improve the rainfall/meltflow figures, steam with an 'effective' enthalpy of 6 MJ kg^{-1} was required (and this still did not produce entirely positive rainfall/meltflow figures). In turn, this large 'effective' enthalpy required a complex heat transfer mechanism below the lake (v). These problems are removed by allowing seepage, and a brine component in the incoming fumarolic fluid (see chapter 4). The heat pipe model of Hurst et al. (1991) is thought to be a likely mechanism of heat transfer between a magma source and the lake (see chapter 5), but with discharge of steam into the lake and seepage of lake-water back into the heat pipe, rather than the complex suggestions of Hurst et al. (1991).

CHAPTER 4

Application of the new mass, energy and chemical balance model to Poás and Ruapehu crater lakes

In this chapter, the model described in chapter 2 is applied to two data sets from the crater lakes of Poás and Ruapehu. The input data sets are presented, and some constraints on the values of two model unknowns, the incoming steam/brine enthalpy ($H_{st/br}$), and the catchment area (A_{catch}) are developed by applying the model for the entire range of possible values for $H_{st/br}$ and A_{catch}, and considering the model outputs. Using constrained values for these two unknowns, model results are presented and described in full. Because field measurements of lake characteristics were taken at uneven intervals (~1 month at both volcanoes), for ease of presentation, the model outputs are smoothed to 30 day averages. The results have implications for possible mechanisms of heat transfer in the hydrothermal and magmatic systems within Poás and Ruapehu that are discussed in chapters 5 and 6, with conclusions drawn presented in chapter 7.

4.1 Application of the new mass, energy and chemical balance model to Poás

4.1.1 Input Data Sets

Measurements of lake temperature, lake level, and rainfall data from Poás visitor's centre are shown in fig. 4.1. Lake magnesium and chloride concentrations are shown in fig. 4.2. All the data is tabulated in appendix A. Lake temperatures can be converted to surface mass and energy flows (see chapter 2) if the lake surface area and local weather conditions are known. Average weather conditions on the crater floor, measured during March/April 1989, can be summarised as follows:

Windspeed at 1 m height (8 weeks):	2.3 m s^{-1},
Air temperature (2 weeks):	15 °C,
Humidity (2 weeks):	80 %.

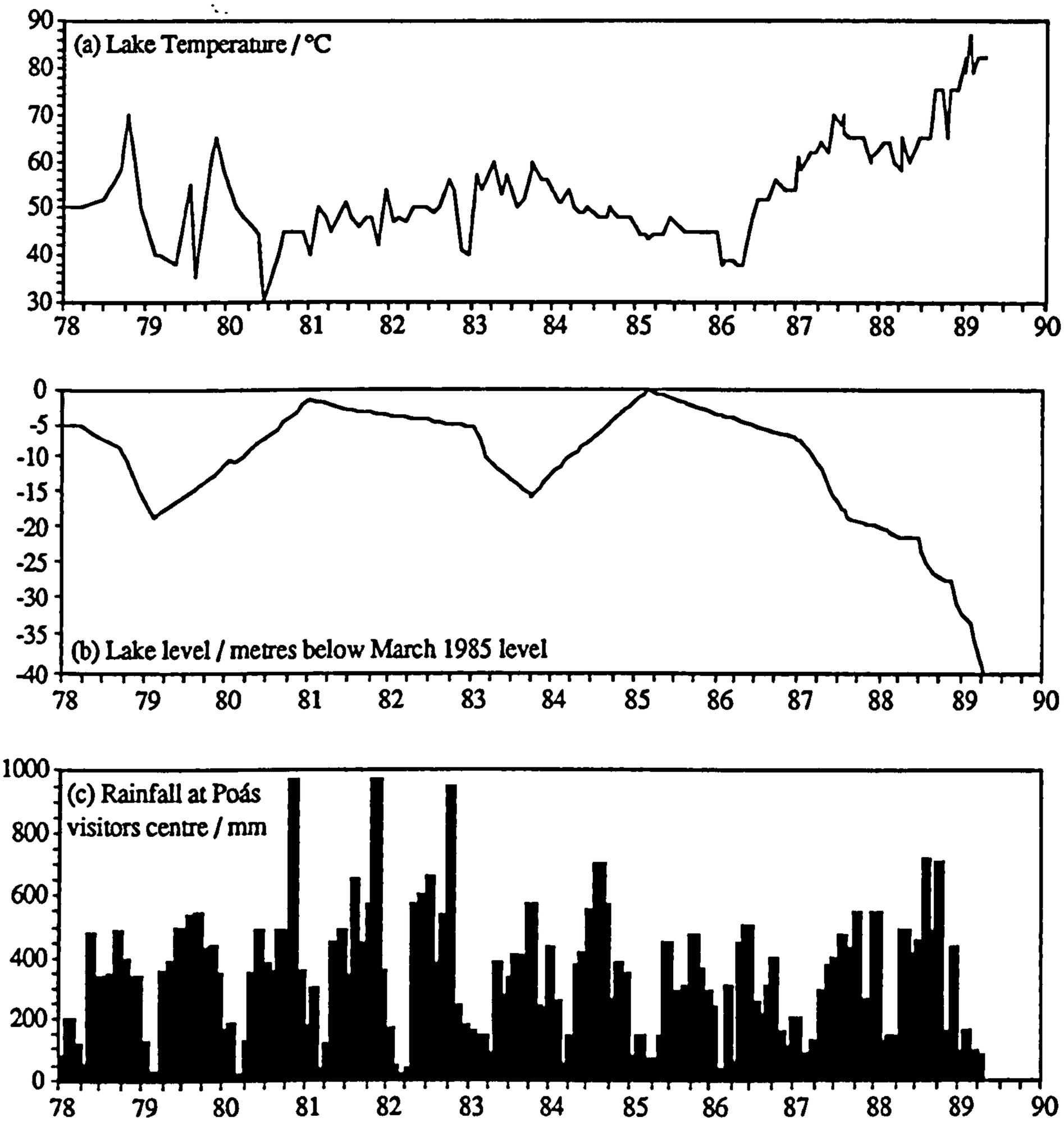

Figure 4.1 *(a) Poás crater lake temperature, measured approximately monthly by J. Barquero, using a maximum recording thermometer at the lakes edge. (b) The estimated level of the lake, relative to March 1985, from photographs (G. Brown, pers. comm.; G. Soto, pers. comm.), and records in SEAN bulletins (see section 3.2), and the survey carried out in March/April 1989 (see section 3.4.1). (c) Monthly rainfall measured at Poás visitors centre weather station (P. Machado (Instituto Costarricense de Electricidad), pers. comm.).*

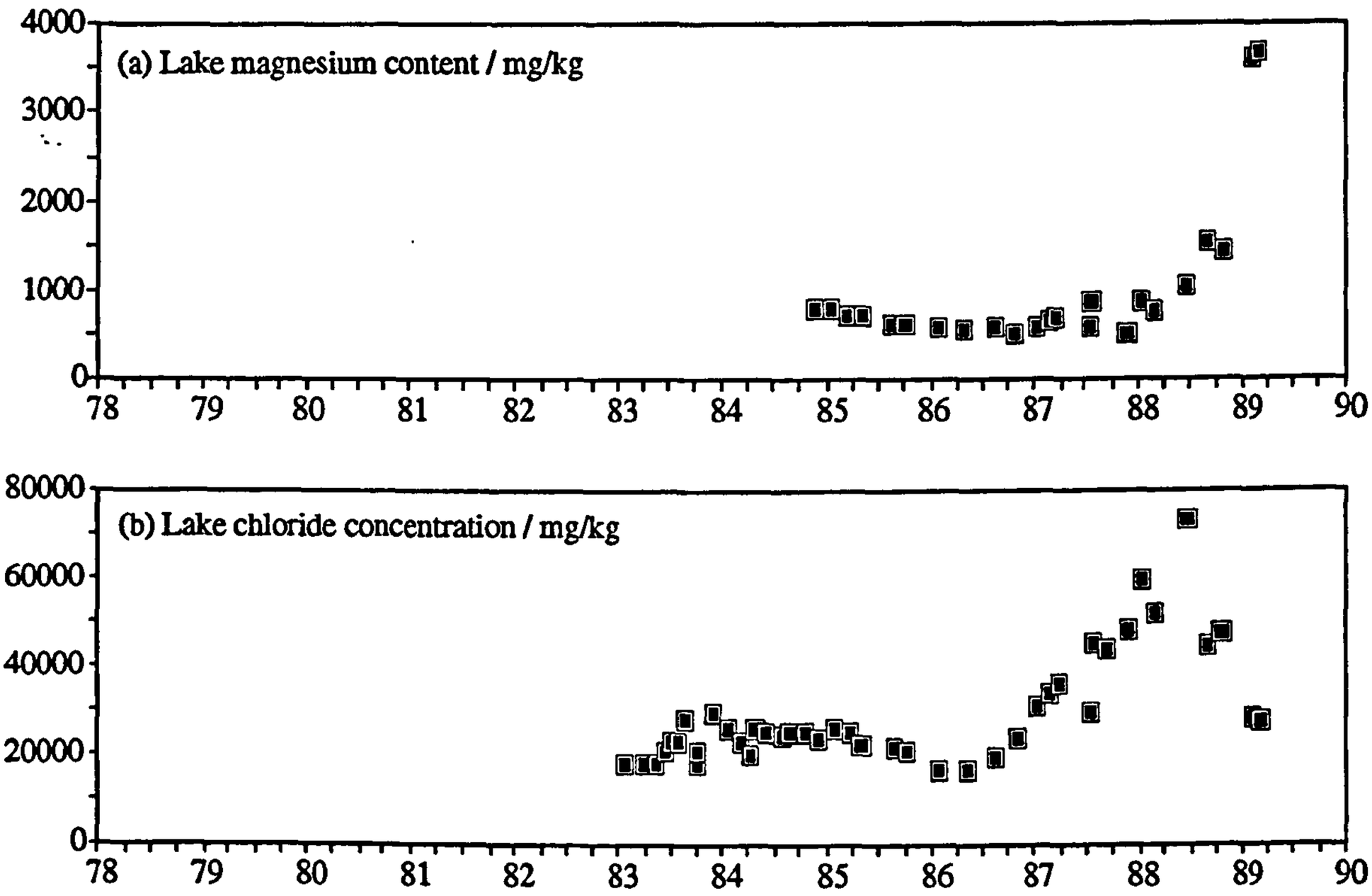

Figure 4.2 *Poás crater lake: (a) Magnesium ion concentration (Rowe et al., 1991b); and (b) chloride ion concentration (J. Barquero, pers. comm.; Rowe et al., 1991b). Analytical errors were estimated as ±5 % for Mg and ±3 % for Cl (Rowe et al., 1991b). With the addition of sampling errors, the symbol sizes approximately represent the overall error.*

Lake level changes can be converted to surface area and lake volume changes if the dimensions of the lake are known. The exposed lake bed was surveyed in March 1989 (figs. 4.3 and 4.4, and see appendix A for data) using an Electronic Distance Measurement (EDM) theodolite, positioned at points 1 and 2 in fig. 4.3, and placing reflector prisms at various sites around the lake bed. The points with a number 85 in them (fig. 4.3) were at the highest levels of remaining sediment, thought to represent the approximate position of the lake surface in March 1985. Points numbered 87 were on a terrace identified in a photograph as the approximate shoreline of the lake in mid-late 1987. The perimeter for February 1989 (fig 4.3) is approximate, inferred from photographs, as is the outline of the remnant lake and mudpools for March 1989. The surveyed points for the 1985 level were then fitted to an outline of the lake from fig. 3.3. Fig. 4.3 was then used to calculate the surface area of the lake at the three dates shown:

March 1985:	8.35×10^4 m^2,
Mid-late 1987:	5.28×10^4 m^2,
February 1989:	2.8×10^4 m^2.

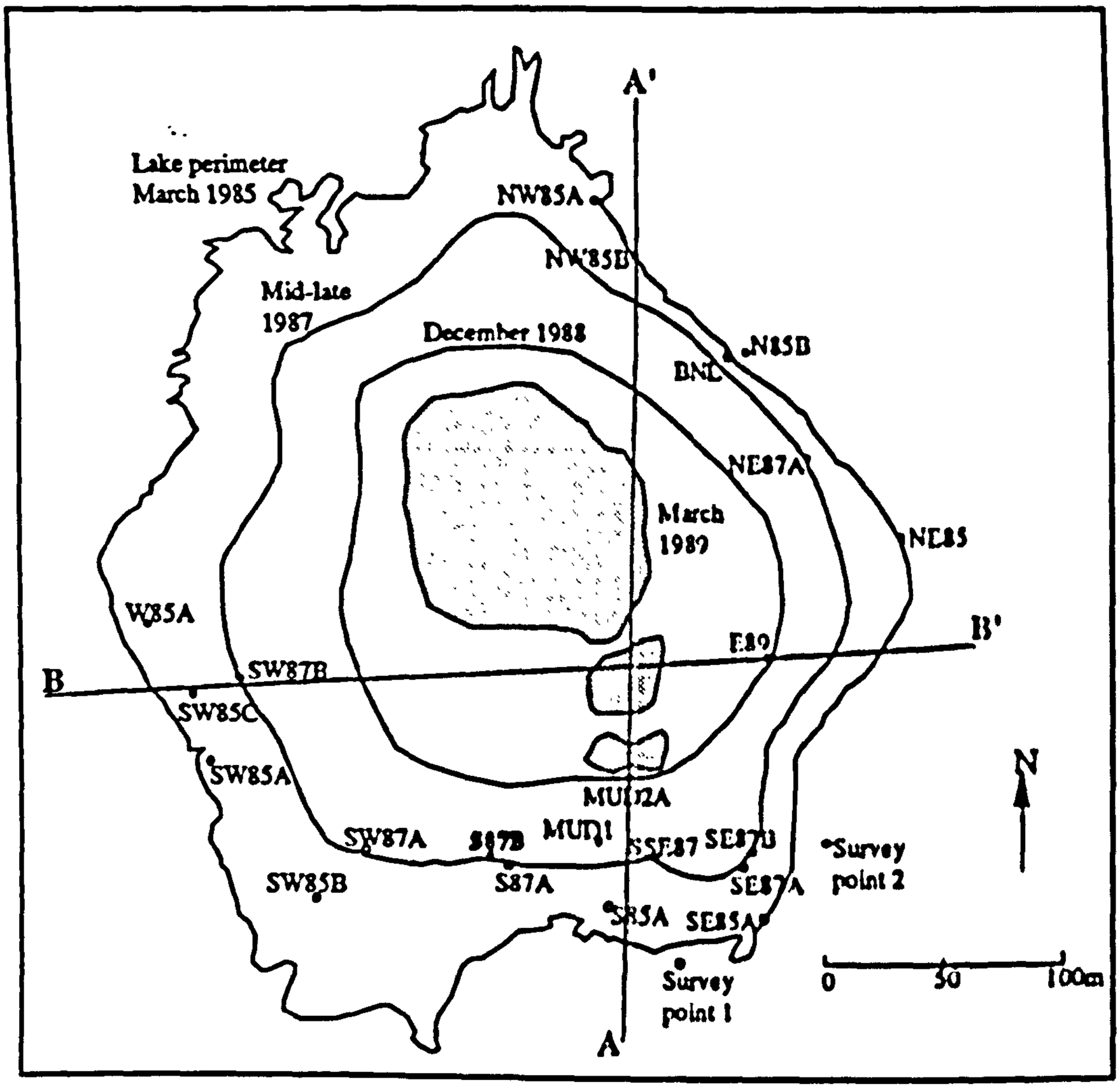

Figure 4.3 *Survey of Poás crater lake basin carried out in March 1989, from points 1 and 2. Points numbered 85 correspond to the highest levels of sediment visible - these were assumed to represent the March 1985 lake margin. The full lake outline was enlarged from fig. 3.3 to fit these points approximately. Approximate lake perimeters for mid-late 1987, February 1989/December 1988, and March 1989 are shown. Two profiles A-A' and B-B' are shown in fig. 4.4.*

The survey also revealed a 33 m drop in level from March 1985 to February 1989. The surface areas can be back-calculated to give effective radii for the lake assuming the surface is circular, i.e. March 1985: 163 m; Mid-late 1987: 130 m; February 1989: 94 m. The depth of the lake was measured in 1985 to be 47 m (Brantley et al., 1987), thus the shape of the lake basin can be approximated by a cone plus a truncated cone (fig. 4.4), with the dimensions as stated. This allows simple computation of surface areas and volumes for a given level.

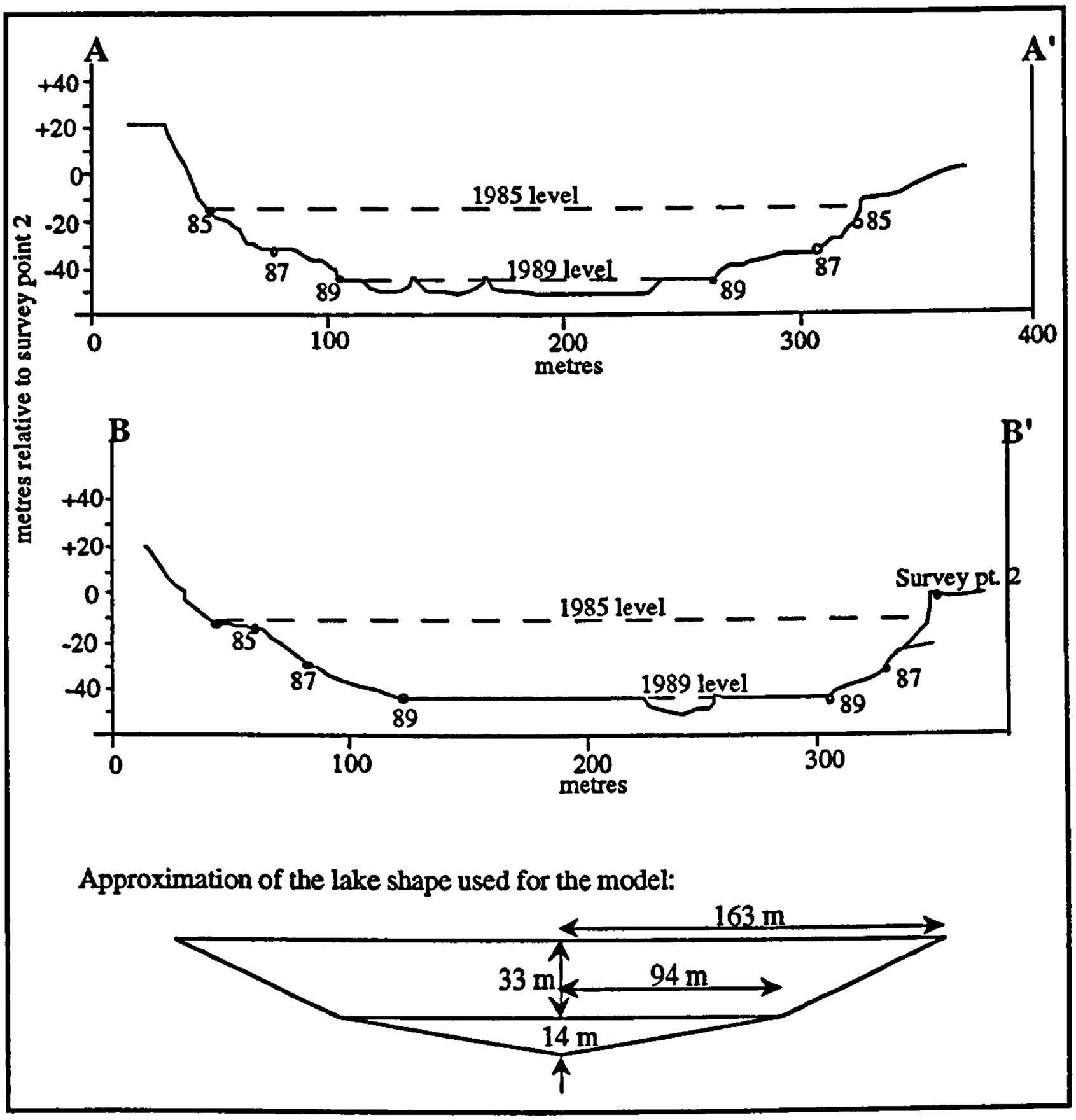

Figure 4.4 *Approximate cross-sections A-A' and B-B' (see fig. 4.3) through Poás crater lake. Points are averages of the nearest points to the line. Also shown is the approximation of the lake shape used in the model, arrived at from the survey, and using the maximum depth measurement of 47 m in 1985 (Brantley et al., 1987).*

Rainfall data have been collected at Poás national park visitor's centre, ~2 km south of the lake, over the time period considered (1978-90) (fig. 4.1c). Assuming that rainfall in the active crater is similar to that at the visitor's centre, the rainfall input to the lake can be estimated by assuming a catchment area. The catchment area of the active crater is ~7.5 x 10^5 m^2, of which ~1.5 x 10^5 m^2 is captured by the valley to the south of the crater, leaving a maximum catchment area for the lake of ~6 x 10^5 m^2 (fig. 3.3). Run-off from the Botos cone is also probably caught by this valley. The lake catchment area could be less than this if rainfall seeps into the ground and directly enters the hydrothermal system, rather than the lake. However, the absence of fumaroles/hot springs (except on the cone and the lake-bed) suggest that the main communication to the hydrothermal system is via fractures in the

cone/lake area. As will be shown below, the lake chemistry data can be used to constrain the value of the catchment area.

4.1.2 Initial intepretation of the chemical data

It is worth noting the implications of the chemical data before applying the model - these general intepretations will be 'fine-tuned' after the model has been applied. Fig. 4.5 shows the variation with time of total Mg and Cl in the lake, i.e. the concentration multiplied by the lake mass. This is more useful than the concentration alone for Poás, because of the large reduction in volume of the lake over the time period considered. The data sets in fig. 4.5 have been split into pre-June 1987 and post-June 1987, i.e. before and after the onset of phreatic activity in the lake. An exponential curve was fitted to the earlier Mg data, and a near horizontal straight line was fitted to the later data (fig. 4.5a). No attempt was made to fit lines to the more erratic Cl data (fig. 4.5b).

Flows of Mg and Cl within the system are shown diagrammatically in fig. 4.6. The exponential decrease in total Mg in the lake during 1985-87 (fig. 4.5a) implies that losses of Mg through seepage were greater than any inputs by brine. The total mass of Mg fell from ~1.5 x 10^6 kg in early 1985 to ~6 x 10^5 kg in June 1987, an average decrease of ~0.01 kg s^{-1}. In turn, this implies that there was a build up of Mg in the brine zone, and/or that Mg was deposited when the lake-water was vaporised, and/or that the Mg was lost completely from the summit system through seepage to the flanks. Evidence for some seepage reaching the lower slopes of the volcano is the observation of acid springs, discharging fluid thought to be derived from the lake (Brantley et al., 1987; Rowe et al., 1991a,b). In the absence of other effects, the Mg content of the brine zone would be expected to increase gradually due to rock dissolution. The relative conservation of total Mg in the lake since June 1987 (fig. 4.5a) implies that losses of Mg from the lake through seepage were matched, to a first approximation, by additions of Mg with brine.

Total chloride in the lake (fig. 4.5b) increased from ~2 x 10^7 kg in early 1983 to ~4.8 x 10^7 kg in early 1985, implying that gains of Cl from steam/brine input exceeded losses through seepage by ~0.4 kg s^{-1}. Total Cl in the lake decreased from 1985 (~4.8 x 10^7 kg) to mid-

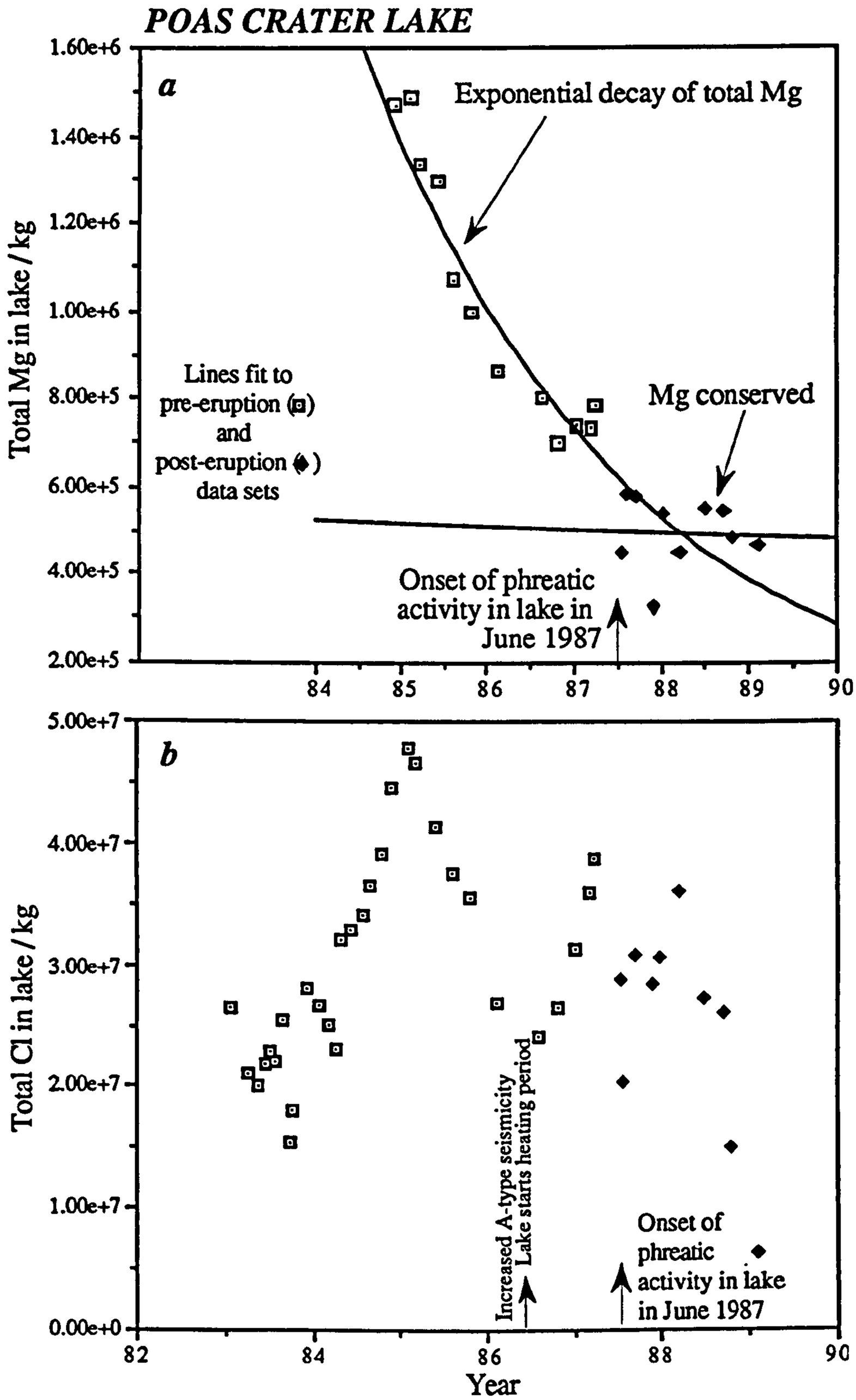

Figure 4.5 *Poás crater lake chemistry: (a) Total mass of magnesium ions, 1985-89; (b) total mass of chloride ions, 1983-89.*

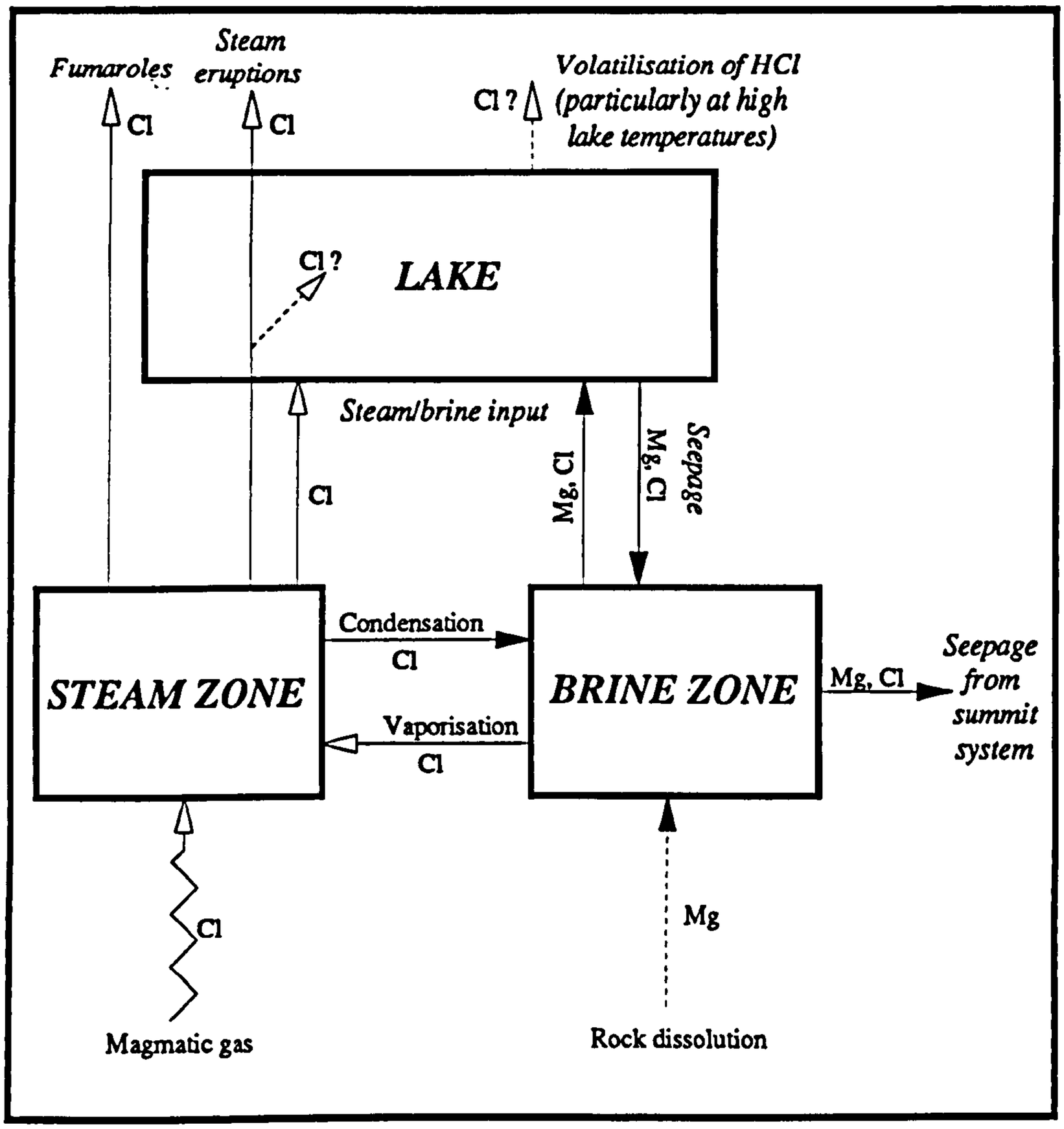

Figure 4.6 *Flows of magnesium and chloride ions in the summit hydrothermal system beneath a crater lake. Mg is added and lost from the lake by brine and seepage respectively. Mg is added to the brine zone from the lake and by dissolution of rock, and is lost to the lake, and through seepage to the flanks of the volcano. Cl is added to the lake by steam/brine input, and possibly during eruptions by steam flushing through the lake; Cl is lost through seepage and possibly surface volatilisation. Cl is lost from the steam zone to the lake, to subaerial fumaroles, to steam eruptions, and by condensation to the brine zone, and is added from magmatic gas and by vaporisation of the brine zone. Cl is added to the brine zone from the lake, and by condensation from the steam zone, and is lost from the brine zone to the lake, by vaporisation to the steam zone, and by seepage to the flanks of the volcano.*

1986 (~2.4 x 10^7 kg), i.e. losses of Cl through seepage exceeded gains from steam/brine input by ~0.5 kg s^{-1}. An increase in the total lake Cl at a rate of ~0.7 kg s^{-1} from mid-1986 (~2.4 x 10^7 kg) to early 1987 (~3.9 x 10^7 kg) followed increased seismicity in the first half of 1986, and coincided with the initiation of a lake heating period. This increase reversed in early 1987 when the total Cl in the lake suddenly fell to ~2 x 10^7 kg, before rising with the onset of steam eruptions in June 1987, stabilising at ~3 x 10^7 kg during the activity, before falling from early 1988 onwards.

Increases in total Cl in the lake suggest addition of Cl from a source beneath the lake. The source is probably either increased vaporisation of a brine zone, or input of a HCl-rich magmatic gas. Decreases in total Cl in the lake suggest a sink for Cl beneath the lake. This sink could be a brine zone storing the Cl, or subsequently losing Cl gained from the lake to sub-aerial fumaroles or seepage to the volcanoes flanks. The situation may be further complicated during steam eruptions, when some Cl may be added to the lake whilst steam passes directly through the lake. Also, at high lake temperatures, surface volatilisation of HCl may become important (this probably caused the decreasing trend of total Cl from 1987 onwards). In the absence of other effects, Cl would be expected to be added to the steam zone by magmatic HCl (either sporadically or continuously); however, the Cl *concentration* in the steam zone would only increase if the magmatic HCl content was greater than that of the steam zone.

4.1.3 Application of the model - constraining input parameters

Constraining the steam/brine enthalpy

The mass-energy-chemistry budget model was applied (as described in section 2.6.1) for the full range of possible values of $H_{st/br}$ (0.8-2.75 MJ kg^{-1}) and A_{catch} (0 - 6 x 10^5 m^2). Superheated steam enthalpies were not used for reasons that will become clear. Using the model outputs of $M_{st/br}$ and M_{os}, values for the magnesium content of the incoming steam/brine ($[Mg]_{st/br}$) for each time interval, Δt, were evaluated using equation (2.6a/b). Results for Poás are shown in fig. 4.7, for extreme values of $H_{st/br}$, and catchment areas of 3 x 10^5 m^2 and 6 x 10^5 m^2. The results were broadly the same in all cases, with a value of

$[Mg]_{st/br} \approx 500$ mg kg^{-1} between 1985-1988, and an increase during 1988. This illustrates that the incoming fluid must have been at least partly brine, and clearly cannot have been *all* saturated or superheated steam, since steam cannot carry significant quantities of Mg.

The value of $H_{st/br}$ is an average of all the incoming vents, and because each vent is assumed to be discharging the same fluid, and some brine must be input, the enthalpy cannot exceed 2.75 MJ kg^{-1}, the value for pure saturated steam. In reality, it would be possible for some vents to be discharging superheated steam (H ~4 MJ kg^{-1}) whilst others were discharging concentrated brine (H ~ 0.8 MJ kg^{-1}), with the proportion of vents such that the overall

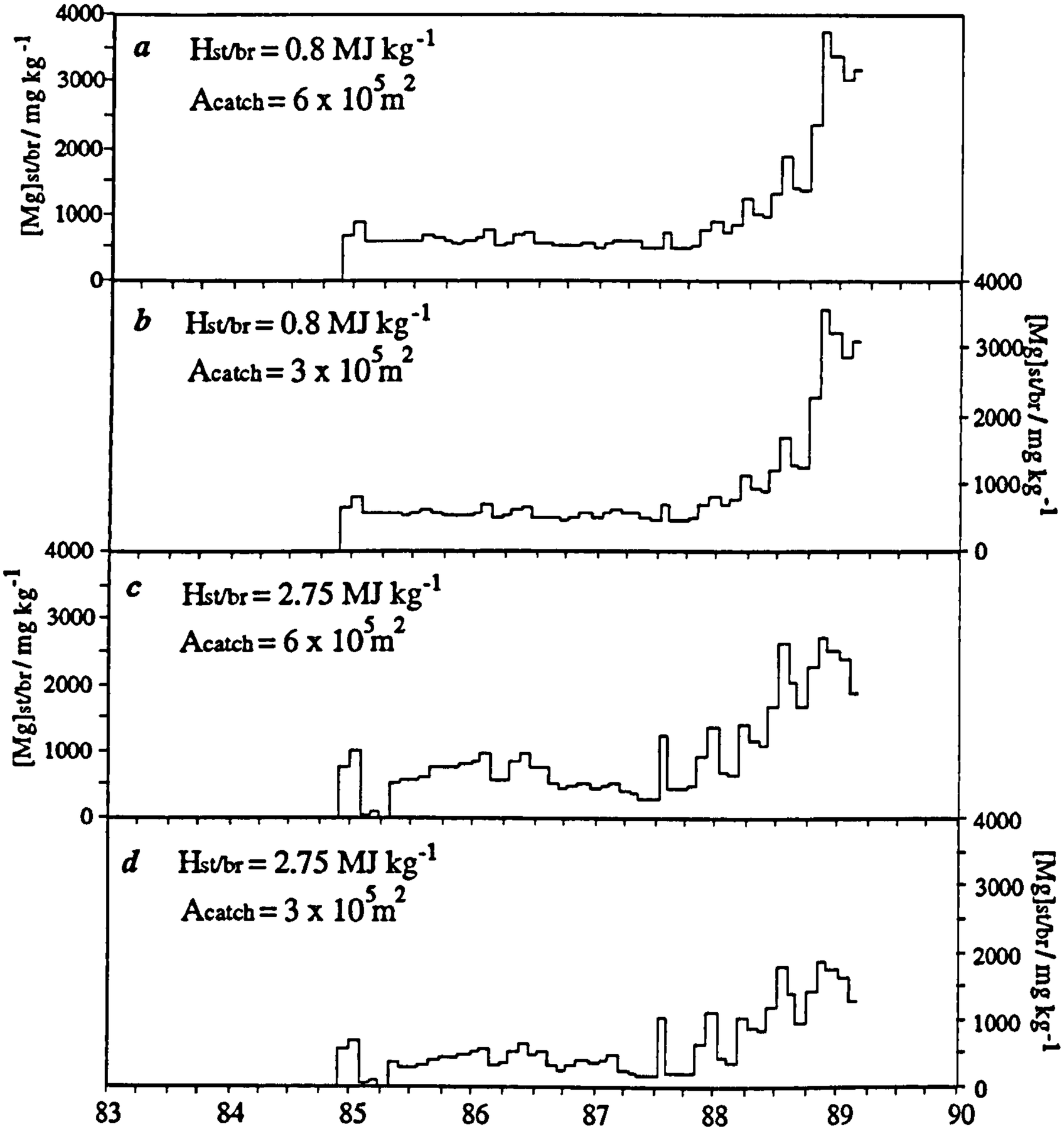

Figure 4.7 *Calculated values for $[Mg]_{st/br}$ at Poás crater lake, for four sets of values of catchment area and steam/brine enthalpy: (a) $A_{catch} = 6 \times 10^5$ m^2, $H_{st/br} = 0.8$ MJ kg^{-1}; (b) $A_{catch} = 3 \times 10^5$ m^2, $H_{st/br} = 0.8$ MJ kg^{-1}; (c) $A_{catch} = 6 \times 10^5$ m^2, $H_{st/br} = 2.75$ MJ kg^{-1}; (d) $A_{catch} = 3 \times 10^5$ m^2, $H_{st/br} = 2.75$ MJ kg^{-1}.*

average enthalpy exceeded 2.75 MJ kg^{-1}. This possibility is considered unlikely, and has not been catered for in the modelling.

The calculated value of $[Mg]_{st/br}$ can be used to estimate the value of $H_{st/br}$. The magnesium concentration in Poás lake-water fell from ~800 mg kg^{-1} in 1985 to ~500 mg kg^{-1} in 1986 before erratically rising again, to over 1000 mg kg^{-1} by mid-1988 (fig. 4.2a). The average calculated value of $[Mg]_{st/br} \approx 500$ mg kg^{-1} therefore suggests that the incoming fluid had a slightly *lower* Mg content than the lake. Presumably, an acidic brine reservoir beneath the lake will be continuously leaching Mg from rocks, thus would be expected to have a *higher* Mg content than the lake. This suggests that the incoming fluid must be a mixture of brine and steam, with the steam 'diluting' the overall Mg content. Fig. 4.8 shows the possible enthalpy values of the steam/brine mixture for different values of the Mg content of the brine reservoir ($[Mg]_{reservoir}$). A typical value of $[Mg]_{reservoir} = 1000$ mg kg^{-1} is chosen, which yields an input enthalpy of 1.8 MJ kg^{-1}, equivalent to 50 wt.% steam, and 50 wt.% brine. This is an approximation, and the enthalpy and proportions will probably vary with time, as will the Mg content of the brine reservoir. However, the data available cannot resolve such differences.

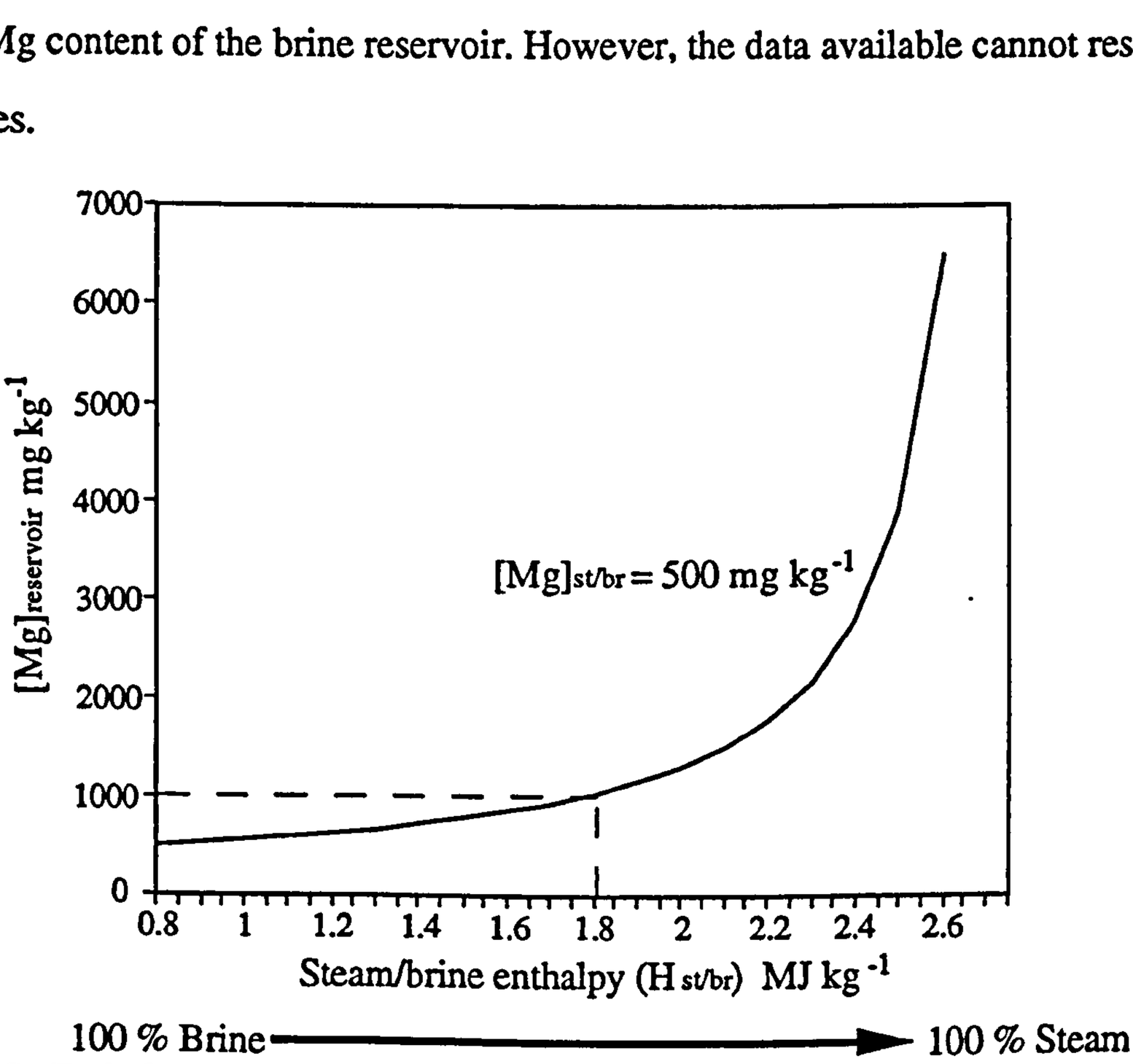

Figure 4.8 *Enthalpy of the steam/brine mixture ($H_{st/br}$) against Mg content of the brine reservoir ($[Mg]_{reservoir}$), for a Mg content in the steam/brine mixture ($[Mg]_{st/br}$) of 500 mg kg^{-1}. A $[Mg]_{reservoir}$ value of 1000 mg kg^{-1} implies an enthalpy of 1.8 MJ kg^{-1}.*

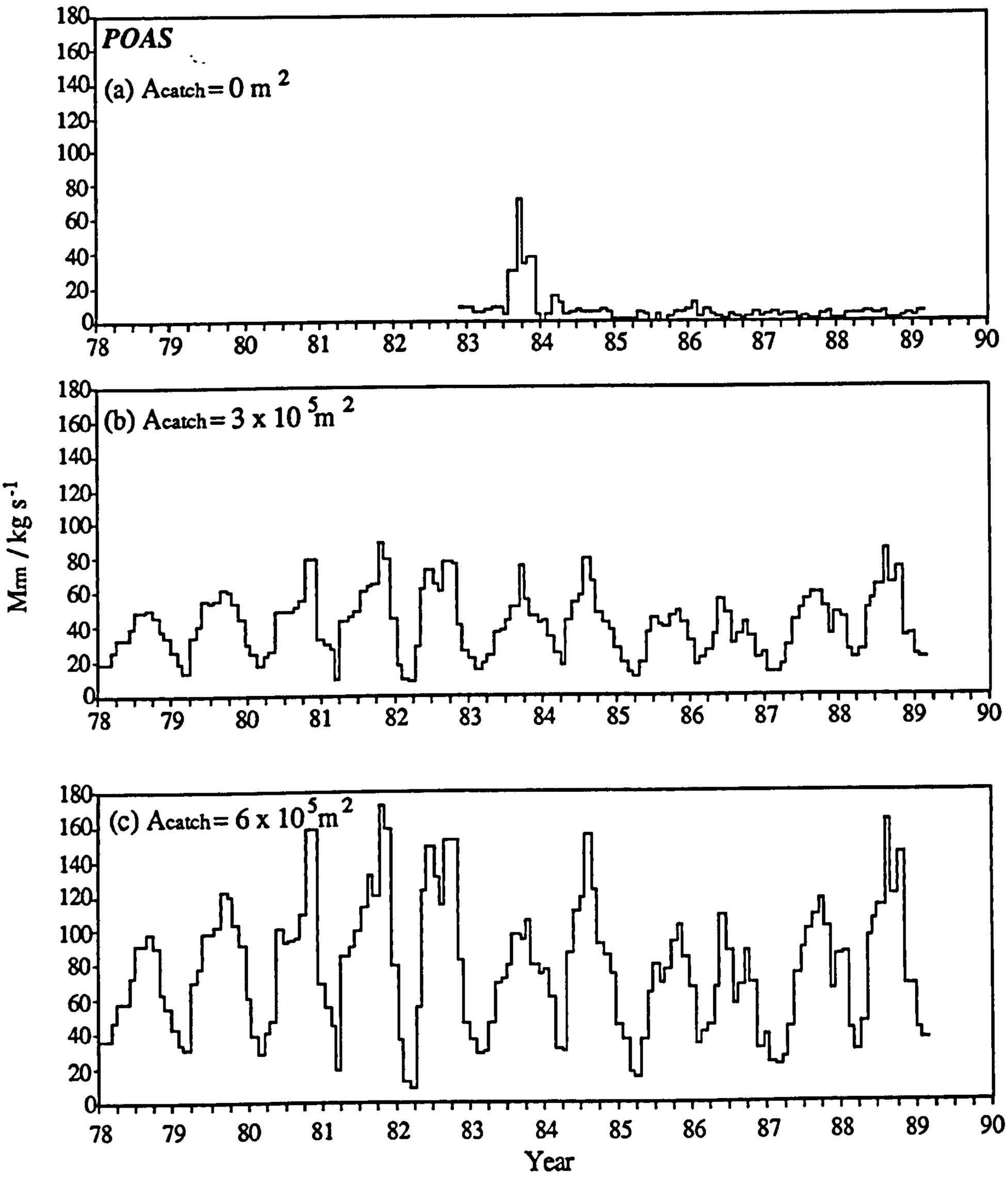

Figure 4.9 *Model outputs of M_{rm}, for three values of catchment area: (a) $A_{catch} = 0\ m^2$; (b) $A_{catch} = 3 \times 10^5\ m^2$; (c) $A_{catch} = 6 \times 10^5\ m^2$. All using $H_{st/br} = 1.8\ MJ\ kg^{-1}$. Note the peak in (a) in late 1983, which is largely swamped in (b), and completely swamped in (c). See text for discussion.*

Constraining the catchment area

Running the model with $H_{st/br}$ fixed at 1.8 MJ kg^{-1}, and varying the catchment area, produced outputs of M_{rm} shown in fig. 4.9. Fig. 4.9a is for $A_{catch} = 0$ m^2, i.e. the only condition imposed by the model was that M_{rm} must be positive. This effectively means that these results are the minimum values of M_{rm} dictated by the chemical balance (equation 2.4). For this unrealistic situation, a significant 'spike' exists in the values of M_{rm} in late 1983. This 'spike' is not evident in the rainfall data for Poás visitors centre (fig. 4.1c), indeed, 1983 is relatively dry compared to 1980-2 and 1984. The 'spike' occurs because a finite amount of rainfall must have been added over this period, in order to account for the change in lake chemistry. The likely catchment area can be estimated by gradually increasing the minimum value for the catchment area until the spike no longer exists in the calculated rainfall. Thus a minimum catchment area of 3×10^5 m^2 (fig. 4.9b) brought the calculated rainfall values up to a more reasonable level, with the 'spike' largely swamped. In fig. 4.9c, $A_{catch} = 6 \times 10^5$ m^2 was used, which produced values of rainfall that completely covered up the 'spike'. As already mentioned, the maximum catchment area suggested by crater drainage is ~6×10^5 m^2, and as this value is consistent with these model results, it will be used as the actual catchment area.

4.1.4 Results and Discussion

Outputs of the mass and energy flows from the model, using $H_{st/br} = 1.8$ MJ kg^{-1} and $A_{catch} = 6 \times 10^5$ m^2, are shown in figs. 4.10 and 4.11. Rates of addition of chloride and magnesium ions, and their calculated concentrations in the incoming steam/brine, are shown in fig. 4.12.

Fig. 4.11 shows that the major energy loss is usually evaporation, and this strongly dictates the required input of energy. In turn, this dictates the mass inflow rate of steam/brine, which is approximately double the rate of evaporation, mainly because of the difference in enthalpies ($H_{st/br} = 1.8$ MJ kg^{-1}, $H_{ev} \approx 2.6$ MJ kg^{-1}). The seepage rate is usually the largest of the mass flows, because it is required to remove the added rainfall, plus the difference between the steam/brine inflow and evaporation outflow.

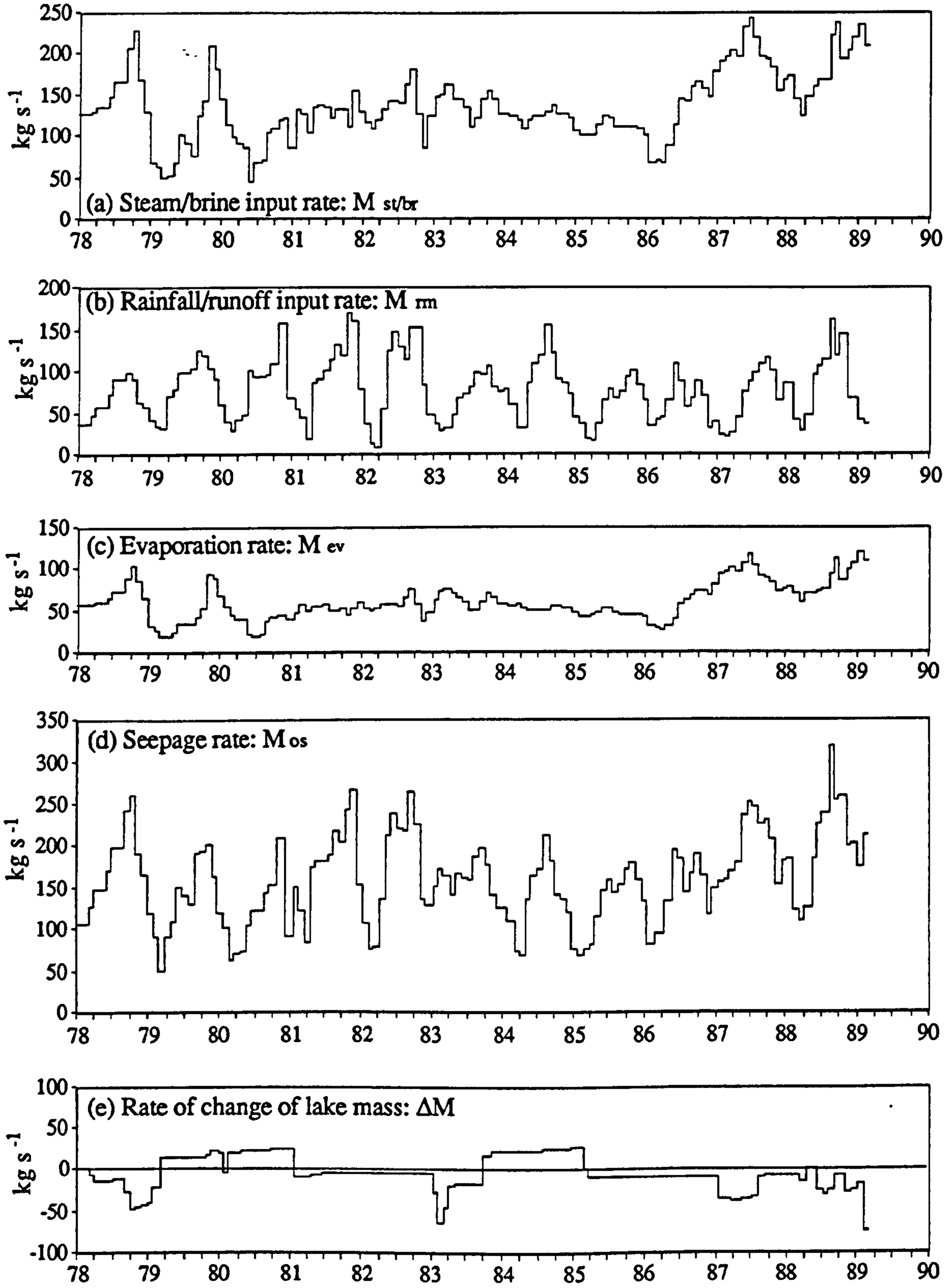

Figure 4.10 *Mass balance for Poás crater lake. Mass flows are in kg s^{-1}, and are 30 day averages. Flows calculated assuming an incoming fluid enthalpy of 1.8 MJ kg^{-1}, and a catchment area of 6 x 10^5 m^2.*

The power input to the lake (fig 4.11a) shows peaks of ~400 MW in 1978 and 1979, associated with the phreatic activity of April-May and September-December 1978, and September 1979 to January 1980 (see section 3.2). The power input fell to below ~100 MW in March 1979 and June 1980, the latter correlating with an A-type seismic swarm (see sections 3.2 and 3.3.4), before steadying at ~200-250 MW over the period 1981-85. This corresponds to the period of high temperature fumaroles on the cone, which appeared in January 1981, with a maximum temperature of ~1000 °C, and gradually fell to ~300 °C by the end of 1985 (fig. 3.5). The next low in the power input (~100 MW) did not occur until early in 1986, again correlating with heightened A-type seismicity in February-May (see section 3.3.4). During 1986-87, the power input steadily rose, the lake level gradually fell (fig. 4.1b), and fumarole temperatures rose to ~600 °C (fig. 3.5). The power input peaked at ~450 MW in June 1987, when lake temperatures reached 70 °C (fig. 4.1a), and minor phreatic activity resumed (section 3.2). Beyond June 1987, the calculated power input to the lake no longer represents the total heat flux through the lake, because of near-continuous phreatic activity between June 1987 and July 1988, during which time steam passed directly through the lake. After July 1988, although phreatic activity largely ceased, the lake had become very shallow (< ~20 m), and large amounts of gas were probably still passing directly through the lake. The lake essentially disappeared in April 1989, thus results end at that date.

Seepage rates (fig. 4.10d) show increases (after removing seasonal variations) in 1980-2 and 1986-89 (from ~100 kg s^{-1} to ~200 kg s^{-1} in both cases). Increases in seepage coincide with increases in the steam/brine input: from ~50 kg s^{-1} (mid 1980) to ~150 kg s^{-1} (late 1982); and from ~70 kg s^{-1} (early 1986) to ~200 kg s^{-1} (1987-89)) (fig. 4.10a). This suggests that seepage may increase with higher fluid fluxes through the lake floor, probably due to the increased disturbance of sediments. When the model was run with a higher value of the input enthalpy (i.e. a larger steam fraction), steam/brine mass inflow was reduced, evaporation and rainfall remained unchanged, and hence seepage was also reduced by an equal amount (equation 2.1). Thus the coincident increases in seepage and steam/brine input will occur for any chosen value of $H_{st/br}$.

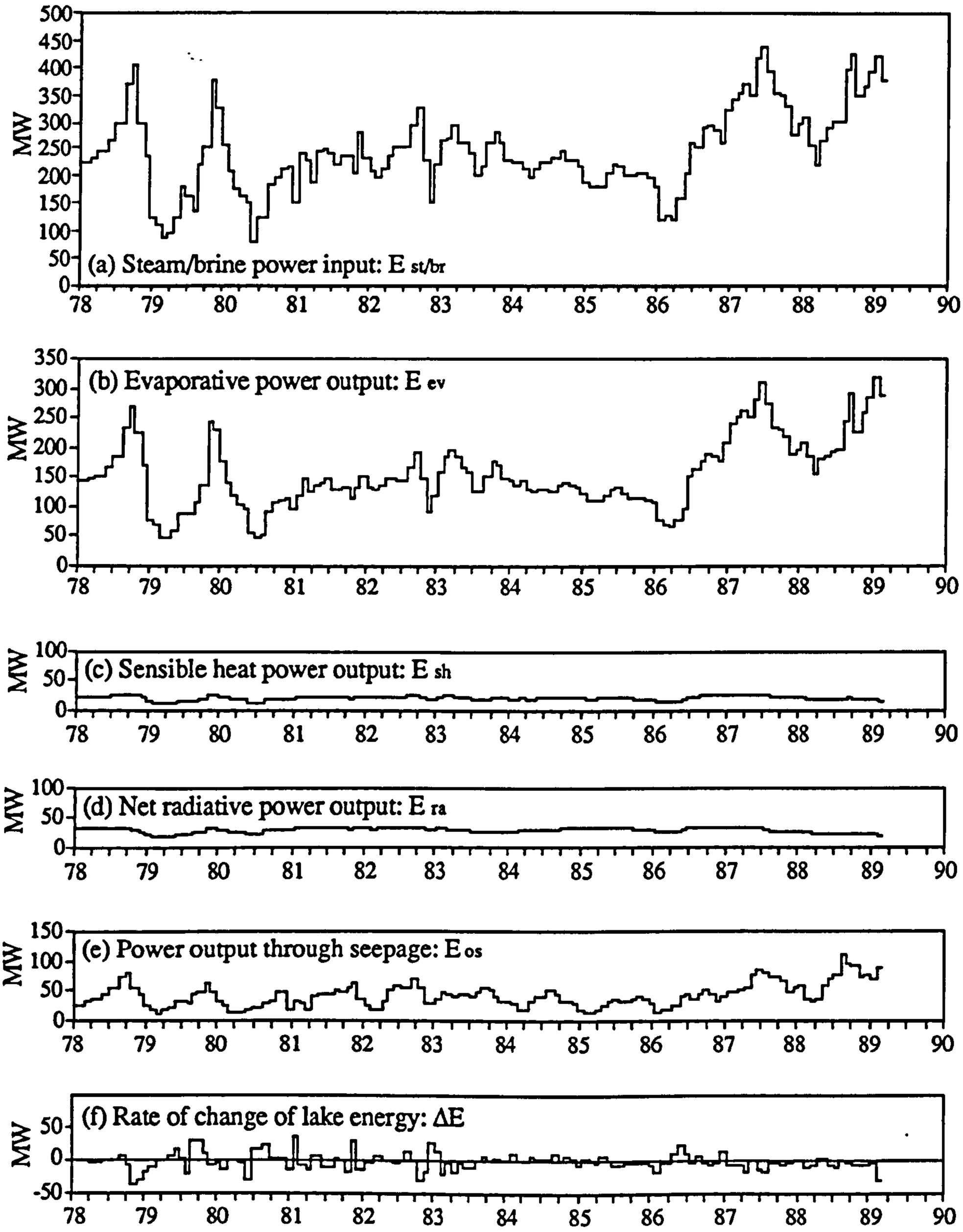

Figure 4.11 *Energy balance for Poás crater lake, with energy flows in MW, calculated as 30 day averages. Assumes an incoming fluid enthalpy of 1.8 MJ kg^{-1}, and a catchment area of 6 x 10^5 m^2.*

The removal of the lake between 1985 and 1989 required an average rate of change of lake mass (ΔM) of only ~-15 kg s^{-1} (fig. 4.10e), a value much smaller than (~10 % of) typical mass flow rates into and out of the lake. Thus a relatively small perturbation in the constituent mass flows can lead to the removal of the lake. An increased steam/brine input alone will tend to add mass to the lake, because the steam/brine input is always greater than the evaporative mass loss (fig. 4.10a,c). For a stable lake volume, the seepage must remove the difference between steam/brine input and evaporation, together with any rainfall/runoff input. Thus the lake will decrease in volume if the seepage increases whilst rainfall/runoff remains 'normal', or if seepage remains 'normal' and rainfall/runoff decreases. Both of these effects occurred at Poás over the period 1985-89: rainfall was below average in 1985-87; and seepage increased with the higher steam/brine influx from mid-1986 onwards. This combination led to the removal of the lake.

The calculated magnesium ion influx averaged ~0.07 kg s^{-1} over the period 1985-87 (fig. 4.12a), and the calculated Mg content of the incoming steam/brine mixture averaged ~500 mg kg^{-1} (fig. 4.12c and c.f. fig. 4.7). From the assumption made earlier in estimating the enthalpy, the Mg content of the brine was 1000 mg kg^{-1}, and the steam zero. An exponential decrease in total lake Mg occurred over this period (fig. 4.5a), at an average rate of ~0.01 kg s^{-1}. Thus the outflux of Mg through seepage must have averaged ~0.08 kg s^{-1} for the period. The calculated Mg influx showed a small increase during late 1987 and early 1988, before rising dramatically during the second half of 1988 to ~0.6 kg s^{-1}. Since June 1987, Mg has been conserved in the lake (fig. 4.5a), implying that losses equalled gains. The calculated Mg content of the incoming mixture rose exponentially following the June 1987 phreatic activity, and reached ~3000 mg kg^{-1} by late 1988 (fig. 4.12c). This mirrored the increase in the Mg concentration of the lake (fig. 4.2a). Model outputs with $H_{st/br} = 1.8$ MJ kg^{-1} show that $M_{os} \approx M_{st/br} \approx 200$ kg s^{-1} for the period 1987-89 (fig. 4.10a,d). This strongly suggests that the incoming steam/brine mixture was simply derived from recycled lakewater seepage, that had been heated and partially vaporised. Mg was not deposited by vaporisation, but retained in the brine. Thus the greater the degree of vaporisation, the more concentrated the incoming brine; however the overall Mg content of the incoming mixture

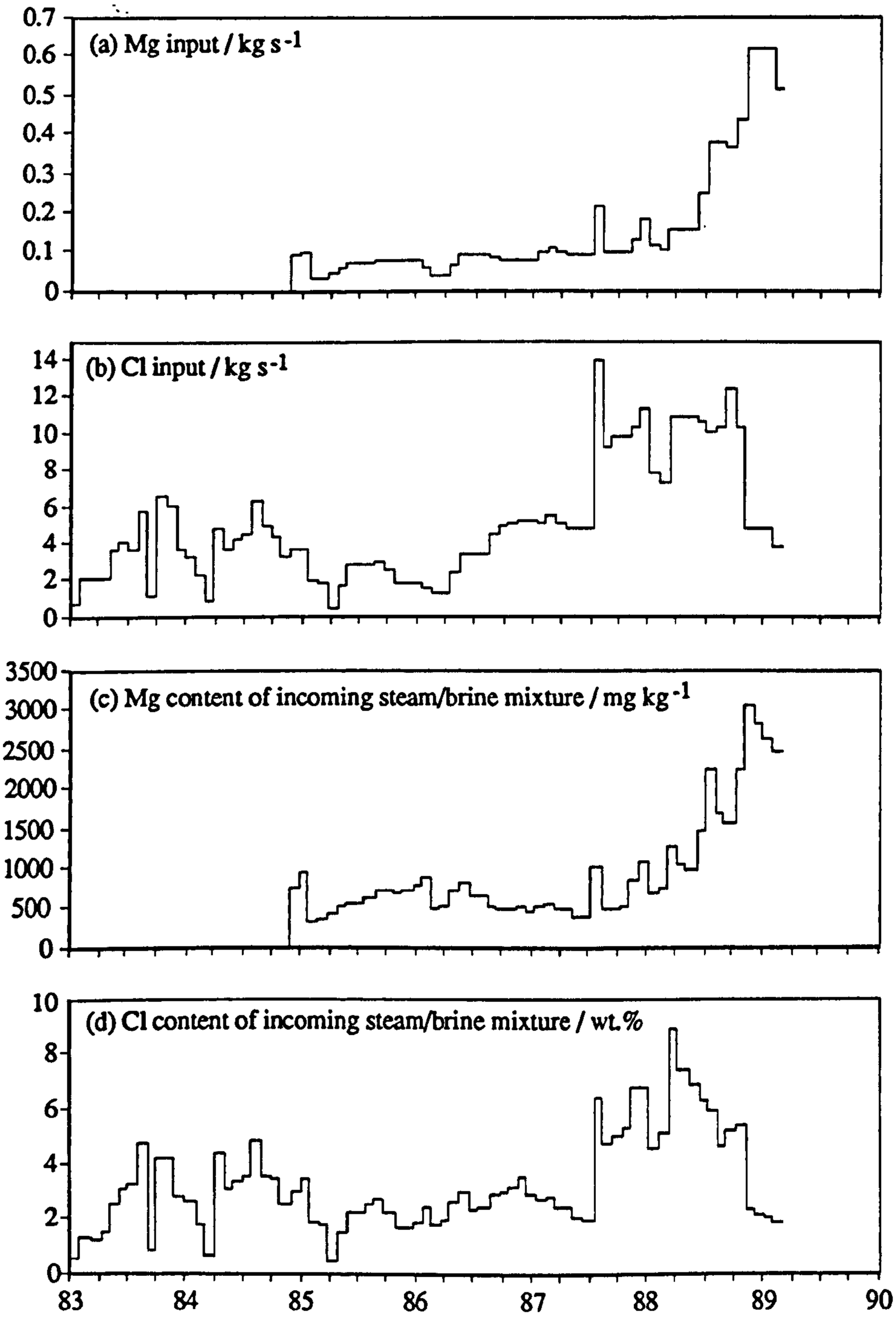

Figure 4.12 *Calculated influxes to Poás crater lake of (a) Mg, (b) Cl, and their calculated contents in the incoming steam/brine mixture: (c) Mg, (d) Cl.*

will remain the same as the lake water it was derived from, due to 'dilution' of the brine by the accompanying steam fraction (assuming all the seepage is returned to the lake).

The calculated chloride content of the incoming steam (fig. 4.12d) is similar to the measured Cl concentrations of the lake (fig. 4.2b), the latter looking like a smoothed version of the former. This supports the idea that the incoming steam/brine was simply recycled lake-water. However, the total Cl in the lake (fig. 4.5b) shows periods of increase (1983 to early 1985; mid-1986 to early 1987; and June 1987 to early 1988), which must represent a source of Cl external to the lake (see section 4.1.2). During 1983-85, high temperature fumaroles were still active on the cone, thus it is probable that some magmatic gas was also entering the lake. Similarly, in 1986-87, fumarole temperatures on the cone rose; thus the external Cl source was probably magmatic gas. In June 1987, coincident with the resumption of phreatic activity in the lake, the Cl influx suddenly increased to ~10 kg s^{-1} from a previous level of ~5 kg s^{-1} (fig. 4.12b), and the Cl content of the incoming steam/brine mixture also suddenly increased to ~6 wt. % from ~2 wt.% (fig. 4.12d). The total Cl in the lake initially rose, then stabilised (see section 4.1.2), implying that the increase in influx was quickly matched by an increase in outflux. This must reflect the increase in Cl concentration of the lake-water (fig. 4.2b), because no significant increases in the mass fluxes of seepage and steam/brine were calculated after June 1987 (fig. 4.10a,d). The sudden increase in Cl could have been caused by a magmatic gas component; alternatively, it could represent a higher steam flux than that suggested by fig. 4.10a, and an unchanged Cl content, with the excess steam passing directly through the lake as a steam eruptions, dumping Cl ions, but not condensing. A combination of these two effects was probably the cause..

4.1.5 Summary and Conclusions for Poás

The results suggest that the heat source for Poás crater lake was saturated steam and hot brine added through lake-floor vents. The steam/brine input was largely derived from heating and partially vaporising lake-water seepage, with additional magmatic gas input during some periods. Phreatic activity in 1978 and 1979 corresponded to periods of heightened fluid influx through lake-floor vents. Magmatic gas input to the lake probably

occurred during 1983-85, associated with the high temperature fumaroles on the cone, and from mid-1986 onwards, associated with the resurgence of fumarole temperatures on the cone, heightened seismicity, the start of a lake heating period, and preceding the phreatic activity of June 1987 to September 1988. Coincident with this activity, the chloride content of the incoming fluid rose dramatically, indicating: (i) a further HCl-rich magmatic gas injection; and/or (ii) that steam was passing through the lake as eruptions, dumping Cl ions, but not condensing, raising the effective chloride content of the added fluid.

The removal of Poás lake over the period 1985-89 was due to: (i) increased seepage, probably caused by the increased fluid influx to the lake disturbing sediments; and (ii) below average rainfall during 1985-87 (inclusive). During the active period of 1987-88, Mg was approximately conserved by the return of nearly all of the brines that were the residue of partial vaporisation of lake-water; however, the lake reduced in volume because not all of the steam produced from the seepage mass was returned. Some of the steam passed directly through the lake as steam eruptions, or was lost as fumaroles. An average net outflow from the lake of only ~15 kg s^{-1} over the four year period was required to cause its removal. This would require only ~15 % of the steam produced from seepage to be lost in this manner, not significantly affecting the enthalpy of the incoming mixture.

The power input to the lake (fig. 4.11a) is nearly independent of the assumed values of $H_{st/br}$ and A_{catch}, and therefore has typical errors of ±~30-40% (see section 2.6.2). Thus the power input has shown a variation between ~70(±25) MW and ~400(±140) MW. The ultimate source of this power must be a magmatic body somewhere beneath the lake, losing heat through: (i) crystallisation and cooling; and (ii) degassing. It seems likely from the Cl data that the 'background' power input to the lake of ~100 MW is supplied by crystallisation and cooling feeding a hydrothermal system, whereas the peaks in power input represent bursts of magmatic gas entering the lake, perhaps also augmented by increased crystallisation and cooling. These processes are considered in detail in chapters 5 and 6, but it is worth initially stating endmember models of the magma volumes involved, when all the heat is derived from:

(I) Crystallisation of magma only;

(II) Crystallisation and cooling from 1000 °C to 250°C of magma;

(III) Degassing of 4 wt.% H_2O magma only;

(IV) Crystallisation, cooling from 1000 °C to 250°C, and degassing of 4 wt.% H_2O magma.

Using magma properties: latent heat of crystallisation 4.18 x 10^5 J kg^{-1}; and specific heat capacity 1046 J kg^{-1} K^{-1}; and assuming the magmatic gas is all water, with an enthalpy of 4 x 10^6 J kg^{-1}, then the masses of magma involved are summarised in table 4.1.

	Power in MW for 1 kg s^{-1} magma	Magma mass rate in kg s^{-1} for 1 MW	Magma mass rate in kg s^{-1} for 70-400 MW	Magma volume rate in km^3 a^{-1} for 70-400 MW
I	0.42	2.4	170 - 960	0.002 - 0.01
II	1.2	0.83	58 - 330	0.0007 - 0.004
III	0.16	6.3	440 - 2500	0.006 - 0.03
IV	1.4	0.73	51 - 290	0.0006 - 0.004

Table 4.1 *Magma mass and volume rates required to supply the calculated power input to Poás crater lake, for the four end-member models described in the text.*

The increase in total lake Cl over the period 1983 to 1985 was ~3 x 10^7 kg (fig. 4.5b), a rate of ~0.5 kg s^{-1}. Taking magma with 4 wt.% water, and a magmatic gas H_2O:HCl ratio of 60:1 (observed in sampled 'magmatic' gases in 1982, section 3.3.6 and Casadevall et al. (1984a)), then this suggests a magma degassing rate of ~750 kg s^{-1}. This degassing rate would supply ~120 MW (model III), compared to the observed power input of ~200 MW for this period (fig. 4.11a). Similarly, in 1986-87, total Cl increased at a rate of ~1 kg s^{-1}, implying a magma degassing rate of ~1500 kg s^{-1}, with an associated power of ~240 MW, similar to the observed power input to the lake (fig. 4.11a).

It therefore seems likely that the degassing model (III) can account for most of the observed energy, with perhaps additional energy from magma crystallisation and cooling. However, the magma volumes required to degas are typically ~0.01 km^3 a^{-1}, or a new cylindrical intrusion of length 1 km, and diameter ~100 m each year. Intrusions of such large size have not been detected gravitationally (e.g. Rymer and Brown, 1989), and are not implied by the observed relatively low level of deformation and seismicity. This paradox is discussed further in the Ruapehu section, and in chapter 6.

4.2 Application of the new mass, energy and chemical balance model to Ruapehu

4.2.1 Input data sets

Measurements of lake temperature, level, and chemistry (magnesium and chloride ion concentrations) have been taken approximately monthly by various New Zealand DSIR (Department of Science and Industrial Research) personnel since 1966, and are shown in fig 4.13 and 4.14. The data is tabulated in appendix B.

Lake temperatures can be converted to surface mass and energy flows (see chapter 2) if the lake surface area, and local weather conditions are known. Weather conditions are poorly constrained as there is no weather station near the summit of Ruapehu. During fieldwork by the present author in March/April 1990, windspeed and other weather conditions were measured at Dome Shelter (fig. 3.8). Despite problems with icing, the total of approximately three weeks of data showed average windspeeds of ~12 m s^{-1} at ~5 m height. Unfortunately, Dome Shelter is in a much more exposed position than Crater Lake, so this windspeed can only define an approximate upper limit for the windspeed above the lake. The average conditions used in the calculation of surface losses are as follows:

Windspeed at 2 m height above lake: 3 m s^{-1},

Air temperature at 2 m height: 0 °C,

Humidity at 2 m height: 70 %.

These values are based on measurements during fieldwork, and took into consideration the estimates made by other authors (Hurst and Dibble, 1981; Hurst et al., 1991).

As at Poás, lake level changes can be converted to lake surface area and volume changes if the dimensions of the lake are known. Bathymetric surveys have been carried out in 1966 (Dibble, 1974), 1970 (Irwin, 1972) and 1983 (Dawson and Sorrell, 1985), and a number of spot depth measurements were made in 1982 (Nairn et al., 1982) (figs.4.15 and 4.16). The surveys revealed large variations in bathymetry, with a maximum depth of 297 m in 1966,

compared to a depth of ~80 m measured by line at the same location in 1970, and then an increase in depth to ~180 m in 1982. The surveys producing shallow results in 1970 and 1983 were mainly carried out using echo-sounding - these surveys had problems finding steep slopes, and also encountered problems with reflections from suspended sediments and rising gas bubbles around the inferred vent regions. Hence the survey of 1983 presumably missed the deeper regions found with the spot measurements of 1982. There is evidence, however, that the bathymetry had changed significantly, possibly due to lava emplacement on the lake floor associated with the eruptions of 1968 or 1969, and then by explosive removal of most of this lava during eruptions in 1975, or possibly in 1971 or 1977. Unfortunately, the exact dates of these changes in bathymetry are unknown, and for the purposes of this model, a constant lake bathymetry will be assumed, based on the cone plus truncated cone approximation given in fig. 4.16. This gives a full lake volume of ~7.4 x 10^6 m^3, and surface area of ~2.0 x 10^5 m^2.

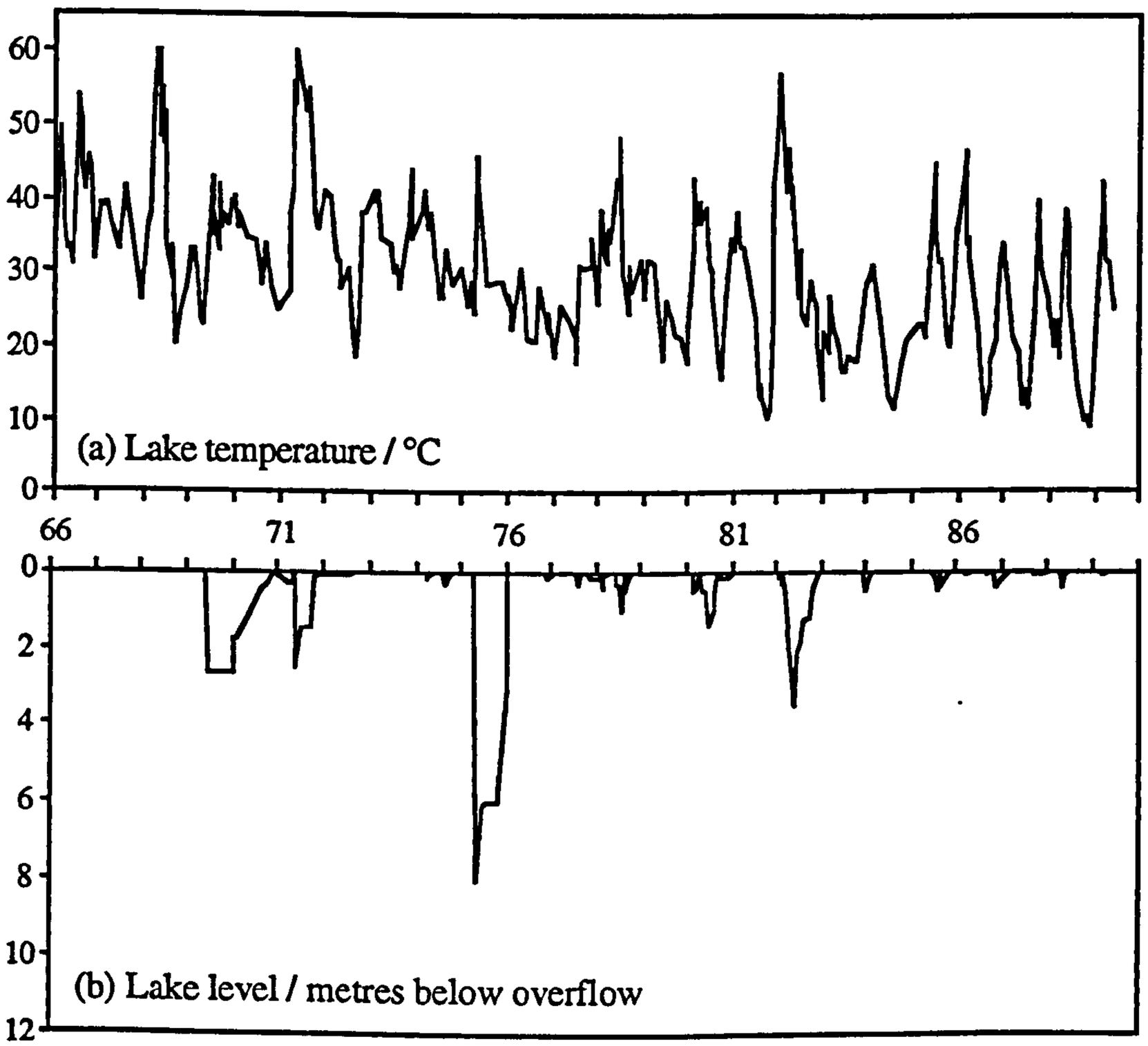

Figure 4.13 *(a) Temperature and (b) level of Crater Lake, Mt. Ruapehu, 1966-89. From measurements made by New Zealand DSIR staff during approximately monthly visits to the outlet site (fig. 3.8).*

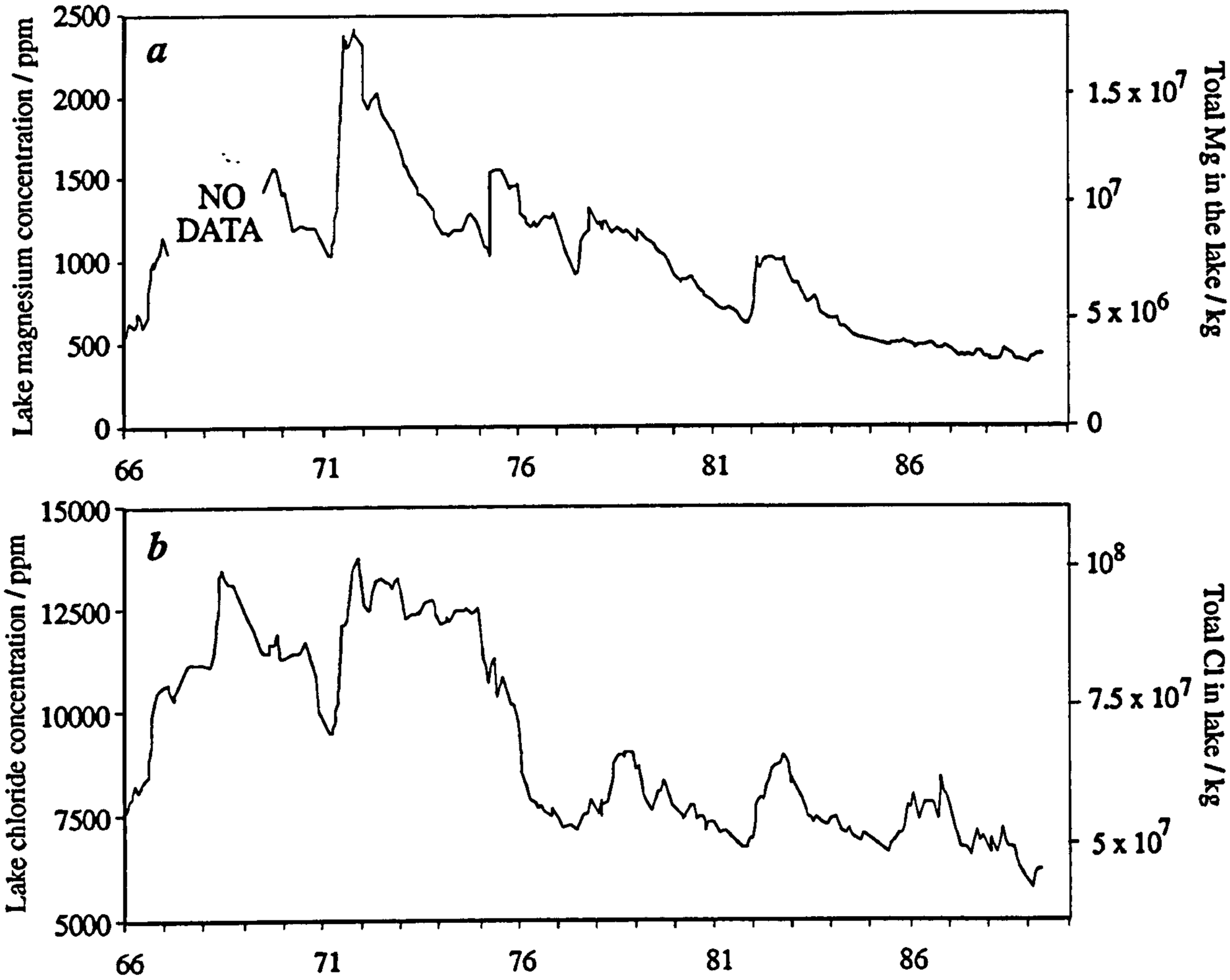

Figure 4.14 *(a) Magnesium and (b) Chloride ion concentrations in Crater Lake, Mt. Ruapehu, 1966-89 (courtesy of DSIR, New Zealand).*

Snow/rainfall at the summit of Ruapehu are unknown; however, the average annual precipitation figure for the Chateau observatory, in Whakapapa village, on the lower Northern flank, is 2.9 m. Precipitation at the summit is almost certainly higher than this value. From the sub-glacial and exposed summit topography, Hurst and Dibble (1981) and Hurst et al. (1991) estimated that the catchment area of Crater Lake is ~8 x 10^5 m^2; thus the likely minimum average rainfall/meltflow input to the lake is ~75 kg s^{-1}. As for Poás, this value can be constrained to a certain degree by the lake chemistry data.

4.2.2 Initial intepretation of the chemical data

Fig. 4.14 shows the variation of Cl and Mg concentration with time. As the lake level has remained virtually constant with time, the total masses (in kg) of each of these ions can simply be found for any one time by multiplying the part per million concentration

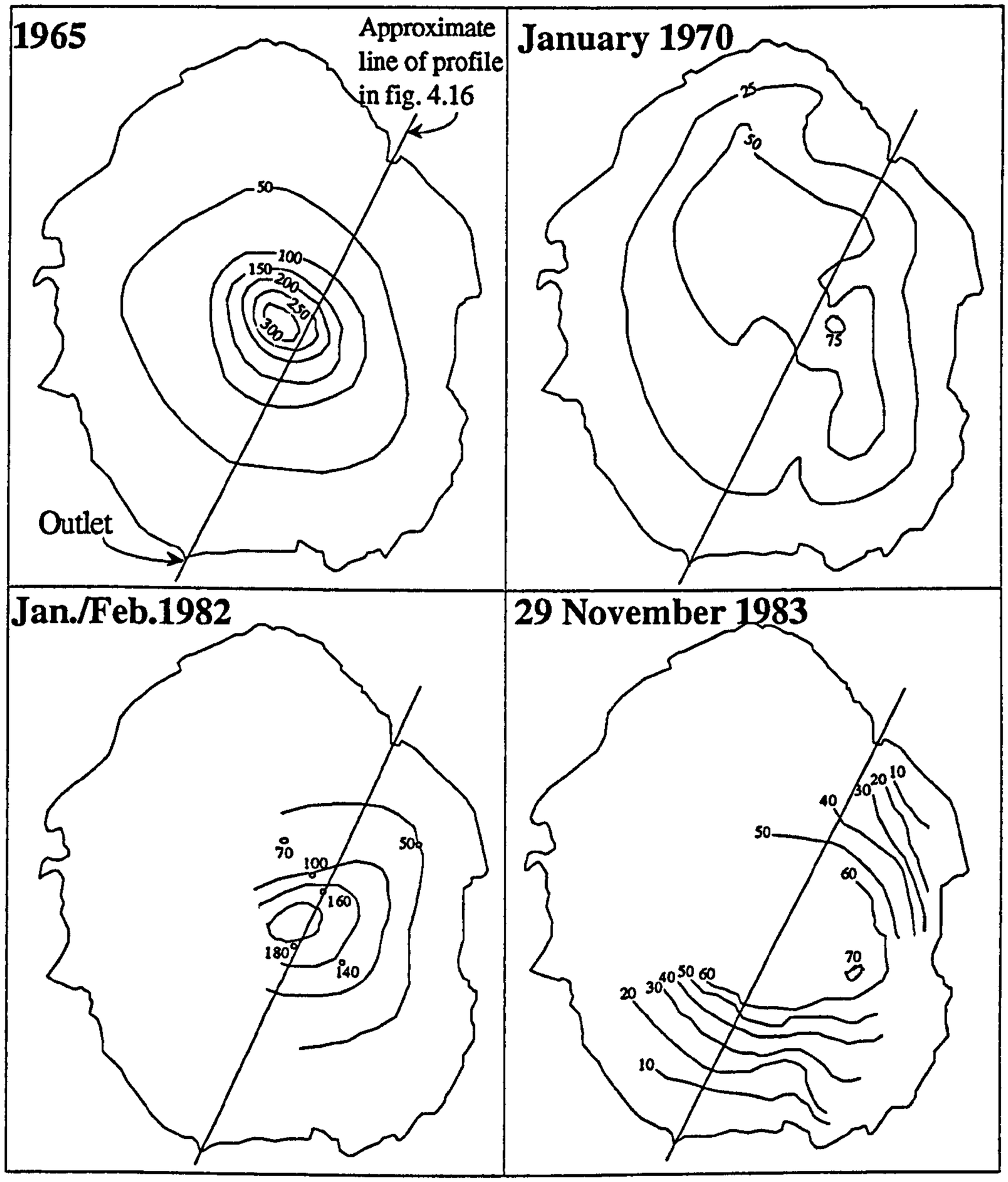

Figure 4.15 *Estimated bathymetries of Crater Lake, Mt. Ruapehu, in: (a) 1965 (from Dibble, 1974); (b) 1970 (from Irwin, 1972); (c) 1982 (from Nairn et al., 1982); (d) 1983 (from Dawson and Sorrell, 1985).*

(10^{-6} kg kg^{-1}) by the volume (~7.4 x 10^6 m^3), the density (~10^3 kg m^{-3}) and 10^{-6}, i.e. ~7.4 x 10^3 kg. Total masses are shown on the right-hand scale of fig. 4.14.

Similarities exist between the Ruapehu data (fig. 4.14) and the Poás data (fig. 4.5). Mg again generally shows exponential decay, interspersed with periods of relative conservation during heightened activity (e.g. 1971, 1975, 1978 and 1982). Periods of conservation of Mg generally follow sudden increases in Mg, associated with phreatomagmatic eruptions (see table 3.2 and fig. 3.9: April/May 1971, 24 April 1975, 2 November 1977, and October

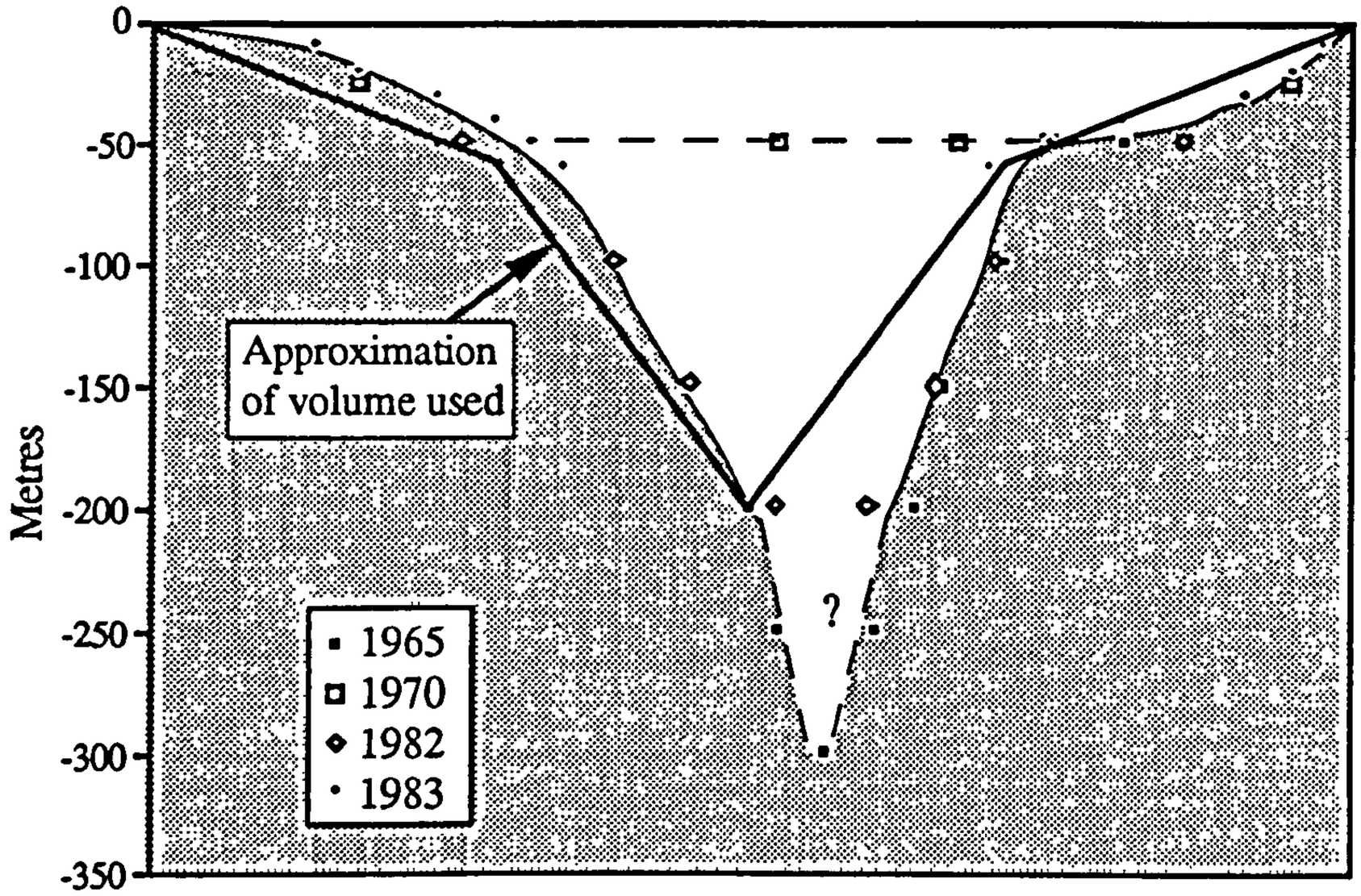

Figure 4.16 *Cross-sections through Crater Lake, Mt. Ruapehu, for the four surveys shown in fig. 4.15, and the approximation of lake volume used for calculating surface areas and volumes in the model: a truncated cone (top radius 250 m, bottom radius 100 m, depth 60 m) plus a cone (depth 120 m).*

1981 to April 1982). These sudden increases were thought to reflect direct interaction between fresh magma and lakewater (e.g. Giggenbach, 1974). Exponential decay of Mg will occur if outputs of Mg exceed inputs. At Ruapehu, the continuous loss of fluid by lakewater outflow will produce an exponential decay of total Mg because the concentration in the lakewater will gradually fall (see equation 2.3).

As at Poás, the Cl data are much more erratic, but there are clear increases of Cl during/directly following the eruptions of 1968, 1971, 1978, 1981-2 and 1985-6. It is worth noting that the largest eruption in this series, in 1975, produced a relatively small increase in Mg, and virtually no increase in Cl. This perhaps indicates a sudden, large eruption, the chemical effects of which largely bypassed the lake, and which was followed by little associated longer-lived activity. It is also interesting to note that the 1985-86 'very small phreatic eruptions' (see table 3.2 and fig. 3.9) produced a significant increase in Cl within the lake, but no associated increase in Mg, perhaps reflecting involvement of magmatic gas, but not magma itself.

The qualitative intepretations of changing Mg and Cl contents disccussed in section 4.1.2 with respect to Poás, and summarised in fig. 4.6, also apply to Ruapehu, with the notable exception of sub-aerial fumarolic discharge. Quantitative intepretations will be made after the model has been applied.

4.2.3 Application of the model - constraining input parameters

Constraining the steam/brine enthalpy

As for Poás, the mass-energy-chemistry balance model was applied (see section 2.6.1) for the full range of possible values for $H_{st/br}$ (0.9-2.75 MJ kg^{-1}), and yearly averages of rain/snowfall/meltflow input ($M_{rm(min)}$) from 0 to 150 kg s^{-1}. Because of the lack of meteorological data, $M_{rm(min)}$ will be assumed to vary sinusoidally throughout the year, peaking in the middle of summer (1st February), and falling to zero in the middle of winter (1st August) (e.g. for an average flow of 75 kg s^{-1}, this implies a peak flow of 150 kg s^{-1} in summer, falling to zero in winter). Taking the model outputs of $M_{st/br}$ and M_{os}, values for $[Mg]_{st/br}$ have been calculated for each time interval using equation (2.6a/b). Results for Ruapehu are shown in fig. 4.17, for extreme values of $H_{st/br}$, and for M_{rm} varying in the ranges 0 to 75 kg s^{-1}, and 0 to 150 kg s^{-1}. The results indicate that the steam/brine nearly always has a finite Mg content, suggesting there is nearly always a significant cation-bearing brine component. This has not been recognised previously at Ruapehu; the models of Hurst and Dibble (1981) and Hurst et al. (1991) both assumed the incoming fluid was a saturated to superheated gas. It is extremely likely that the incoming steam:brine ratio varied with time over the period considered, however, this remains a poorly constrained variable. For the present, a constant ratio will be assumed, as for Poás. The average calculated $[Mg]_{st/br}$ concentrations are approximately the same in all the cases in fig. 4.17: ~1000 mg kg^{-1} between 1966 and 1979, and ~500 mg kg^{-1} from 1979 to 1989. Referring to fig. 4.8, if a value of $[Mg]_{reservoir} \approx 2000$ mg kg^{-1} is assumed for the more magmatically active period preceding 1979, and a value of ~1000 mg kg^{-1} is assumed since 1979, then this suggests an average input enthalpy value of ~1.8 MJ kg^{-1}. This value will be used for further modelling.

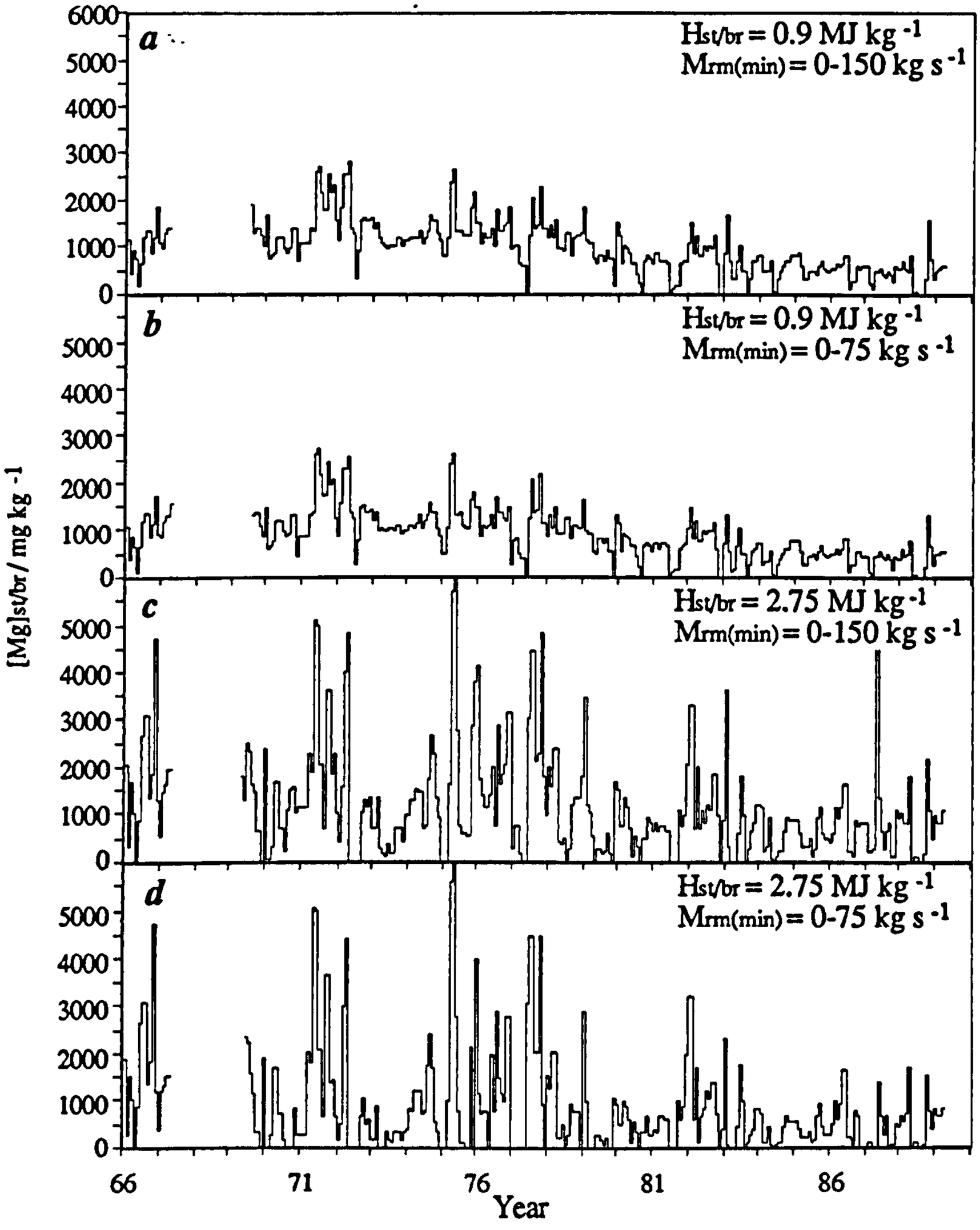

Figure 4.17 *Calculated model outputs of $[Mg]_{st/br}$ for Crater Lake, Mt. Ruapehu, using four sets of values for the minimum rainfall and the steam/brine enthalpy: (a) $M_{rm(min)}$ = 0-150 kg s^{-1}, $H_{st/br}$ = 0.9 MJ kg^{-1}; (b) $M_{rm(min)}$ = 0-75 kg s^{-1}, $H_{st/br}$ = 0.9 MJ kg^{-1}; (c) $M_{rm(min)}$ = 0-150 kg s^{-1}, $H_{st/br}$ = 2.75 MJ kg^{-1}; (d) $M_{rm(min)}$ = 0-75 kg s^{-1}, $H_{st/br}$ = 2.75 MJ kg^{-1}.*

Constraining the rainfall input

The same method used earlier with the Poás data will now be used on the Ruapehu data. The model was run with $H_{st/br}$ fixed at 1.8 MJ kg^{-1} and with various values of $M_{rm(min)}$, the minimum acceptable rainfall/meltflow. Model outputs of rainfall/meltflow are shown in fig. 4.18, for three values of $M_{rm(min)}$. Fig. 4.18a is for $M_{rm(min)}$ = 0 kg s^{-1}, i.e. the only constraint is that the model outputs of M_{rm} must be positive. Deviations from zero indicate that the chemical balance (equation 2.4) has forced there to be some rainfall input, in order to produce the observed variation in lake chemistry. As with the Poás data, spikes in the rainfall are unlikely, so the real value of rainfall input can be found by running the model with higher values of $M_{rm(min)}$, until the spikes are swamped. The average 'spike' peaks at around 100-200 kg s^{-1}; therefore it is not suprising that some spikes still exist when $M_{rm(min)}$ = 0-75 kg s^{-1} (sinusoidal variation between 0 kg s^{-1} in winter and 75 kg s^{-1} in summer) is imposed (fig. 4.18b), whereas with $M_{rm(min)}$ = 0-150 kg s^{-1}, the spikes are largely swamped (fig. 4.18c). The large spike in late 1975/early 1976 is ignored because this is due to the sudden increase in lake level (fig. 4.13b) following the eruption of April 1975, when the exact details of the lake level variation were somewhat uncertain. Fig. 4.18c suggests an yearly average rainfall input of ~75 kg s^{-1}, the same value that was predicted earlier (see section 4.2.1) on the basis of rainfall data from the flank, and the estimated catchment area of the lake basin. Thus a sinusoidal variation between 0 and 150 kg s^{-1} will be used as a minimum value for rain/snowfall/meltflow input.

4.2.4 Results and discussion

Outputs of the mass and energy flows from the model, using $H_{st/br}$ = 1.8 MJ kg^{-1} and $M_{rm(min)}$ = 0 - 150 kg s^{-1} are shown in figs. 4.19 and 4.20. Rates of addition of chloride and magnesium ions, and their calculated concentrations in the incoming steam/brine, are shown in fig. 4.21.

The power input to the lake (fig. 4.20a) shows peaks of ~1000 MW in 1968, 1971 and 1982, corresponding to eruptive periods when lake temperatures rose to ~60 °C (fig. 4.13a). Other eruptive periods show similar, but smaller increases in lake temperature and hence

power input (e.g. 1966, 1972, 1973, 1978, 1980, 1985-89). However, some eruptions are associated with only minor changes in power input to the lake, notably the two largest eruptions in this time series, in 1969 and 1975. As suggested earlier, perhaps the effects ofthese large eruptions largely bypassed the lake, and were accompanied by little longer-lived activity.

It can clearly be seen from fig. 4.20b-f that evaporation is the dominant form of heat loss at high heat fluxes, but that energy losses due to sensible heat, net radiation and seepage/overflow, together with the buffering effect of heating lake water, become more important at lower lake temperatures. The rate of change of lake mass (fig. 4.19e) is usually zero, because the lake is normally overflowing. Decreases in lake mass are usually due to lahars generated by explosive eruptions, e.g. 1969, 1971, 1975 and 1982. However, the flows shown in fig. 4.19e are not representative of the lahar flows, because they are 30-day averages, whereas the lahars were produced over only a few minutes.

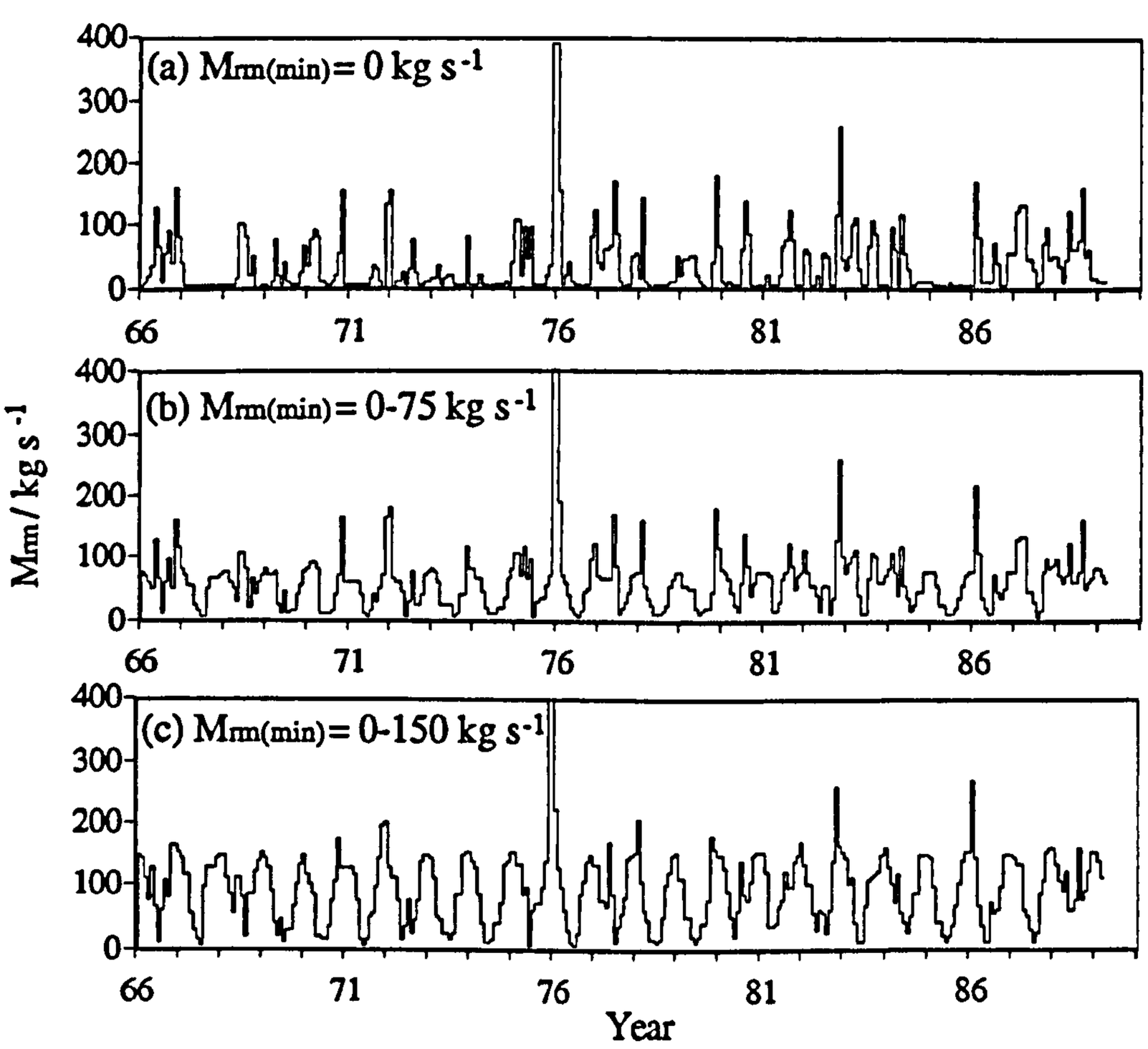

Figure 4.18 *Model outputs of M_{rm}, for three input values of minimum rainfall: (a) $M_{rm(min)} = 0$ kg s^{-1}; (b) $M_{rm(min)} = 0$-75 kg s^{-1}; (a) $M_{rm(min)} = 0$-150 kg s^{-1}. All using $H_{st/br} = 1.8$ MJ kg^{-1}.*

The general trend (i.e. after removing the peaks) of the steam/brine power input graph (fig. 4.20a) is decreasing, from a background level of ~300 MW in 1966 to ~50 MW in 1989. This is perhaps indicative of a long-term reduction of permeability within the hydrothermal system beneath the lake, and/or thickening of the conductive boundary layer between a deep magma body and the hydrothermal system (see chapter 5). Another interesting feature is the cyclic lake heating/cooling periods shown in fig. 4.20f, for the years 1985-89. Before this time, the rate of change of lake energy was erratic, but since 1985, peaks in lake temperature have been followed by exponential decreases, i.e. the lake loses energy rapidly from its

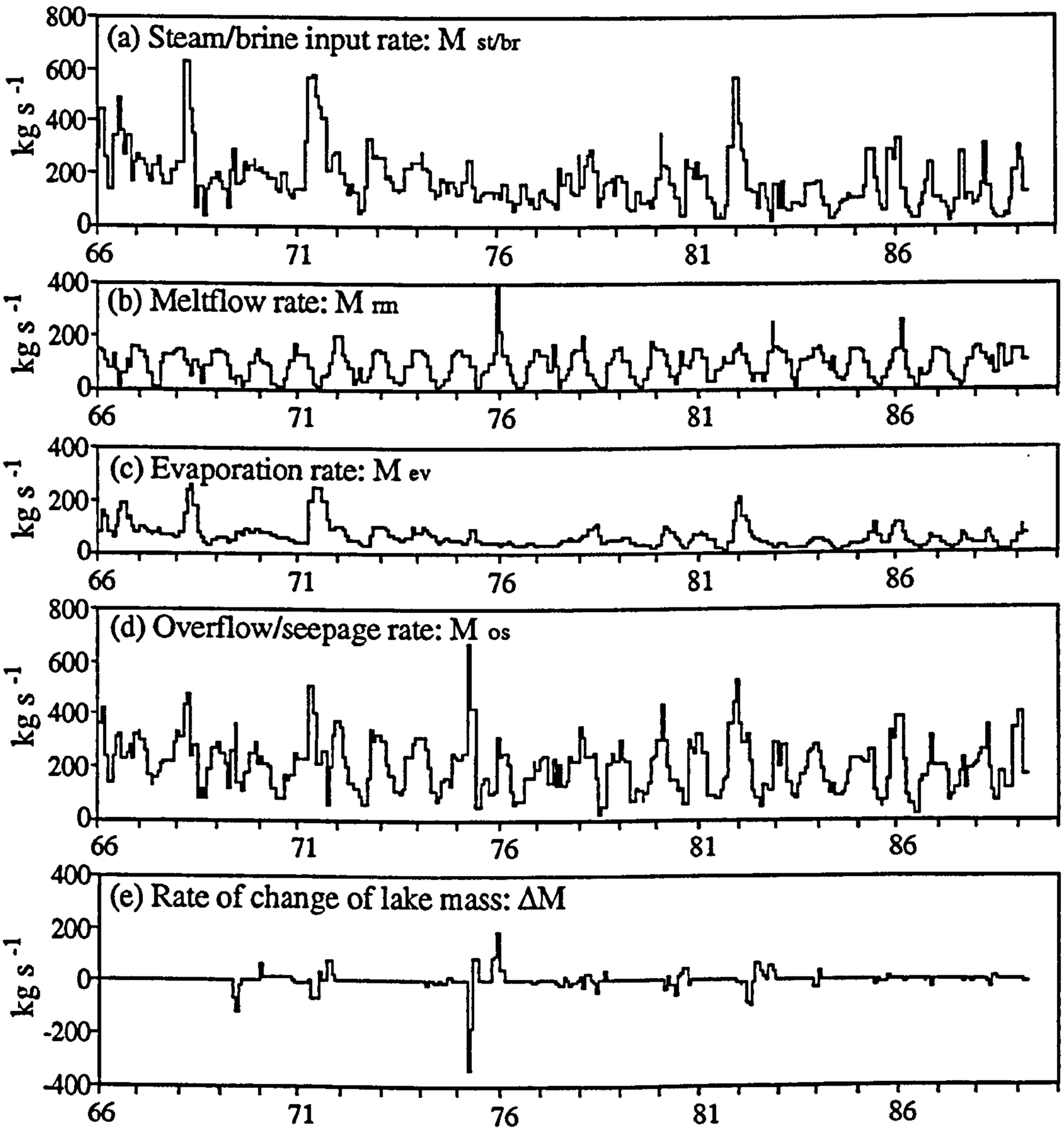

Figure 4.19 *Mass balance for Crater Lake Mt. Ruapehu. Flows are 30 day averages, calculated assuming a steam/brine enthalpy of 1.8 MJ kg^{-1}, and a minimum rainfall of 0-150 kg s^{-1}.*

initial high temperature, then cools more slowly as its temperature approaches ambient. Cooling periods of typically 6 to 9 months were ended by approximately 3 months of renewed heating, either initiated by, and/or with accompanying, and/or culminating in, minor phreatic activity. This probably represents a cyclic process operating within either the magmatic or hydrothermal system beneath the lake. Hurst et al. (1991) suggested the

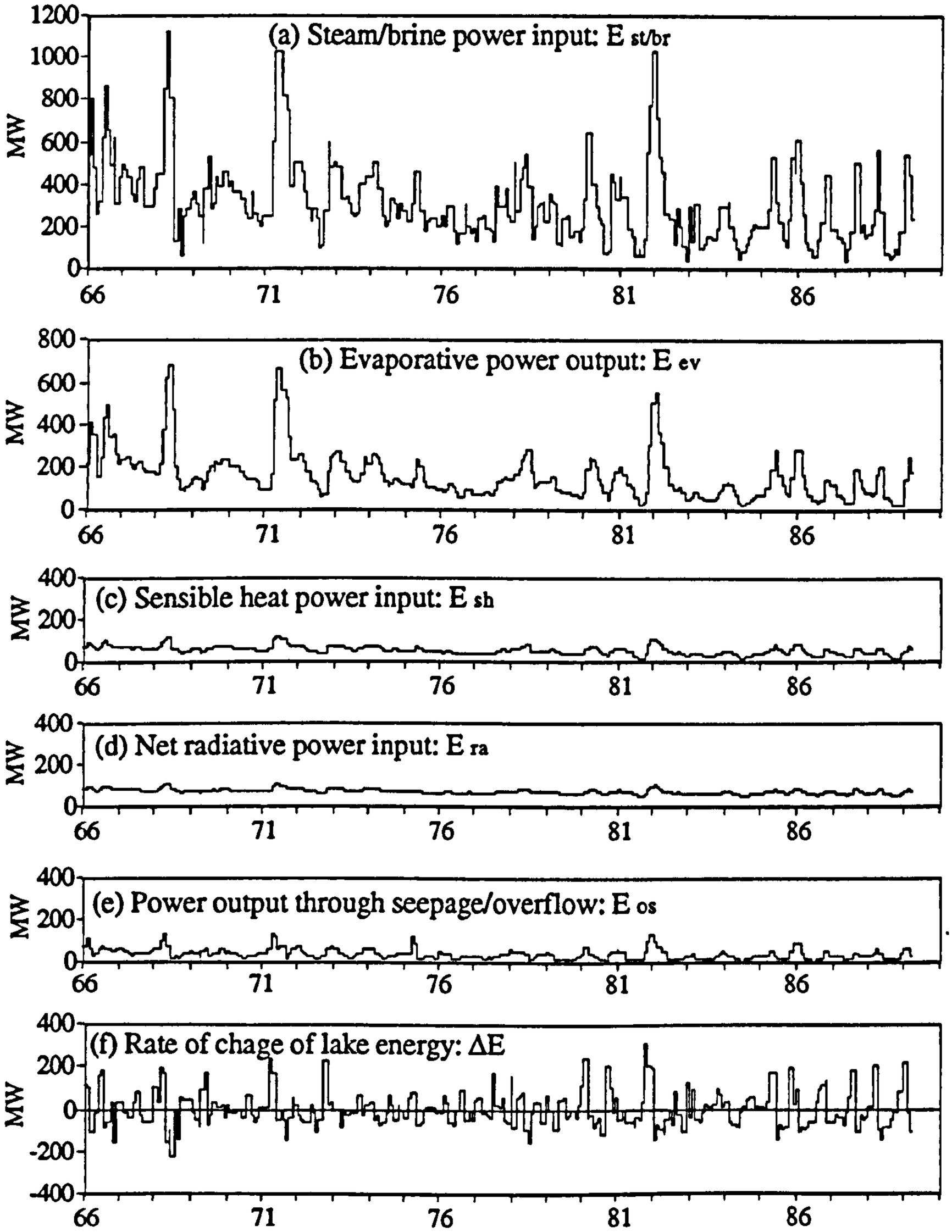

Figure 4.20 *Energy balance for Crater Lake, Mt. Ruapehu, with energy flows in MW, calculated as 30 day averages. Assumes* $H_{st/br} = 1.8\ MJ\ kg^{-1}$, *and* $M_{rm(min)} = 0\text{-}150\ kg\ s^{-1}$.

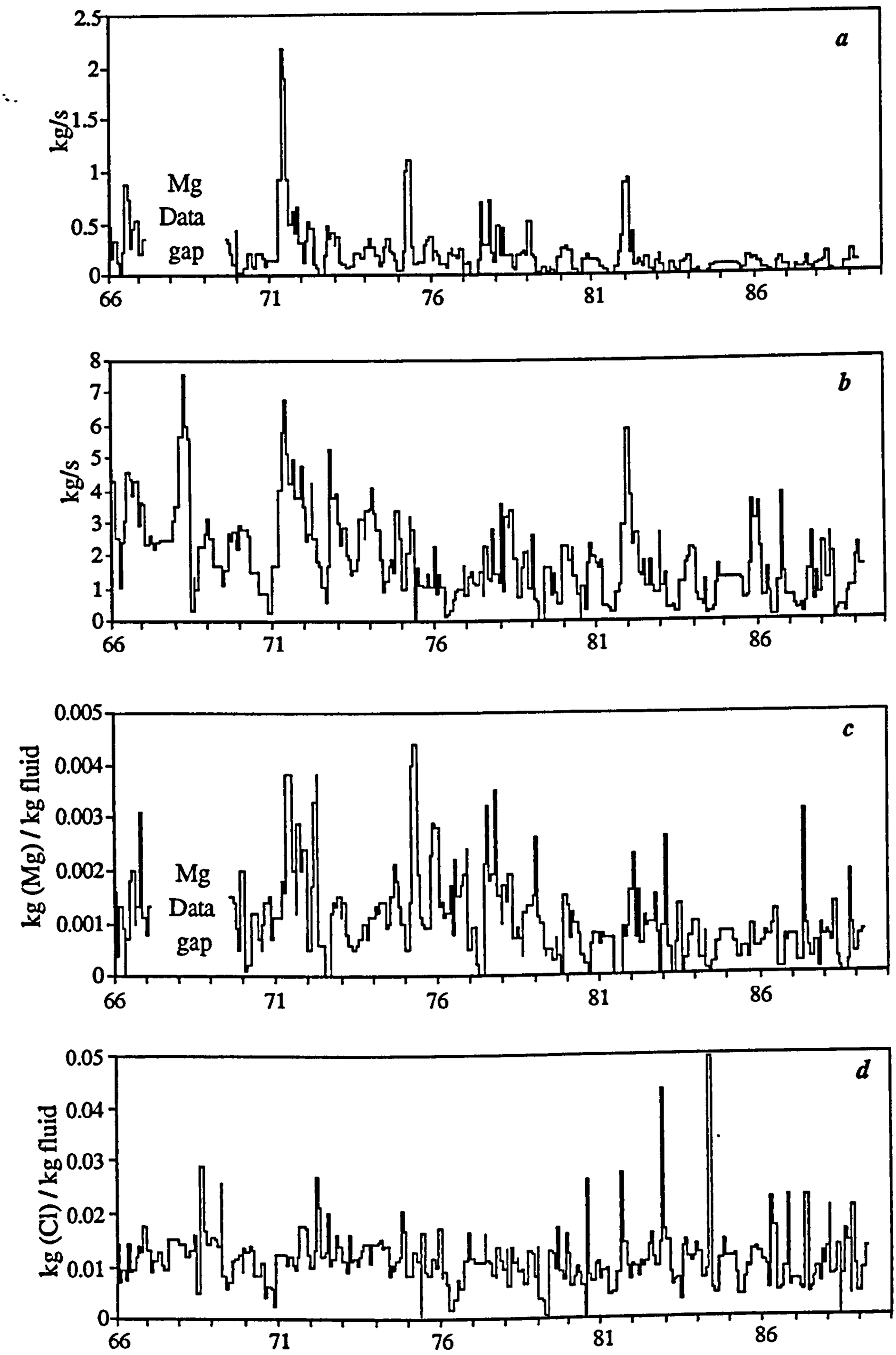

Figure 4.21 *Ruapehu Crater Lake chemical fluxes: (a) Mg input; (b) Cl input; (c) Mg content of the incoming fluid; (d) Cl content of the incoming fluid.*

cyclicity may be caused by a reduction (upon reaching a critical temperature) in the viscosity of a sulphur layer on/beneath the lake floor, which previously had been blocking vents, resulting in a sudden release of gas. After release of the gas build-up, gas flows and temperatures would reduce, allowing the sulphur to increase in viscosity again, sealing the system. The cyclicity may be more fundamentally related to the magmatic degassing process (see chapter 6).

Typical flows of magnesium into Crater Lake are between 0 and 0.5 kg s^{-1}, rising to 1 or 2 kg s^{-1} during/following magmatic eruptions in 1971, 1975 and 1982 (fig. 4.21a). The concentrations of Mg in the incoming fluid (fig. 4.21c), as already mentioned, averaged ~1000 mg kg^{-1} between 1966 and 1979, and ~500 mg kg^{-1} between 1979 and 1989. Assuming the brine component carries all the Mg, this suggests that the Mg content in the brine is about twice these values. Influx of chloride to Crater Lake also shows peaks (of ~5 to 7 kg s^{-1}) associated with eruptions, most notably those in 1968, 1971 and 1982 (fig. 4.21b). Following eruptions, Cl input gradually decreases to 1 or 2 kg s^{-1}, but more slowly than the decrease in Mg influx. This perhaps reflects a longer-lived Cl source following eruptions (e.g. continuing magmatic degassing), compared to a relatively short-lived Mg source (e.g. the available ions are rapidly leached from new magma). This can also be seen in the lake concentration data (fig. 4.14), where Mg decays quite smoothly following sudden inputs, whereas Cl is often sustained following eruptions, implying a continuing input, and then erratically decays. The Cl content of the incoming fluid (fig. 4.21d) is remarkably constant at around 10000 mg kg^{-1} (or 1 wt.%). This perhaps reflects the approximate HCl composition of magmatic gas; otherwise, magmatic gas inputs should produce significant deviations. The lake composition will tend towards that of the incoming fluid if the concentrating effect of evaporation is approximately equal to the diluting effect of adding rainfall/meltflow. Figs. 4.19b and c show both flows to be similar, but rainfall/meltflow dilution is slightly greater than evaporation, thus the overall Cl content of the lake should decrease in the absence of external sources. The incoming fluid concentrations of both Mg and Cl are generally similar to their concentrations within the lake, suggesting that for much of the time the incoming fluid is simply derived from the partial vaporisation of seepage. The

fact that the average mass flows of steam/brine input and overflow/seepage are roughly the same (fig. 4.19a,d; 100-200 kg s^{-1}) also supports this mechanism.

On a more detailed scale, the Mg content of the incoming fluid increases to ~4000 mg kg^{-1} (~8000 mg kg^{-1} in the brine) following phreatomagmatic eruptions in 1971, 1975 and 1977, before erratically decaying to near normal levels (fig. 4.21c). This suggests that the source of the Mg probably was fresh magmatic material emplaced during these eruptions, breaking down by reaction with acidic lake-water (c.f. Giggenbach, 1974); alternatively, the source of Mg could be a concentrated brine reservoir beneath the lake. Assuming that the source of Mg is new magma, then the volume of magma leached can be estimated.

Taking the 1971 eruption (the largest introduction of Mg), the increase in total Mg in the lake was ~10^7 kg (fig. 4.14a) over 104 days, a rate of ~1 kg s^{-1}. The Mg content of seven Ruapehu lavas analysed by Cole et al. (1986) averaged ~3 wt. %. Therefore, a minimum of ~3 x 10^8 kg of magma must have been leached to supply the Mg introduced to the lake, at a rate of ~40 kg s^{-1}. Over this eruptive period, the calculated power input to the lake averaged ~900 MW (fig. 4.20a). Referring to table 4.1, 40 kg s^{-1} of magma crystallising, cooling to 250 °C, and degassing 4 wt. % water (model IV), will only release ~60 MW. The simplest explanation for this discrepancy is that the volume of magma leached of Mg was only ~7 % of the magma that crystallised, cooled, and degassed, i.e. the magma volume involved was ~5 x 10^9 kg. However, the other possibility is that a much larger volume of gas was released. Total chloride in the lake increased by ~2 x 10^7 kg over the same period, at a rate of ~2 kg s^{-1}. Assuming the source of the chloride is magmatic HCl, and also assuming the magma contains 4 wt. % water, and 0.08 wt % HCl (i.e. a H_2O:HCl ratio of 50:1, typical of that observed in magmatic gases), then the volume of magma required to have degassed is ~2.5 x 10^{10} kg, at a rate of ~3000 kg s^{-1}. Referring to table 4.1, 3000 kg s^{-1} of 4 wt. % water magma degassing would supply ~500 MW (model III), and ~100 kg s^{-1} of magmatic water. The remainder of the power (400 MW) could have been released by part of this magma volume (~10 %, 3 x 10^9 kg) crystallising and cooling, and the Mg mass could be accounted for if only ~1 % of this magma is leached. The assumptions made about the water and chloride contents of the magma may be wrong, however, the Cl content of the magma

would have to be 0.4 wt.% (5 times higher), for the entire power to be due to degassing, crystallisation, and cooling of the same volume of magma (model IV). This is a possibility, but the more typical Cl content, with an accompanying larger magma volume degassing and only partially crystallising, is the preferred option. A magma mass of 2.5×10^{10} kg will occupy a volume of ~10^7 m^3. Assuming a cylindrical intrusion, 1 km in length, this volume would have a diameter of over 100 m. Deformation of only a few centimetres was observed over the eruptive period (P. Otway, in Nairn et al., 1979), suggesting such a large intrusion is unlikely. If the intrusion is of smaller diameter, but extends to greater than ~1 km depth, then much of the magma will remain at pressures too high for it to efficiently lose its dissolved volatiles. A dynamic new mechanism of degassing is developed in chapter 6, where volatile-rich magma rises within a small intrusion, reaches near enough to the surface to degas efficiently, then subsequently sinks back down the same intrusion, to be replaced by more rising, volatile-rich magma.

4.2.5 Summary and Conclusions for Ruapehu

As for Poás, the results suggest that heat source of Crater Lake was the addition of saturated steam and hot brine. For much of the time, the steam/brine input was simply derived from the partial vaporisation of seepage, augmented sometimes by magmatic gas. Input of magmatic HCl is thought to be responsible for the increases in lake Cl in 1968, 1971, 1977-78, 1982 and 1985-86, in each case associated with either phreatomagmatic or phreatic eruptions. The estimated volume of magma degassed during these periods is ~1×10^{10} kg to ~2.5×10^{10} kg in each case. Increases in lake Mg occurred in 1971, 1975, 1977-78 and 1982, and are thought to have been caused by leaching of new magma. The estimated volume of magma leached during these periods needs only to be approximately one hundredth of the volume degassed. The degassed magma volumes are much larger than those implied by deformation surveys, suggesting that magma recycling mechanism, between a minor shallow intrusion and a deeper chamber, is operating during/following eruptive periods (see chapter 6). The long term decrease in background power input to the lake perhaps indicates a gradual reduction in the permeability of the hydrothermal system beneath the lake, and/or a thickening of the conductive boundary layer between magma and

the hydrothermal system (see chapter 5). The cyclic heating and cooling of the lake observed since 1985 perhaps represents the build-up and break-down of a sulphur layer on the lake bed (Hurst et al., 1991), alternatively, and more likely, it could represent a cyclic process within either the magmatic or hydrothermal systems.

Magma mass and volume rates required to produce the calculated power outputs at Ruapehu, from the models I-IV (see section 4.1.5) are summarised in Table 4.2.

Model	Magma mass rate in kg s^{-1} to produce 50-1000 MW	Magma mass rate in km^3 a^{-1} to produce 50-1000 MW
I	120-2400	0.0015-0.03
II	42-830	0.0005-0.01
III	320-6300	0.004-0.08
IV	37-730	0.0005-0.009

Table 4.2 *Magma mass and volume rates required to supply the calculated power input to Crater Lake, Mt, Ruapehu, for the four end member models described in section 4.1.5.*

CHAPTER 5

Heat Transfer in Magmatic and Hydrothermal Systems: 1. Conduction and Convection.

5.1 Introduction

In chapter 4, data from the crater lakes of Poás and Ruapehu were used to calculate mass, energy and chemical fluxes into the lakes. In turn, these fluxes represent the output of a hydrothermal or degassing system directly beneath the lake, that extends downwards to a magmatic heat source. The upper parts of such a system involve the downward percolation of lake-water seepage, and the modelling presented earlier suggests that part of the water is returned to the lake as hot brine, while part is vaporized and returned as steam. The ultimate heat source driving this process must be a magmatic reservoir underlying the system, supplying heat by conduction and volatile degassing. Advection of heat by degassing of magma will be considered in detail in chapter 6. In this chapter, heat transfer by conduction from the magmatic system to the hydrothermal system, and the physical behaviour of both systems will be addressed, and generalised models developed. Because the two processes of conduction and degassing will occur simultaneously, and indeed probably produce complicated interactions, heat transfer models integrating these processes in the cases of Poás and Ruapehu will be presented in chapters 6 and 7.

A simple model of heat transfer from a magma body is shown in figure 5.1. Within the magma body, convection and/or latent heat release through crystallisation will be the major forms of heat transfer. In section 5.2, it is shown that heat loss mechanisms involving a stationary conductive boundary layer (CBL) above convecting magma, or above magma convecting and crystallising, are unlikely to provide the power outputs observed at Poás and Ruapehu. Instead, infiltration of a CBL at the roof of a magma body by a hydrothermal system (Lister, 1974), directly releasing latent and specific heat, is the favoured mechanism. At high heat loss rates to the hydrothermal system, glass formation may occur rather thancrystallisation. Across the CBL, temperatures fall from ~1000 °C in the magma to

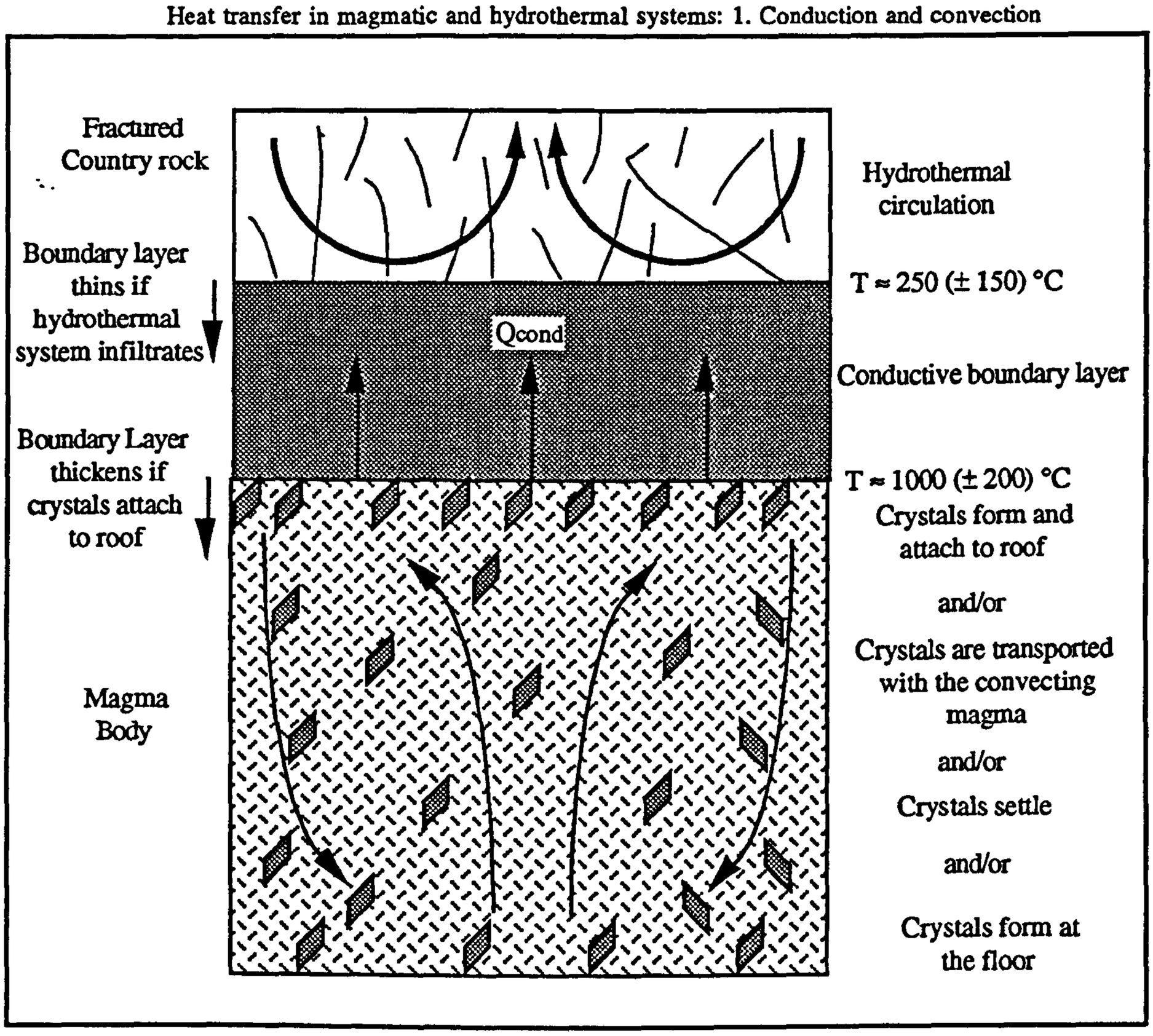

Fig. 5.1 *Cartoon of the magmatic and hydrothermal system. Conductive heat losses from the magma body will depend upon the thickness of the boundary layer.The magma can provide heat by convecting and crystallising. The different crystallisation and convection possibilities are discussed further in fig. 5.4 and section 5.2.*

~250 °C in the hydrothermal system (e.g. Hardee, 1982; Cann et al., 1985; Carrigan, 1986). Within the CBL, cooling will induce contraction and fracturing. At high temperatures, however, the rock will rapidly deform and close fractures. The 'cracking temperature' was defined by Lister (1974) as the temperature at which fracturing due to thermal contraction overcame annealing due to rock creep, and fractures that developed would stay open. The cracking temperature was thought to fall in the range 700-900 K (427-627 °C) (Lister, 1983), although a value of 725 °C was quoted by Carrigan (1986). Calculations in section 5.3 suggest that the cracking temperature may have a much larger possible range, probably related to the rate of heat transfer occurring. This cracked margin represents the closest position to the magma, and the highest temperature, that downward percolating fluid can attain. Directly beneath this cracked zone, heat transfer will occur solely by conduction.

Above, if the permeability of the country rock is sufficient, and water is present at its saturation (boiling point for pressure) temperature, two-phase convection (steam-water counterflow) will dominate. In the region at the top of the CBL, between the cracking temperature and the water saturation temperature (i.e. where fractures are open, but only superheated steam is present), single phase convection of superheated steam is not thought to occur, and again conduction dominates (see section 5.3.4).

Two-phase convection in hydrothermal systems involves downflowing liquid and upflowing vapour, and is a much more potent form of heat transfer than single phase convection. This is because of the large density difference between steam and water, and also the large enthalpy difference between the two (i.e. the latent heat capacity). A simple one-dimensional model of steam-water counterflow (Hardee, 1982) is described in section 5.4, allowing estimates to be made of possible permeabilities, and pressure-depth and temperature-depth profiles of the hydrothermal systems at Poás and Ruapehu (see section 5.5).

The model depicted in fig. 5.1 is clearly flawed if gas is escaping from the magma, violating the 'impermeable' conductive boundary layer (CBL) assumption. However, in the first instance it will be assumed that gas escape occurs over short periods and/or from limited areas, and can be ignored. Interaction between gas escape and the CBL will be considered in the following two chapters.

5.1.1 Thermal Conductivity

Thermal conductivity is defined as the rate at which energy will cross a unit area under the driving potential of a unit temperature gradient perpendicular to the area. This can be written as the heat conduction equation:

$$Q_{cond} = -k \frac{dT}{dz} \quad (5.1),$$

where Q_{cond} is the conductive heat flux (units: W m^{-2}), k is the thermal conductivity (W m^{-1} K^{-1}), and dT/dz is the temperature gradient (K m^{-1}). The negative sign is because heat flows in the direction of decreasing temperature. Typical conductivity values of volcanic rocks lie in the range 1-5 W m^{-1} K^{-1} (Jessop, 1990), and 108 samples of andesite measured

by Roy et al. (1981) averaged 2.26 W m^{-1} K^{-1} (minimum 1.35, maximum 4.86).

5.2 The Magma/Country Rock Boundary: Heat Flux from the Magma

Country rock immediately surrounding a magma chamber is likely to be similar in composition to the magma, thus a conductivity of 2.3 W m^{-1} K^{-1} will be assumed for material surrounding magma bodies at Poás and Ruapehu. Figures 4.11 and 4.20 indicate a power input to both lakes of ~10^2-10^3 MW. For the steady-state, this must represent the power input to the base of the hydrothermal system, and hence the power output from the magmatic system. Assuming the upper surface of a magma body has an area somewhere between that of the crater (~10^6 m^2) and that of the lake (~10^5 m^2), this corresponds to a heat flux of 10^2-10^4 W m^{-2}. Using equation (5.1), and assuming a temperature drop from ~1000 °C in the magma to ~250 °C in the hydrothermal system, implies a CBL ~0.2-20 m thick above the magma.

5.2.1 Convection and crystallisation in the magma

Brandeis and Jaupart (1986) investigated the interaction of thermal convection and crystallisation in magma chambers. They derived a characteristic time scale for crystallisation using typical crystal nucleation and growth rates, and a characteristic time scale for the onset of convection. The time scale for the initiation of crystallisation was ~10^3-10^4 s, whilst that for convective instability varied with magma viscosity from ~10^2 s for basaltic magmas, to ~10^7s for felsic magmas. Thus crystallisation will tend to occur after the onset of convection in low viscosity magmas, but before the onset of convection in more viscous magmas. Brandeis and Jaupart (1986) found that for magmas with viscosity greater than ~10^4 Pa s, crystallisation occurred before convection, and the increase in viscosity associated with the crystals (see below) inhibited the development of significant thermal convection.

Magma viscosity

Clearly, one of the critical properties of magma is its viscosity. Viscosities of the magmatic systems at Poás and Ruapehu are unknown, but can be estimated. Viscosity is a function of

magma composition, temperature, dissolved volatile content, phenocryst content and bubble content (Bottinga and Weill, 1972; Shaw, 1972; Jaupart and Tait, 1990). Cole et al. (1986) presented petrographic and geochemical analyses of a number of lavas from Ruapehu, ranging from basalt to dacite. Using the analysis of a basic andesite, sample no. 14737 (Cole et al., 1986), given in table 5.1, the viscosity of this andesite melt (crystal-free viscosity μ_l) has been calculated for a range of temperatures and water contents (fig. 5.2a,b). The overall magma viscosity (μ_m) will vary with phenocryst volume fraction (Φ) according to the relation (Jaupart and Tait, 1990):

$$\mu_m = \mu_l \left(1 - \frac{\Phi}{\Phi_c}\right)^n \qquad (5.2)$$

where $\Phi_c \approx 0.65$ and $n \approx -1.625$. The variation of viscosity with crystal content is illustrated in fig. 5.2c, up to a volume fraction of 0.5. It can be seen from fig. 5.2c that for a temperature of 1000 °C, and a phenocryst concentration of 37.9 volume % (table 5.1), the viscosity of Ruapehu basic andesite should fall in the range from ~20 Pa s (4 wt. % H_2O) to ~10^4 Pa s (0 wt. % water). The presence of bubbles in magma tends to increase its viscosity. This effect is considered in chapter 6, and is essentially only important at very high gas volume fractions (>~0.5); for the discussion in this chapter, it will be ignored.

Models of heat flux from magma bodies

Four models of the heat flux from a magma body are shown in fig. 5.3. Model A assumes the magma is not crystallising, and has a spatially fixed upper CBL, which receives heat from convecting magma below. This situation represents a cooling superheated magma, or a magma body with a deeper heat source. The Rayleigh number in the magma will be given by:

$$Ra = \frac{\rho\, g\, \alpha\, \Delta T\, h^3}{\kappa\, \mu_m} \qquad (5.3),$$

where ρ is the density, g is the acceleration due to gravity, α is the coefficient of thermal expansion, ΔT is the temperature difference across the magma body, h is the depth of the body, κ is the thermal diffusivity, and μ_m the dynamic viscosity (see table 5.2 for values).

Oxide	Wt. %
SiO_2	56.5
TiO_2	0.7
Al_2O_3	18.2
Fe_2O_3	1.4
FeO	6.8
MnO	0.1
MgO	4.7
CaO	7.6
Na_2O	3.2
K_2O	0.8
P_2O_5	0.1

Mineral	Volume %
Plagioclase	28.7
Augite	2.0
Orthopyroxene	6.7
Fe-Ti oxide	0.5

Table 5.1 *Geochemical and petrographic analysis of a basic andesite from Ruapehu (data from Cole et al. (1986))*

The Nusselt number, or ratio of heat transferred by convection (Q_{conv}) relative to that which would be transferred by conduction (Q_{cond}) in the absence of convection, will be given by (Turner, 1973):

$$Nu = \frac{Q_{conv}}{Q_{cond}} = 0.1\ (Ra)^{1/3} \qquad (\text{if } Ra > 10^5) \quad (5.4).$$

Substituting equations (5.1) and (5.3) into (5.4), and noting that $k = \rho\ \kappa\ c_m$, where c_m is the specific heat capacity of the magma, gives (Martin et al., 1987; Worster et al., 1990):

$$Q_{conv} = 0.1 \left(\frac{\rho^4\ c_m^3\ g\ \alpha\ \kappa^2\ \Delta T^4}{\mu_m} \right)^{1/3} \qquad (5.5)$$

Re-arranging this equation to give ΔT:

$$\Delta T = \left(\frac{Q_{conv}^3\ \mu_m}{(0.1)^3\ \rho^4\ c_m^3\ g\ \alpha\ \kappa^2} \right)^{1/4} \quad (5.6)$$

Substituting values of properties for andesite (table 5.2), the variation of ΔT with viscosity can be found, for the upper and lower values of Q_{conv} (fig. 5.4a). The temperature difference across the magma body, ΔT, will actually represent the temperature difference

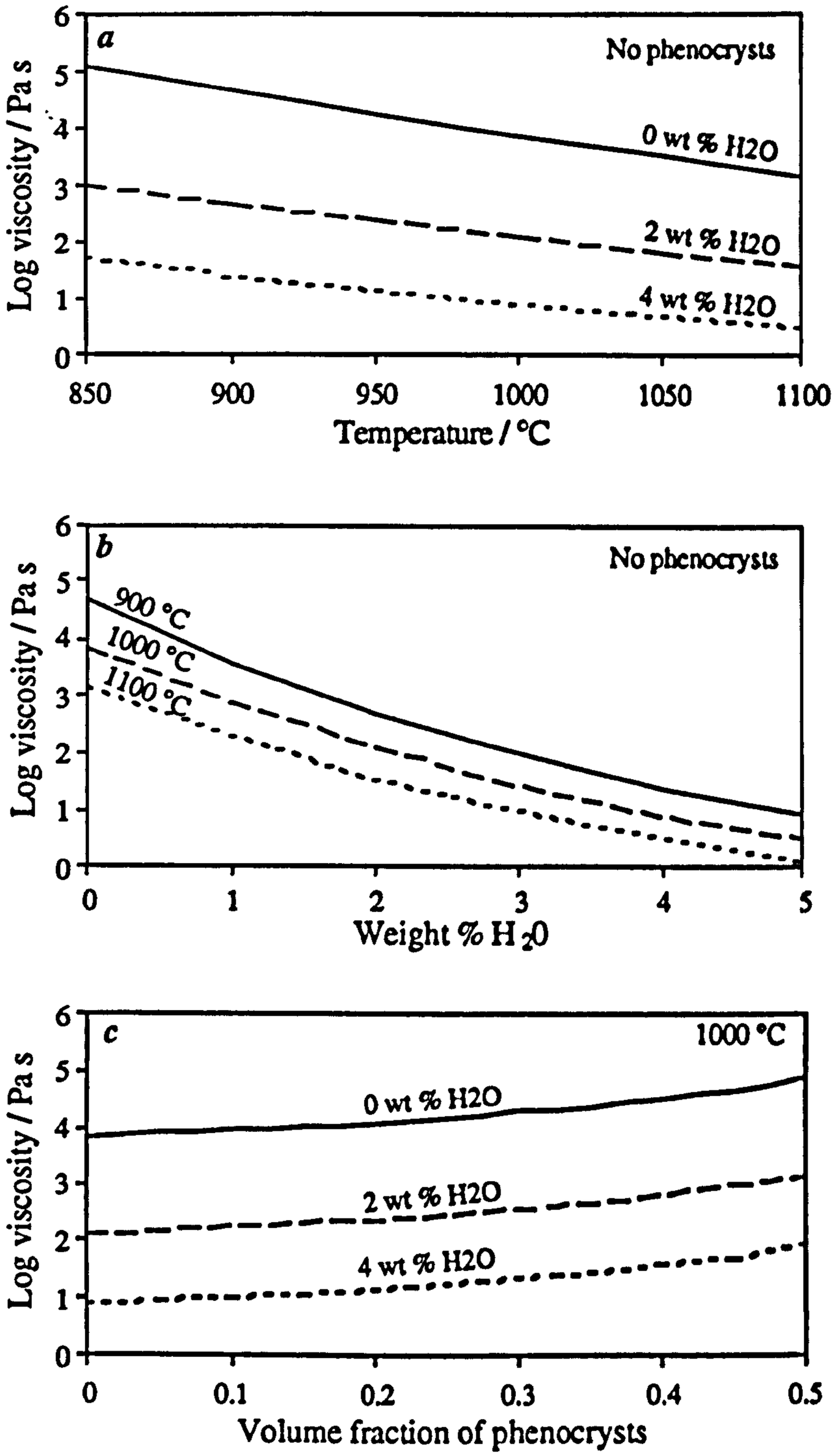

Fig. 5.2 *Calculated viscosities of Ruapehu basic andesite (table 5.1): variation with (a) temperature; (b) water content; (c) phenocryst content. From McBirney and Murase (1984) and Tait and Jaupart (1990).*

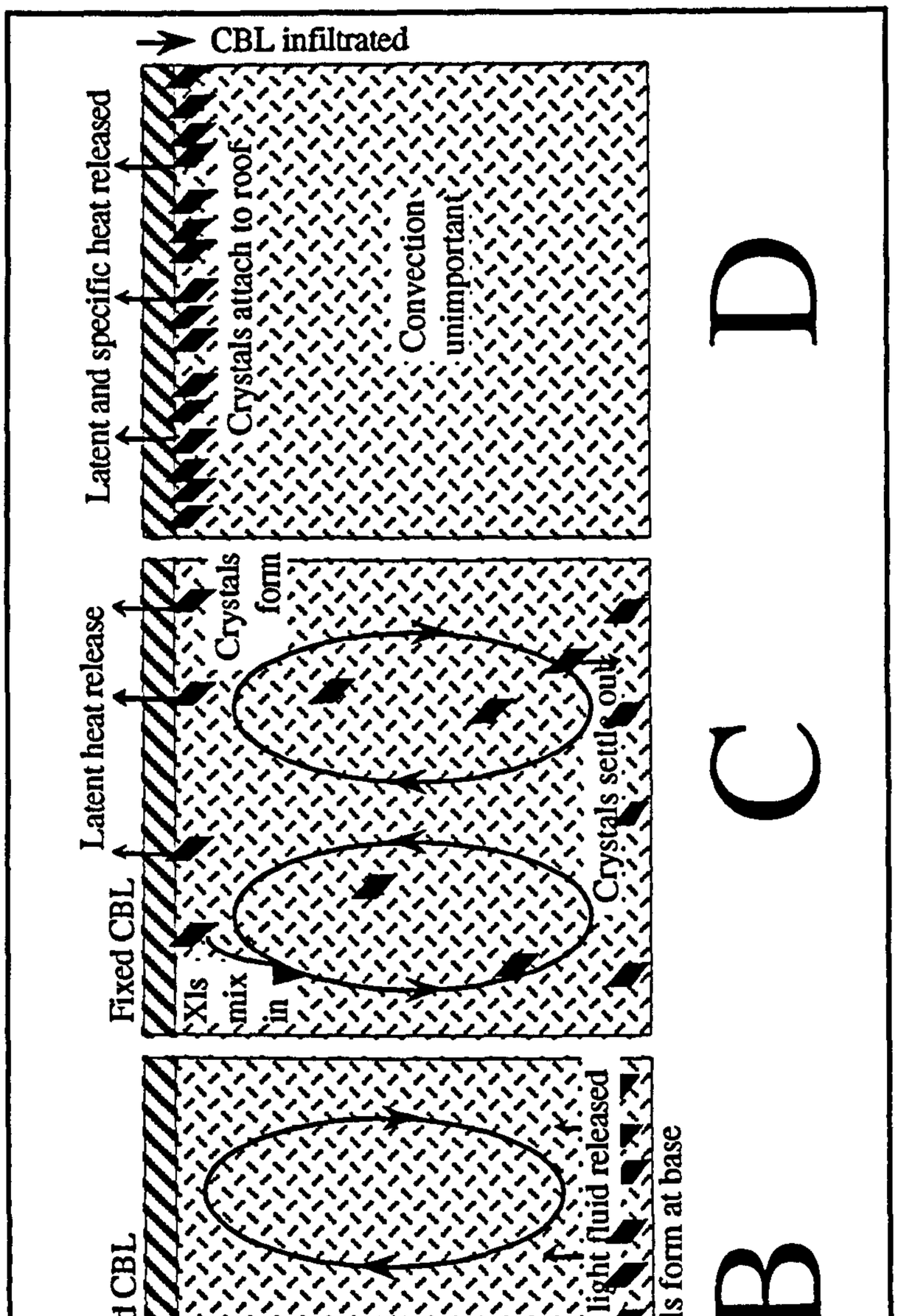

Figure 5.3 Models of heat transfer within and from magma bodies. See text for discussion.

across a thin thermal boundary layer at the roof of the body, whilst beneath this layer, the magma can be assumed to be homogeneous. Using the calculated viscosity range (20 - 10^4 Pa s), and the range of heat flux (10^2 - 10^4 W m^{-2}), suggests that the lower bound of the heat flux requires $\Delta T \approx$ 6-40 K, and the upper bound requires $\Delta T \approx$ 200-1000 K. A maximum value of ΔT (for non-superheated magmas) is ~200 K, the typical span between liquidus and solidus temperatures. With ΔT this large, however, crystallisation should occur within the boundary layer. Typical values of ΔT required to drive turbulent convection are less than 1 K, and values greater than this are unlikely to be sustained (Worster et al., 1990). Thus the upper bound of the heat flux is impossible simply with convecting magma and no crystallisation, and the lower bound is unlikely, even with a low viscosity magma. If the boundary layer is assumed to be dominated by conduction, and it transfers all the heat supplied by convection (i.e. $Q_{cond} = Q_{conv}$), its thickness (δ) can be estimated using equation (5.1) (see fig. 5.4b):

$$\delta = k\frac{\Delta T}{Q_{conv}} = \left(\frac{c_m\ \kappa^2\ \mu_m}{(0.1)^3\ Q_{conv}\ g\ \alpha}\right)^{1/4} \qquad (5.7)$$

Magma property	Symbol	Value
Density	ρ	2450 kg m^{-3}
Coefficient of thermal expansion	α	5×10^{-5} K^{-1}
Thermal diffusivity	$\kappa = \frac{k}{\rho\ c_m}$	9×10^{-7} m^2 s^{-1}
Thermal conductivity	k	2.3 W m^{-1} K^{-1}
Specific heat capacity	c_m	1000 J kg^{-1} K^{-1}
Latent heat capacity	L_m	4.2×10^5 J kg^{-1}
Dynamic viscosity	μ_m	~20-10^4 Pa s

Table 5.2 *Andesite magma properties: symbols and values used in the text. Values from Tait and Jaupart (1990), Jessop (1990), Hardee (1982) and McBirney and Murase (1984).*

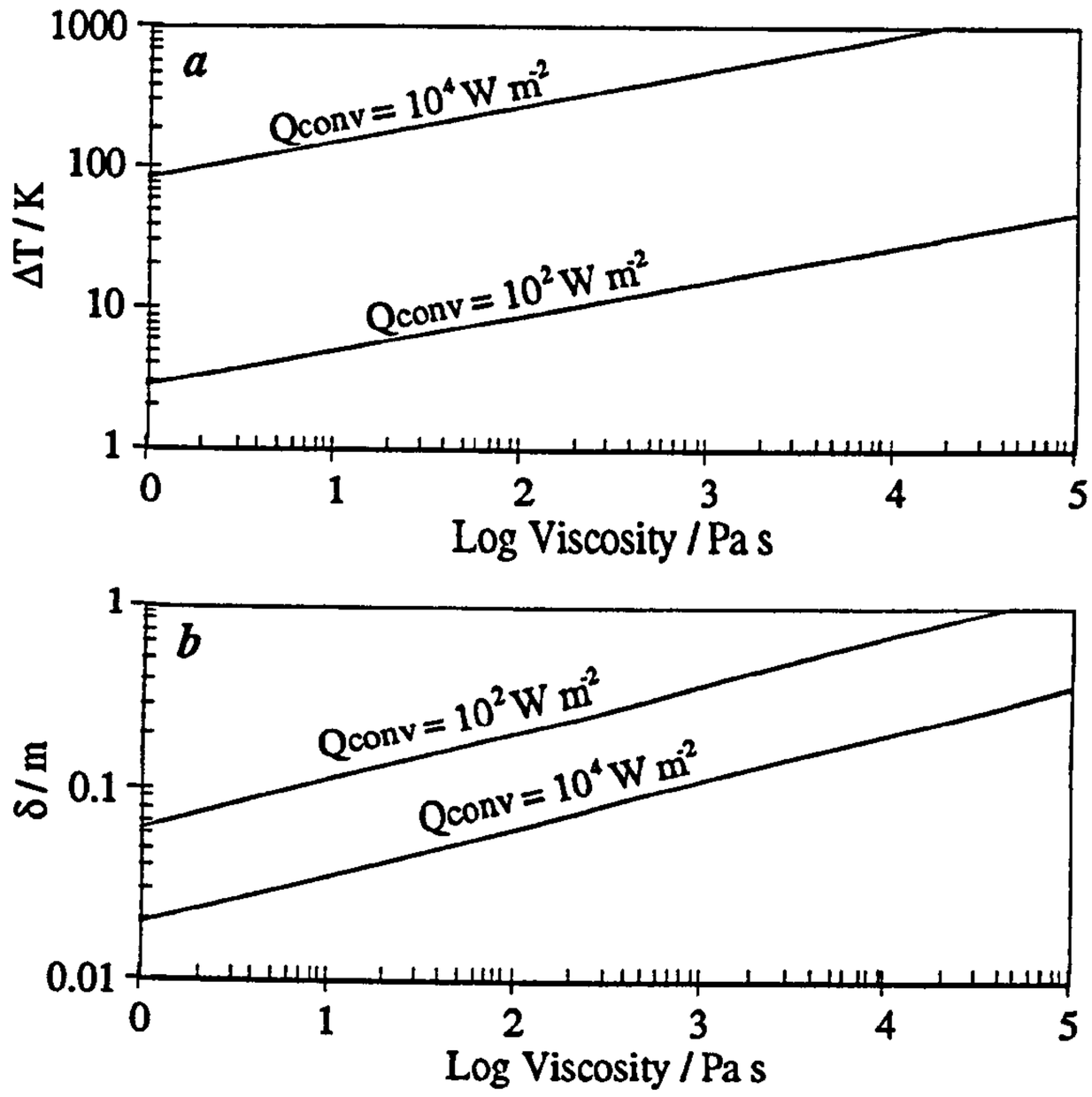

Fig. 5.4 *(a) Temperature difference required to drive thermal convection, and (b) thickness of the CBL at the roof of a magma body, both against viscosity for two heat fluxes out of the magma body.*

Models involving crystallisation will now be considered. Model B (fig. 5.3) represents a magma body crystallising at its base - this is thought to occur in most magma chambers because the liquidus temperature increases with pressure, thus supersaturation is more likely at greater depth (Tait and Jaupart, 1990). In this situation, convection within the chamber can be enhanced if the crystallising phase is more dense than the melt, as it will leave a residual fluid lighter than the melt which will rise; this process is called compositional convection. Martin et al. (1987) considered a mafic magma crystallising olivine, and concluded that compositional bouyancy effects approximately equalled those due to thermal bouyancy. It follows therefore,that model B would require a temperature difference half that required in model A to produce the same bouyancy. However, the heat must still be conducted through an upper boundary layer, and as ΔT is half the model A value, the thickness will need to be half the value. This model still requires very high values of ΔT to produce the observed heat fluxes by convectional processes in the chamber; thus it is also considered unlikely.

In model C (fig. 5.3), crystallisation is occurring at the top of the magma body, directly beneath a fixed CBL. Latent heat is thus directly supplied to the CBL. Assuming all the latent heat is released to the CBL, the rate of crystallisation per unit roof area (Q_{cr}, units (m^3 s^{-1}) m^{-2}) required to produce a heat flux from the magma (Q_{mag}) can be calculated:

$$Q_{cr} = \frac{Q_{mag}}{\rho\ L_m} \qquad (5.8)$$

where L_m is the latent heat of crystallisation of magma (see table 5.2 for value). For Q_{mag} = 10^2 - 10^4 W m^{-2}, requires Q_{cr} in the range 10^{-7} m s^{-1} (≈ 3 m a^{-1}) to 10^{-5} m s^{-1} (300 m a^{-1}). If the CBL position and thickness are to remain fixed, then these crystals must be removed from the roof region. This could occur by entrainment in convecting magma, or by crystal settling. The terminal settling velocity (v_t) of a sphere in a viscous fluid, where the flow is laminar, should obey Stokes law:

$$v_t = \frac{d^2\ g\ \Delta\rho}{18\ \mu} \qquad (5.9),$$

where d is the sphere diameter, and $\Delta\rho$ is the density contrast between the sphere and the fluid. For the Poás lavas, the densest commonly erupted phenocryst is bronzite-hypersthene (3500 kg m^{-3}) (Thorpe et al., 1981). For the settling velocity to exceed the lower bound on the crystallisation rate of 3 m a^{-1} (i.e. for crystals to escape the upper layer), phenocryst diameters must exceed ~0.06 mm (μ = 20 Pa s), or ~1 mm (μ = 10^4 Pa s). Diameters an order of magnitude larger would be required to outpace a crystallisation rate of 300 m a^{-1}. These values are comparable to the phenocryst sizes commonly observed in erupted lavas at Poás and Ruapehu (generally < 1mm). This suggests crystal settling is a possible mechanism for the removal of crystals from the roof region, especially if the magma has a low viscosity, or is producing a relatively small heat flux.

Alternatively, crystals could be removed from the roof by entrainment into convecting magma. These crystals need to be removed from the magma at a rate equal to their entrainment, otherwise the viscosity of the magma will rise, convection will slow, and heat losses will gradually fall (although the time scale of such a phenomena may be much larger than the time scale of observations). Martin and Nokes (1988) found that crystal settling was

still a powerful method of differentiation in a turbulently convecting magma chamber, despite the fact that settling velocities were generally much less than mean vertical convective velocities (i.e. crystals were usually carried with the convecting magma). In laboratory experiments, dense particles were approximately uniformly distributed throughout a convecting fluid of lower density. However, at the base of the convecting fluid, velocities decreased to zero, allowing settling of particles to the floor to occur. The total number of particles in suspension (N) fell exponentially with time (t) according to the relation (Martin and Nokes, 1988):

$$N = N_0 \exp\left(\frac{-v_t\, t}{h}\right) \quad (5.10),$$

where v_t was the terminal settling velocity, N_0 was the initial number of particles, and h was the depth of the fluid. A steady-state situation can be imagined where the flux of crystals being incorporated into the magma at the roof equals the flux of crystals settling at the floor. Crystal settling must now occur at the floor, and, following the same arguments as above, is a possible mechanism, but encounters problems with high viscosity magmas, or at high heat fluxes. Higher viscosity magmas will tend to entrain more crystals than they deposit, thus the overall crystal content in the magma body will gradually rise, increasing viscosity (fig. 5.2c), hence slowing convection. Thus Q_{mag} will slowly decrease with time, and the upper CBL will gradually thicken. This may occur, but the situation envisaged in model D is thought to be more likely.

In model D, crystals that form at the roof of the magma attach and thicken the CBL. The CBL will only remain a constant thickness if the layer is thinned from above at the same rate. This can occur if an overlying hydrothermal system infiltrates the CBL (e.g. Lister, 1974; Hardee, 1980; Carrigan, 1986); this process is considered in section 5.3. The heat flux from the magma (Q_{mag}) consists of both the latent heat of crystallisation, and the specific heat released in cooling from magmatic temperatures (T_m) to temperatures within the hydrothermal system (T_w). Assuming a constant thickness layer:

$$Q_{mag} = - u \rho (L_m + c_m (T_m - T_w)) \quad (5.11a),$$

where u is the infiltration velocity. Using the magma properties in table 5.2, this gives a

velocity of ~3.5 x 10^{-8} m s^{-1} (1.1 m a^{-1}) for $Q_{mag} = 10^2$ W m^{-2}, and ~3.5 x 10^{-6} m s^{-1} (110 m a^{-1}) for $Q_{mag} = 10^4$ W m^{-2}. These are approximately one third of those for simple latent heat release only. Convection of magma is relatively unimportant as the release of latent and specific heat at the roof will be much greater than any heat flux due to convection. Model D is thought to be the most likely mechanism for producing the observed fluxes at Poás and Ruapehu. The magma body involved could be smaller in area than the lake, which was suggested earlier as a minimum only as a guideline. Small intrusions crystallising and cooling at rapid rates would fit model D equally well, assuming the infiltration velocity can reach very high values, and new intrusions occur regularly. At high infiltration rates (when u is greater than a critical value u_{crit}), crystal nucleation and growth may not be sufficient to keep up with the rate of infiltration, and glass formation may occur. When a glass forms, no latent heat is released, thus equation (5.11a) will change to:

$$Q_{mag} = - u \rho c_m (T_m - T_w) \quad (\text{if } u > u_{crit}) \quad (5.11b)$$

This equation ignores the possibility that at values just above the critical velocity, some crystallisation may still be occurring; the effect is negligible, however. Brandeis and Jaupart (1986) quoted typical nucleation rates of ~0-7 x 10^6 m^{-3} s^{-1}, and typical growth rates of ~0-6 x 10^{-8} m s^{-1}. Maximum nucleation and growth rates occurred with an undercooling of ~30 °C. The upper value of the crystal growth rate perhaps defines the critical infiltration rate. This is only ~2 m a^{-1}, near the lower end of the range required to produce the observed heat flux. However, Worster et al. (1990) stated a growth law for diopside growing into undercooled melt (Kirkpatrick et al., 1974), that suggests crystallisation may be able to proceed at much faster rates. The implications of a limited crystallisation rate are discussed in section 5.3.4.

An infiltrating hydrothermal system is therefore the preferred model from a magmatic standpoint, in order to produce the heat fluxes observed at Poás and Ruapehu. The heat flux will now be considered from the point of view of the hydrothermal system.

5.3 The Magma/Country Rock Boundary: Heat Flux into the Hydrothermal System

Lister (1974) was the first person to consider the physics of water penetration into magma. He considered that high heat flux hydrothermal systems separated from magma by a stationary boundary layer either required CBLs that were too thin, or unrealistically large magma surface areas. Lister (1974, 1983) therefore formulated a model where hydrothermal fluid, penetrating crystallising and cooling magma, provided a concentrated heat source. Magmatic latent and specific heat could be released directly into the hydrothermal system. With this model, production of 10^2-10^3 MW can be generated by crystallising and cooling (by ~750 K) ~80-800 kg s^{-1} (~0.12-1.2 m^3 s^{-1}) of magma. The model of Lister (1974, 1983) is summarised in section 5.3.2, but first the parallel approach taken by Hardee (1980, 1982) will be stated. The two different approaches are combined to formulate a new model in section 5.3.3.

5.3.1 Modelling a cracking front - Hardee (1980, 1982)

The best documented natural example of an infiltrating cracking front is from Kilauea Iki lava lake, Hawaii (Hardee, 1980). The lava lake formed in 1959, and was ~750 m in diameter and ~120 m deep. The lake initially developed a crust which thickened at a rate proportional to the square root of time, as predicted by conductive cooling (Hardee, 1980). After about five years, however, the solidification rate stabilised at a value of ~2.1 m a^{-1}, with a constant CBL thickness of ~11.3 m (Hardee, 1980). The CBL then migrated downwards at constant velocity, and a two-phase hydrothermal convection zone (see section 5.4) developed above the CBL, with a temperature of 100 °C. Hardee (1980) developed a one-dimensional model of the solidification front, ignoring heat losses to the floor and the walls; this is reasonable since the lake was much wider than deep.

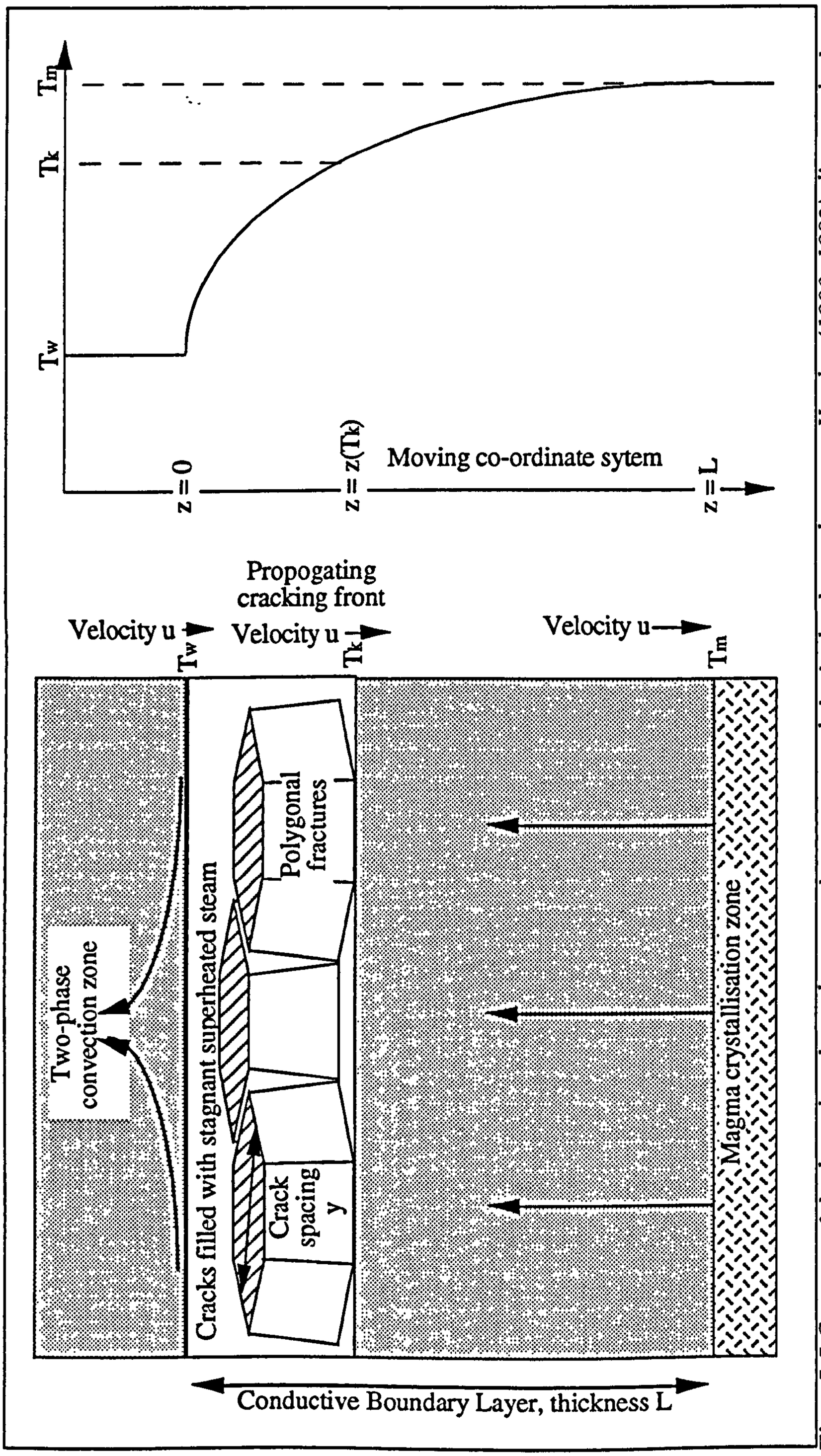

Fig. 5.5 *Cartoon of the boundary layer between the magma and the hydrothermal system. Hardee (1980, 1982) disregards the cracked region following from the theory of Lister (1974, 1983), however, it can only be considered part of the CBL if the superheated steam within the cracks remains stagnant. A moving co-ordinate system is used, with z = 0 at the top of the CBL. At the scale considered, the 2PZ can be assumed to be isothermal.*

In a stationary co-ordinate system, the one dimensional energy equation, in the absence of advected heat, is (Hardee, 1980):

$$\frac{\partial^2 T}{\partial x^2} = \frac{1}{\kappa}\frac{\partial T}{\partial t} \quad (5.12),$$

where x is distance, and t is time. Using a moving co-ordinate system (Schneider, 1957, and see fig. 5.5), and defining two new variables:

$$z = x - u\,t, \qquad t` = t$$

where z is the depth below the top of the CBL, which is moving at velocity u, and t` is time in the moving reference frame. Hence the following can be written:

$$\frac{\partial z}{\partial x} = 1, \qquad \frac{\partial z}{\partial t} = -u, \qquad \frac{\partial t`}{\partial x} = 0, \qquad \frac{\partial t`}{\partial t} = 1,$$

so that:

$$\frac{\partial T}{\partial x} = \frac{\partial T}{\partial z}\frac{\partial z}{\partial x} + \frac{\partial T}{\partial t`}\frac{\partial t`}{\partial x} = \frac{\partial T}{\partial z}$$

$$\frac{\partial^2 T}{\partial x^2} = \frac{\partial^2 T}{\partial z^2}$$

$$\frac{\partial T}{\partial t} = \frac{\partial T}{\partial z}\frac{\partial z}{\partial t} + \frac{\partial T}{\partial t`}\frac{\partial t`}{\partial t} = -u\frac{\partial T}{\partial z} + \frac{\partial T}{\partial t`} \quad (5.13)$$

In the quasi-steady-state of the moving co-ordinate system, $\partial T / \partial t` = 0$ (Schneider, 1957), thus equation (5.12) becomes:

$$\frac{\partial^2 T}{\partial z^2} = \frac{\beta}{L}\frac{\partial T}{\partial z} \quad (5.14)$$

where β is a dimensionless variable equal to $-u\,L / \kappa$, and L is the CBL thickness. Equation (5.14) has the general solution:

$$T(z) = A\frac{L}{\beta}\exp\left(\frac{\beta\, z}{L}\right) + B$$

where A and B are constants. Hardee (1980) solved this using the boundary conditions:

$$T = T_w \text{ at } z = 0$$

$$T = T_m \text{ at } z = L,$$

to give:

$$T(z) = T_w + \frac{(T_m - T_w)\,(\exp(\beta z/L) - 1)}{\exp(\beta) - 1} \qquad (5.15a)$$

and:

$$\frac{\partial T}{\partial z} = \frac{\beta}{L}\,\frac{(T_m - T_w)\exp(\beta z/L)}{\exp(\beta) - 1} \qquad (5.16)$$

Assuming that the heat flux into the base of the CBL is provided by only crystallising magma (specific heat will be released within the CBL), then (assuming $u < u_{crit}$):

$$-k\left(\frac{\partial T}{\partial z}\right)_{z=L} = -\rho\, L_m\, u \qquad (5.17)$$

which, substituting equation (5.16), $\beta = -u\,L / \kappa$, and $c_m = k / \rho\,\kappa$, gives:

$$\frac{(T_m - T_w)\ \exp(\beta)}{\exp(\beta) - 1} = -\frac{L_m}{c_m}$$

re-arranging to give exp (β) as the subject of the formula:

$$\exp(\beta) = \frac{1}{\left(1 + \frac{c_m}{L_m}(T_m - T_w)\right)} \qquad (5.18a)$$

taking the logarithm, and again substituting $\beta = -\,u\,L / \kappa$, gives (Hardee, 1980):

$$u = \left(\frac{\kappa}{L}\right) \ln\left(1 + \frac{c_m}{L_m}(T_m - T_w)\right) \qquad (5.19a)$$

In Kilauea Iki lava lake, $T_m \approx 1070$ °C, $T_w \approx 100$ °C, and $L \approx 11.3$ m. Using these values together with typical basaltic magma properties of $c_m \approx 1046$ J kg^{-1} °C^{-1}, $L_m \approx 4.18 \times 10^5$ J kg^{-1}, $\kappa \approx 5 \times 10^{-7}$ m^2 s^{-1}, yields $u \approx 5.4 \times 10^{-8}$ m s^{-1} (1.7 m a^{-1}). This is close to the value of 2.1 m a^{-1} observed, suggesting that the theory is broadly correct. Hardee (1982) also described the solidification of a lava lake at Heimaey, Iceland, over the period 1973-78. This lava lake cooled in a similar manner to Kilauea Iki. The equivalent observed values of L

and u were ~5 m and ~5 m a^{-1}, with a magma temperature of 1050 °C. Substituting these values of L and T_m into equation (5.19a), with the other values as before, yields $u \approx 4$ m a^{-1}, again showing good agreement with the observed infiltration rate. If the solidifying lava has a pre-existing phenocryst mass fraction (f), then equation (5.19a) can be more accurately written:

$$u = \left(\frac{\kappa}{L}\right) \ln\left(1 + \frac{c_m}{L_m\,(1 - f)}\,(T_m - T_w)\right) \quad (5.19b)$$

A near perfect fit with the theory occurs if f = 0.3 for Kilauea Iki, and f = 0.4 for Heimaey.

Heat transfer from the conductive boundary layer to the two-phase zone

Two-phase convective heat transfer in water-rich, permeable rocks overlying a magma body has been studied by numerous authors, including: White et al. (1971), Sondergeld and Turcotte (1977), Schubert and Straus (1977, 1979, 1980), Straus and Schubert (1977), Hardee (1982), and Ingebritsen and Sorey (1988). Hardee (1982) developed a one dimensional model involving down-flowing liquid and upflowing vapour. The model is stated fully in section 5.4. The fact that the model is one-dimensional again implies it is applicable to systems much wider than they are thick. He found that the maximum convective heat flux ($Q_{convmax}$) occurred for an optimum value of liquid volume fraction in the two-phase zone (see section 5.4), and was dependent on only the permeability (D, m^2), and the properties of the fluid:

$$Q_{convmax} = D\left(\frac{g\,L_w\,(\rho_l - \rho_v)}{[(\nu_v)^{0.5} + (\nu_l)^{0.5}]^2}\right) = D\,C_H \qquad (5.20),$$

where L_w is the latent heat of vaporisation of water, and ρ_l, ρ_v, ν_l, ν_v are the densities and kinematic viscosities of the liquid and vapour, respectively, evaluated for saturation pressure and temperature conditions at a certain depth. The expression containing the fluid properties (C_H) was evaluated for various temperatures by Hardee (1982), given in table 5.3. The value of C_H, and hence the heat flux, will be smaller if the liquid volume fraction in the 2PZ is not at its optimum value. Thus the permeability in equation (5.20) is the *minimum* possible to support such a heat flux.

Temperature / °C	Pressure / N m^{-2}	$C_H = \frac{g\ L_w\ (\rho_l - \rho_v)}{[(\nu_v)^{0.5} + (\nu_l)^{0.5}]^2}$ / W m^{-4}
100	1.01×10^5	8.38×10^{14}
150	4.76×10^5	2.46×10^{15}
200	15.6×10^5	4.98×10^{15}
250	39.8×10^5	7.71×10^{15}
300	85.9×10^5	9.01×10^{15}
350	165×10^5	5.36×10^{15}
374.15	221×10^5	0

Table 5.3 *Evaluation of term involving fluid properties (C_H) in equation (5.20), using properties of saturated water/steam, for various water temperatures (from Hardee, 1982).*

The heat flux supplied to the two-phase zone (2PZ) must equal the heat flux leaving the top of the CBL (equation (5.11a), with the addition of a pre-existing phenocryst mass fraction f); thus, assuming $u < u_{crit}$ (i.e. crystallisation is not inhibited) then (Hardee, 1980):

$$Q_{convmax} = -k\left(\frac{\delta T}{\delta z}\right)_{z=0} = -\,u\,\rho\,(L_m\,(1-f) + c_m\,(T_m - T_w)) \quad (5.21),$$

i.e. the latent and specific heat released by crystallising and cooling the magma to temperature T_w. The negative sign is because the heat flux is upwards whilst the infiltration velocity is downwards. Taking the heat flux magnitude, and substituting equation (5.20) into (5.21) gives the minimum permeability required to support such a heat flux (Hardee, 1980):

$$D_{min} = \left(\frac{\rho\ u}{C_H}\right)(L_m\,(1-f) + c_m\,(T_m - T_w)) \quad (5.22a).$$

The model of Hardee (1982) therefore suggests that if the 2PZ is operating at optimum efficiency (i.e. the maximum heat transfer is occurring for the permeability; see section 5.4), the infiltration velocity, and hence heat flux, will be directly proportional to permeability.

5.3.2 Modelling a cracking front - Lister (1974, 1983)

Lister's (1974, 1983) physical model for the penetration of water into hot rock developed a relation between cracking front propagation velocities, crack spacings and created permeabilities, for a given magma temperature, cracking temperature, and infiltrating water

temperature. He visualized the cracking front as group of polygonal columns advancing into the CBL (fig. 5.5). Lister (1983) suggested a convective boundary layer may exist in the region where the newly cracked rock is still cooling. However, if this region is so hot that only superheated steam can exist in the cracks, then for single-phase convection to occur, the Rayleigh number in the cracked zone of the CBL (Ra_{cz}) must exceed a critical value of 40, where (Hardee, 1982):

$$Ra_{cz} = \frac{\rho_s \, g \, \alpha_s \, \Delta T \, D \, H}{\kappa_r \, \mu_s} \qquad (5.23)$$

where subscript 's' refers to superheated steam properties, and 'r' to rock properties, and H is the thickness of the proposed convective boundary layer. The following analysis assumes that convection does not occur in this region; this assumption is checked (and found valid), at the end of the analysis.

Lister (1974, 1983) used the only available work on crack propogation velocities in geological media: that of Martin (1972). Martin (1972) related crack propagation velocities (u: m s^{-1}) in quartz to the tensional stress (σ_t: N m^{-2}), crack spacing (y: m) and the cracking temperature (T_k: K):

$$\sigma_t = 0.041 \, \phi \, y^{-0.5} \, \ln\left(3.16 \times 10^7 \, u - 14.6 + \frac{12900}{T_k}\right) \qquad (5.24),$$

where ϕ is a 'fudge-factor' to convert the equation from quartz to country rock, assumed equal to one for the purpose of modelling (Lister, 1983). The temperature difference ΔT_k, is that required to cause excess horizontal tension (i.e. fracturing) at the cracking boundary, and is related to the tensional stress (σ_t) and the creep stress (σ_c) by (Lister, 1974):

$$\Delta T_k = -\sigma_t \left(\frac{d\sigma_c}{dT}\right)^{-1} \qquad (5.25),$$

where the differential is evaluated at constant effective strain rate, thought by Lister to be reasonable over the small temperature range ΔT_k. This differential was found to be (Lister, 1974):

$$\frac{d\sigma_c}{dT} \approx \frac{-1.49 \times 10^6}{T_k^2} \qquad (5.26).$$

Substituting equations (5.26) and (5.24) into (5.25), and assuming u lies between 3×10^{-9} and 3×10^{-5} m s^{-1} (0.1-1000 m a^{-1}), and T_k lies between 373 and 1373 K (i.e. the entire range possible), ΔT_k approximates (~±25 %) to:

$$\Delta T_k \approx 0.1\ y^{-0.5} \qquad (5.27).$$

This temperature difference should approximately equal the radial temperature difference (ΔT_r, the temperature difference between the centre and edge of a column at the cracking front) associated with conductive cooling of the polygonal columns. Lister (1974) approximated the polygonal column to a cylinder, which, for the steady cooling case, gives:

$$\frac{\partial T}{\partial t} \pi r^2 = 2 \pi r \kappa \frac{\partial T}{\partial r} \quad ,$$

where r is the cylinder radius. The radial temperature difference for a cooling cylinder with diameter y (equivalent to the crack spacing in the polygonal case) will be given by:

$$\Delta T_r = - \int_{T(r=0)}^{T(r=y/2)} \partial T = - \frac{\partial T}{\partial t} \int_{r=0}^{r=y/2} \frac{r}{2 \kappa} \partial r = - \frac{\partial T}{\partial t} \frac{y^2}{16 \kappa}$$

Lister (1974) then used the solution for $\partial T/\partial t$ within a boundary moving at velocity u (Carslaw and Jaeger, 1959):

$$\frac{\partial T}{\partial t} = - \frac{u^2}{\kappa} (T_m - T_k) \quad (5.28a),$$

However, this is for the situation involving no latent heat release (i.e. it is correct if $u > u_{crit}$). The correct equation for the case where latent heat is being released can be found using equation (5.13), again with $\partial T / \partial t` = 0$, and substituting equation (5.16) with $\beta = -u L / \kappa$, gives:

$$\frac{\partial T}{\partial t} = \frac{u^2}{\kappa} \frac{(T_m - T_w) \exp (\beta z/L)}{\exp (\beta) - 1} \quad (5.28b),$$

This equation can be rationalized by eliminating the exponents. Rewriting equation (5.15a):

$$\exp (\beta z/L) - 1 = \frac{(T(z) - T_w) (\exp (\beta) - 1)}{(T_m - T_w)} \quad (5.15b).$$

Rewriting equation (5.18a):

$$\exp(\beta) = \frac{L_m}{L_m + c_m (T_m - T_w)} \qquad (5.18b),$$

and hence:

$$\exp(\beta) - 1 = \frac{- c_m (T_m - T_w)}{L_m + c_m (T_m - T_w)} \qquad (5.18c)$$

substituting this into equation (5.14b) gives:

$$\exp (\beta z/L) - 1 = \frac{- c_m (T(z) - T_w)}{L_m + c_m (T_m - T_w)} \qquad (5.15c)$$

and hence:

$$\exp (\beta z/L) = \frac{L_m + c_m (T_m - T(z))}{L_m + c_m (T_m - T_w)} \qquad (5.15d).$$

Substituting equations (5.15d) and (5.18c) into equation (5.28b) yields, at the cracking temperature, i.e. $T(z) = T_k$:

$$\frac{\partial T}{\partial t} = - \frac{u^2}{\kappa} \left(\frac{L_m + c_m (T_m - T_k)}{c_m} \right) \qquad (5.28c)$$

This is the correct equation for use within a moving cooling boundary layer with latent heat being supplied to its base. The same procedure taken by Lister (1974, 1983) will now be followed, using this value of $\partial T/\partial t$. Thus the radial temperature drop across a conductively cooled polygon, ΔT_r, is given approximately by:

$$\Delta T_r \approx \frac{u^2 y^2 (L_m + c_m (T_m - T_k))}{16 \kappa^2 c_m} \qquad (5.29).$$

Remembering that the radial temperature difference induced by cooling at the cracking front should equal the temperature drop required to produce fracturing, we can equate ΔT_k and ΔT_r (Lister, 1974), which gives the crack spacing (y) in terms of the infiltration velocity (u), the thermal diffusivity of the rocks (κ), the specific and latent heat capacity of the magma (c_m and L_m) the magma temperature (T_m) and the cracking temperature (T_k):

$$y = \left(\frac{1.6 c_m \kappa^2}{u^2 (L_m + c_m (T_m - T_k))} \right)^{2/5} \qquad (5.30).$$

Lister (1983) used an approximation that related the permeability to the crack spacing, cracking temperature and water temperature, given by the equation:

$$D \approx \left(\frac{\sqrt{2}}{12}\right) \alpha^3 \, y^2 \, (T_k - T_w)^3 \qquad (5.31).$$

Thus, substituting equation (5.30), the permeability created by the cracking process can be approximated by:

$$D = \left(\frac{\sqrt{2}}{12}\right) \alpha^3 \, (T_k - T_w)^3 \left(\frac{1.6 \, c_m \, \kappa^2}{u^2 \, (L_m + c_m \, (T_m - T_k))}\right)^{4/5} \qquad (5.32a).$$

This represents another expression relating cracking front advance velocity and permeability, the other by Hardee, given by equation (5.22a).

5.3.3 Combining the theories of Hardee and Lister.

Making the assumption that the cracked and uncracked zone between the magma and the 2PZ transfers heat only by conduction, and that the 2PZ operates at optimum efficiency for the created permeability (i.e. $D_{min} = D$; see section 5.4), then the theories of Lister (1974, 1983) and Hardee (1980, 1982) are both applicable to the CBL. This suggests that equations (5.22a) and (5.32a), relating u and D are both valid, and implies that the cracking temperature must be a function of infiltration velocity. Thus, equating equations (5.22a) and (5.32a) eventually yields the relation between T_k and u:

Rewriting (5.32a):

$$D = a \, f(T_k) \, u^{-8/5} \qquad (5.32b),$$

where:

$$a = \left(\frac{\sqrt{2}}{12}\right) \alpha^3 \left(1.6 \, c_m \, \kappa^2\right)^{4/5}$$

$$\text{and} \qquad f(T_k) = \frac{(T_k - T_w)^3}{(L_m + c_m \, (T_m - T_k))^{4/5}}$$

Also rewriting (5.22a), making $D_{min} = D$:

$$D = b\,u \qquad (5.22b),$$

where:

$$b = \frac{\rho}{C_H}\left(L_m\,(1 - f) + c_m\,(T_m - T_w)\right)$$

Equating (5.22b) and (5.32b) leads to:

$$u = \left(\frac{a\,f(T_k)}{b}\right)^{5/13} \qquad (5.33),$$

Equation (5.33) is shown graphically in fig. 5.6, for four cases. Curves B represent a basaltic (ρ = 2700 kg m^{-3}, k = 1.57 W m^{-1} K^{-1}, T_m = 1070 °C) magma body overlain by a low temperature (T_w = 100 °C) 2PZ (e.g. Kilauea Iki lava lake (Hardee, 1980)). This curve suggests that for the solidification rates observed in Kilauea Iki lava lake (u = 2.1 m a^{-1}), the cracking temperature was only marginally above 100 °C, much lower than the range suggested by Lister (1983) (427 - 627 °C). This suggests that any fractures that formed at temperatures above ~100 °C were rapidly closed by creep.

There is another field example of cracking front infiltration, which showed much faster infiltration rates. The 1973 basaltic lava flow from Heimaey volcano, Iceland was cooled with water in an attempt to slow it down (Björnsson et al., 1982). An area of ~7000 m^2 wassprayed with ~100 kg s^{-1} of water. After two weeks, the flow was excavated and revealed that magma was ~12 m below the surface, implying an average infiltration rate of ~330 m a^{-1}. Referring to fig. 5.6, this infiltration rate is close to the upper limit suggested by the theory (~310 m a^{-1} for f=0; 330 m a^{-1} for f=0.16; 365 m a^{-1} for f=0.35), and implies a cracking temperature near magmatic temperature (1070 °C), again, outside the range proposed by Lister (1983). The theory suggests that the rapid advance velocities inhibit rock creep as an effective annealing process at very high temperatures, even up to magmatic.

Also shown on fig. 5.6 is curve A, representing an andesitic magma (ρ = 2450 kg m^{-3}, k = 2.3 W m^{-1} K^{-1}, T_m = 1000 °C) overlain by 2PZ at 250 °C, thought perhaps to be more representative of the Poás and Ruapehu systems. The conductivity value used has little effect

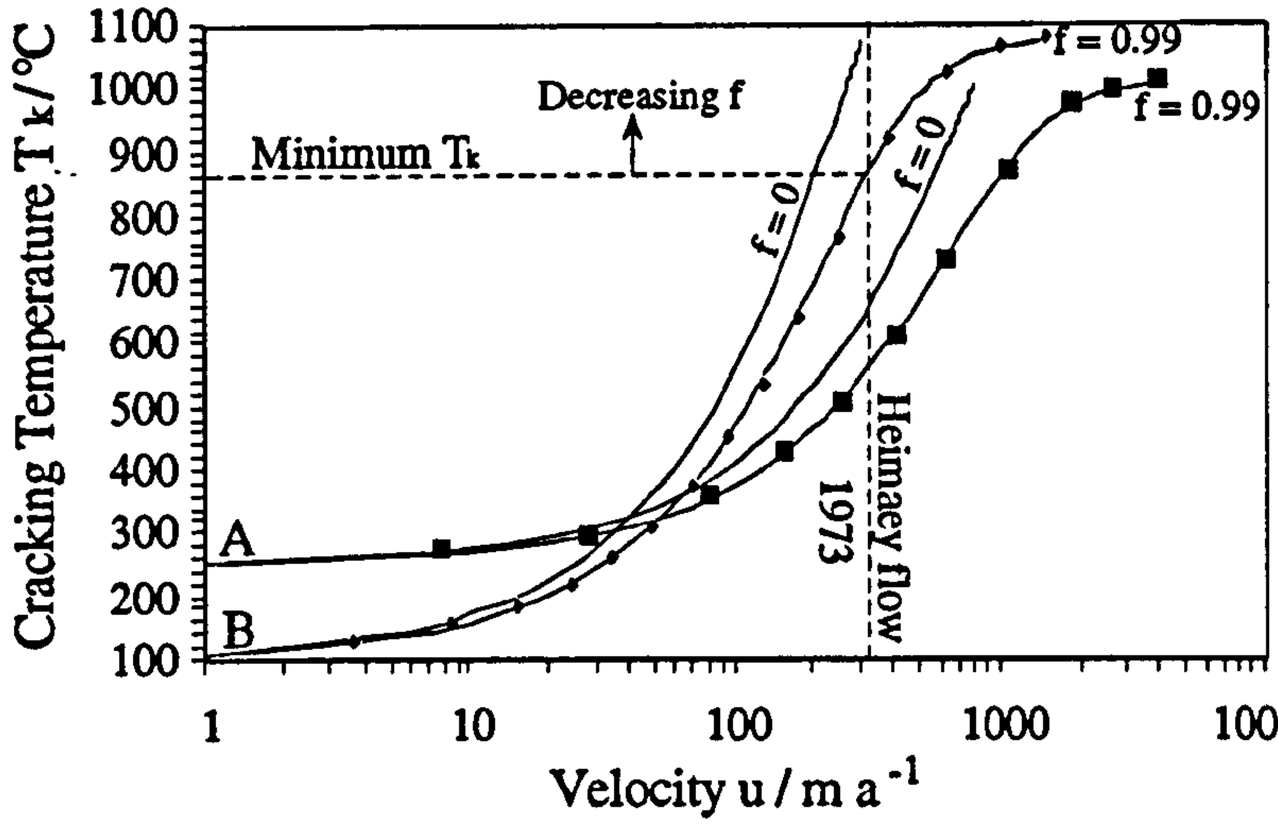

Fig. 5.6 *Calculated cracking temperature against infiltration velocity, from equation (5.33), for two different situations, A, andesite magma overlain by a 250 °C hydrothermal system, and B, basaltic magma at the surface, being cooled by a hydrothermal system at 100 °C. Two values of f (0 and 0.99), the pre-existing phenocryst mass fraction, are shown for each situation, the upper value represents the situation where essentially no latent heat is released, i.e. glass formation. This curve is probably more applicable at high infiltration velocities, and there is probably a gradational swap-over between the two curves over a velocity range. The dotted line shows the infiltration velocity (~330 m a^{-1}) observed when a lava flow from Heimaey, Iceland, was sprayed with water, and indicates a minimum cracking temperature of ~860 °C. It is notable that the theory with f = 0 predicts a maximum infiltration velocity of ~310 m a^{-1}, very close to the observed value. The symbols are calculated using equation (5.35), i.e. for $u > u_{crit}$. They are the same as the f ≈ 1 outputs.*

on the results; the critical parameter is the 2PZ temperature, and resulting value of C_H assumed. Non-optimum conditions in the 2PZ will imply a lower value of C_H (see section 5.4), giving a higher value for the constant b in equation (5.22b), and hence a lower value of u for a given T_k in equation (5.33). This suggests even higher cracking temperatures for a given infiltration velocity, when the 2PZ is not working at optimum conditions.

5.3.4 Confirming the original assumptions

The combination of the work of Lister and Hardee assumed that the newly cracked region, containing superheated hydrothermal steam, did not convect. We can now check if the Rayleigh number given by equation (5.23) exceeded its critical value. Taking the logarithm of equation (5.15d), and substituting $\beta = - u L / \kappa$, gives, at $T(z) = T_k$, the thickness of the cracked region:

$$z(T_k) = \left(\frac{\kappa}{u}\right) \ln \left(\frac{L_m + c_m\,(T_m - T_w)}{L_m + c_m\,(T_m - T_k)}\right) \qquad (5.34)$$

For the purpose of evaluating convection in the CBL, this thickness corresponds to H in equation (5.23). The variation of CBL thickness, L, and $z(T_k)$ with infiltration velocity are shown in figs. 5.7 and 5.8, for the cases A and B considered above. The cracked region of the CBL is typically only ~10 cm in thickness over the range of velocities, and it only constitutes a significant portion of the CBL at very high velocities (> 100 m a^{-1}), and hence high cracking temperatures.

The Rayleigh number for the cracked region (Ra_{cz}) can now be evaluated using equation (5.23), with $\Delta T = (T_k - T_w)$, $H = z(T_k)$, D as in equation (5.22), and calculating the coefficient of thermal expansion (α_s), density (ρ_s) and dynamic viscosity (μ_s) of superheated steam at the average temperature of the cracked region $(T_k + T_w)/2$, using polynomials fitted to steam table data (ESDU, 1968, 1978). The Rayleigh number in the cracked region for cases A and B is given in fig. 5.9, assuming a pressure of 10^5 N m^{-2} for B, and 10^7 N m^{-2} for A. Although Ra_{cz} rises with T_k in both cases, the Rayleigh number does *not* exceed the critical value of 40, suggesting that convection of superheated steam does not occur in the cracked region, confirming the original assumption, and validating the amalgamation of the two theories.

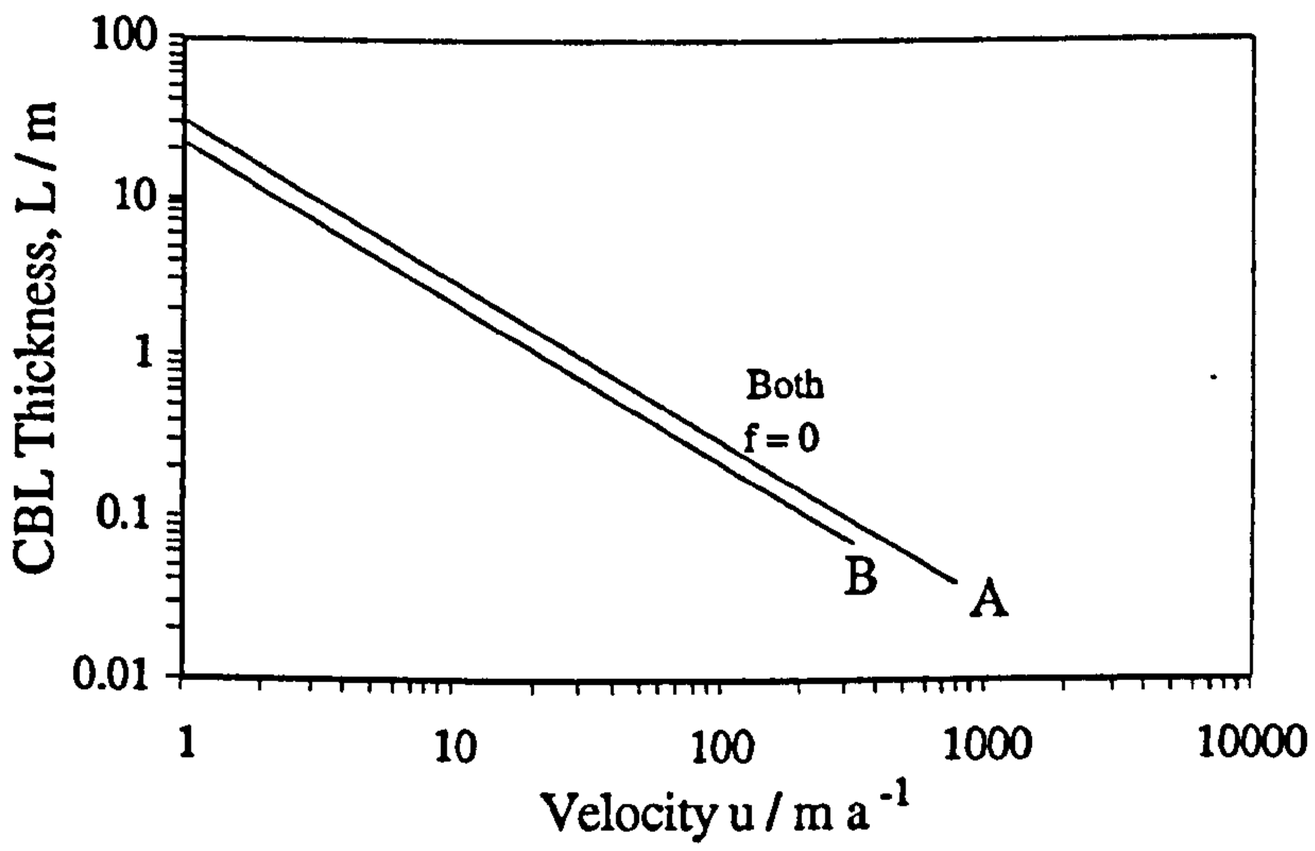

Fig. 5.7 *Thickness of the conductive boundary layer against infiltration velocity, from equation (5.18), for the two situations A and B, as described in fig. 5.6. Only the solutions for f = 0 are given; at f = 1, the thickness cannot be calculated, because the model sees no lower boundary.*

One other approximation of the theory is the assumption that $u < u_{crit}$, implying that equation (5.11a) should be used rather than (5.11b). If the infiltration velocity exceeds thismaximum value, then essentially no latent heat is released into the base of the CBL, and Lister's original equation (5.28a) should be used rather than (5.28c). Thus equation (5.32a) should be rewritten as:

$$D = c\, f_2(T_k)\, u^{-8/5} \qquad (5.32c)$$

where:

$$c = \left(\frac{\sqrt{2}}{12}\right)\alpha^3 \left(1.6\, \kappa^2\right)^{4/5}$$

and $$f_2(T_k) = \frac{(T_k - T_w)^3}{(T_m - T_k)^{4/5}}$$

Equation (5.22a) should be rewritten as:

$$D = d\, u \qquad (5.22c),$$

where:

$$d = \frac{\rho\, c_m\, (T_m - T_w)}{C_H}.$$

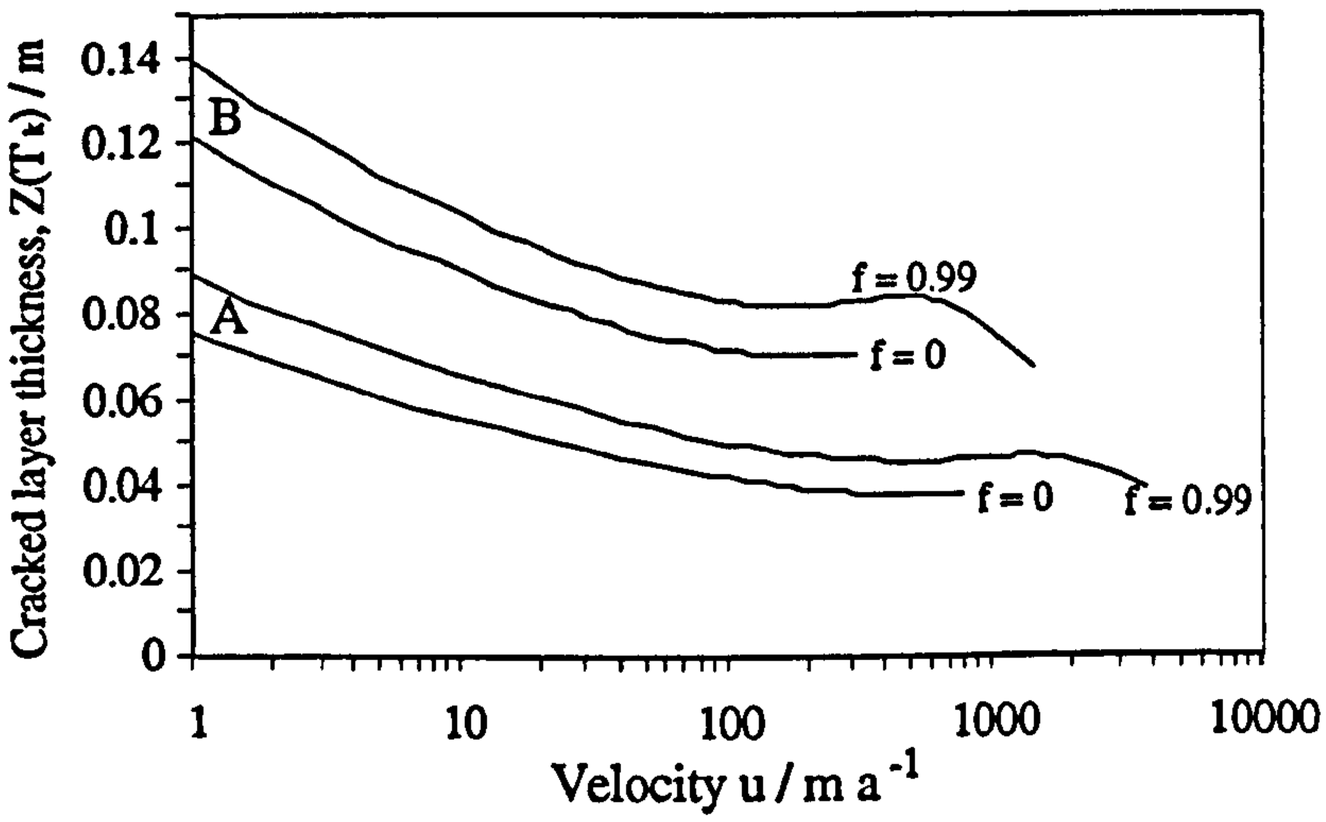

Fig. 5.8 *Thickness of the upper, cracked portion of the CBL, $z(T_k)$, given by equation (5.34). A and B, and the values of f, as in fig. 5.6.*

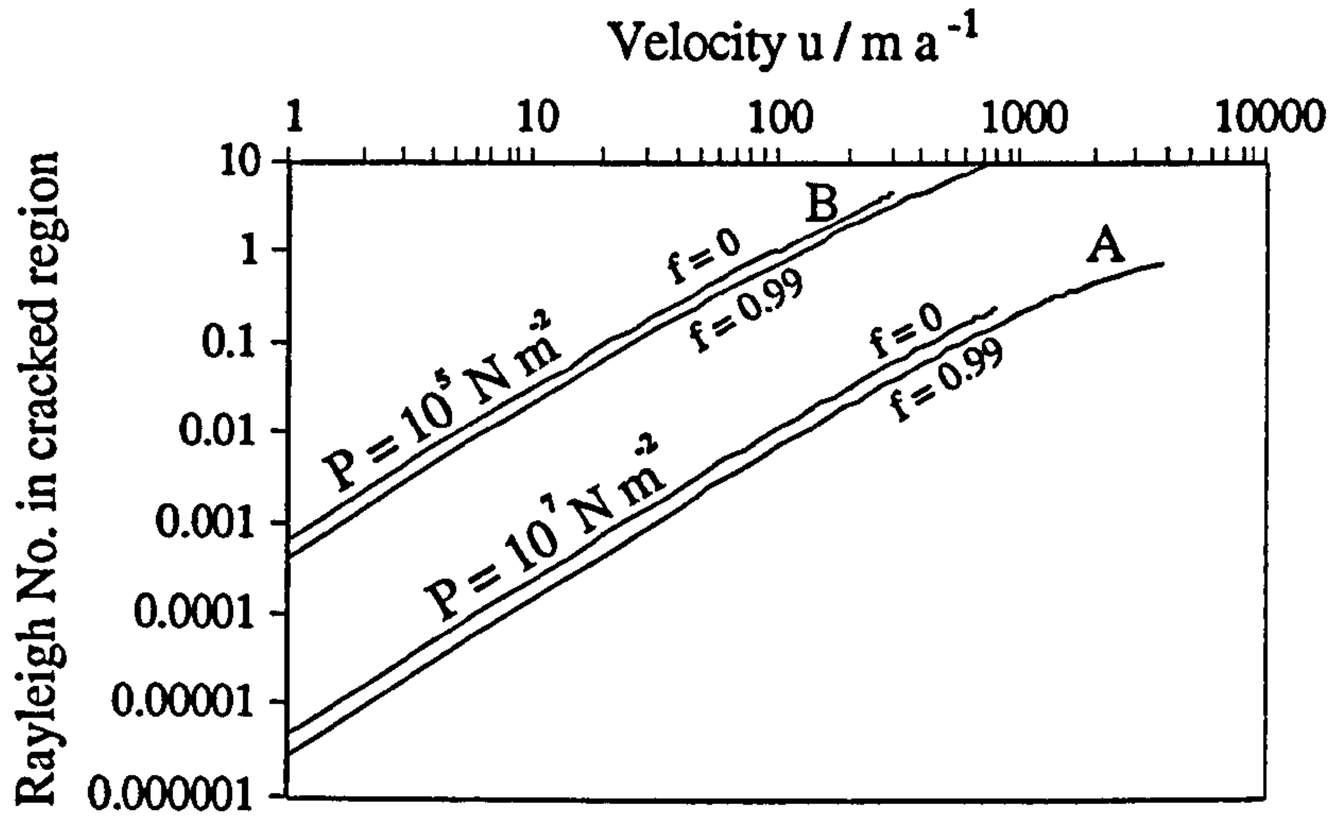

Fig. 5.9 *Calculated Rayleigh numbers within the cracked region of the CBL, for the same situations as in fig. 5.6. The critical value of 40 is never reached, thus convection does not occur.*

Equating equations (5.22c) and (5.32c) leads to:

$$u = \left(\frac{c\, f_2(T_k)}{d}\right)^{5/13} \qquad (5.35),$$

Plotting the results of equation (5.35) on fig. 5.6 shows that limiting the crystallisation rate is equivalent to using a pre-existing phenocryst fraction (f) of near one in equation (5.33). This is because glass formation releases no latent heat, the same as f = 1. The divergence of the f = 0 and f ≈ 1 situations is greatest at temperatures approaching magmatic. The infiltration velocity is limited in the crytallising case, but unlimited in the glass-forming case, where the cracking temperature asymptotically approaches the magmatic temperature at high infiltration velocities (fig. 5.6). The CBL thickness, L, is unspecified at $L_m = 0$, or f = 1 (e.g. see equation (5.18)), essentially because the model 'sees' no specific lower bound to the CBL. The cracked region thickness, $z(T_k)$, however, can still be calculated, by putting $L_m = 0$ into equation (5.34), yielding:

$$z(T_k) = \left(\frac{\kappa}{u}\right) \ln\left(\frac{T_m - T_w}{T_m - T_k}\right) \qquad (5.36).$$

The effect of this equation is equivalent to using equation (5.34) with f ≈ 1, as shown in fig. 5.8, for the two cases A and B. Values of Ra_{cz} are not significantly affected (fig. 5.9).

5.3.5 Summary

The heat flux into the hydrothermal system from the magma has been modelled as an infiltrating front, that propogates into the magma. The parallel theories of Lister (1974, 1983) and Hardee (1980, 1982) have been combined to produce a new model of the behaviour of the conductive boundary layer between the magmatic and hydrothermal systems. The temperature distribution within the CBL has been modelled as a downwards migrating conducting layer of constant thickness, being supplied by latent heat of crystallisation at its base, and with internal release of specific heat, as the layer cools (Hardee, 1980). The advective heat flux through this layer has been balanced with a convective heat flux in the overlying two-phase hydrothermal zone (Hardee, 1982). Heat flux within the 2PZ is directly proportional to permeability, thus a relationship between the infiltration velocity and permeability can be found (equation (5.22)).

Lister's (1974, 1983) theory uses the fact that cooling rock will contract, thus within the cooling CBL, fractures will develop. The temperature difference required to induce contractional fracturing should be equal to the radial temperature difference caused by conductive cooling of a polygon at the cracking front. The infiltration velocity is related to the crack spacing and the cracking temperature. Permeability is a function of crack spacing, thus a relationship between infiltration velocity and the created permeability can be found (equation (5.32)).

Combining the two equations relating u and D produces a relationship between u and the cracking temperature, T_k. The relationship depends somewhat upon the pre-existing phenocryst content (f) of the magma, and whether the crystallisation rate can keep up with the infiltration. If crystallisation is inhibited, glass formation will occur, with no release of latent heat. This is equivalent to assuming a value of f = 1. If crystallisation is allowed to proceed, the infiltration velocity will be limited - calculated values are ~300 m a^{-1} for a basalt at the surface, and ~800 m a^{-1} for andesite overlain by a 250 °C 2PZ (fig. 5.6). At these values of u, $T_k \approx T_m$, the magma temperature. The new theory predicts T_k can take any value between T_m and T_w, the overlying 2PZ temperature, whereas Lister (1983)

suggested that T_k fell in the range 427-627 °C.

5.4. Heat Flux within the Hydrothermal System

Hydrothermal systems redistribute energy and mass in response to circulating H_2O fluids (Norton, 1984). Any thermal perturbation in fluid-rich, permeable rocks will tend to initiate hydrothermal activity. White et al. (1971) developed a generalised model of a typical hydrothermal system, based upon 'The Geysers' (California, USA) and Larderello (Italy) geothermal fields. This model involved a liquid-rich zone at shallow depth, where pressures increased with depth along a hydrostatic gradient, and temperatures followed the Clapeyron (boiling point for pressure) curve. This liquid-rich layer was ~400 m thick at The Geysers, and transferred heat by both conduction and convection. Below this region, a vapour-dominated two-phase reservoir existed, typically a few kilometres thick, where heat transfer was due to upwards flow of vapour, and downwards flow of liquid. In this reservoir, pressures increased more slowly than in the upper layer, because of the lower density, vapour-rich fluid, and temperatures remained on the Clapeyron curve. Beneath this zone, White et al. (1971) postulated a convecting brine layer, which received heat by conduction from a magmatic source. This remains the accepted view of many systems. However, as already pointed out in sections 5.2 and 5.3, an infiltrating cracking front is much more likely than a stationary conductive magma boundary in a high heat flux system. This also requires a very thin vapour layer within the CBL, and almost certainly a 2PZ directly above this, if pressures are below the critical point for the hydrothermal fluid.

The heat flux through a hydrothermal system, operating in a steady-state, will be the same at each depth, thus the maximum heat flux possible for the system will be defined by the layer with the lowest heat transfer capability. Convecting, single phase layers, of either liquid or vapour, have much lower heat transfer capabilities than 2PZs. As such, in a high heat flux system, single phase layers cannot be extensive in thickness. The physical nature of 2PZs will now be considered in detail.

5.4.1 The two-phase zone

Lowell (1991) stated the governing equations of two-phase flow of a saline fluid in a porous

medium. For a one-dimensional system, there are 14 equations with 14 unknowns; however, the complexities of inter-relationships between variables are poorly known, making the solution of such a system 'beyond our present capabilities' (Lowell, 1991). Bearing this in mind, the relatively simplistic, one-dimensional model of a 2PZ containing pure water, with no net through-flow, and a constant permeability, derived by Hardee (1982) will briefly be restated in this section, in order to get some idea of the possible structure of a 2PZ.

At a given level in a 2PZ, downflowing liquid (volume fraction γ, velocity U_l) will co-exist with an upflowing vapour (volume fraction $(1 - \gamma)$, velocity U_v). Assuming a steady-state, closed system, the mass balance can be written:

$$\rho_l U_l \gamma = \rho_v U_v (1 - \gamma) \qquad (5.37).$$

The resulting heat flux (Q_{conv}) can also be written:

$$Q_{conv} = \rho_v U_v (1 - \gamma) h_v - \rho_l U_l \gamma h_l \qquad (5.38),$$

where h is enthalpy. Substituting equation (5.37) into (5.38) leads to:

$$Q_{conv} = \rho_l U_l \gamma L_w \qquad (5.39),$$

where the latent heat, $L_w = h_v - h_l$. Also writing the Darcy equations for fluid flow:

$$U_l = \frac{D}{\rho_l \nu_l}\left(g \rho_l - \frac{d P}{dz}\right) \qquad (5.40),$$

$$\text{and} \qquad U_v = \frac{D}{\rho_v \nu_v}\left(\frac{dP}{dz} - g \rho_v\right) \qquad (5.41),$$

where D is the 2PZ permeability, and ν_v and ν_l are the kinematic viscosities of vapour and liquid respectively. Elimination of the pressure gradient between these two equations, followed by the substitution of U_v from equation (5.37) gives:

$$U_l = \frac{D\left(1 - \frac{\rho_v}{\rho_l}\right) g}{\nu_l + \left(\frac{\gamma}{1 - \gamma}\right)\nu_v} \qquad (5.42).$$

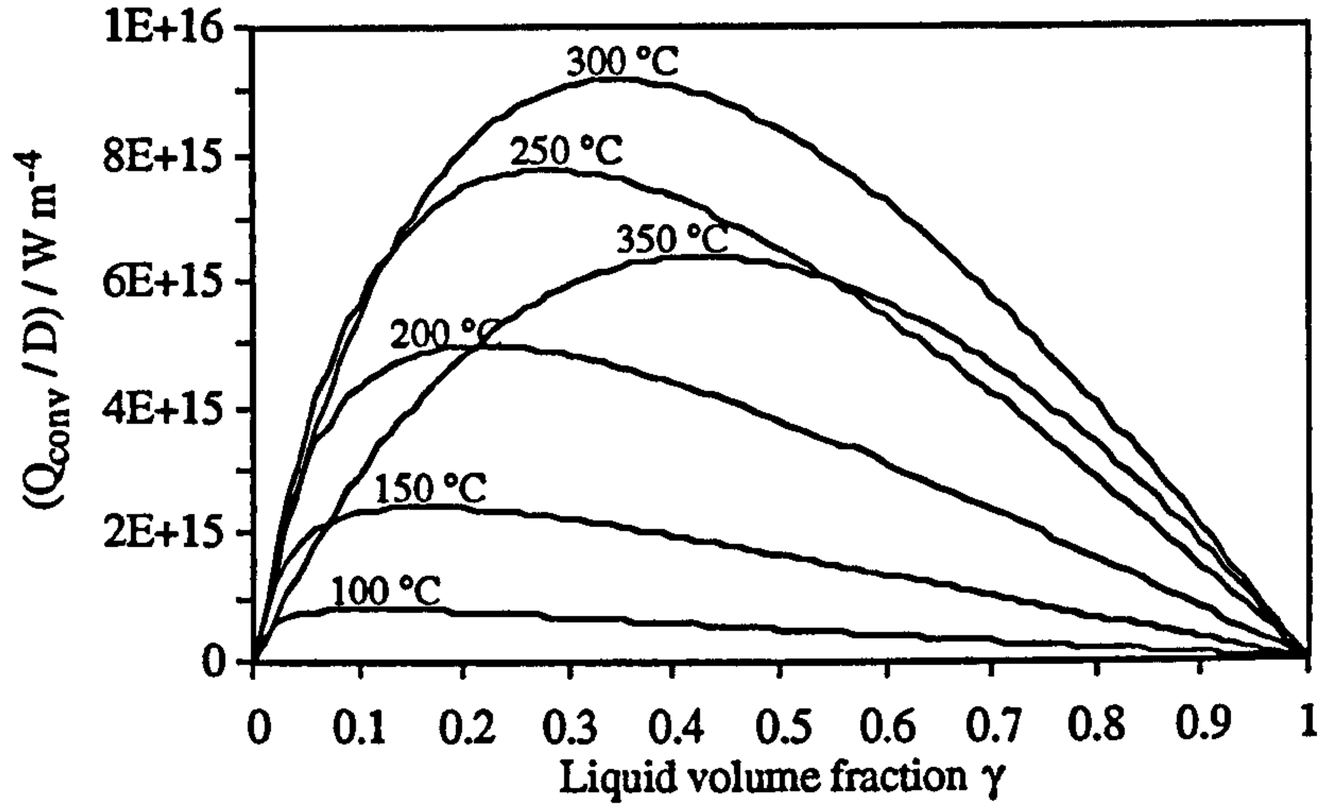

Fig. 5.10 *Variation of (Q_{conv} / D) with liquid volume fraction (γ), for six fluid temperatures (100 - 350 °C).*

Substituting this into equation (5.39) to eliminate U_l, yields the general equation for the heat flux:

$$Q_{conv} = D\left(\frac{\gamma\,(1-\gamma)\,g\,L_w\,(\rho_l - \rho_v)}{(1-\gamma)\,\nu_l + \gamma\,\nu_v}\right) \qquad (5.43).$$

For a fixed value of D, Q_{conv} will vary with γ. The maximum value of Q_{conv} ($Q_{convmax}$), stated by equation (5.20), can be found by differentiating equation (5.43) with respect to γ, and finding the value of γ when $\partial Q_{conv}/\partial\gamma = 0$. This was found by Hardee (1982) to be:

$$\gamma = \gamma_{opt} = \frac{1}{1 + \left(\frac{\nu_v}{\nu_l}\right)^{1/2}}$$

Substitution of this optimum value of γ into equation (5.43) yields the maximum heat flux, given by equation (5.20). The optimum value of γ represents the liquid volume fraction that produces the maximum heat transfer for a given permeability. The variation of (Q_{conv} / D) with γ is shown in fig. 5.10, for six different 2PZ temperatures. The peaks of these curves occur at $\gamma = \gamma_{opt}$, and represent the values of C_H given in Table 5.3. Maximum heat transfer occurs at ~280 °C with $\gamma \approx 0.3$.

As already noted, for a steady-state 2PZ, the vertical heat transfer at each depth must be constant. Thus, assuming the permeability and areal extent of the zone also do not vary with depth, (Q_{conv} / D) will be constant with depth. Within a two-phase zone, vapour and liquid

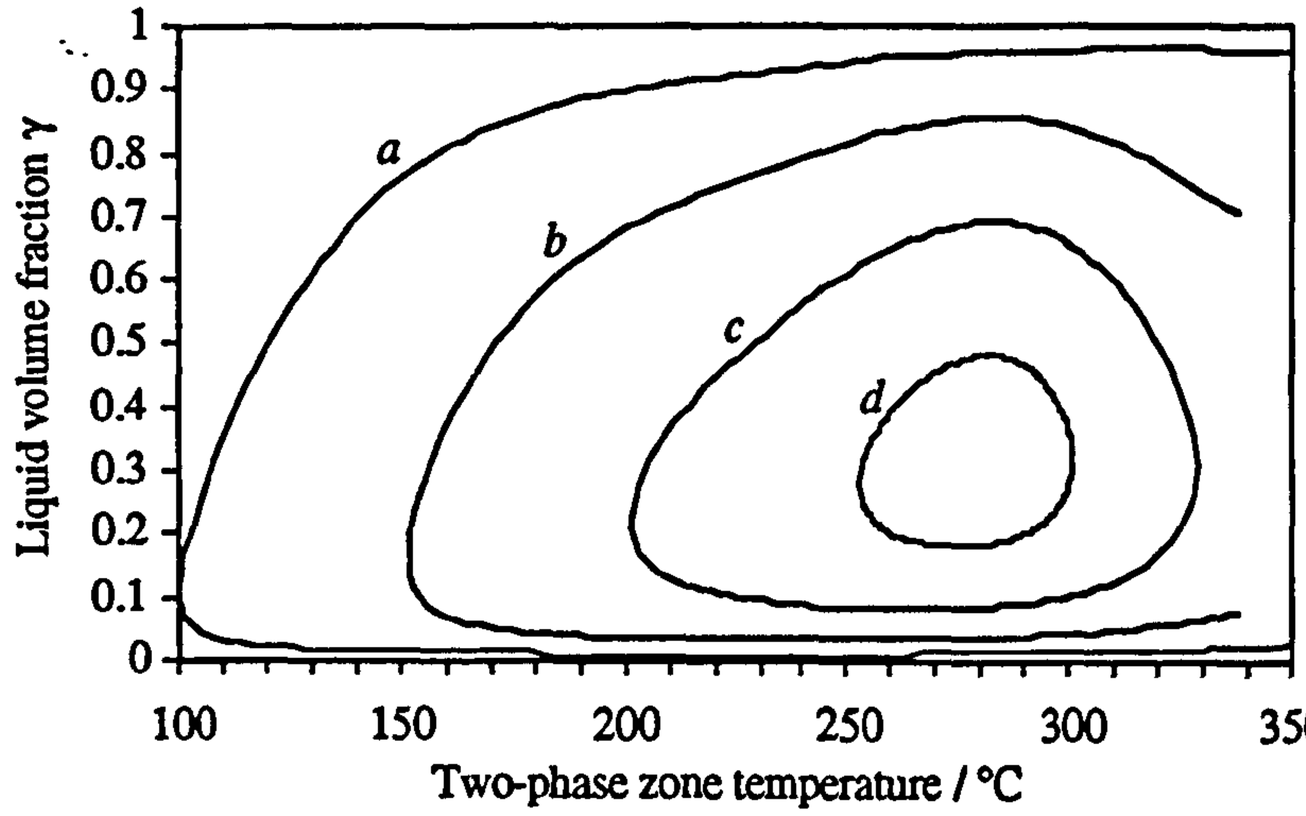

Fig. 5.11 *Solutions for γ, from equation (5.45), with (a) (Q_{conv} / D) = 8.38 x 10^{14} W m^{-2}; (b) (Q_{conv} / D) = 2.5 x 10^{15} W m^{-2}; (c) (Q_{conv} / D) = 5 x 10^{15} W m^{-2}; (d) (Q_{conv} / D) = 7.5 x 10^{15} W m^{-2}.*

will be present at temperatures on the Clapeyron curve, i.e. as pressure reduces towards the top of the zone, temperatures must also fall. Fig. 5.10 shows that for a constant value of (Q_{conv} / D) there is a relation between 2PZ temperature and γ, with two possible values of γ within a range of temperatures. Outside this temperature range, the (Q_{conv} / D) value cannot be reached. The possible range of γ and T for a given value of (Q_{conv} / D) can be found by re-arranging equation (5.43) to give:

$$a\gamma^2 + b\gamma + c = 0 \qquad (5.44)$$

where:

$$a = g L_w (\rho_v - \rho_l),$$

$$b = g L_w (\rho_l - \rho_v) + \frac{Q_{conv}}{D} (v_l - v_v),$$

$$\text{and} \quad c = -\frac{Q_{conv}}{D} v_l.$$

Equation (5.44) is a quadratic, with two roots given by:

$$\gamma = \frac{-b \pm \sqrt{b^2 - 4ac}}{2a} \qquad (5.45)$$

Fitting polynomials to the variation of ρ_l, ρ_v, ν_l, ν_l and L_w with saturation temperature and pressure (i.e. on the Clapeyron curve), yields values of γ against T, for a given value of (Q_{conv} / D). Four examples are given in fig. 5.11, for $(Q_{conv} / D) = 8.38 \times 10^{14}$, 2.5×10^{15}, 5×10^{15}, and 7.5×10^{15} W m^{-4} (c.f. values of C_H in table 5.3). Temperatures are only extended up to ~350 °C, because fitting of polynomials for the water/steam properties near the critical temperature encountered large errors. Hardee (1982) only considered the vapour-rich root of equation (5.44).

As can be seen from fig. 5.11, the liquid volume fraction varies considerably with temperature (and hence depth). Hardee (1982) noted that for $(Q_{conv} / D) = 8.38 \times 10^{14}$ W m^{-4}, the vapour-rich root reached a minimum value at a temperature of ~250 °C. He suggested that γ could not increase with depth, because this would require a source of liquid, not compatible with the one-dimensional model. However, I disagree with this assertion. The liquid volume fraction profile represents a steady-state, and the mass flows up and down at each level are equal (equation 5.37); thus an increase in γ with depth does not require an external source, just as a decrease in γ with depth did not require an external sink. Any change in γ will simply be accounted for by an adjustment in the velocities (U_l, and U_v) so as to conserve mass. The only requirement is that the steady-state γ profile can initially be attained from a transient state. I assume this is a possibility.

Steady-state temperature and pressure distributions within the 2PZ with depth, for a given value of (Q_{conv} / D), can also be found for each root of γ. Pressure gradients can be calculated by taking equations (5.40) and (5.42), which combine to give the pressure gradient:

$$\frac{dP}{dz} = g\left(\frac{\rho_l \nu_v \gamma + \rho_v \nu_l (1 - \gamma)}{\nu_v \gamma + \nu_l (1 - \gamma)}\right) = f(T) \quad (5.46),$$

which is just a function of the fluid properties, and can be evaluated for a given temperature, using polynomials, as above. Making the approximation that f(T) remains constant over a small change in temperature (ΔT) and pressure (ΔP), then the pressure and temperature profile with depth (z) can be found iteratively using the procedure:

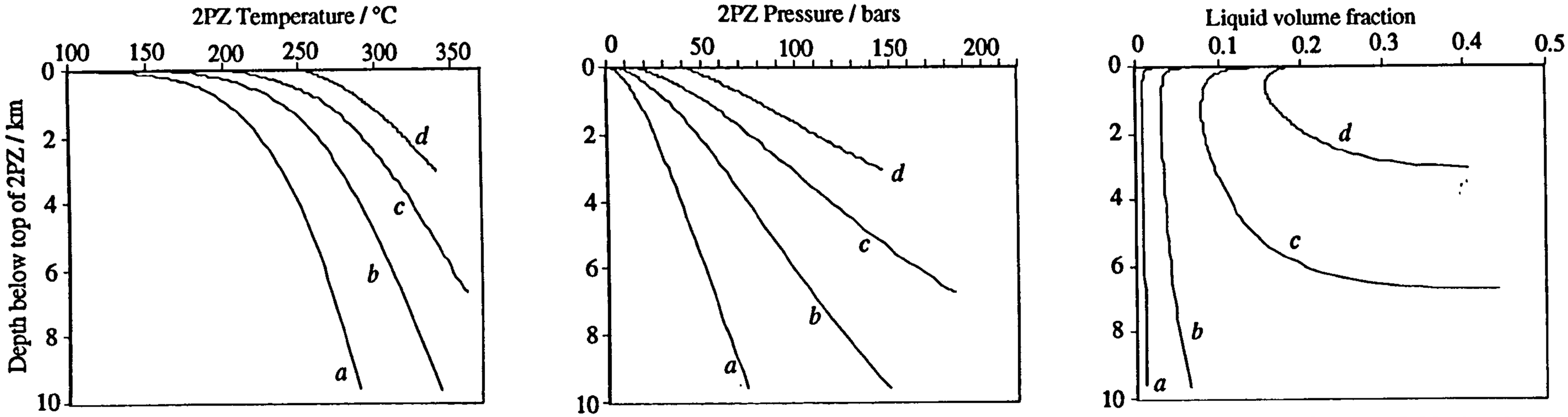

Fig. 5.12 *2PZ temperature, pressure and liquid volume fraction profiles for the four values for (Q_{conv}/D) used in fig. 5.11, for the vapour-rich root of χ*

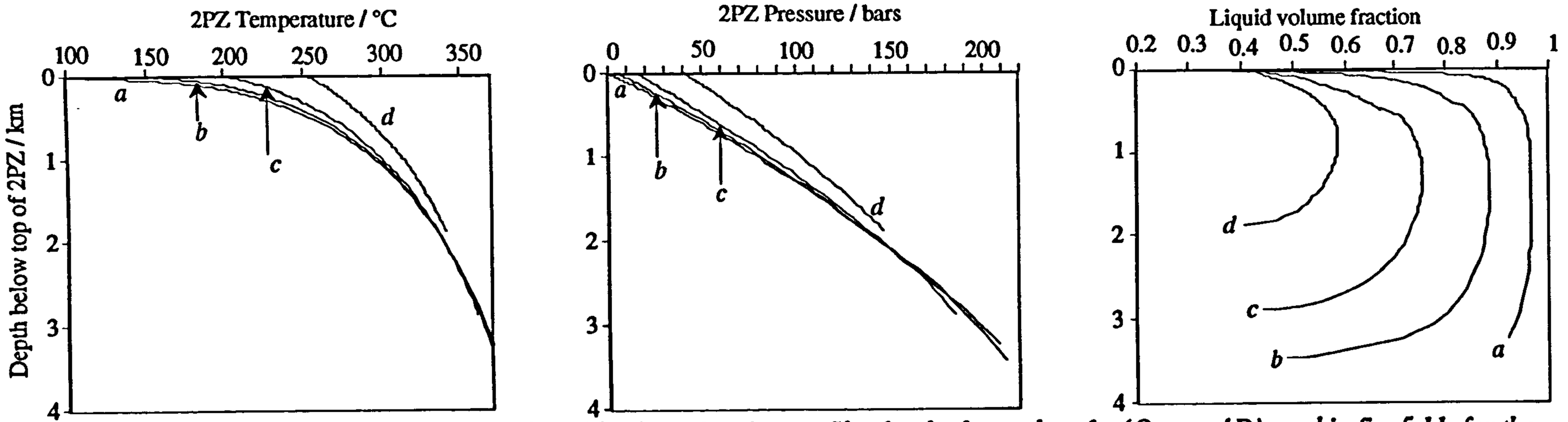

Fig. 5.13 *2PZ temperature, pressure and liquid volume fraction profiles for the four values for (Q_{conv}/D) used in fig. 5.11, for the liquid-rich root of χ*

$$z_{n+1} = z_n + \Delta z_n \qquad (5.47),$$

where $$\Delta z_n = \frac{\Delta P_n}{f(T_n)},$$

where $$\Delta P_n = P_{n+1} - P_n,$$

where $$P_n = P_{sat}(T_n),$$

where $$T_n = T(z_n),$$

and $$T_{n+1} = T_n + \Delta T,$$

where the iteration to the temperature is ΔT, over n steps. T_1 is the temperature at the top of the 2PZ, which will have a minimum possible value for a given (Q_{conv} / D), e.g. see fig. 5.11. Calculated temperature, pressure, and liquid volume fraction against depth profiles, for four values of (Q_{conv} / D), are shown in fig. 5.12 (for the vapour-rich root) and fig. 5.13 (for the liquid-rich root).

Thus for a given value of (Q_{conv} / D), two possible temperature and pressure distributions for the 2PZ can be defined. Fig. 5.11 defines the maximum and minimum temperatures (and hence pressures), and figs. 5.12 and 5.13 the maximum vertical extent of the zone. Pressure gradients within the vapour-rich zone are close to vapourstatic, whereas those in the liquid-rich zone are nearer hydrostatic. Pressure gradients within the hydrothermal system have important implications for any gases escaping from the magma (see chapter 6). The upper and lower boundaries of the 2PZ can occur at any point along the curves in figs. 5.12 and 5.13. As discussed in section 5.3.1, the lower boundary in a region of high heat flow will almost certainly be the very thin superheated vapour zone, which forms the upper part of the CBL above a magma body, providing that pressures are below the critical point for the hydrothermal fluid (221.2 bars for pure water, increasing with salt content).

5.4.2 The upper boundary of the two-phase zone

The 2PZ can be present up to the surface, in which case the upper temperature must be 100 °C (assuming 1 bar atmospheric pressure) (e.g. Kilauea Iki and Heimaey lava lakes, Hardee (1982)). This limits (Q_{conv} / D) to 8.38×10^{14} W m^{-4} (Table 5.3; fig. 5.10). Alternatively, the 2PZ may be overlain by liquid layer or a vapour layer.

For a system open at the surface, a vapour zone is not a steady-state possibility. Vapour

rising will adiabatically decompress and cool, and for the saturation temperatures and pressures at the top of the 2PZ, the vapour will always condense before it reaches atmospheric pressure. The liquid will fall downwards, thus the vapour zone will actually degenerate into an upwards extension of the 2PZ. This point has important implications for any surface fumaroles at temperatures greater than boiling point for atmospheric pressure: they must either (i) be at higher than atmospheric pressure; (ii) represent output from a non-steady-state hydrothermal system; (iii) be a discharge direct from the cracked zone of the CBL; (iv) represent a non-hydrothermal source (e.g. magmatic gas); or (v) have gained heat from somewhere (e.g. exothermic chemical reactions; passage through a recent, still hot intrusion).

Schubert and Straus (1980) posed the question: how does a water layer overlying a vapour-dominated layer remain stable ? They found that the phase change stabilized the boundary, but only at permeability values less than ~4 x 10^{-17} m^2. For the heat fluxes at Poás and Ruapehu (> 100 W m^{-2}), it can be seen from equation (5.20) and the values for C_H in table 5.3, that the permeability must be ≥ 10^{-14} m^2. Thus any water layer within permeable rocks, overlying a high-permeability 2PZ should be unstable, suggesting that it would also degenerate into an upwards extension of the 2PZ. If the 2PZ discharges directly into the lake, however, then the pressure at the top of the 2PZ will equal the lake-bottom pressure, given simply by the head of water in the lake. The temperature at the top of the 2PZ will also be given by the Clapeyron curve. Thus deeper lakes have the potential to give the 2PZ a higher heat transfer capability - depths for the (Q_{conv} / D) values used are given in table 5.4.

Many of the assumptions made in this, and previous sections are doubtful, to say the least, within real volcanic systems. Permeability is likely to be variable in space and time, as is the

C_H or ($Q_{convmax}$ / D) / W m^{-4}	Lake depth / m
8.4 x 10^{14}	0
2.5 x 10^{15}	40
5 x 10^{15}	150
7.5 x 10^{15}	410

Table 5.4 *Values of C_H (or ($Q_{convmax}$ / D) corresponding to different lake depths, i.e. different pressures at the top of the 2PZ.*

efficiency of the 2PZ, its areal extent, and the heat flux through it. The idealised model presented should be viewed only as a guideline to the real situation.

5.5 Implications for the internal structure of Poás and Ruapehu

The generalised models discussed in the previous sections will now be considered with the internal structure of Poás and Ruapehu in mind. The power input to both lakes of 100 - 1000 MW from an area of ~10^5 - 10^4 m^2 (i.e. the entire lake bed to approximately one tenth of it) implies a heat flux through the lake floor of ~10^3 - 10^5 W m^{-2}. At Poás, where the lake depth has been ~0 - 50 m, this implies a subsurface permeability when no lake was present of ~10^{-12} m^2 (for a heat flux of 10^3 W m^{-2}) to ~10^{-10} m^2 (10^5 W m^{-2}) or, when a ~50 m deep lake was present permeabilities in the range ~4 x 10^{-13} (10^3 W m^{-2}) to ~4 x 10^{-11} m^2 (10^5 W m^{-2}). Similarly at Ruapehu, where the lake depth has varied between ~70 - 300 m, the corresponding subsurface permeabilities are ~3 x 10^{-13} to ~3 x 10^{-11} m^2 (70 m deep) and ~1.5 x 10^{-13} to ~1.5 x 10^{-11} m^2 (300 m). These values are for 2PZs working at optimum efficiency (i.e. the optimum value of γ at their upper temperature), and discharging directly into the lakes. Higher permeabilities are required if non-optimum conditions exist. The idea of the 2PZ discharging into the lake invalidates the constant permeability model of the 2PZ, effectively putting a region of infinite permeability at the top. However, if we assume the region of condensation in the bottom of the lake is very thin, and can be ignored, then the model is valid, so long as the upwards flux of condensing vapour is matched by a downwards flux of lake-water into the top of the 2PZ proper. This approximation removes the requirement of a CBL at the base of the lake, and provides a connection for the fluids in the lake and the hydrothermal system, suggested by the mass and chemical balances in chapter 4.

The temperature and pressure regimes in the 2PZs are also partially constrained by the models, at Poás, the 2PZ is probably somewhere between curves (a) and (b) on figs. 5.12 and 5.13. At Ruapehu, the 2PZ is probably between curves (b) and (c) on figs. 5.12 and 5.13.

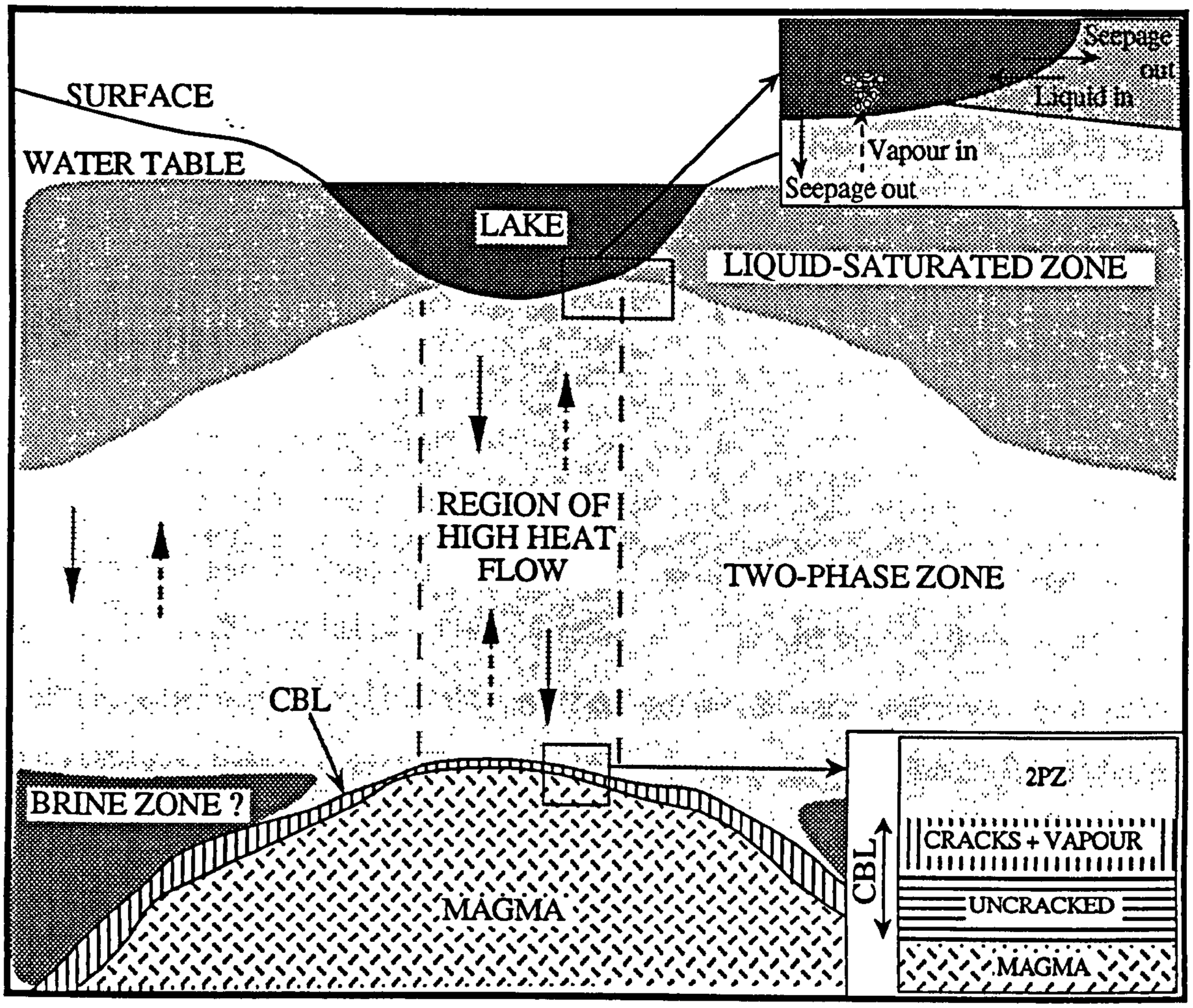

Fig. 5.14 *Cartoon of the system envisaged at Poás and Ruapehu, with a region of high heat flow 2PZ separating the lake from a magma body. The magma has a thin CBL, being infiltrated by a cracking front, and the 2PZ discharges directly into the lake. Seepage is also returned as heated brine, as demanded by the chemical balance, but the major heat flow mechanism is essentially separate from the single-phase brine recycling system.*

At the base of the 2PZ, in the region of high heat flow, which is probably just restricted to an area a few hundred metres around the vent region, there must be a CBL above a hot magma body. As described in section 5.3, this CBL will have an upper cracked region (of order a ~10 cm thickness), with the cracks filled with stagnant, superheated vapour, and a lower, impermeable region. This CBL will be migrating downwards at a rate determined by the removal of heat by the 2PZ. Assuming a steady-state 2PZ working at optimum efficiency, then the thickness of the CBL, and its infiltration velocity, should fall near the curve A (for an andesite) in fig. 5.7. A heat flux of ~10^2 - 10^4 W m^{-2} requires an infiltration velocity of ~1 - 100 m a^{-1} (assuming f = 0), and suggests a CBL thickness of ~30 - 0.3 m, with an upper cracked region of thickness only ~4 - 8 cm. The cracking temperature of the

magma (fig. 5.6) will be only marginally above the temperature at the base of the 2PZ for the slower velocity, assumed in fig. 5.7 to be 250 °C, but will be ~400 °C for a velocity of ~100 m $\dot{a}^{-1}$.

A cartoon of what the hydrothermal system might look like in cross-section is shown in fig. 5.14. Away from the region of high heat flow in the vent region, a more classical hydrothermal system may develop, similar to that suggested by White et al. (1971), with an upper liquid saturated zone, and possibly a lower brine zone between the magma and a 2PZ. In these regions of lower heat flux, a thicker CBL will develop above the magma body.

One problem with this model of the system beneath Poás and Ruapehu is that the mass and chemical balance results from chapter 4 required lake water to seep out, become heated (but not totally vaporised), and return to the lake as a mixture of steam and hot brine. This would only be possible if the process of brine recycling was essentially separated from the main heat transfer system directly beneath the lake, and occurred out the lake sides, or in localised liquid saturated regions beneath the lake. Down-going liquid in the 2PZ will presumably dump most of its metal ions upon vaporisation, creating the possibility of a mineralised zone in the region of high heat flow. This creates problems because during some periods, metal ions are conserved within the lake, i.e. inputs equal outputs. In such a situation, any deposition of metal ions in a 2PZ must be balanced by leaching of metal ions from a brine zone.

This illustrates one of many other problems: all these models are drastically simplified, and the real situation will probably be largely non-steady state, have variable permeability due to mineral deposition, a variable cross-sectional area of high heat flow with depth, variable fluid compositions and hence properties, and three-dimensional flow of fluids. Such simple models can, at best, only present a rough picture of the real situation.

CHAPTER 6

Heat Transfer in Magmatic and Hydrothermal Systems: 2. Magma Degassing

6.1 Introduction

Gas escape represents an advective heat loss from a magma. In this chapter, the physical process of magma degassing is reviewed, and the implications for heat transfer in volcanic systems explored. In the final section, degassing mechanisms that are likely to operate in the volcanoes studied during the present project are considered.

Many samples have been taken of gases directly exiting lava lakes, flows and domes. These are assumed to represent pure magmatic gas, but probably contain some non-magmatic components. Another problem is whether these gases accurately represent the composition of volatiles dissolved in the magma, because fractionation during degassing is unknown (Matsuo, 1991). A selection of magmatic gas analyses is presented in table 6.1. Water is usually the major gas (typically ~50-80 vol. %), followed by CO_2 (typically ~10-20 vol. %), and sulphur gases (SO_2, H_2S), with lesser amounts of other species (e.g. H_2, HCl, HF).

There have been a number of estimates of gas fluxes from volcanoes. For SO_2, estimates are possible using a correlation spectrometer (COSPEC) (Stoiber et al., 1983). The COSPEC measures the concentration of SO_2 in a volcanic plume by comparing the attenuation of certain wavelengths with respect to a clear sky. The approximate size and concentration of the plume can be determined, and fluxes calculated using measured windspeeds. The fluxes have uncertainties of typically 30-40 %. Fluxes of other gases can then be estimated from gas sampling to ascertain ratios between the gas species and SO_2 (e.g. Menyailov et al., 1986; Rose et al., 1986). Some estimated volcanic SO_2 fluxes are given in table 6.2.

A magma will become super-saturated when a dissolved volatile exceeds its solubility limit in the magma (see section 6.2). Solubility falls with decreasing pressure. Thus super-saturation can occur for two reasons: (i) decompression; or (ii) crystallisation of a phase (or

	H_2O	CO_2	S_t	H_2	HCl	HF	Reference
Erta'Ale 1971	75.4	13.8	8.6	-	-	-	Giggenbach and Le Guern, 1976
Erta'Ale 1974	79.4	10.4	7.4	-	-	-	
Nyiragongo 1959	44.6	47.6	3.6	-	-	-	
Stromboli 1964	85.5	7.5	1.1	-	-	-	
Etna 1970	64.5	5.1	28.8	-	-	-	
Surtsey 1964	79.2	9.4	4.7	-	-	-	
Surtsey 1965	86.9	5.1	2.6	-	-	-	
White Island 1971	81.5	12.8	5.4	-	-	-	
White Island Feb 1984	87.3	8.7	2.8	-	1.17	0.035	Rose et al., 1986
Kilauea 1918/19	35-69	18-50	11-18	-	-	-	Gerlach, 1986
Poás 1982	79.5	10.5	14.2	1.9	0.66	0.10	Casadevall et al., 1984
Momotombo 1985	92.0	4.5	2.1	0.8	0.46	0.01	Menyailov et al., 1986
Augustine 1986	84.3	2.34	6.79	0.59	5.69	0.09	Symonds et al., 1990
Mt. St. Helens 1980	91.6	6.94	0.28	0.85	-	-	Gerlach & Casadevall,1986

Table 6.1 *Compositions (in vol. % at STP) of volcanic gas discharges thought to represent magmatic gases.*

	SO_2 flux tonnes / day	Reference
Poás Feb 1982	700±180	Casadevall et al., 1984
Mt. St. Helens July 1980	1500±500	Casadevall et al., 1983
Nevado del Ruiz 1985-90	1000-10000	Williams et al., 1990
White Island Nov 1983	1230±300	Rose et al., 1986
White Island Nov 1984	320±120	Rose et al., 1986
Kilauea 1979-84	100-300	Casadevall et al., 1987
Etna 1975-87	1000-25000	Allard et al., 1991

Table 6.2 *Estimates of SO_2 flux at a range of volcanoes.*

phases) within the magma that rejects the volatile, thereby increasing the volatile concentration in the residual melt. Super-saturation is a pre-requisite for vesiculation (see section 6.3).

Gas loss from sub-surface magmas is a poorly understood process. For gas to escape, a driving pressure difference across the magma/country rock boundary and a suitable pathway

for the gas are required. Pressure and permeability regimes around magma bodies need, therefore, to be considered in detail (see section 6.4).

In section 6.5 the behaviour of gas after leaving the magma is modelled. Reversible adiabatic expansion is considered, and indicates that if this is the decompression mechanism, then very shallow magma sources are required to produce high temperature fumaroles, if the magma is at lithostatic, or even hydrostatic pressures. Conversely, if irreversible adiabatic expansion occurs, then high temperature fumaroles can originate at any depth. The passage of gas to the surface is likely to be non-adiabatic, however, and a model is developed of the steady flow of compressible fluid through a rough cylindrical conduit, with conductive heat losses to the wall rocks. For typical volcanic fumaroles, the model predicts a maximum source depth for a given surface temperature, e.g. ~300 m for a 500 °C fumarole.

As indicated in chapter 4, if the heat and HCl outputs of Poás and Ruapehu are supplied solely by degassing, very large volumes of magma need to be degassed; much larger than those likely to be available as shallow intrusions. Similar inconsistencies have been found at other volcanoes, e.g. Nevado del Ruiz (Williams et al., 1990), Lonquimay and Lascar (Andres et al., 1991). One possibility (S. Blake, pers. comm.) is that large volumes of magma at depth could degas through minor intrusions that reach near to the surface, acting as chimneys. A physical model of such a situation is developed in section 6.6.

6.2 Solubility of volatiles in magmas

Each gas species will have a solubility limit in a particular composition magma at a given pressure (Hamilton et al., 1964). This solubility limit decreases with decreasing confining pressure (e.g. see fig. 6.1). Thus if a magma is decompressed, as during ascent, or if a volatile in solution increases in concentration during crystallisation of a phase (or phases) that rejects that volatile, then the melt composition will eventually cross the solubility curve (as indicated in fig. 6.1), and become super-saturated in that volatile. Decompression typically occurs over much shorter timescales (hours to days) than crystallisation (months to years) (Westrich et al., 1988). Therefore volatile exsolution associated with decompression

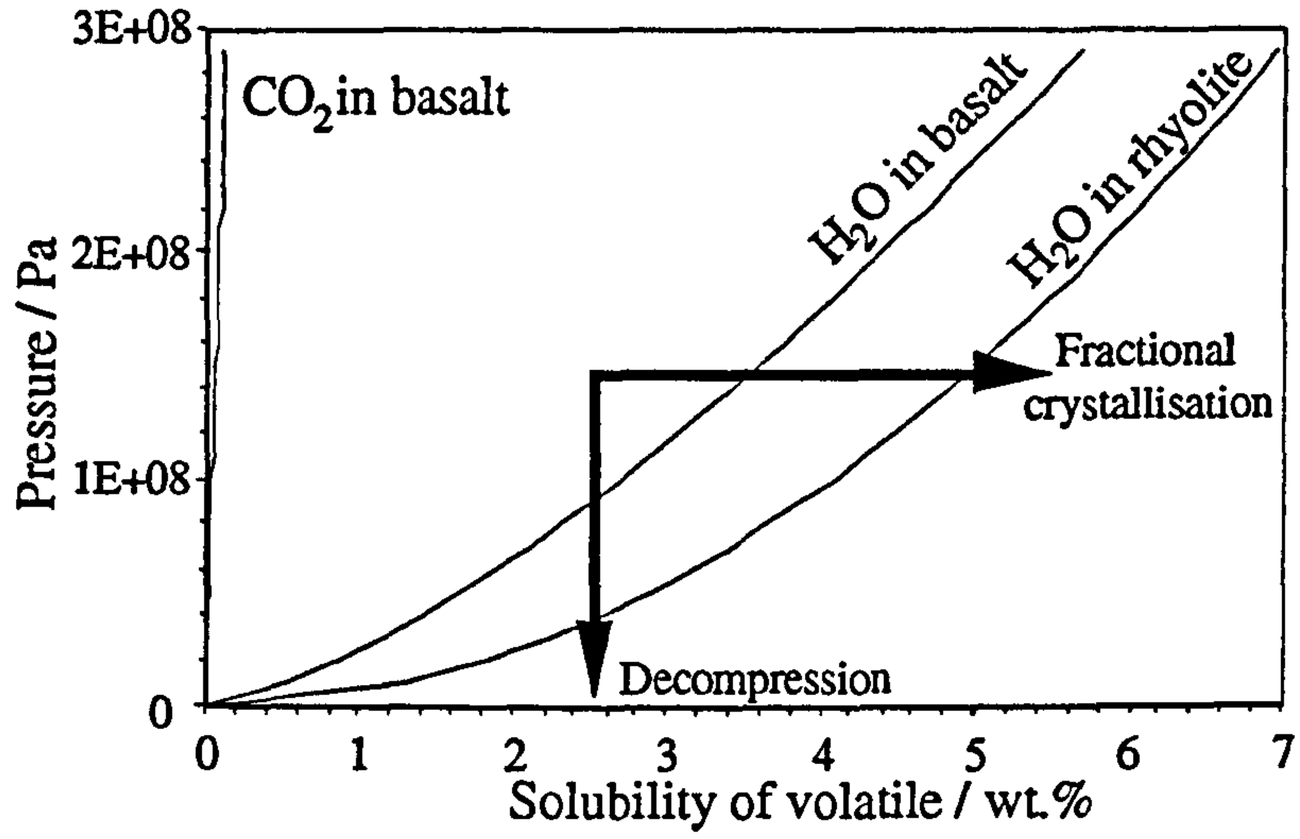

Figure 6.1 *Solubility of water and CO_2 in basalt, and water in rhyolite, as a function of pressure. Curves are from equations (6.1a-c). Arrows indicate paths for a decompressing magma, and a magma fractionally crystallising a mineral phase that rejects water.*

effects will occur within ascending magmas, whilst exsolution due to crystallisation will generally take place within immobile, cooling magmas (e.g. Tait et al., 1989).

Commonly used solubility formulae, where x is the mass fraction and P is the pressure in Pa, are as follows (Burnham, 1979; Stolper and Holloway, 1988):

$$\text{Water in basalt:} \qquad x = 6.8 \times 10^{-8} P^{0.7} \qquad (6.1a)$$

$$\text{Water in rhyolite:} \qquad x = 4.1 \times 10^{-6} P^{0.5} \qquad (6.1b)$$

$$CO_2 \text{ in basalt:} \qquad x = 4.4 \times 10^{-12} P \qquad (6.1c)$$

These are the solubilities plotted in fig. 6.1. It can immediately be seen that CO_2 is much less soluble than water in basalt, and thus will tend to be present as a gas phase within magma at much greater depths. Solubilities of SO_2 and HCl in magmas are poorly understood due to reaction between these species and the melt (Matsuo, 1991). This discussion will be limited mainly to the solubility of water in magmas.

6.3 Magma Vesiculation

Once a magma has become super-saturated in a volatile, bubble nucleation should begin (Sparks, 1978; Gerlach, 1986). However, Bottinga and Javoy (1991) disputed this

assertion, and pointed out that there are many instances of magmas being super-saturated in volatiles by at least a factor of five at the point of eruption. Super-saturation can occur in liquids if there is a process operating that inhibits bubble nucleation or growth. Surface tension in silicate melts can be a large obstacle to bubble nucleation; however the presence of surface agents (e.g. oxygen and sulphur ions) on bubble walls will lower bubble nucleation activation energies (Sparks, 1978). Surface tension effects can also be overcome if the nucleation process is heterogeneous (i.e. is controlled by the presence of solid boundaries); for example, bubble nucleation on phenocryst surfaces (Sparks, 1978). The presence of fluid inclusions trapped inside growing crystals is one possible example of this phenomenon (Roedder, 1965). Volatile exsolution will be limited by the rate of diffusion of dissolved gas in the melt (Sparks, 1978). At low diffusivities, melt surrounding a bubble will rapidly become drained of volatiles, and exsolution will cease until dissolved gas diffuses into this zone from the surrounding, volatile-rich melt. However, despite these complexities, vesiculation does occur, and the laboratory-derived solubility formulae (equations (6.1a-c)) are the best indication of the pressure at which gas will separate from magma.

6.3.1 Behaviour of gas bubbles in magma

Because gas bubbles in a magma are buoyant, they will tend to rise. The terminal velocity of a rising bubble in a liquid (density ρ_l, viscosity μ_l) will be given by Stokes Law:

$$v_t = \frac{d^2\, g\, \Delta\rho}{18\, \mu_l} \qquad (6.2),$$

where d is the bubble diameter, and $\Delta\rho$ is the difference in density between the liquid and the gas, i.e. $\Delta\rho \approx \rho_l$. (This is equivalent to equation (5.9) for crystal settling.) Thus for the Ruapehu basic andesite (table 5.2) with viscosity ~20-10^4 Pa s, and density ~2600 kg m^{-3}, the terminal velocities of bubbles with various diameters are given in table 6.3. These bubble rise velocities will be relative to the magma; thus bubble separation can only be ignored if the magma is moving at a much greater rate than the bubbles.

Bubbles within a magma chamber will always tend to rise, and accumulate near the chamber roof. Vergniolle and Jaupart (1990) suggested that the build-up and subsequent collapse of a

foam layer at the roof of a shallow basaltic magma chamber at Kilauea was the cause of fire-fountaining episodes. Bubbles within a convecting magma will move with the magma, but with an additional upward velocity component. At the top of a convection cell, magma must reduce its vertical velocity to zero, giving the bubble the chance to escape to the stagnant roof region. Thus bubble accumulation at the roof is analogous to crystal accumulation at the floor.

	μ = 20 Pa s	$\mu = 10^4$ Pa s
d = 1 mm	7×10^{-5} m s^{-1} (2000 m a^{-1})	1.4×10^{-7} m s^{-1} (4 m a^{-1})
d = 1 cm	7×10^{-3} m s^{-1} (200 km a^{-1})	1.4×10^{-5} m s^{-1} (400 m a^{-1})
d = 10 cm	0.7 m s^{-1} (20000 km a^{-1})	1.4×10^{-3} m s^{-1} (40 km a^{-1})

Table 6.3 *Terminal rise velocities for bubbles of three diameters in magmas at each end of the range of viscosities calculated for the Ruapehu basic andesite (see fig. 5.2).*

6.3.2 Vesiculation due to magma decompression

Exsolution and subsequent expansion of volatiles from rising magma is one of the major driving forces behind explosive volcanism (the other being interaction of magma with ground water to produce phreatic explosions). As magma rises, it decompresses, and eventually reaches the solubility limit for its dissolved volatiles. At this point, given the provisos above, vesiculation should occur. As magma continues to rise, the gas volume fraction will increase due to both expansion and further exsolution of volatiles. Assuming a closed system (i.e. gas is not lost from the magma), and that the magma rise velocity is much greater than the bubble rise velocity relative to the magma (i.e. gas essentially does not separate from the magma), the gas volume fraction (α) can be calculated as a function of pressure. At an initial pressure (P_i), the magma is just saturated in volatiles, i.e. $\alpha(P_i) = 0$. Reducing the pressure to P_z, vesiculation will occur, and a unit volume of magma at P_z will contain a mass of gas (m_g) and liquid (m_l), where:

$$m_g = \alpha(P_z)\, \rho_g \qquad (6.3)$$

$$m_l = (1 - \alpha(P_z))\, \rho_l. \qquad (6.4)$$

The mass of gas produced can also be written in terms of the reduction in solubility (Jaupart and Tait, 1990):

$$m_g = m_l\,(x(P_i) - x(P_z)) \qquad (6.5),$$

where x(P) is the dissolved volatile mass fraction at pressure P. Substituting equations (6.3) and (6.4) into (6.5), and making $\alpha(P_z)$ the subject of the formula gives (Jaupart and Tait, 1990):

$$\alpha(P_z) = \frac{1}{1 + \left(\dfrac{\rho_g(P_z)}{(x(P_i) - x(P_z))\,\rho_l(x)}\right)} \qquad (6.6)$$

The gas density (ρ_g) will be given by the perfect gas approximation:

$$\rho_g = \frac{M\,P}{R\,T} \qquad (6.7)$$

where M is the molar mass (M_{H_2O} = 18.015 g mol^{-1}), and R is the gas constant (8.31 J mol^{-1} K^{-1}). The density of steam at 1000 °C and 10^8 Pa is ~170 kg m^{-3}. The density of the melt (ρ_l) is thought to increase with loss of dissolved volatiles (Burnham and Davis, 1971; Silver and Stolper, 1985; Lange and Carmichael, 1990), following the equation:

$$\rho_l = \rho_0\,(1 - \beta\,x) \qquad (6.8)$$

where ρ_0 is the anhydrous melt density, x is the mass fraction of the volatile, and β_{H_2O} = 1.6; although values of β_{H_2O} possibly have as wide a range as 0 to 2.5, depending upon magma composition, temperature and pressure (Lange and Carmichael, 1990). Loss of CO_2 also results in an increase in density, with a value of β_{CO_2} = 0.8 (Lange and Carmichael, 1990).

Jaupart and Tait (1990) stated that magma viscosity (μ_m) would increase with increasing gas volume fraction according to the equation:

$$\mu_m = \mu_l\left(1 - \frac{\alpha}{\alpha_c}\right)^n \qquad (6.9)$$

where μ_l is the viscosity of bubble-free magma, $\alpha_c \approx 1$, and $n \approx -2.5$. Thus for a bubble volume fraction (α) of 0.6, viscosity is increased by an order of magnitude. The viscosity of the melt also increases as its dissolved water content decreases (e.g. fig. 5.2b). Fitting a line to the calculated viscosity values of Ruapehu basic andesite for various water contents (fig. 5.2b), and assuming a crystal content of 37.9 vol.% (table 5.2), and a temperature of 1000 °C, yields the following relation between viscosity and mass fraction of dissolved water (x):

$$\mu_l = 10^{(4.44 - 100\,x + 6.77\,x^2)} \quad (6.10)$$

Equations 6.1, and 6.6-6.10 can be used to investigate the behaviour of a batch of rising basaltic andesite magma. In fig. 6.2 depth profiles (assuming a lithostatic pressure gradient, with country rock density 2500 kg m^{-3}) of gas volume fraction, density, and viscosity for a rising magma are shown, using the properties of Ruapehu basic andesite, and solubility equation (6.1a), and assuming the magma initially contained 2 wt.% water. Values of density and viscosity are calculated assuming a closed system (i.e. no gas loss, fig. 6.2, dashed lines), and also for an open system (all gas lost, solid lines).

Sparks (1978) suggested that above a gas volume fraction of 0.75, magma would fragment, leading to an explosive eruption. This would occur at ~300 m depth in the closed system depicted in fig. 6.2. Jaupart and Allègre (1991) calculated that for a closed silicic system, an initial magma water content in excess of 0.16 wt. % would lead to explosive eruption, if the magma approached the surface. In most situations however, the system is partly open, and some gas will be lost from the rising magma, lowering the likelihood of fragmentation (e.g. Eichelberger et al., 1986). Jaupart and Allègre (1991) suggested that during an explosive eruption, such as that of Mt. St. Helens in May 1980, the overpressure (pressure above lithostatic) in the chamber, and hence the velocity of magma continuing to rise in the conduit, will gradually fall. With slower magma velocities, more gas will be lost. Thus the volume of gas lost from the rising magma will gradually increase, and eventually the erupted gas volume fraction will fall below 0.75, changing the eruptive regime from explosive to effusive. Gas loss is considered further in section 6.4.

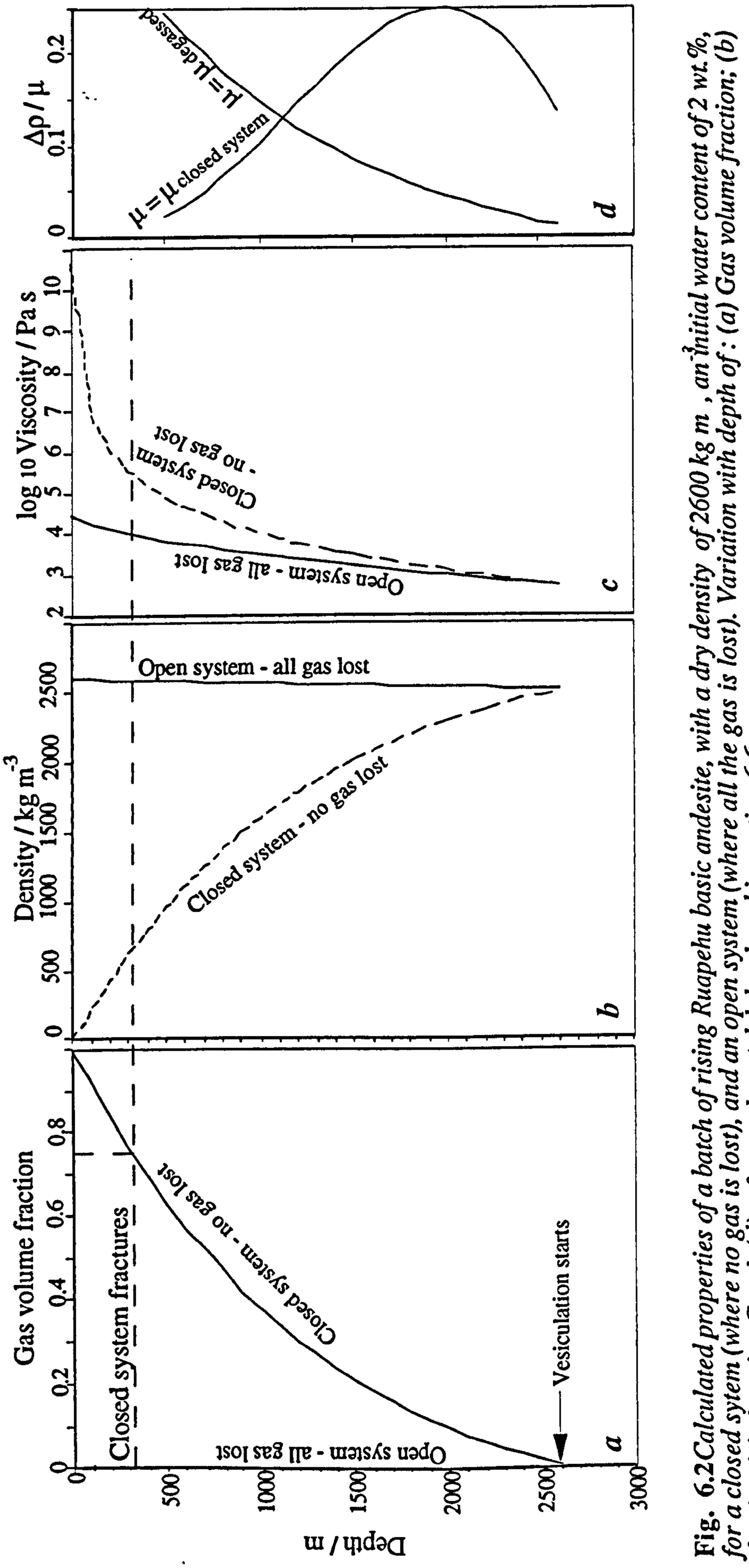

Fig. 6.2 Calculated properties of a batch of rising Ruapehu basic andesite, with a dry density of 2600 kg m^{-3}, an initial water content of 2 wt.%, for a closed sytem (where no gas is lost), and an open system (where all the gas is lost). Variation with depth of: (a) Gas volume fraction; (b) density; (c) viscosity. Graph (d) refers to the model developed in section 6.6.

From the evidence of high temperature fumaroles at Poás, and chloride-rich gas inputs to the lakes of Poás and Ruapehu, magmatic gas has often been discharged without an associated magmatic eruption. This is true of many volcanoes, and implies at least partially open system behaviour. This could be an indication of magma rising and vesiculating in a conduit, but failing to reach the surface. Indeed, the rise of magma may be halted because gas is lost from the top of the conduit, increasing the bulk density of the magma, (i.e. a system essentially open at the top) and hence reducing its buoyancy to the point where it will start to sink. Further buoyant, volatile-rich, rising magma could replace the degassed magma. A model of such a situation is developed in section 6.6.

6.3.3 Vesiculation due to magma crystallisation

Crystallisation leads to exsolution of volatiles due to the reaction known as 'secondary boiling' (Burnham, 1985):

$$H_2O\text{-saturated melt} \rightarrow H_2O\text{-poor crystals} + H_2O \text{ vapour.}$$

This process is shown diagrammatically in fig. 6.1 as a horizontal line. It usually is a much slower process than decompression, and may follow decompression in the case of intrusions, unless the magma has already been quenched to a glass (Westrich et al., 1988). Blake (1984), Burnham (1985) and Tait et al. (1989) have suggested that crystallisation in a volatile-saturated magma chamber, causing gas exsolution, will (if the system is sufficiently closed) lead to overpressures and subsequent fracture of the chamber walls, producing brecciation, intrusion, and possibly eruption (fig. 6.3). Thus vesiculation due to crystallisation can precede, as well as follow, that due to decompression.

Tait et al. (1989) calculated that only a few percent crystallisation of a volatile-saturated, shallow (few km depth), sealed magma chamber would be sufficient to generate overpressures great enough to trigger eruptions. Rates of heat loss from the magma will govern the crystallisation rate (chapter 5). Tait et al. (1989) suggested that the major determinant of heat loss is convection within the magma. Low viscosity, mafic magmas will crystallise faster, and hence exhibit more frequent eruptions, than more viscous, felsic

magmas. Typical repose periods between predicted 'events' are a few years for mafic magmas, increasing to a few hundred years for felsic magmas (Tait et al., 1989). However, as already discussed in chapter 5, if heat losses from the magma are controlled by a high permeability hydrothermal system surrounding the magma (Hardee, 1982), then losses can exceed those suggested by convection within the magma. In this situation, the hydrothermal system will infiltrate the magma, creating permeability by thermal contraction and cracking (Lister, 1983). This mechanism will help release gas trapped within the infiltrated magma, and the presence of fractures may also assist any already exsolved gas within the magma chamber to escape, thus reducing the chamber pressure before a critical level is reached.Thus an infiltrating hydrothermal system will tend to open (but perhaps not completely) the 'closed-system' magma chamber.

6.4 Gas escape from magma

Mechanisms of gas escape from magmas are poorly understood. Gas will tend to leave the magma because it is less dense, and is therefore buoyant. Buoyant gas will tend to move towards areas of low pressure, following paths with the steepest pressure gradient. The structure and pressure profile across the magma/country rock boundary is therefore of primary importance in understanding the escape and subsequent behaviour of magmatic gases.

6.4.1 Structure of the magma/country rock boundary

Assuming that the magma is at sufficiently low pressures to be exsolving volatiles, there will be a gas phase present as rising bubbles. The bubbles will presumably be in thermodynamic equilibrium with the magma, i.e. at magmatic temperature and pressure. These bubbles will collect at the roof of the magma body, beneath/within a conductive boundary layer (see section 6.3.1 and fig. 6.4). Their rise will be slowed as they enter cooler, more viscous magma in the boundary layer. In chapter 5, conduction was assumed to be the only heat transfer process operating across the boundary layer, however, advection of heat by gas must also occur in some situations. Gas escape requires a pathway for the gas, i.e. a fracture

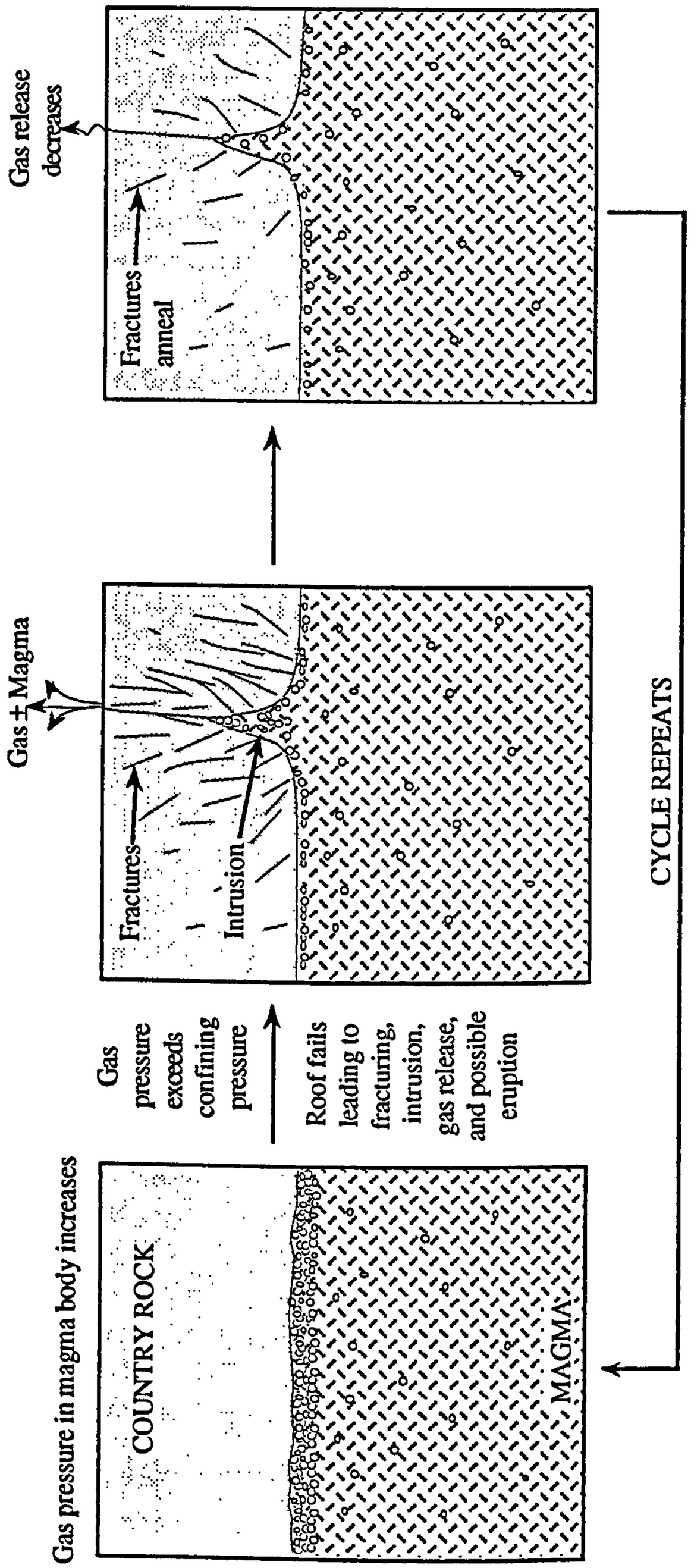

Fig. 6.3 *Time series of a vesiculating magma chamber gradually building up pressure until the confining pressure is exceeded, and the roof fails leading to gas release, intrusion, and possibly eruption. Following the explosive event, gas release will decrease, fractures will anneal, and the chamber will re-seal, allowing the cycle to repeat.*

of some kind. It was demonstrated in chapter 5 that infiltration of the CBL by the hydrothermal system will create fractures, and that the cracking temperature increases with infiltration velocity (fig. 5.6). According to the theory presented in section 5.3, cracks at temperatures approaching magmatic can be opened (and remain open) at high infiltration rates (of the order 10^2 - 10^3 m a^{-1}). Making the assumption that the presence of gas does not strongly affect the cracking theory, then this is one possible method of creating a pathway for the gas to escape (fig. 6.4).

Another mechanism of gas escape would be if the build-up of gas at the roof of a magma body created overpressures in excess of the confining pressure, leading to fracturing of the roof, gas release, probably intrusion, and possibly eruption (fig. 6.3; Tait et al., 1989). This would produce a sudden large outburst of gas, rather than a gradual, sustained release. Following such an event however, the fractures explosively created will take time to anneal, allowing further degassing to occur.

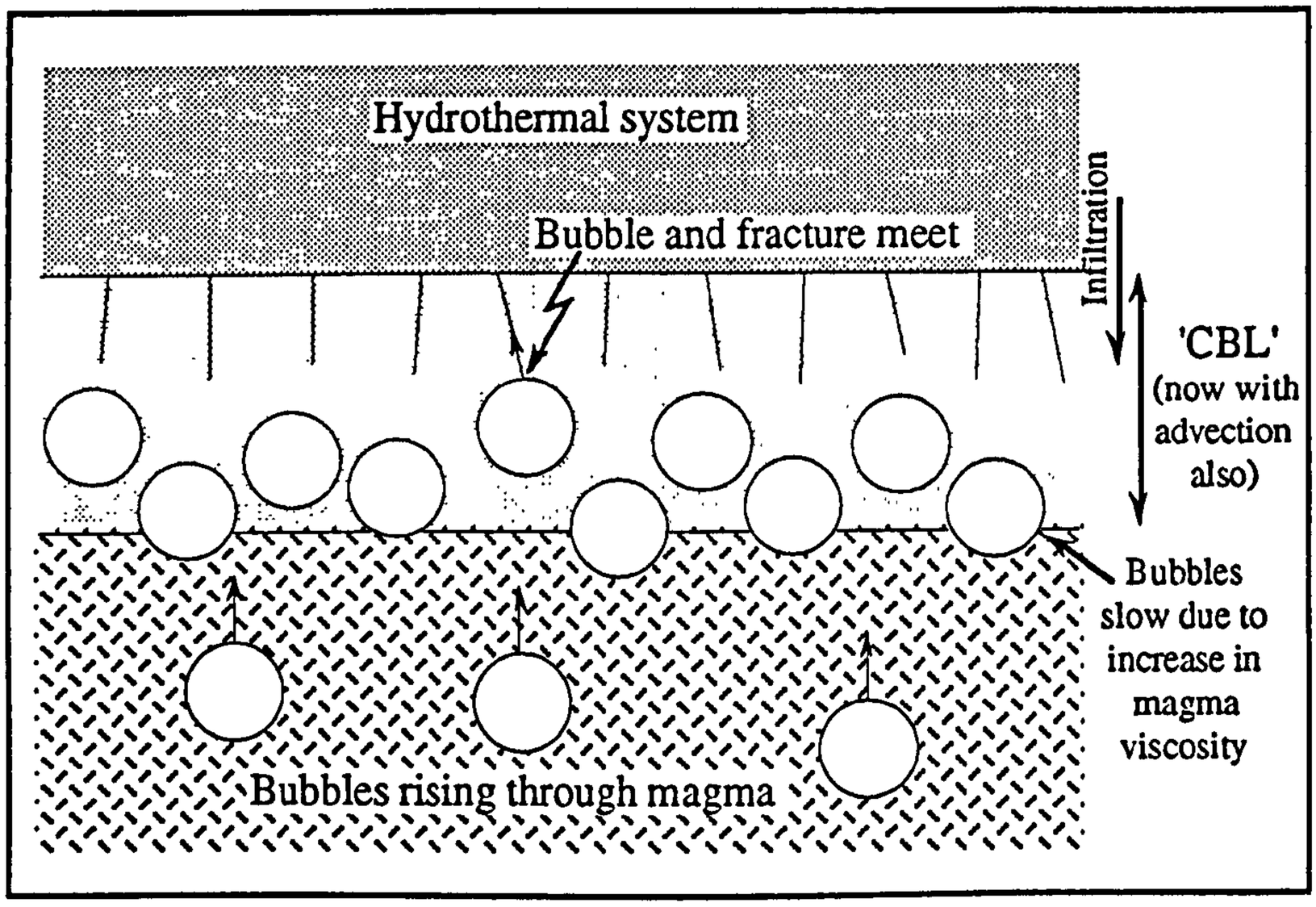

Fig. 6.4 *Schematic diagram of the country rock/magma boundary, with hydrothermal infiltration of the CBL, and gas bubble build-up within the lower parts of the CBL. Bubbles will discharge into fractures, thus traversing the CBL, adding an advective heat loss term; thus the assumption of only conduction within the layer is violated, and the theories presented in chapter 5 will be somewhat modified. This effect is assumed negligible in the present work.*

6.4.2 Fluid pressures across a horizontal magma/country rock boundary

Volatiles within a magma will be at approximately magmatic temperatures and pressures. Pressures within a magma are likely to be near lithostatic, or slightly higher if exsolved gases are impeded from escaping (e.g. fig. 6.3). However, it is possible that sub-lithostatic pressures can occur, if the magma does not fully support the rock directly above it. This could occur, for example, if a flank eruption partially drained a magma reservoir, or if extensive degassing resulted in a magma density increase (equation 6.8), and hence volume decrease. Negligible replenishment of magma from a deeper source is also required. The roof will temporarily be supported by shear stresses, but such an unstable situation is unlikely to persist for long periods, and eventually edifice deflation and/or collapse (e.g. pit craters) will occur, increasing magma pressures. Very low pressure (i.e. near atmospheric) magma sources will exsolve volatiles rapidly, and are unlikely to produce sustained gas outputs, unless volatiles are rising through the magma from a deeper source. This is only a viable mechanism in low viscosity, basaltic magmas (table 6.3).

Gas pressures outside the magma will be controlled by the overlying head of hydrothermal fluid, plus a frictional resistance force. A liquid dominated and/or low permeability hydrothermal system will have fluid pressures near hydrostatic, whereas a vapour dominated, high permeability system open at the surface will have fluid pressures near atmospheric. Pressure profiles may vary laterally with permeability and temperature.

The escape of gas from the magma will almost always promote rapid decompression, from approximately lithostatic pressure to near hydrostatic or atmospheric. If the model of a cracked boundary layer developed in chapter 5 still holds, this decompression will largely occur within the permeability transition zone (PTZ) of the conductive boundary layer (CBL). Calculated thicknesses of the PTZ were only a few centimetres (fig. 5.8).

An opposing view of the permeability adjacent to the magma is expressed by many authors (Burnham, 1985; Westrich et al., 1988; Jaupart and Allègre, 1991), who have suggested that because gas release is accompanied by rapid decompression and expansion, the entire

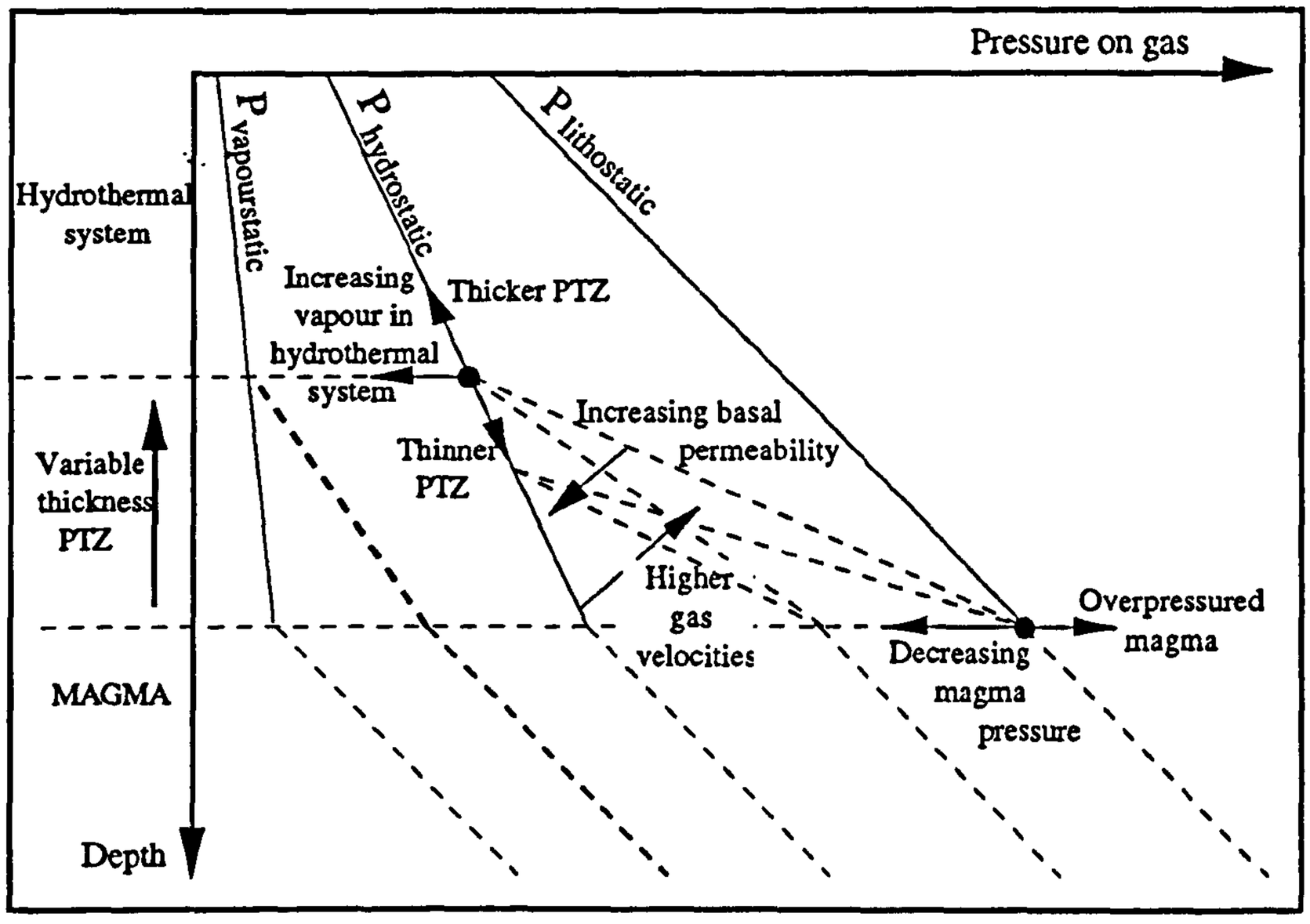

Fig 6.5 *Gas pressures against depth for a range of situations where a magma is degassing into a hydrothermal system. Dashed lines represent potential gas pressure paths. The two large dots represent points that can move, one depends upon magma pressure, the other on the thickness of the PTZ. Higher gas velocities will increase pressures in the PTZ, and higher permeability values at the base of the PTZ will lower pressures there.*

CBL will become brecciated, producing high permeabilities next to the magma. A dynamic situation can be envisaged where a combination of two processes will be occurring: (i) explosive decompression creating permeability, and (ii) rapid rock creep annealing fractures. At high gas fluxes the first process will probably dominate, perhaps even disrupting the entire CBL, and reducing the width of the PTZ to zero, whilst the latter process will become increasingly important with decreasing gas flux, allowing the build-up of a coherent CBL, and widening the PTZ to the size suggested by $z(T_k)$. The pressure drop is not necessarily limited to the PTZ; at high gas velocities, it may extend further into the country rock due to frictional forces.

The whole range of situations is summarised in fig. 6.5. The thickness of the PTZ will fall with increased brecciation, associated with higher gas fluxes. This effect will tend to feed back on itself, because a thinner PTZ will probably mean more rapid decompression of escaping gas, and hence more brecciation. The pressure drop across the PTZ will be limited by the density of fluid in the hydrothermal system, and the minimum thickness of the PTZ

will be limited by the rate of high temperature annealing of fractures (Lister, 1983). The second, independent effect, is the fall in magmatic pressure, caused by magma shrinkage or withdrawal, leading to an overlying rock column less well supported by the magma. The minimum pressure on the magma will then be limited to the hydrothermal fluid pressure. Decreased magma pressures will lead to increased volatile exsolution due to decompression; this will increase gas fluxes, and hence tend to increase brecciation. However, opposing this effect, the fall in magma pressure will reduce the pressure drop upon leaving the magma, and hence tend to decrease brecciation. Magma pressures below lithostatic are believed to be temporary, and deformation (deflation) of the volcanic edifice will tend to increase them back to lithostatic. A complex dynamic evolution of such situations can be envisaged.

6.4.3 Fluid pressures across a vertical magma/country rock boundary

The second situation to consider is the horizontal profile across a vertical magma/country rock boundary, that could represent the wall of a magma chamber, conduit or dyke. A range of possible situations is depicted in fig. 6.6.

Pressures inside the magma will depend upon the roof conditions (see above), but gradients will be approximately lithostatic (strictly magmastatic), or slightly higher if the magma is rising or over-pressured. Horizontal pressure gradients within the magma are unlikely to be large, because a gas-charged magma will be much more compressible (Jaupart, 1991). Small gradients can be envisaged however, for example, if the magma is rising in a conduit, maximum velocities would occur in the conduit centre, and hence pressures would also be higher in the centre. Jaupart and Allègre (1991) briefly reviewed the fluid dynamics of bubbly flow in a conduit, and concluded that pressure gradients, and the gas bubble distribution within the magma, are poorly constrained. They developed a model of gas loss from a conduit intruding permeable material, assuming average values of the magma pressure and the gas volume fraction at a given depth, and applying Darcy's law. They gave the following expression for the gas flux per unit area of conduit wall (kg s^{-1} m^{-2}):

$$q = - \frac{\rho_g \alpha D}{\mu_g} \left(\frac{\partial P}{\partial r}\right)_{r=a} \qquad (6.11)$$

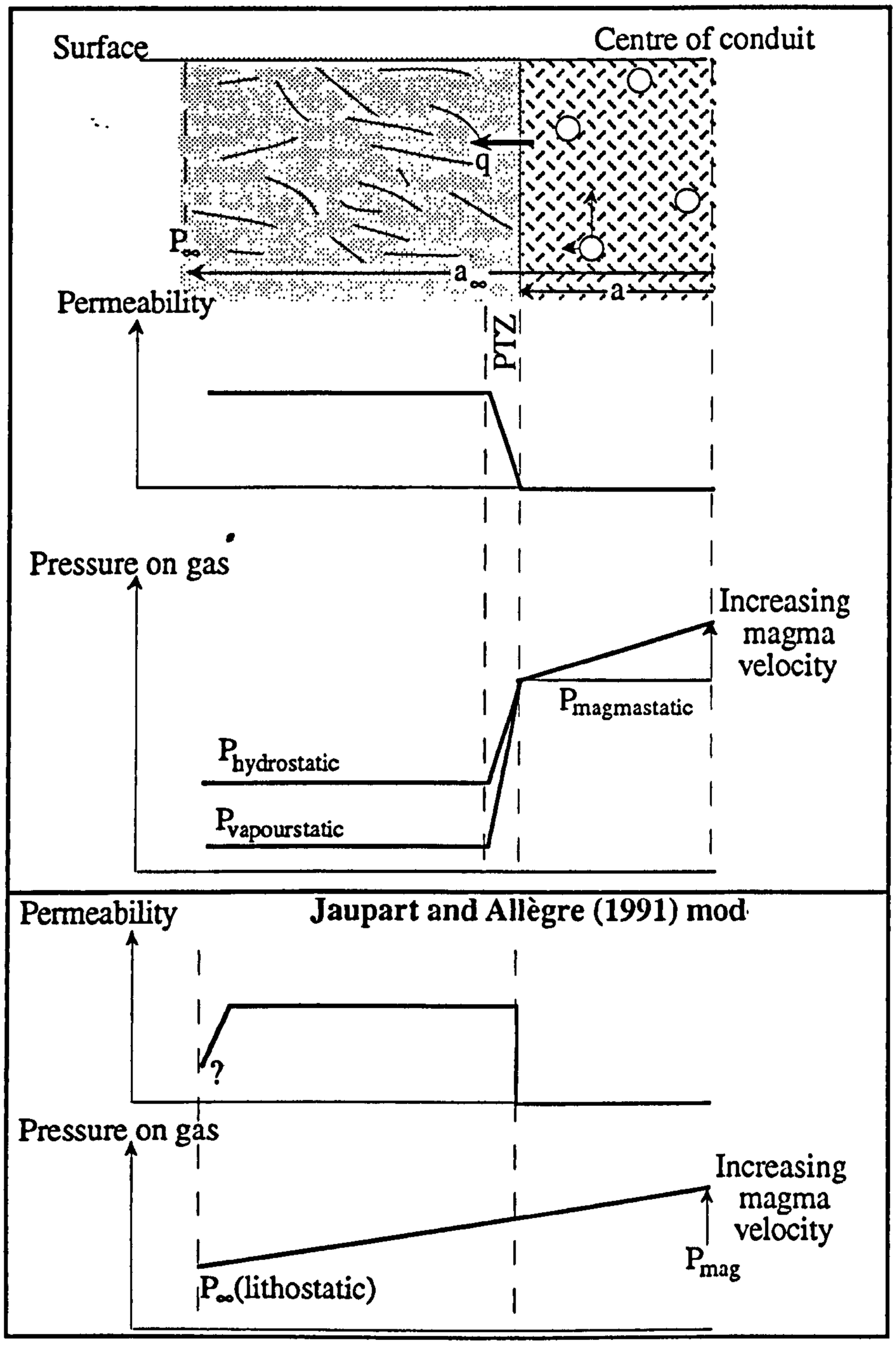

Fig. 6.6 *Possible pressure and permeability regimes around a vertical magma conduit. Pressures within the magma will be near magmastatic, or higher if the magma is rising. Fluid pressures within the hydrothermal system will be controlled by the head of hydrothermal fluid. The pressure transition probably occurs across the transition in permeability expected at the boundary (upper diagram). However, the Jaupart and Allègre (1991) model of gas loss assumes an ambient lithostatic pressure (P_∞) within the country rocks, high permeabilities at the magma/country rock boundary, decreasing at a finite distance (a_∞) from the centre of the conduit, and a linear horizontal pressure gradient from the centre of the conduit out to the radius a_∞ All of these assumptions are debatable, and illustrate the degree of uncertainty in the structure and behaviour of such a system.*

where α is the gas volume fraction, D is the country rock permeability, μ_g is the gas viscosity, r is the radial distance from the centre of the conduit, and a is the conduit radius. Jaupart and Allègre (1991) derived the following expression for the radial pressure gradient at the edge of the conduit:

$$\left(\frac{\partial P}{\partial r}\right)_{r=a} = \left(\frac{P + P_\infty}{2\ P}\right)\left(\frac{P - P_\infty}{a\ \ln\ (a\ /\ a_\infty)}\right) \qquad (6.12a)$$

where P is the pressure in the centre of the conduit, P_∞ is the pressure at $r = a_\infty$, approximately the radius of the region of enhanced permeability, i.e. the distance at which the pressure returns to its ambient value. The ambient pressure was assumed to be lithostatic (actually, fluid pressures are likely to be lower), thus the first expression in brackets was approximately equal to one. The value of a_∞ was assumed to be approximately (a e) (where e = 2.71828), thus the natural log term reduced to ~-1, simplifying the expression to:

$$\left(\frac{\partial P}{\partial r}\right)_{r=a} \approx -\left(\frac{P - P_\infty}{a}\right) \qquad (6.12b)$$

An expression for the vertical pressure gradient was found using momentum conservation, and mass conservation for the gas molecules allowed calculation of the variation of gas volume fraction up the conduit. Jaupart and Allègre (1991) found that gas loss from magma rising in a leaky conduit affected the behaviour of the system, changing the eruption regime from explosive to effusive, by lowering the erupted gas volume fraction to below 0.75. The important parameters are the initial velocity near the base of the conduit, the radius, and the permeability of the country rocks.

The Jaupart and Allègre (1991) model has been adapted by the present author to investigate the behaviour of basaltic andesite rising in a conduit. The model will remain valid if the gas and magma do not separate during flow, i.e. the relative bubble rise velocity is much less than the magma rise velocity. In the model outputs discussed here, this is the case as long as bubble diameters do not exceed a few cm in low viscosity magma (20 Pa s) (see table 6.3). In such a case, the behaviour is more likely to resemble the situation discussed by Vergniolle and Jaupart (1990) for Kilauea volcano (see section 6.3.1). Model outputs of vertical magma

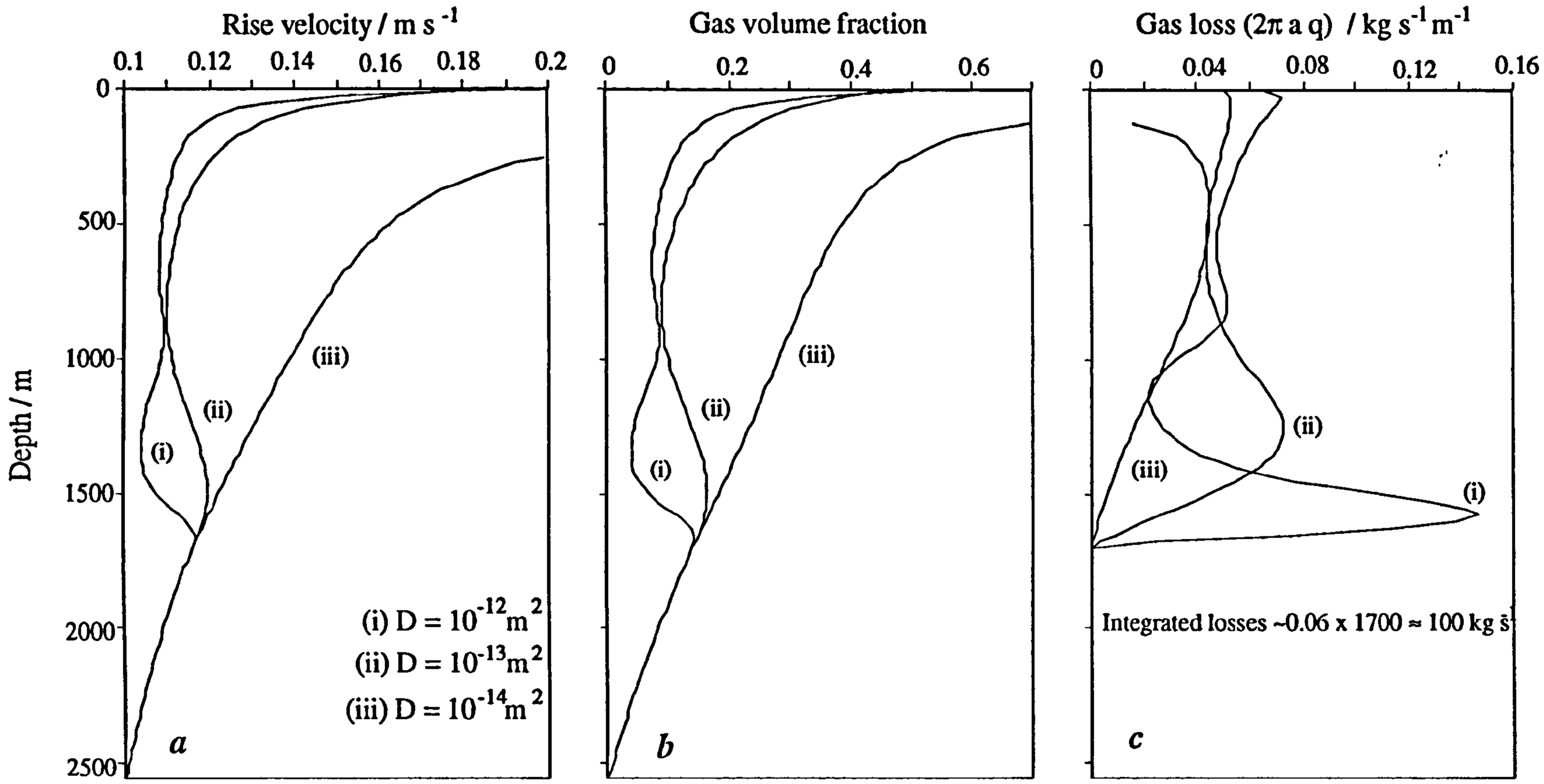

Fig. 6.7 *Behaviour of a batch of degassing 2 wt. % water basaltic andesite magma, rising in a cylindrical conduit of diameter 5 m, using the Jaupart and Allègre (1991) model, and taking three values for the permeability of the surrounding rocks. (a) Magma rise velocity, assuming an initial velocity of 0.1 m/s prior to vesiculation, which starts at ~2500 m; (b) Gas volume fraction; (c) Gas loss from the pipe per unit length of pipe - total losses can be found by inegrating under the curves, yielding approximate gas fluxes of ~100 kg/s of magmatic water in cases (i) and (ii). See text for discussion.*

velocity, gas volume fraction, and gas loss, for basaltic andesite rising in a 5 m diameter conduit are shown in figs. 6.7a-c. Fig. 6.7a shows the calculated variation in vertical velocity with depth, for three values of the country rock permeability ($D = 10^{-12}$, 10^{-13}, and 10^{-14} m^2). Fig. 6.7b shows the calculated gas volume fraction, and fig. 6.7c shows the gas flux per unit length of the conduit. With high permeability surroundings (curve (i)), gas is lost rapidly (fig. 6.7c) once the magma pressure in the conduit exceeds lithostatic pressure (at ~1700 m depth in fig. 6.7). This results in a decrease in the gas volume fraction (fig. 6.7b), and a decrease in velocity. This decrease in velocity reduces pressures, and hence gas loss, allowing gas to build up again within the magma. The rising magma proceeds through acceleration and deceleration cycles, before accelerating at shallow levels because of the rapid exsolution that occurs as pressures reduce to atmospheric. At lower values of permeability, gas loss is more difficult, and at a permeability of 10^{-14} m^2, gas loss proceeds at a slower rate than gas exsolution throughout the rise of the magma, thus the gas volume fraction increases continuously, until the fragmentation limit is reached at shallow depth, and an explosive eruption would occur.

The total gas flux can be found by integrating under the curves in fig. 6.7c, yielding approximate values of 100 kg s^{-1} of magmatic H_2O for cases (i) and (ii). This value is consistent with the gas fluxes observed at Poás and Ruapehu. However, this exact kind of situation, with continuous upflow of magma, does not normally occur at Poás or Ruapehu, because magma rarely reaches the surface. The results suggest that gas loss from magma rising in a small conduit intruded into permeable rocks is a viable mechanism of producing the gas fluxes observed at Poás and Ruapehu, provided that a sink for the rising magma can be found. A model where rising magma degasses and sinks back down the same conduit is developed in section 6.6.

Fluid pressures in the country rock are likely to be controlled by the density of the hydrothermal fluid, and any frictional forces associated with flow of fluid through the permeable rock. Frictional forces will be higher the lower the permeability, and the higher the fluid velocities. The Jaupart and Allègre (1991) model assumes lithostatic pressures within the country rock; however, hydrostatic pressures are probably more likely. At lower

pressures, gas loss will even more vigorous; thus the gas outputs from the model are probably minimum values, and effective degassing may occur at even lower permeabilities than those suggested here.

6.5 Behaviour of gas after leaving the magma

Gas within a magma can be assumed to be in equilibrium with the melt, at magmatic temperatures and pressures. On leaving the melt, the gas decompresses (see previous section), and enters a regime where it will almost certainly be hotter than its surroundings. Three different pressure-temperature paths will now be considered for the decompressing gas. Stating the first law of thermodynamics:

$$dU = dQ + dW \qquad (6.13),$$

where dU is the change in internal energy of the gas, dQ is the heat exchanged with the surroundings, and dW is the work done by the gas. The first two cases considered are assumed to be adiabatic, thus $dQ = 0$, but involve the gas doing different amounts of work. The more work done by the gas, the greater the drop in internal energy, and hence temperature. Case I is a slow, reversible expansion, where the gas passes through a sequence of equilibrium states, doing work against confining pressure. Case II is a sudden irreversible expansion, such as high pressure steam expanding into a vacuum; in this case, no work is done, thus the internal energy (and temperature, for a perfect gas) remains constant. Cases I and II are simplistic models; Case III considers a more realistic situation, where the vertical flow of decompressing gas through a rough fumarole conduit with conductive heat lost to the walls. Work is done by the gas against gravity, increasing the gases potential energy. The gas also changes velocity, and hence kinetic energy; acceleration implies that the gas does work; deceleration implies that work is done on the gas. The gas freely expands in case IIIa, but does work against confining pressure in case IIIb. Frictional resistance to flow is included, as are conductive heat losses (negative dQ) to the conduit walls.

Case I: Reversible adiabatic expansion

For an adiabatic situation, equation (6.13) becomes:

$$dU = dW$$

For a reversible expansion, where gas passes through a sequence of equilibrium states doing work against confining pressure, this can also be written:

$$c_v\, dT = -\, P\, dV,$$

where c_v is the specific heat capacity at constant volume, T is temperature, P is pressure, and V is the molar volume. For a perfect gas:

$$P\, V = R\, T,$$

and

$$P\, dV + V\, dP = R\, dT,$$

where R is a gas constant equal to the universal gas constant divided by the mass of one mole of the gas. Hence:

$$c_v\, dT = V\, dP - R\, dT$$

and since $R = c_p - c_v$ for a perfect gas, where c_p is the specific heat capacity at constant pressure,

$$c_p\, dT = V\, dP,$$

and hence:

$$\frac{c_p}{R}\,\frac{dT}{T} = \frac{dP}{P} \qquad (6.14a)$$

Integrating equation (6.14a) between initial and final temperatures and pressures yields:

$$T_f = T_i \left(\frac{P_f}{P_i}\right)^{R/c_p} = T_i \left(\frac{P_f}{P_i}\right)^{\frac{\gamma\,-\,1}{\gamma}} \qquad (6.14b),$$

where the subscripts i and f refer to initial and final states, and γ is the ratio of specific heats c_p/c_v. The value of γ does not vary by more than a few percent from 1.3 over the entire range of pressures and temperatures considered for the three most common magmatic gases water, carbon dioxide, and sulphur dioxide (table 6.1). Equation (6.14b) can be used to estimate the pressure of the magmatic (1000 °C) source, given a fumarole temperature at atmospheric pressure (~10^5 Pa).

In fig. 6.8a, temperature profiles of slowly decompressing water vapour are shown, assuming $\gamma = 1.3$. This illustrates the large temperature drop that accompanies reversible adiabatic decompression of a magmatic gas, and for high temperature (>500 °C) fumaroles, requires a magmatic source at pressures of less than 10^6-2 x 10^6 Pa. These pressures occur at ~40-80 m lithostatic pressure, or ~100-200 m hydrostatic pressure. Steam originating at pressures greater than ~2 x 10^7 Pa will intercept the water saturation curve before reaching the surface, and will then behave as a two-phase mixture. Steam at high temperature (>500 °C), and low pressure (10^5 - 10^6 Pa) has a density of only ~1 kg m^{-3}, implying that if the magma is at vapourstatic pressures, high temperature (>500 °C) surface fumaroles can theoretically be created from magma at several kilometres depth. However, vapour rising through a permeable medium will encounter frictional forces (see case III), increasing pressures above vapourstatic, and permeability will probably decrease with depth, limiting this possible mechanism to the upper 1-2 km of the crust. This suggests that if reversible expansion occurs, high temperature fumaroles, such as those at Poás (fig. 3.5), either require shallow (<200 m depth) magmatic sources, or imply a vapour-dominated hydrothermal system within 1-2 km of the summit, underlain by a magma at near vapour-static pressures.

Case II: Irreversible adiabatic expansion

If the decompression is rapid and irreversible, such as the free expansion of pressurized gas into a vacuum, then no work is done (dW = 0), and there is no change in internal energy (dU = 0). This implies that for perfect gases, the temperature remains constant. For real

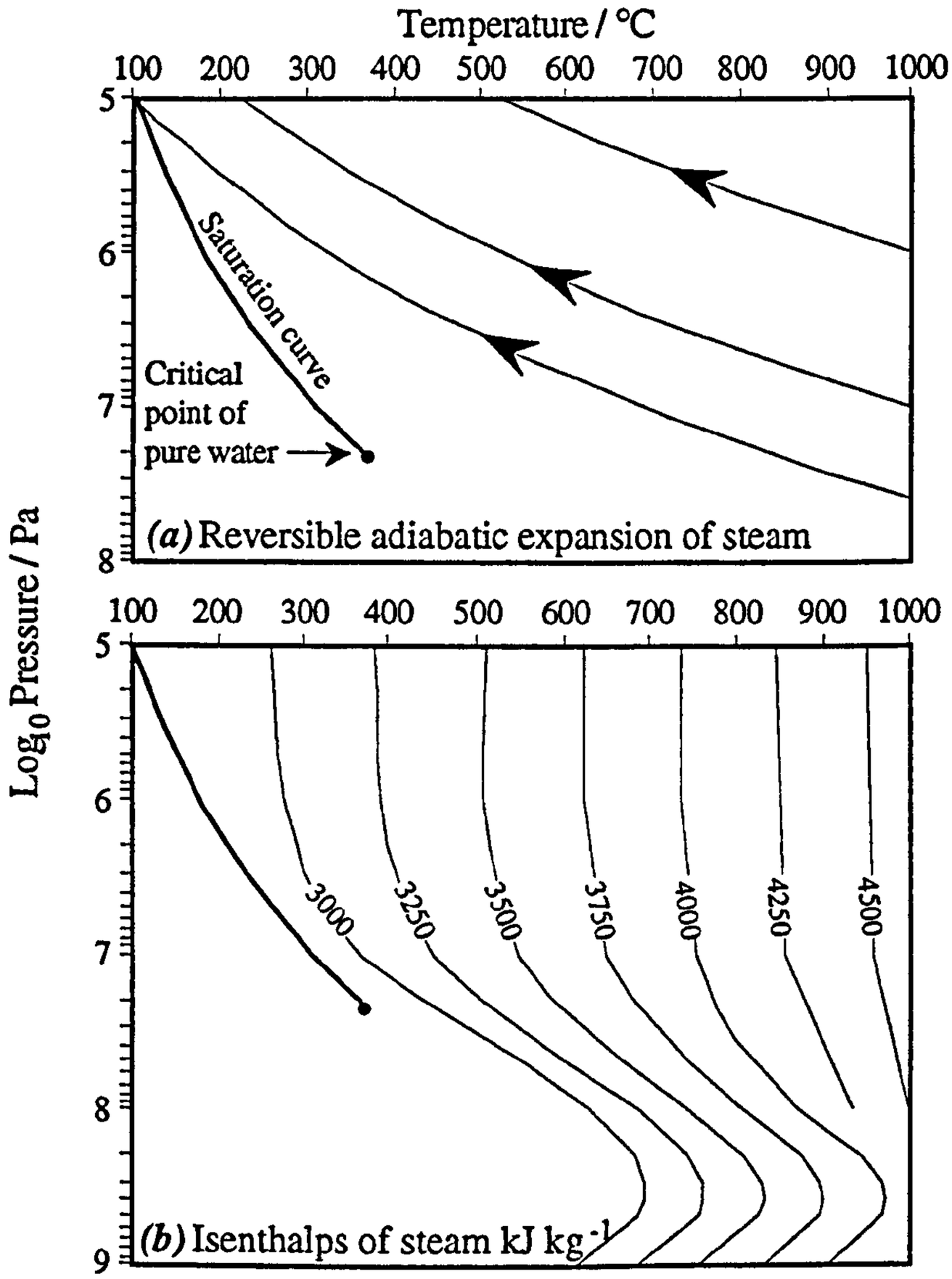

Figure 6.8 *Gas temperature against pressure for: (a) reversible adiabatic expansion of steam; and (b) irreversible adiabatic (isenthalpic) expansion of steam. The saturation curve, and the critical point for steam are also shown.*

gases, intermolecular forces play a role, and the gas can either cool or heat during decompression. This is known as the Joule-Thompson (or Joule-Kelvin) effect, and the important fact is that enthalpy is conserved. The temperature change associated with irreversible decompression can therefore be found by plotting isenthalps on a P-T diagram. This has been done for steam in fig. 6.8b; CO_2 and SO_2 behave more like perfect gases over this temperature and pressure range, because they are further away from their critical points. Thus if the expansion is irreversible, then no constraint can be put on the depth to the magmatic source simply from fumarole temperature.

Case III: Steady flow of compressible gas through a rough fumarole conduit

This case aims to be more realistic than cases I and II, and considers the steady flow of compressible gas through a rough cylindrical fumarole conduit of constant radius (r_o). The general flow considered is depicted in fig. 6.9, and four governing equations for the flow can be stated. Because the flow is steady, the mass flux (G; kg s^{-1} m^{-2}) must be constant, giving the continuity equation:

$$\rho v = G \qquad (6.15),$$

where ρ is the density, and v is the velocity. Assuming a perfect gas, the equation of state is:

$$P = \rho R T \qquad (6.16)$$

Equations (6.15) and (6.16) can be combined to give:

$$P v = G R T \quad (6.17a)$$

or, in differential form:

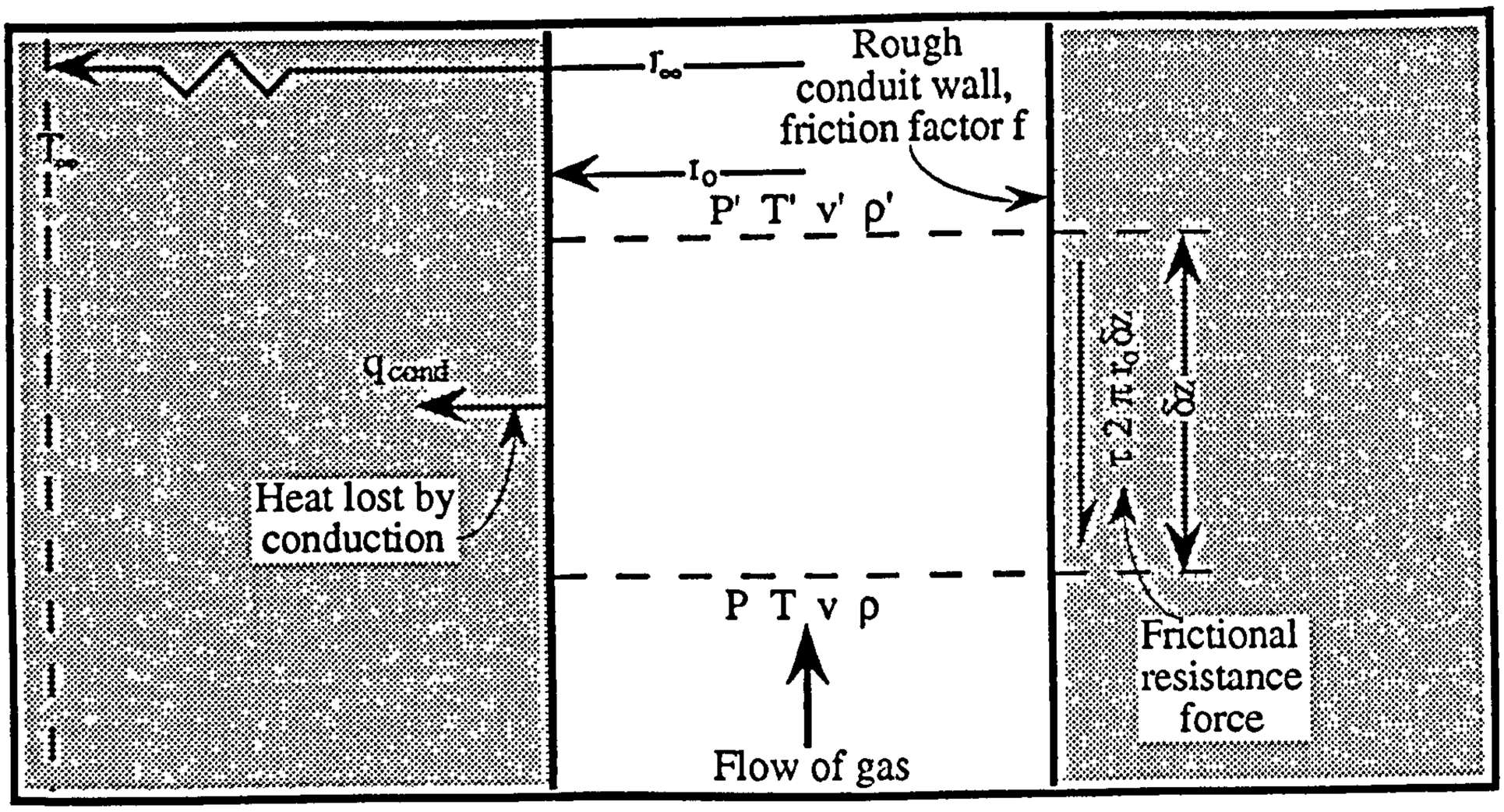

Figure 6.9 *Cartoon of the flow in the fumarole conduit, illustrating the meanings of the symbols: P is pressure; T is temperature; v is velocity; ρ is density; τ is shear stress; r_o is radius; r_∞ is distance to ambient temperature T_∞; δz is the thickness of the vertical element; and q_{cond} is the conducted heat flux.*

$$\frac{dP}{P} = \frac{dT}{T} - \frac{dv}{v} \qquad (6.17b)$$

Applying conservation of momentum across the element δz:

$$P\,A - \left(P + \frac{d\,P}{dz}\,\delta z\right)A - \tau\,2\,\pi\,r_o\,\delta z = \rho\,v\,A\left(v + \frac{d\,v}{dz}\,\delta z\right) - \rho\,v\,A\,v$$

where A is the cross-sectional area of the pipe ($\pi\,r_o^2$), τ is the shear stress (frictional force per unit area), and z is vertical distance. The two terms in brackets correspond to P' and v' in fig. 6.9. This equation simplifies to:

$$dP + \frac{2\,\tau}{r_o}\,\delta z + \rho\,v\,dv = 0 \qquad (6.18a)$$

The shear stress is related to the coefficient of friction, f, by (Streeter and Wylie, 1975):

$$\tau = \frac{f\,\rho\,v^2}{8},$$

where f is a function of the Reynolds number and the roughness of the pipe wall (Moody, 1944). Substituting this into (6.18a) gives:

$$dP + \frac{f\,\rho\,v^2}{4\,r_o}\,\delta z + \rho\,v\,dv = 0 \qquad (6.18b)$$

The first law of thermodynamics, or conservation of energy, can also be applied:

$$dU = dQ + dW$$

where
$$dQ = -\left(\frac{q_{cond}\,2\,\pi\,r_o\,\delta z}{\rho\,\pi\,r_o^2\,\delta z}\,\frac{\delta z}{v}\right) = -\frac{2\,q_{cond}}{\rho\,v\,r_o}\,\delta z$$

and
$$dW = -P\,dV - g\,\delta z - v\,dv$$

where q_{cond} is the conducted heat flux through the fumarole conduit wall (W m^{-2}). For an adiabatic situation, dQ = 0, and for a free expansion, P dV = 0. The two terms - g δz and - v dv are the changes in potential and kinetic energy of the gas, with all terms in energy per unit mass.

The frictional force impedes the acceleration of the gas, thus the velocity (and hence kinetic energy) does not increase as much as it should to balance the drop in pressure. The energy must go somewhere however, thus for an adiabatic flow, the internal energy (and hence temperature) increases; this is frictional heating. If the flow is not adiabatic, then the frictional energy can, at least partly, be conducted away.

Conductive heat losses are estimated by assuming a wall rock conductivity (k = 2.3 W m^{-1} K^{-1}), and assuming steady-state conduction. Because vertical temperature gradients are much smaller than radial temperature gradients in all of the cases discussed here, the temperature distribution around (and hence conductive heat flux from) an element can be found by solving Laplace's equation:

$$\frac{d^2T}{dr^2} + \frac{1}{r}\frac{dT}{dr} = 0$$

with boundary conditions:

$$T = T_{gas} \qquad r = r_o$$

$$T = T_\infty \qquad r = r_\infty$$

where T_∞ is the background temperature, which is reached at distance r_∞ from the centre of the conduit. This yields the temperature gradient, and hence conductive heat flux, at the wall of the conduit:

$$q_{cond} = -k\left(\frac{dT}{dr}\right)_{r=ro} = -k\frac{(T_{gas} - T_\infty)}{r_o \ln\left(\frac{r_\infty}{r_o}\right)} \qquad (6.19)$$

Case IIIa: Free expansion, PdV = 0

The appropriate energy equation for this case is:

$$dU = c_v\, dT = -v\, dv - \left(g + \frac{2\, q_{cond}}{G\, r_o}\right)\delta z \qquad (6.20a)$$

Equations (6.17b) and (6.20a) can be rewritten:

$$dv = -\frac{c_v\, dT}{v} - \frac{\delta z}{v}\left(g + \frac{2\, q_{cond}}{G\, r_o}\right) \quad (6.20b)$$

$$dP = P\left(\frac{dT}{T} - \frac{d\,v}{v}\right) \quad (6.17c)$$

Substituting equations (6.16), (6.17c) and (6.20b) into the momentum equation (6.18b), and re-arranging, yields:

$$dT = \delta z\left(\frac{f\, G\, v^4 - (4\, r_o\, g\, G + 8\, q_{cond})\,(v^2 - R\, T)}{4\, G\, r_o\,(c_v\,(v^2 - R\, T) - R\, v^2)}\right) \quad (6.21a)$$

Case IIIb: Gas does work against expansion, PdV ≠ 0

In this case, the appropriate energy equation is:

$$dU = c_v\, dT = -P\, dV - v\, dv - \left(g + \frac{2\, q_{cond}}{G\, r_o}\right)\delta z \quad (6.20c)$$

By comparison of the relations: $\rho\, v = G$ and $\rho\, V = 1$, it follows that:

$$\frac{dv}{v} = -\frac{d\rho}{\rho} = \frac{dV}{V}, \text{ and that: } P\, dV = P\, V\frac{dv}{v} = R\, T\frac{dv}{v}$$

following the same procedure as in case IIIa, this yields:

$$dT = \delta z\left(\frac{f\, G\, v^2\,(v^2 + R\, T) - (4\, r_o\, g\, G + 8\, q_{cond})\,(v^2 - R\, T)}{4\, G\, r_o\,(c_v\,(v^2 - R\, T) - R\,(v^2 + R\, T))}\right) \quad (6.21b)$$

and, re-arranging equation (6.20c), and substituting for P dV:

$$dv = \frac{-\,v}{R\, T + v^2}\left(c_v\, dT + \left(g + \frac{2 q_{cond}}{G\, r_o}\right)\delta z\right) \quad (6.20d)$$

Results for Cases IIIa and IIIb

White et al. (1971) found that vertical temperature gradients in geothermal areas were often found to be on or near the saturation curve for pure water, taking pressures to be hydrostatic for depth. For the results presented here, I have assumed that this is the ambient temperature profile, $T_\infty(z)$. The model was run for various values of r_∞, in the range 1-100 m, but for $r_\infty \gg r_o$, q_{cond} is nearly constant.

Equations (6.21a and b) were used to find the small temperature drop across element δz, assuming T, v and q_{cond} are approximately constant. Equations (6.20b and d) then yielded the change in velocity, and equation (6.17c) the change in pressure across the element. The new values were then fed in to the next element, and the process repeated iteratively. The approach taken was to specify surface conditions, i.e. $P = P_{atm} = 10^5$ Pa, and then calculate, by iteratively working downwards, values of temperature, pressure, and velocity against depth until $T = T_{mag}$ for different values of T_{atm}, r_o, exit velocity and r_∞.

Both cases yielded essentially identical results. Pressure drops of usually less than 10^5 Pa along conduits of up to ~1 km were calculated, indicating that the decompression may not be rapid enough to be irreversible, hence the model where $PdV \neq 0$ was favoured. Results were not found to be strongly dependant upon f, thus a constant value of 0.1 was used, appropriate for turbulent flow in a rough pipe (Moody, 1944).

Initially, temperature against depth profiles were found for surface fumaroles at 500 °C, for various values of r_o, r_∞, and v_{exit} (fig. 6.10). Fumarole conduits rarely exceed 20 cm in diameter, thus $r_o = 0.1$ m was taken as a maximum value. Exit velocities of ~100 m s^{-1} were found to produce the least cooling on ascent, and hence indicated the maximum depth to source. Exit velocities below ~100 m s^{-1} led to larger conductive losses, and above ~100 m s^{-1}, the gases were found to undergo rapid accelerations, where the increase in kinetic energy drained heat from the gas. Increasing the distance to ambient conditions (r_∞) to more than 100 m only decreased the amount of cooling marginally, as the radial temperature gradient at the wall remains approximately constant for $r_\infty >> r_o$. Thus the lower curve on fig. 6.12 ($r_o = 0.1$ m, $r_\infty = 100$ m, $v_{exit} = 100$ m s^{-1}) will be used to estimate the maximum depth to magma for a given fumarole temperature. Greater depths to magma would be produced if a lower value of the wall rock conductivity (k) was used, or if the ambient temperature profile was hotter, for example if the fumarole was surrounded by other hot fumaroles. Other effects not catered for by this model, that could affect the depth to magma, are the assumptions of a perfect gas, constant conduit area, steady flow, and no heat sources/sinks within the flow (e.g. exothermic/endothermic chemical reactions). The effect of deviations from these assumptions has yet to be addressed.

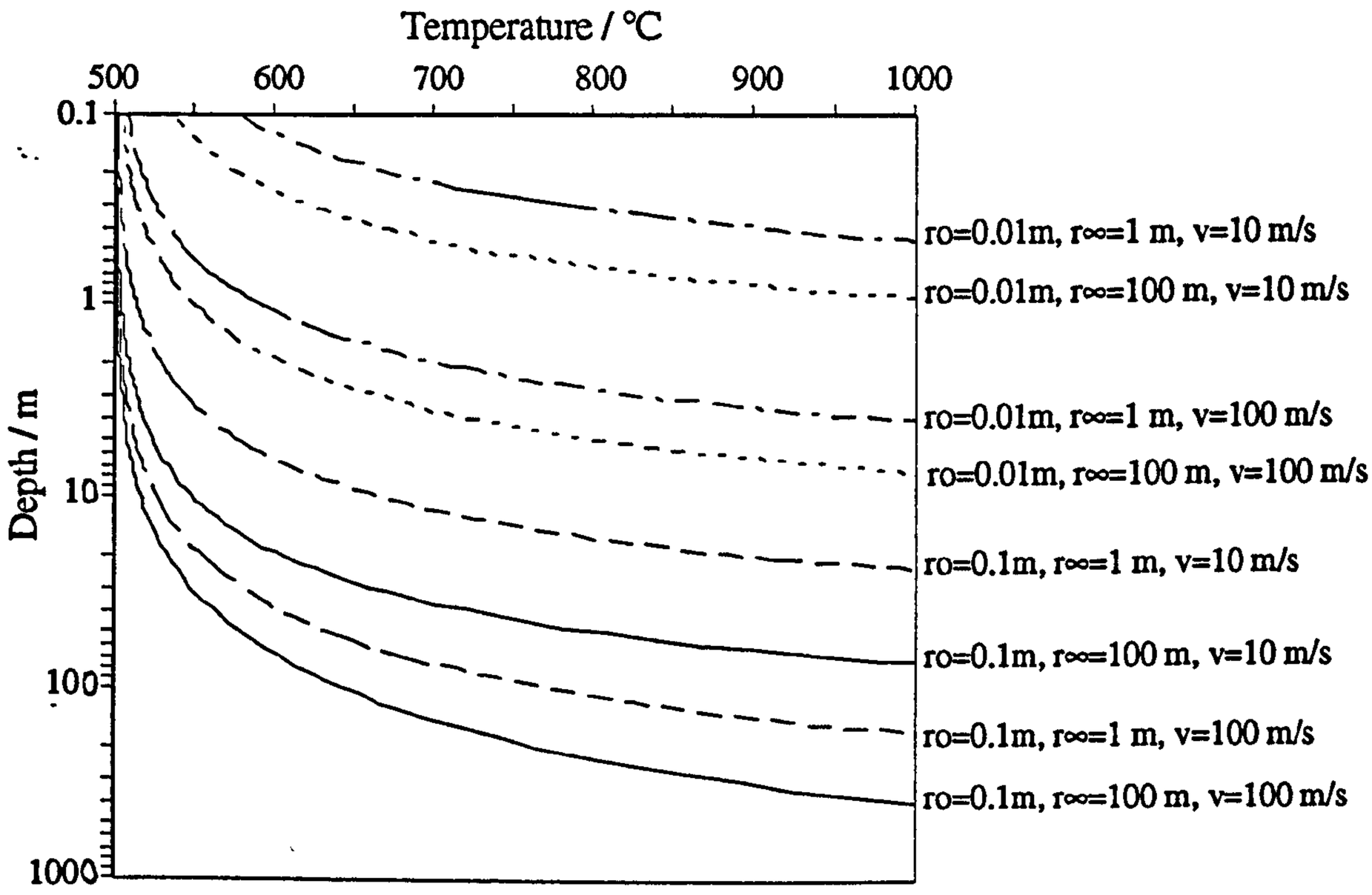

Figure 6.10 *Calculated temperature-depth 'rise paths' leading to a 500 °C surface fumarole, for different values of the conduit radius (r_o), the distance to ambient temperatures (r_∞), and the exit velocity (v).*

Fumarole temperatures at Poás fell from 960 °C in May 1981 to ~300 °C in August 1985. In the model presented here, the exit temperature will vary with: (i) the depth of the magmatic source (z_o); (ii) the conduit radius (r_o); (iii) the distance to ambient temperature (r_∞); and (iv) the surface exit velocity (v_{exit}). For example, these factors will vary if: (i) the magma is infiltrated, crystallised and cooled; (ii) minerals are deposited within the conduit; (iii) the surrounding hydrothermal system encroaches on the fumarole; and (iv) the velocity of the gas leaving the magma changes. The cooling at Poás could have been due to all or any of factors (i) to (iv) above. Applying the model with $r_o = 0.1$ m and $r_\infty = 100$ m, the 960 °C fumarole was found to have originated at ~14 m depth ($v_{exit} = 100$ m s^{-1}) or ~2.4 m depth ($v_{exit} = 10$ m s^{-1}), assuming a magma source temperature of 1000 °C. Taking these two situations as starting points, the dependence of fumarole temperature on factors (i) to (iv) has been calculated (fig. 6.11).

Fig. 6.11a shows the effect of increasing the source depth (z_o), keeping r_o, r_∞, and v_{exit} constant. For temperatures to fall to 300 °C, fig. 6.11a indicates that z_o must have increased to ~1000 m ($v_{exit} = 100$ m s^{-1}) or ~200 m ($v_{exit} = 10$ m s^{-1}).

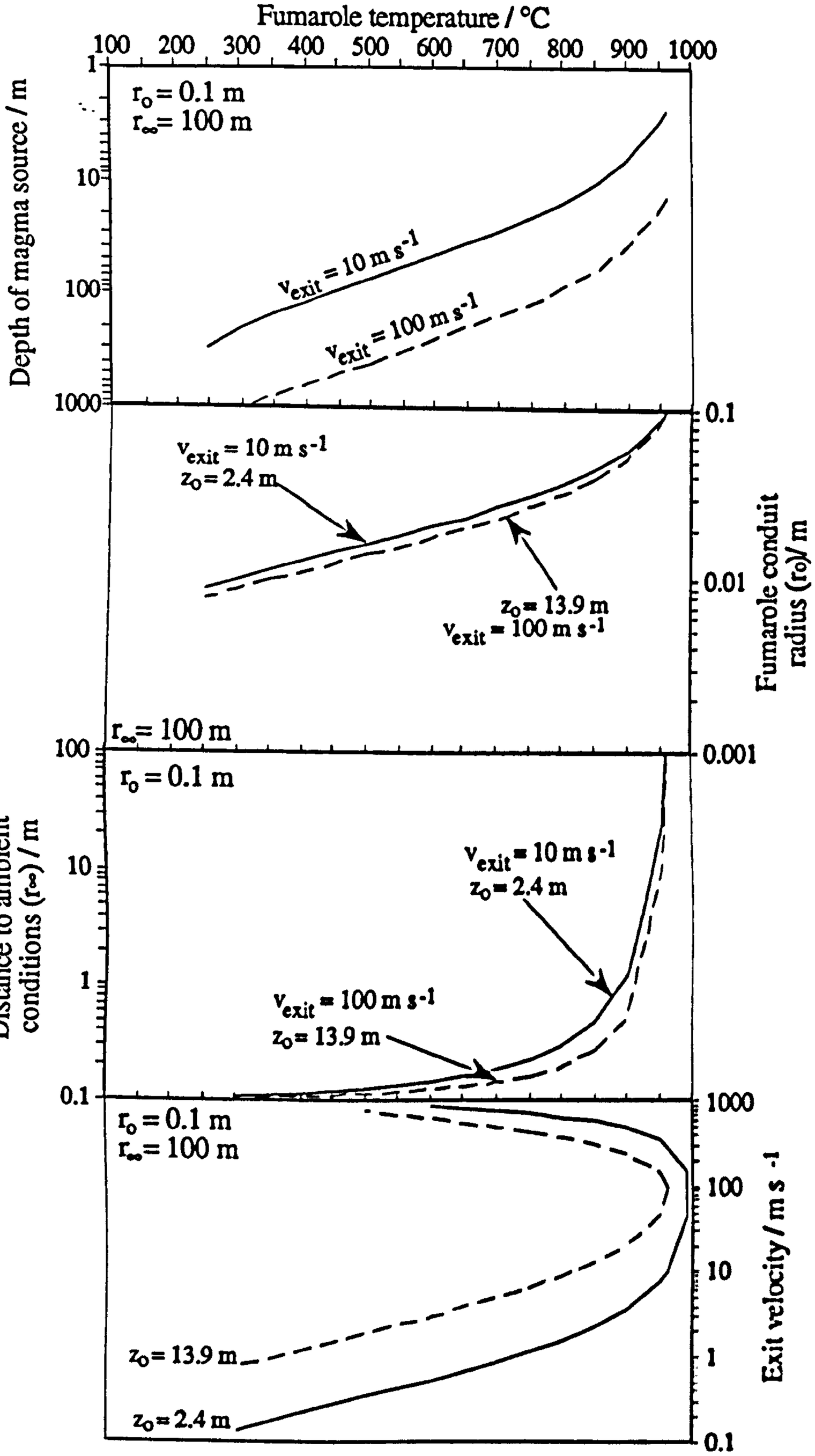

Figure 6.11 *The effect on fumarole temperature of varying: (a) depth to magma source (z_o); (b) conduit radius (r_o); (c) distance to ambient conditions (r_∞); and (d) exit velocity (v_{exit}).*

Fig. 6.11b shows the effect of reducing the conduit radius, keeping z_o, r_∞, and v_{exit} constant. Temperatures will fall to 300 °C if the radius is reduced by approximately one order of magnitude (i.e. from 0.1 m to ~0.01m) for both exit velocities.

Fig. 6.11c shows the effect of reducing r_∞, whilst keeping z_o, r_o, and v_{exit} constant. There is little affect until ambient conditions are reached at only a few conduit radii from the fumarole, then q_{cond} is strongly affected by small encroachments. If this is the only cause of cooling to 300 °C, a dramatic reduction of r_∞ from 100 m to 10.6 cm (i.e. ambient conditions within 6 mm of the conduit wall) if v_{exit} = 100 m s^{-1}, or ~11 cm (10 mm from the wall) if v_{exit} = 10 m s^{-1}.

Fig. 6.11d shows the effect of a varying exit velocity, keeping z_o, r_o, and r_∞ constant. This figure illustrates that exit temperatures peak at an exit velocity of ~100 m s^{-1}. Therefore the fumarole with an initial exit velocity of 10 m s^{-1} can actually slightly increase in temperature from 960 °C if the exit velocity increases, up to ~100 m s^{-1}. At velocities higher than this, temperatures decrease because heat energy is converted to kinetic energy in order to accelerate the gas. The maximum amount of cooling for fast gases is dictated by the point at which the velocity reaches the speed of sound in the gas, at ~700-800 m s^{-1}. Decreasing the exit velocity below ~100 m s^{-1} also results in cooling, and this is probably more typical of a temporally cooling fumarole field. A reduction of exit velocity from 100 m s^{-1} to ~0.8 m s^{-1}, or from 10 m s^{-1} to ~0.1 m s^{-1} will reduce temperatures from 960 °C to 300 °C.

As mentioned earlier, the calculated pressures at the base of the fumarole conduit are only slightly above atmospheric pressure. This suggests that rapid, irreversible (Case II) decompression occurs as the gas escapes the magma, with essentially no drop in temperature. After this rapid decompression, the gas then rises to the surface, with behaviour as described by case III.

6.6 A new degassing model for shallow intrusions

Many volcanoes produce significant magmatic gas fluxes during periods with little or no associated eruption of magma (e.g. Etna (Allard et al., 1991), Ruiz (Williams et al., 1990),

Mt. St. Helens (Casadevall et al., 1983), White Island (Rose et al., 1986)). The degassing models of Eichelberger et al. (1986) and Jaupart and Allègre (1991) consider a magma conduit with a continuous upwards flow of magma. As stated in section 6.4, the gas flux into Poás and Ruapehu lakes can be produced from a relatively small magma conduit (~2.5 m radius), but this would imply large volumes of erupted magma (~5000 kg s^{-1}). No magmatic eruptions have been recorded at Poás over the period considered, and only minor volumes of magma have been intermittently erupted at Ruapehu.

In chapter 4, four models for producing the heat outputs observed at Poás and Ruapehu were put forward (tables 4.1, 4.2). The degassing model (III) suggested that ~0.004-0.08 km^3 a^{-1} (~300-6000 kg s^{-1}) of 4 wt.% H_2O magma (twice these rates for 2 wt.% H_2O) was required to degas to sustain the power outputs observed. Such large volumes are very unlikely to represent intrusions that reach near enough to the surface (<1 km) to degas effectively. Large intrusive volumes would be likely to produce large scale deformation and seismicity, and would also be seen by other geophysical monitoring techniques. More extreme examples of this problem are seen at other volcanoes. For example, at Nevado del Ruiz volcano, SO_2 fluxes have remained at levels of between 10^3 and 10^4 t d^{-1} since the 1985 eruption (Williams et al., 1990). Isotopic studies of the SO_2 suggest that its most likely source is a magma reservoir (Williams et al., 1990). Such large and prolonged gas fluxes suggest a minimum magma volume of between 0.92-9.2 km^3 has degassed over the period 1985-89 (Williams et al., 1990). The absence of large-scale deformation around the summit of Ruiz led Williams et al. (1990) to suggest that a large, shallow crystallising chamber was present.

An alternative possibility to this suggestion is that a large volume of magma at depth can degas by magma circulation between the deep magma and a minor shallow intrusion (S. Blake, pers. comm.). A model has been developed of this situation, the basis of which is defined in fig. 6.12. A large chamber at depth has a pipe connecting it to the near surface environment. The exsolution pressure for water in the magma is crossed part way up the pipe. Thus magma above this level will vesiculate until the melt reaches the saturation level

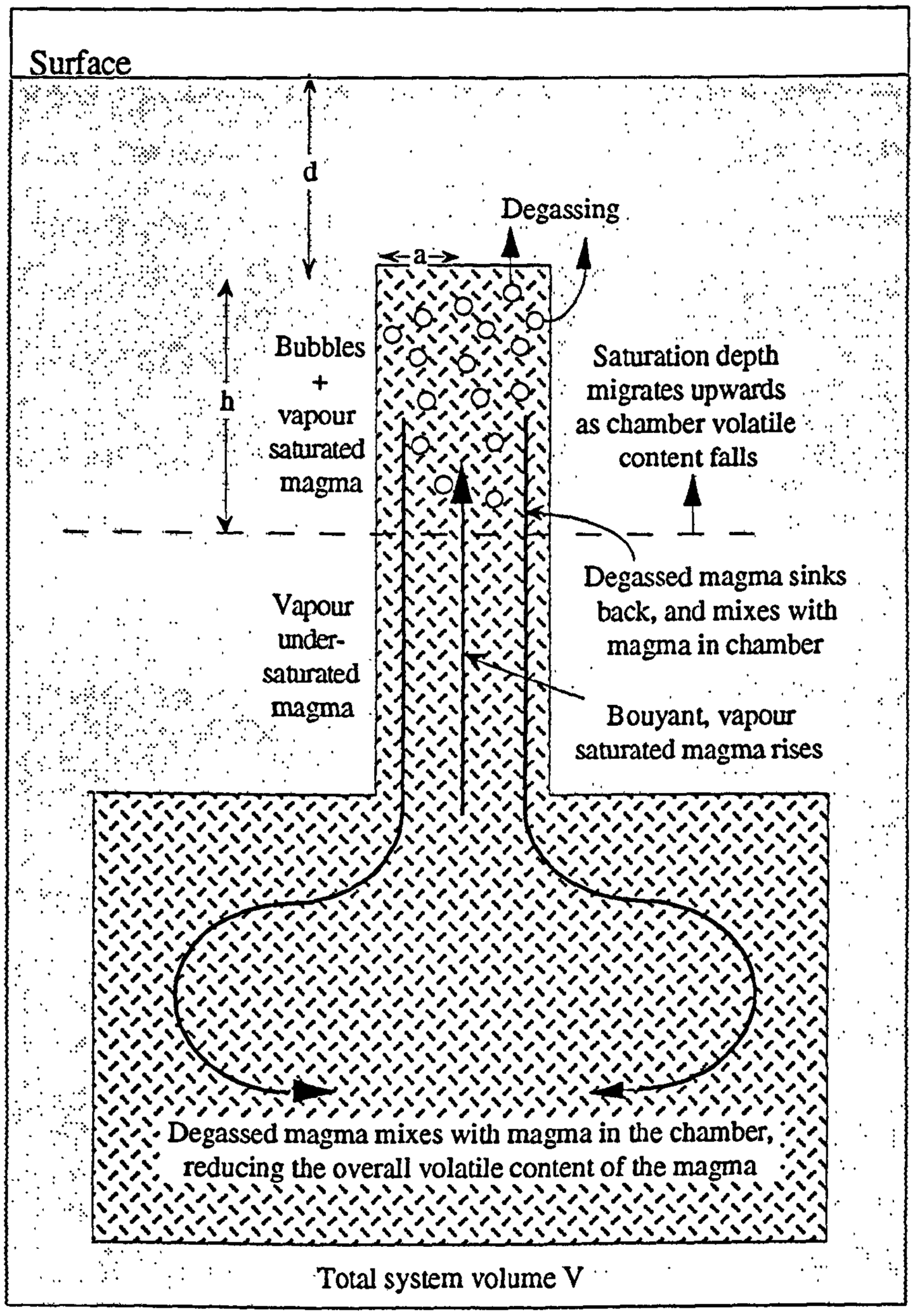

Fig 6.12 *Schematic diagram of the problem considered. A pipe, radius a, is connected to a magma chamber. The magma volatile saturation pressure occurs at a depth h from the top of the pipe. Above this level, gas is exsolved from the magma, and lost to the surrounding system. The denser, degassed magma sinks back down the conduit and mixes with the magma in the chamber. Buoyant, volatile rich magma rises up the pipe. The saturation depth, h gradually decreases with time, until the whole chamber is degassed to the volatile saturation content dictated by the pressure at the top of the pipe.*

for the pressure. The gas is assumed to be lost from the vesiculated magma near the top of the pipe. The degassed melt will have increased in density (equation (6.8)), thus will tend to sink back down the pipe, to be replaced by buoyant, volatile-rich magma. The volumetric flow rate (Q) for such a process will take an analogous form to that of the pipe-flow equation, yielding:

$$Q = \frac{C_1 a^4 g \Delta\rho}{\mu} \quad (6.22),$$

where C_1 is a constant, a is the pipe radius, g is the acceleration due to gravity, $\Delta\rho$ is the density difference between rising volatile-rich and descending degassed magma, and μ is the viscosity of the more viscous of the two magmas.

Laboratory experiments were carried out using golden syrup in a glass tube to find a value for C_1 (S. Blake, pers. comm.). A column of dense, viscous fluid (neat syrup) was emplaced above a column of less dense, less viscous fluid (diluted syrup). The fluids overturned, with the lower fluid intruding the upper, at a near constant flow rate. Three experiments were carried out, using a variety of density and viscosity contrasts, and different pipe radii. The value of C_1 was found to be ~0.03.

The density contrast and viscosity will vary in the vesicular region of the pipe, because of the varying gas volume fraction and volatile content (equations 6.8, 6.9, 6.10). Assuming a constant value of radius with depth, the long-term value of Q will be limited by the minimum value of $(\Delta\rho / \mu)$ at any level within the pipe. For example, in fig. 6.2d, the variation of $(\Delta\rho / \mu)$ with depth is shown for the vesicular part of the conduit, assuming completely closed system behaviour. Two curves are plotted, one using the viscosity of the rising bubble rich magma, and one using the viscosity of the descending degassed magma. At high vesicularities, the viscosity of the rising magma exceeds that of the descending magma, however, the minimum value of $(\Delta\rho / \mu)$ occurs within the lower, unvesiculated part of the pipe. This raises the possibility that the upper part of the conduit may overturn rapidly, perhaps producing a gas outburst, then wait for the lower part of the conduit to overturn. Partly open system behaviour, i.e. leaky pipe walls, will also affect the value of $(\Delta\rho / \mu)$ in

the vesicular part of the pipe. Such complications are ignored in the present study, but are possible areas of further research.

The descending, partly degassed magma is assumed to mix with a deep, volatile-rich magma reservoir, lowering the volatile content of the chamber. Thus the rising magma has a gradually decreasing volatile content with time (assuming the deep chamber is not replenished from below). Circulation will cease when the volatile content decreases to the point when vesiculation does not occur in the pipe.

The gas flux leaving the conduit can be found by simply multiplying the upwards mass flux of magma by the difference in ascending and descending volatile mass fractions (x_a, x_d):

$$Q_{H_2O} = Q \rho_l (x_a - x_d) \qquad (6.23),$$

where ρ_l is the density of the volatile-rich, bubble-free, ascending magma, and the descending volatile mass fraction is given by:

$$x_d = s (P_{top})^n \qquad (6.24),$$

where s and n are constants (c.f. equations (6.1a-c)), and P_{top} is the pressure at the top of the pipe.

Calculations are performed in an iterative way, choosing time steps smaller than the time taken for the magma in the degassing zone of the pipe to be replaced, given by:

$$\Delta t \leq \pi a^2 h / Q \qquad (6.25).$$

In all cases, the model predicts approximately exponential decreases in gas flux with time, as observed at Mt. St. Helens 1980-82 (Casadevall et al., 1983) and Augustine 1986 (Symonds et al., 1990). Fig. 6.13 shows three model outputs, for a basaltic andesite magma in a pipe of radius 6 m attached to a chamber of volume 0.1 km^3. The three lines in fig. 6.13 correspond to three different depths to the top of the pipe. This affects the results because the magma will lose a greater proportion of its volatiles for shallow depths to the pipe top (equation 6.24), hence more gas will tend to be liberated. But working against this effect is the fact that for greater pipe depths, degassed magma viscosity will decrease with increasing

residual volatile content (equation 6.10). This is illustrated in fig. 6.14, where the initial flux from the pipe is shown against the depth to the top of the pipe, for three different initial water contents. All the plots show a peak at a certain depth; above this depth, the effect of increasing viscosity outweighs the advantage of the release of proportionally more gas. Below this depth, the decrease in the proportion of gas released outweighs the effect of decreasing viscosity. The flux falls to zero at the saturation pressure for the amount of the

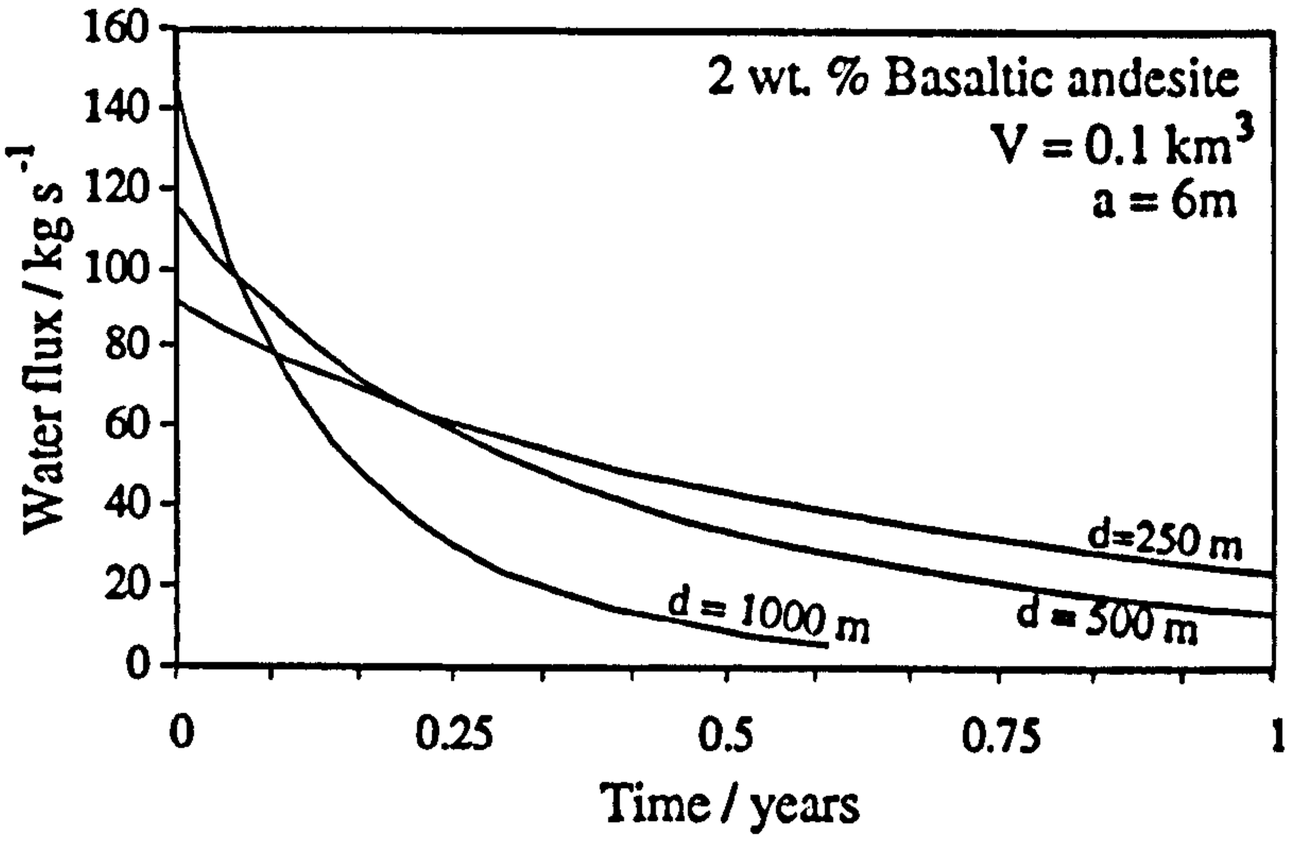

Fig. 6.13 *Model outputs from the pipe degassing model for the input parameters shown. The output fluxes and timescales shown are typical of possible degassing events at Poás (e.g. 1978, 1979) and Ruapehu (e.g. 1985-89).*

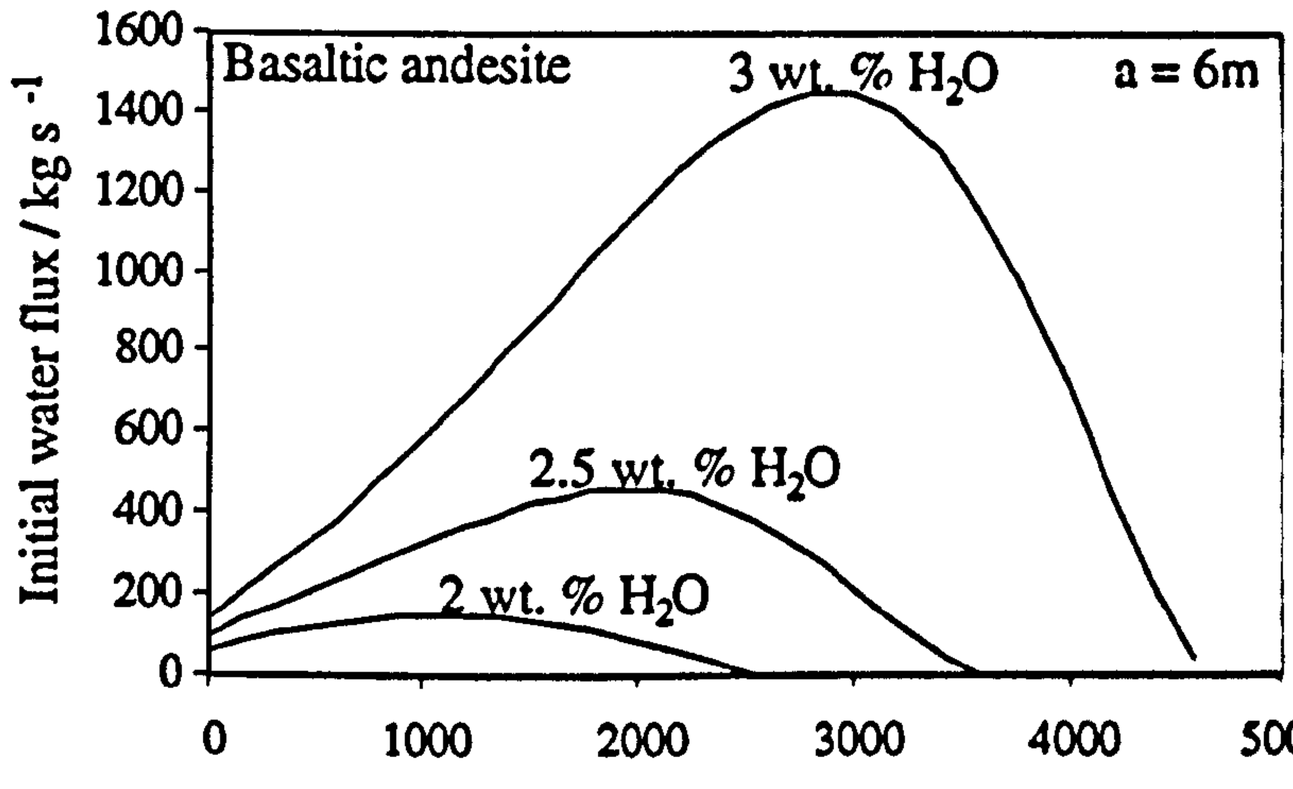

Fig. 6.14 *Variation of the initial water flux with the depth to the top of the pipe, for initial water contents of 2, 2.5, and 3 wt.%. See text for discussion.*

volatile. Lithostatic pressure gradients with a country rock density of 2500 kg m^{-3} are assumed in figs. 6.13 and 6.14.

The gas flux is proportional to the radius to the fourth power, i.e. doubling the radius increases the flux 16-fold; in addition, the decay time is reduced 16-fold. Changing the chamber volume simply changes the decay time proportionately.

6.6.1 Application of the new degassing model to Mt. St. Helens

The model has been applied to the well-studied degassing regime following the May 1980 Mt. St. Helens eruption. SO_2 fluxes following the major eruption were measured, using a COSPEC, from July 1980 onwards (Casadevall et al., 1983). A geochemical model for the evolution of magmatic gas composition at Mt. St. Helens has been developed by Gerlach and Casadevall (1986). Using the evolution of the H_2O/SO_2 ratio given by Gerlach and Casadevall (1986), approximate magmatic H_2O fluxes can be calculated from the SO_2 fluxes. An equation for the variation of the viscosity of Mt. St. Helens 1980 dacite with water content, using the glass composition given by Rutherford et al. (1985), a crystal content of 40 vol.%, and a temperature of 930 °C, is given by:

$$\mu_m = 10^{(8.86 - 113\,x + 6.63\,x^2)} \qquad (6.26)$$

The model was then applied, using an initial magma water content of x = 0.046 (Rutherford et al., 1985). The initial water flux is independent of the volume of the system. The approach taken was to use various fixed values of d (250, 500, 1000 m), and then find the pipe radius required to fit the peak flux of ~1100 kg s^{-1} of magmatic H_2O. The decay times of these different combinations of d and a was then calculated for various values of the total system volume, V. Results are shown in fig. 6.15. The squares in fig. 6.15 represent values of the magmatic H_2O flux from Mt. St. Helens during 1980-81, and have typical error bars of ±40 %. The results indicate that if the depth to the top of the circulating pipe (d) is between 250 m and 1 km, the radius of the conduit should fall in the range ~35-50 m, and the chamber tapped has a volume of ~0.5-1 km^3.

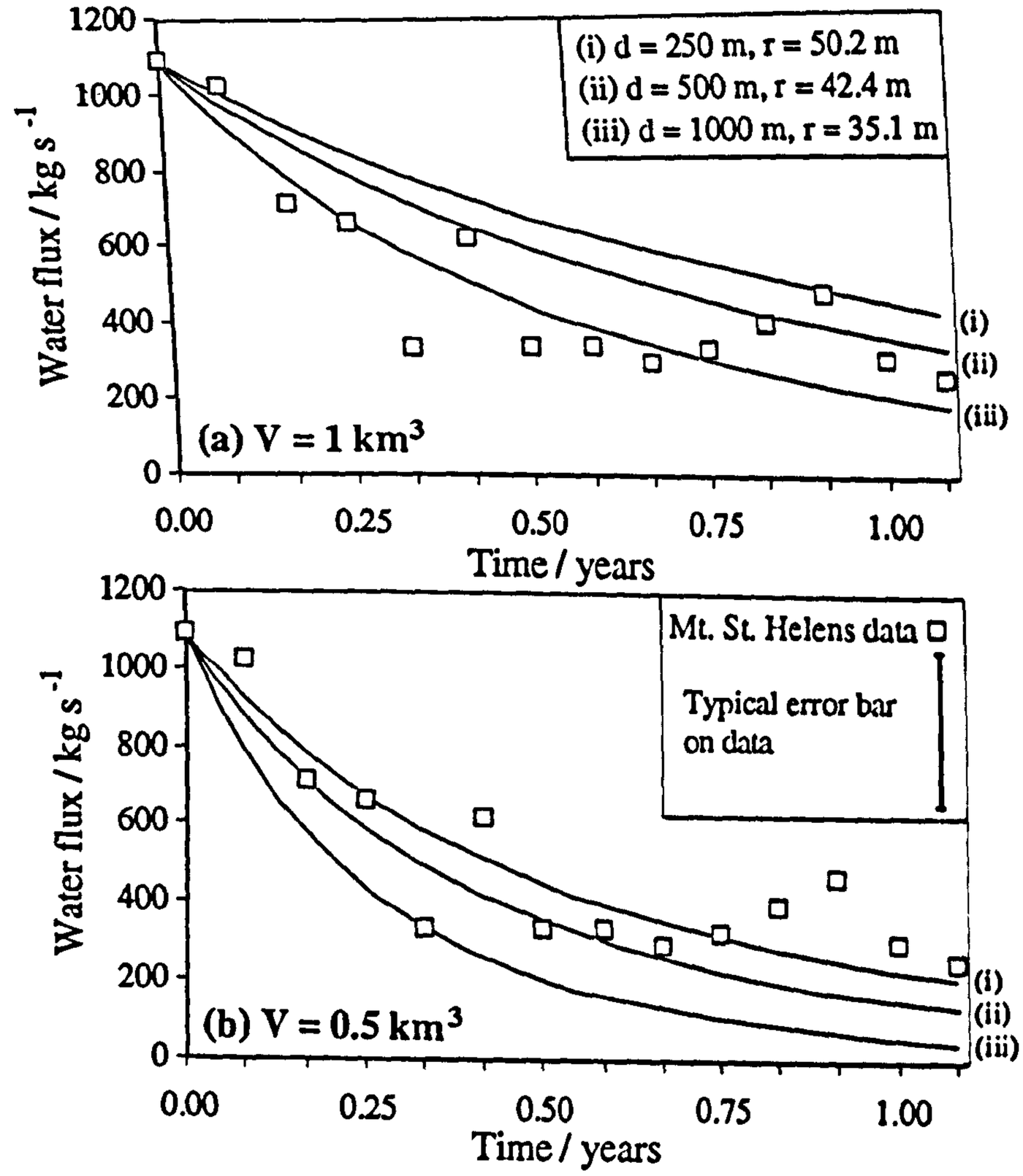

Fig. 6.15 *Comparison of model outputs and observed gas fluxes at Mt. St. Helens, 1980-81. Errors on the data are ±30-40 %. (a) Assuming a total system volume of 1 km³; (b) V = 0.5 km³.*

Scandone and Malone (1985) developed a physical model of the feeding system of Mt. St. Helens during 1980. They suggested that a deep magma reservoir, of volume ~10-20 km³, at 7 to 9 km depth, was connected to the surface by a conduit of radius ~50 m. Carey and Sigurdsson (1985), from their model of the dynamics of the plinian phase, suggested that a deep (below the saturation level of the magma) conduit of diameter ~95 m fed the eruption of May 18th, 1980. Thus the conduit dimensions derived from the degassing model are consistent with previous models. The calculated chamber volume, however, is an order of magnitude smaller than that suggested from geophysical evidence. This perhaps reflects the fact that downflowing magma only mixed with the upper part of the chamber, or that the chamber is actually subdivided into smaller components (c.f. Kilauea magma chamber, Ryan, 1988).

6.7 Implications for Poás and Ruapehu

From the evidence of inputs of HCl at both Poás and Ruapehu lakes, and from the presence of high temperature fumaroles at Poás, magmatic degassing is thought to have occurred, at least intermittently, at both volcanoes. Degassing often accompanies and follows magmatic eruptions at Ruapehu (e.g. 1971). Using inferred Cl contents of the magma, it was shown in chapter 4 that very large volumes of magma need to be degassed to produce the observed influxes of Cl. For example, during the 1971 activity at Ruapehu, degassing of ~3000 kg s^{-1} of 4 wt. % water magma, with 0.08 wt. % Cl was needed, or even higher rates if the Cl content is lower. The magma volumes involved are unlikely to represent stagnant intrusions, because of the large size required, and the lack of supporting geophysical evidence.

Instead, it is proposed that small intrusions, emplaced into the permeable hydrothermal system rocks, rapidly degas, and internally circulate, removing the denser, degassed magma downwards, replacing it with buoyant, volatile-rich magma. This process could be terminated by hydrothermal infiltration of the intrusions (see chapter 5), effectively freezing them, or by the reduction in volatile content of the circulating magma system to the point where vesiculation no longer occurs. Magmatic gas bursts of ~100 kg s^{-1} H_2O, exponentially decaying with a half-life of one or two months are typical of lake heating periods of Poás and Ruapehu. Such bursts can be produced by the emplacement of small pipe-like intrusions, of radius ~6 m, at depths of a few hundred metres, tapping deep (a few km) magma volumes of ~0.1 km^3 (e.g. fig. 6.13). Longer lived events could reflect either multiple intrusions, or the tapping of larger deep volumes, or smaller pipe radii, or possibly intrusions reaching to shallower depths (e.g. d=250m in fig. 6.13), which cause the degassed magma to be dryer, and hence more viscous.

The high temperature fumaroles at Poás can be used to estimate the depth of the magma source, using the fumarole model (Case III) presented in section 6.5. Using a distance to ambient temperatures (r_∞) of 100 m and a fumarole conduit radius (r_o) of 10 cm, and assuming exit velocities are such that they give the maximum depth to magma, then estimated depths to magma at 1000 °C are shown in fig. 6.16. This implies very shallow

magma was emplaced in late 1980, and remained until at least early 1985. New shallow magma was intruded in mid-1986, remaining hot until mid-1988. The short-term variation in the inferred depths perhaps reflects new intrusions, but probably just fluctuations in either the hydrothermal regime overlying the magma (i.e. r_∞ or T_∞), or variation of the fumarole conduit radius (r_0), or the exit velocity.

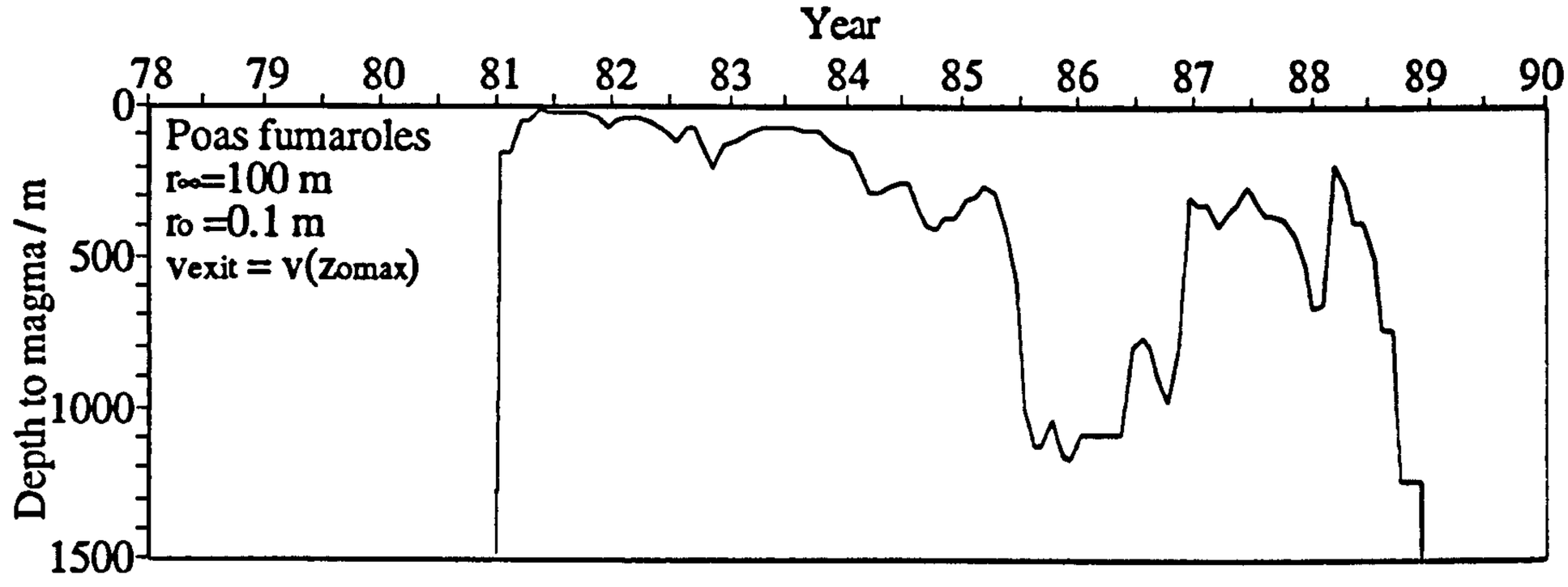

Fig. 6.16 *Calculated depths to magma at Poás, inferred from the fumarole temperatures in fig. 3.5, using the fumarole model (Case IIIb) developed in section 6.5, using parameters so as to maximise the depth of source (i.e. these depths are maxima).*

CHAPTER 7

Conclusions and Implications

7.1 A model for crater lake systems

A general model of a crater lake system was developed in chapter 2. Mass, energy, and chemical flows into and out of the lake were balanced, forming three equations (2.1, 2.2, and 2.6), with five unknowns: the steam/brine input rate ($M_{st/br}$); the overflow/seepage rate (M_{os}); the chemical content of the steam/brine ($[X]_{st/br}$); the enthalpy of the steam/brine ($H_{st/br}$); and the rainfall/meltflow input rate (M_{rm}). In order to solve the three equations, two of these 'unknowns' must be constrained as tightly as possible from independant sources. Input data required by the model are: the temporal variation in lake temperature, chemical content, and level, which combined with the shape of the lake basin give the lake's surface area and volume; and average values of windspeed, humidity and air temperature above the lake.

In chapter 4, the generalised model was applied to data sets from the crater lakes of Poás and Ruapehu. The model was run using various assumed values of incoming fluid enthalpy and minimum rainfall, within sensible ranges. These two variables were then constrained by considering model outputs of incoming fluid chemistry and calculated rainfall, for the various different input values. At both volcanoes, the incoming hydrothermal fluid usually had a significant magnesium content (figs.4.7 and 4.17), requiring the presence of a brine component, since steam carries negligible quantities of metal ions. This suggested that the inflowing fluid enthalpy must lie somewhere between that of hot brine (~0.8 MJ kg^{-1}) and saturated steam (~2.75 MJ kg^{-1}). An enthalpy value of 1.8 MJ kg^{-1} was consistent with model outputs at both volcanoes, and was the assumed value used at Poás and Ruapehu. This enthalpy corresponds to an input of ~50 wt.% brine and ~50 wt.% steam. It is likely that these proportions vary with time; however, this variation cannot be discerned from the data, so the same value was used over the whole period modelled. Minimum rainfall estimates were constrained by increasing them until model outputs of the rainfall mass inflow rate did not contain significant spikes. Given that rainfall data are recorded at Poás,

the only variable is the catchment area; this method suggested a catchment area of ~6 x 10^5 m^2 at Poás, and an average rainfall influx of ~75 kg s^{-1} at Ruapehu, peaking at ~150 kg s^{-1} in summer, and falling to ~0 kg s^{-1} in winter; all of these values are reasonably consistent with values expected from simple inspection of the summit topography and local rainfall values.

The calculated power input to the lake at Poás varied between ~100-500 MW over the period 1978-89 (fig. 4.11). This corresponds to a heat flux of ~100-5000 W m^{-2} from the lake surface, which is also probably typical of the heat flux through the system beneath the lake. Values for the power input to Crater Lake, Ruapehu, over the period 1966-89 (fig. 4.20), show variations between ~50-1000 MW, suggesting a heat flux of ~10^2-10^4 W m^{-2} through the sub-lake system. These heat fluxes were used in chapters 5 and 6 to constrain possible heat transfer processes operating beneath the lakes.

Additional constraints were derived from the lake chemistry. Increases in total lake chloride (figs. 4.5b, 4.14b) were interpreted as periods of magmatic HCl addition to the system, allowing magmatic gas fluxes to be calculated. Net HCl influxes of up to ~2 kg s^{-1} were observed. Using typical weight ratios of $HCl:H_2O$ in magmatic gases of ~1:50, and assuming a magma with a water content of 2-4 wt.%, this implies magma degassing rates of up to ~5000 kg s^{-1}, or ~0.06 km^3 a^{-1}. These rates of degassing would supply up to ~400 MW as hot magmatic gas, suggesting that degassing can provide a large proportion of the power during some periods.

7.2 Heat transfer processes

The ultimate source of volcanic heat must be magma crystallising, cooling, and perhaps degassing. Magmatic degassing has been considered separately in this study.

7.2.1 Hydrothermal infiltration of magma

A conductive boundary layer will exist over all of the contact between hot magma and cool country rock. A spatially fixed CBL is not thought to be a possibility for a heat flux of 10^4 W m^{-2}, because underlying andesitic magma will not supply sufficient heat by convection

alone, and if crystallisation occurs directly beneath the conductive boundary, the layer will thicken, reducing conduction. Crystals could settle from the roof of the magma body, but this is only an efficient process for low viscosity magmas. The most likely heat transfer mechanism is thought to be infiltration of the CBL by the overlying hydrothermal system, inducing crystallisation at the same rate, thus maintaining a constant thickness, downwards migrating CBL. This releases specific and latent heat directly into the hydrothermal system. Power outputs of 10^2-10^3 MW are produced by crystallisation and cooling of ~10^2-10^3 kg s^{-1} of magma. Infiltration rates of ~1-100 m a^{-1} into CBL's of thickness ~30-0.3 m provide heat fluxes of ~10^2-10^4 W m^{-2}.

In chapter 5, two previous models of infiltration (Lister, 1974, 1983; Hardee, 1980, 1982) were combined to produce a new model. The new model relates the permeability created by the cracking process (Lister, 1974), to the permeability required for sufficient convection within the hydrothermal system to remove the heat flux exiting the boundary layer (Hardee, 1982). A relationship between infiltration velocity and cracking temperature is predicted by the new model (fig. 5.6). The cracking temperature is the temperature at which contractional cracks induced by cooling are not closed by rock creep, and remain open. Previous infiltration models have either assumed a range of possible cracking temperatures (Lister (1974, 1983): 427-627 °C), or ignored the fact that cracking occurs (Hardee, 1980, 1982). In the new model, the cracking temperature can be anywhere between that of the magma (at high infiltration rates), and that of the overlying hydrothermal system (at low infiltration rates) (fig. 5.6). The infiltration velocity reaches a maximum value when the cracking temperature equals the magma temperature. Basalt near the surface (i.e. overlain by a 2PZ at ~100 °C) has a predicted maximum infiltration velocity of ~300 m a^{-1}, very close to the value observed when a lava flow from Heimaey, Iceland, was sprayed with water for two weeks. Andesite magma overlain by a 2PZ at ~250 °C, has a predicted maximum infiltration rate of ~800 m a^{-1} (fig. 5.6). These maximum rates will be less if the 2PZ is not working at optimum efficiency for its permeability. Optimum efficiency occurs at a certain liquid:vapour ratio for a given temperature within the 2PZ, defined by the properties of the hydrothermal fluid (see section 5.4).

Cracking will occur within the CBL, and the cracks will be filled with stagnant superheated steam. The Rayleigh number within the cracked region was calculated for the complete range of infiltration velocities and cracking temperatures (fig. 5.9), and never exceeded its critical value. Therefore conduction will still dominate the cracked region, and it can still be considered part of the CBL. The thickness of the cracked region has been calculated to be only ~5-15 cm (fig. 5.8) over the range of conditions appropriate for Poás and Ruapehu, and it only represents a significant proportion of the CBL at high infiltration velocities ($>\sim$100 m a^{-1}).

At high infiltration rates, crystallisation may be inhibited, leading to glass formation, and no release of latent heat. This was modelled in chapter 5 by setting the pre-existing phenocryst mass fraction (f) to near one. As a value of f=1 is approached, the bottom of the CBL is undefined, as the whole magma body looks like crystallised, 1000 °C magma. Using f=0.99, the model predicts that the infiltration velocity becomes essentially unlimited, with the cracking temperature asymtotically approaching the magma temperature (fig. 5.6). A slightly thicker cracked region is produced (fig. 5.8), but Rayleigh numbers remain sub-critical (fig. 5.9). Glass formation is not thought to normally occur at Poás or Ruapehu, but may be induced during some very high heat flux events.

The bulk of a high heat flux hydrothermal system is likely to be a two-phase zone, because single phase liquid or vapour zones have much lower heat transfer capabilities, due to their much smaller contrast in density and enthalpy between upflowing and downflowing fluids. Hardee's (1982) model of a 2PZ yields the optimum liquid volume fraction as a function of temperature (fig. 5.10), and also the liquid volume fraction profile through a steady-state system limited by the layer with the lowest heat transfer capability. The latter constraint imposes non-optimum conditions throughout the rest of the 2PZ (fig. 5.11). The model gives two possible solutions for the liquid volume fraction within the non-optimized part of the 2PZ, one a vapour-rich root, and the other a liquid-rich root. Hardee (1982) only considered the vapour-rich root. Profiles of temperature, pressure and liquid volume fraction against depth through theoretical steady-state, constant area, and constant permeability 2PZ's are given in figs. 5.12 and 5.13. The profiles suggest that the heat fluxes at Poás and

Ruapehu can be produced within country rock of permeability ~10^{-10}-10^{-14} m^2 (these permeabilities will be created by the cracking process), with a down-going liquid volume fraction of ~0.05-0.4 in the vapour-rich case (and an up-flowing vapour volume fraction of ~0.95-0.6), or $\gamma \approx 0.35$-0.95 in the liquid-rich case. Pressures gradients will be close to hydrostatic in a liquid-rich 2PZ, and less in the vapour-rich 2PZ. Temperatures will remain on the saturation (Clapeyron) curve for a given pressure.

In summary, to produce a flux of 10^2-10^4 W m^{-2}, as at Poás and Ruapehu, the CBL must migrate at ~1-100 m a^{-1}, and have a thickness of ~30-0.3 m, with an upper cracked region of thickness ~8-4 cm. The overlying hydrothermal system must have permeabilites in the range ~10^{-10}-10^{-14} m^2, depending upon the heat flux, and the temperature (and hence pressure) at the top of the 2PZ. This is likely to be controlled by the depth of the lake; deeper lakes will have higher bottom pressures, thus the underlying hydrothermal system can supply the heat flux with a lower permeability.

7.2.2 Magmatic degassing

Magma vesiculation and advection of heat by degassing were considered in chapter 6. Volatile solubility in magmas decreases with decreasing pressure (fig. 6.1), thus a magma will become super-saturated in a volatile if sufficient decompression occurs, or if the magma crystallises enough volatile-poor phases, increasing the volatile concentration in the remaining melt. Super-saturation is a pre-requisite for vesiculation, and, once a bubble forms, it will tend to rise at its terminal velocity (equation 6.2). Thus bubbles will tend to accumulate at the roofs of vesiculating magma bodies, slowing their ascent as they enter the more viscous, cooler magma in the CBL (fig. 6.4). Gas will escape given a suitable route and a driving pressure gradient. Within the magma, gas bubbles will remain at magmatic temperatures (~1000 °C) and pressures. Magma pressure must exceed lithostatic for intrusion to occur, thus a newly emplaced intrusion should be at near lithostatic pressures. In contrast, fluid pressures within a surrounding hydrothermal system are likely to be near hydrostatic (e.g. figs. 5.12 and 5.13); thus a large pressure difference will exist between gas inside and outside a new intrusion. Mechanisms of gas escape are poorly understood at present, but fractures created by rapid hydrothermal infiltration (chapter 5) may provide

pathways that will open at near magmatic temperatures, allowing the escape of hot gas. The high pressure differential at the boundary may also facilitate cracking. Significant gas escape can probably occur through the walls of a magma conduit emplaced into a sufficiently permeable country rock (figs. 6.7 and 6.8), although the permeability in the contact region is likely to show rapid temporal and spatial variation. Once gas has left the magma, it will rapidly decompress. A fluid dynamic model of compressible gas flow in a rough conduit with conductive heat losses to the walls was developed in section 6.5. Results from the model suggest that high temperature fumaroles originate from shallow magma, e.g. 500 °C fumaroles indicate magma at depths less than ~300 m (figs. 6.11a, 6.16).

Calculated values for the chloride input to both Poás and Ruapehu lakes suggest the addition of magmatic HCl over some periods (chapter 4). This is not suprising, since some of these periods are associated with magmatic eruptions at Ruapehu, and high temperature fumarolic activity at Poás. However, the calculated volumes of magmatic HCl, and estimated degassed magma volumes are much larger than expected, and require large, shallow intrusions, e.g. ~0.01 km^3 during the 1971 eruption of Ruapehu. Geophysical evidence suggests that such large intrusions have not occurred. One method of bringing a larger magma volume close to the surface is if recirculation of magma within a small intrusion can occur (fig. 6.11). The increase in density associated with loss of volatiles (equation 6.8) suggests that degassed magma will tend to sink, whilst volatile-rich magma will rise. A model has been developed of the circulation within, and the gas flux from, a pipe-like intrusion that extends from a deep magma reservoir to close to the surface. Results from the model suggest that the degassing rates observed can be modelled as pipe-like intrusions of diameter ~10 m, connected to deep reservoirs of magma of volume >~0.05 km^3.

Whilst high gas fluxes are emanating from such intrusions, hydrothermal infiltration may be inhibited by the insulating vapour 'cushion' surrounding the intrusion. However, infiltration and crystallisation will probably occur as gas release wanes, perhaps accelerating the demise of degassing. The relationship between gas release and infiltration is an area requiring further work.

7.3 A model for activity at Poás 1978-1989

The four most instructive diagrams for the interpretation of activity at Poás are the depth to magma (fig. 6.15), the total Cl content of the lake (fig. 4.5b), the power input to the lake (fig. 4.11a), and observed eruptions (fig. 3.4), summarised in fig. 7.1. Heat is believed to be transferred at Poás through hydrothermal infiltration of magma feeding two-phase hydrothermal convection, augmented by periods of magmatic degassing. Some seepage from the lake forms the down-going fluid in the two-phase zone, and is returned as vapour, in zones of high heat flow. Other seepage is heated and returned to the lake without vaporisation, probably within brine-only zones located away from regions of high heat flow.

The inferred depth to magma (fig. 7.1a) indicates that an intrusion was emplaced to within a few metres of the surface of the cone in late 1980. Intrusive activity may have commenced as early as July 1980, when an A-type seismic swarm was observed, and the power input to the lake (fig. 7.1c) started increasing. A magma degassing rate of at least 1000 kg s^{-1} over the four years 1981-84 is suggested by the observed gas flux in 1982 (Casadevall, 1984a), and the inferred magmatic gas input to the lake during 1983-85 (fig. 7.1b), implying a minimum degassed magma volume of ~0.05 km^3. Modelling predicts (chapter 6) that a small, internally circulating intrusion (a pipe of radius ~5m) of 2 wt.% H_2O basaltic andesite, reaching to within a few metres of the surface, connected to a deeper magma volume (>0.05 km^3), could supply gas at the required rate (e.g. fig. 6.12).

The depth to magma increased to ~1 km in mid-1985 (fig. 7.1a), and net HCl input to the lake ceased (fig. 7.1b), suggesting that the upper part of the 1980/81 intrusion had become largely solidified. This period of declining activity ended in 1986, when increased A-type seismicity between February and May preceded a rise in lake power input (fig. 7.1c), a rise in fumarole temperatures (and hence a decrease in inferred depth to magma (fig. 7.1a)), and a net input of HCl to the lake (fig. 7.1b). This is interpreted as a period of new intrusion and degassing, centred on the cone/southern lake area, with a magma degassing rate of over 2000 kg s^{-1} (assuming a 2 wt.% water magma). This can be modelled in a similar way to the 1980/81 intrusion, as recirculation within a pipe of diameter ~10 m.

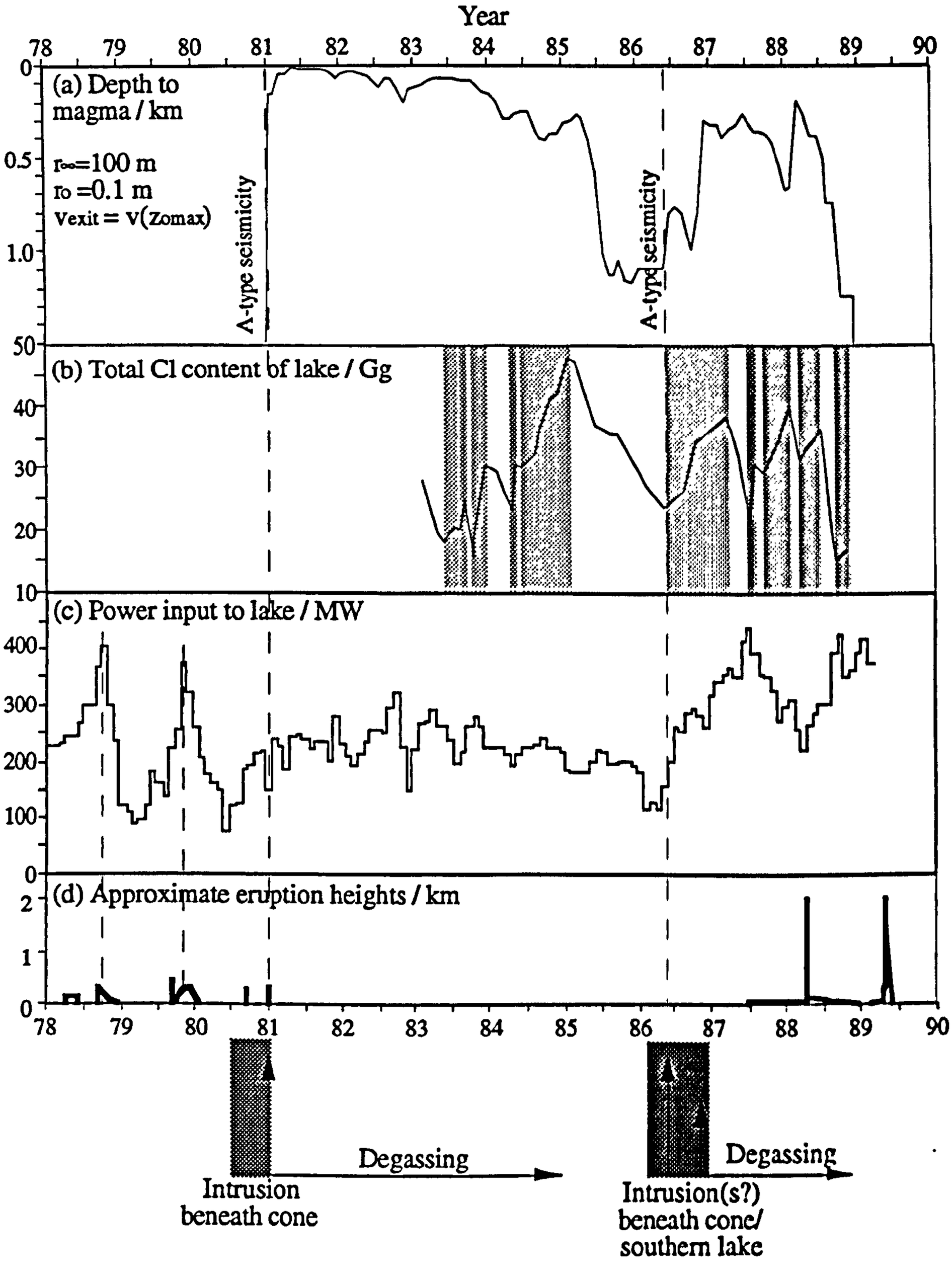

Fig. 7.1 *Summary diagram for Poás: (a) inferred depth to magma (fig. 6.16); (b) total Cl content of lake, with shading indicating periods of increase (fig. 4.5b); (c) calculated power input to the lake (fig. 4.11a); and (d) approximate eruption heights (fig. 3.4). The shading in the lower diagram indicates the time window of possible intrusion, with the vertical arrows indicating the most likely times, followed by degassing.*

However, presumably because the intrusion was closer to the lake, the effect on the lake was much more significant, with heating to 70 °C by mid-1987, accompanied by a fall in level of ~20 m, the resumption of phreatic activity (fig. 7.1d), and eventually the complete removal of the lake by April 1989. The fall in lake level is thought partly to be due to decreased rainfall, but also to increased seepage. Increased seepage could have helped cool the sub-lake intrusion, perhaps explaining the rapid increase in depth to magma (decrease in cone fumarole temperatures) observed from early 1988 onwards, with vaporised seepage lost from the system as fumaroles or steam eruptions. Alternatively, an active shallow intrusion may have remained beneath the lake after early 1988, but with magmatic gas loss unrecorded due to direct passage of HCl through the system, either by volatilisation from the hot (>70 °C) lake surface, or as gas-rich eruptions. With essentially no lake present since April 1989, and no high temperature fumaroles on the cone, monitoring of power output and magmatic gas escape is now rather difficult.

Phreatic eruptions in 1978 and 1979 (fig. 7.1d) were not accompanied by any observed fumarolic activity, and the lake chemistry was not monitored at that time, thus the causes of the eruptions are more uncertain. They probably represent similar intrusive activity to 1980/81 and 1986, but perhaps smaller scale, and centred beneath the lake. Alternatively, they could represent gas bursts from a deep magma body (e.g. fig. 6.3, with no intrusion), or perhaps increased hydrothermal heat flux due to a sudden increase in permeability.

In summary, Poás has experienced at least two shallow intrusive phases over the period 1978-89, one in 1980/81, the other in 1986. These were both followed by outgassing of at least ~0.05 km^3 of magma. These volumes are unlikely to represent the intrusion volumes, but, instead, minimum volumes of deeper reservoirs that become connected to the surface by narrow intrusions. Modelling indicates that pipe-like basaltic andesite intrusions of diameter ~10 m would produce these degassing rates. Freezing of the upper parts of these intrusions by hydrothermal infiltration probably ends their activity. Further energy was supplied to the lake by the addition of saturated steam, discharging from a two-phase hydrothermal zone, and the addition of hot brines. The 2PZ was fed by magmatic latent and specific heat, probably released by infiltration of the CBL above the same magma reservoir feeding the intrusions. A schematic cross-section is shown in fig. 7.2.

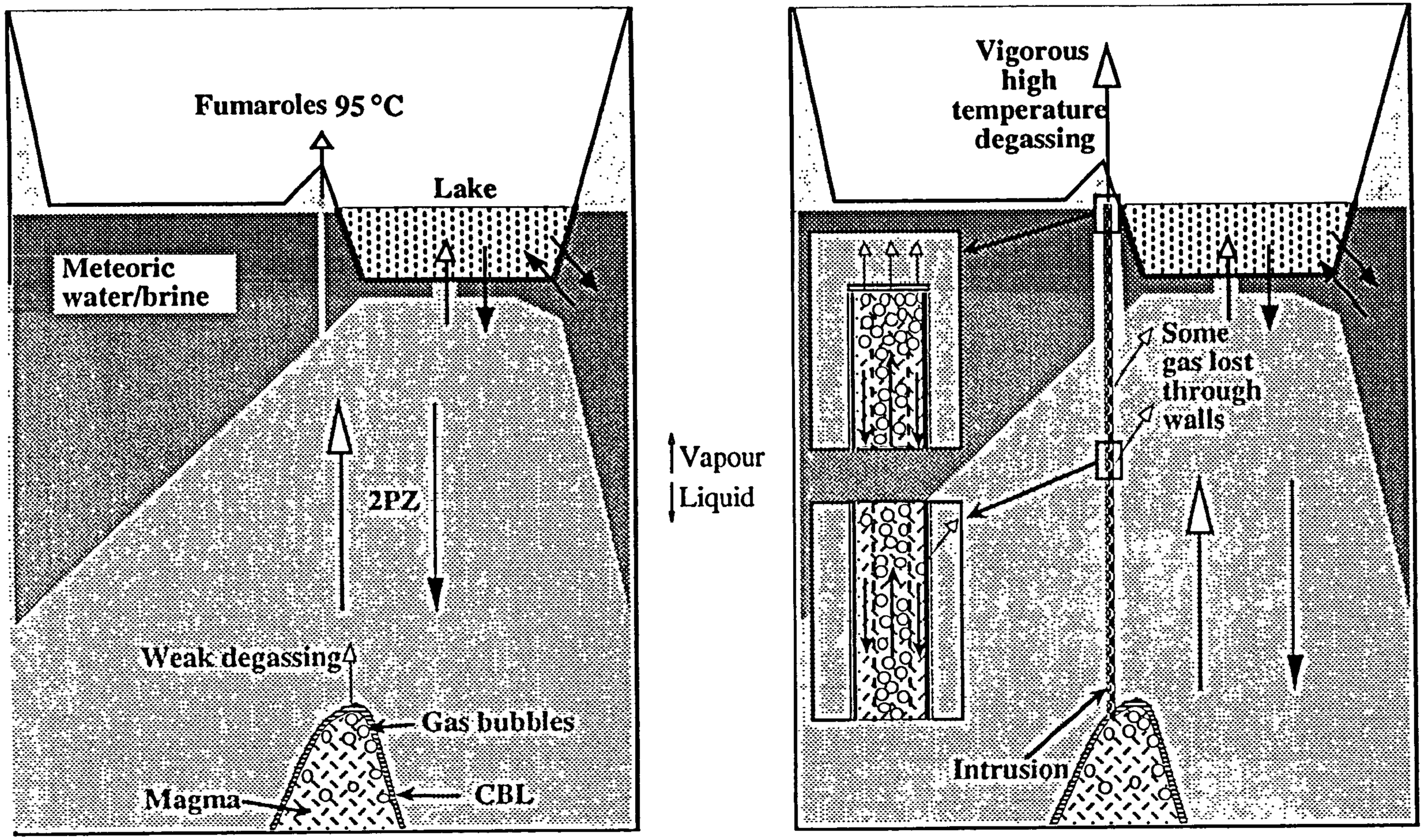

Fig. 7.2 *Schematic cross-sections through the upper part of Poás during: (a) low-level activity: a large magma body at an arbitrary depth (probably ~0.5-3 km) feeds a 2PZ via an infiltrating CBL, probably with some degassing from the deep reservoir; and (b) high activity: a minor intrusion to shallow depth beneath the cone facilitates vigorous degassing with internal circulation. Situation (b) is thought to have occurred in 1980/81, and in 1986, but with the intrusion(s) closer to the lake.*

7.4 A model for activity at Ruapehu 1966-1989

The four most useful diagrams for the interpretation of activity at Ruapehu are the total Mg and Cl contents of Crater Lake (fig. 4.14a,b), the calculated power input to the lake (fig. 4.20a), and observed eruptions (fig. 3.9), summarised in fig. 7.3. As at Poás, heat is thought to be transferred by magma-fed hydrothermal convection, and degassing, with the lake water acting as the source of downwards percolating hydrothermal fluid, which is partly vaporised, and returned as a steam/brine mixture.

Phreato-magmatic eruptions occurred frequently over the period 1966-89 (table 3.1), and can be seen within the data as major introducers of Mg to the lake (dark shaded bands on fig. 7.3a: 1966, (1968 and 1969, both missing Mg data), 1971, 1975, 1977, and 1981). These are interpreted as periods of leaching of the new magma by the acidic lake water and shallow hydrothermal system. Eruptions were generally accompanied, or followed, by strong increases in the Cl content of the lake (fig.7.3b, dark shaded bands), and were followed by weaker periods of intermittent addition of Cl. These are interpreted as periods of magmatic degassing. However, as observed at Poás, the volume of magma degassed (typically 1000-3000 kg s^{-1}) is much larger than the intruded volumes expected from geophysical evidence. In addition, volumes of magma leached of Mg (up to ~40 kg s^{-1}) are also much smaller than degassed volumes.

These observations suggest that conduits that fed magmatic eruptions remained mobile following the eruptions, allowing the recirculation and degassing of deep magma volumes. Pipe-like intrusions of diameter ~10-15 m, connected to deep volumes of >~0.05 km^3 can provide the observed gas fluxes. The intermittent character of degassing may reflect additional, minor intrusions, or perhaps rapid overturn of the top part of the pipe, producing gas bursts, followed by quiescence as the lower part of the conduit 'catches up' (section 6.6; fig. 6.2d), or blocking of gas flow within the hydrothermal system or from lake floor vents.

Magmatic gas inputs can probably provide the peaks observed in the power input to the lake (fig. 7.3c), with a background component supplied by a magma-fed hydrothermal system. The fall in background power input from ~300 MW in 1966 to ~50 MW in 1989 reflects

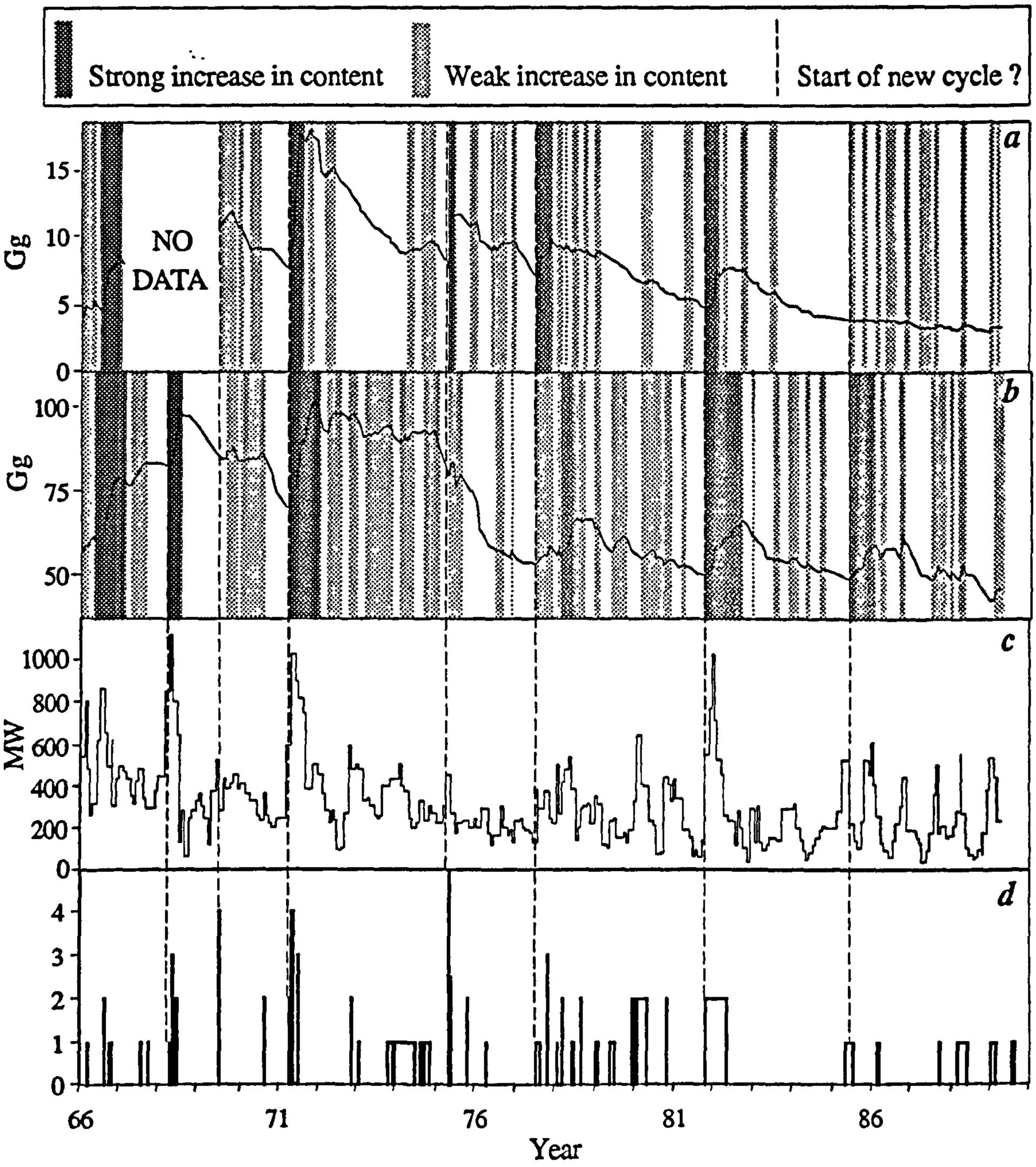

Fig. 7.3 *Summary diagram for Ruapehu: (a) total Mg content of the lake, with dark bands indicating periods of rapid increase, light bands indicating periods of weak increase (fig. 4.14a); (b) total Cl, as for (a) (fig. 4.14b); (c) calculated power input to lake (fig. 4.20a); (d) eruption magnitudes (fig. 3.9). Dashed lines indicate possible cycle boundaries.*

either (i) a decrease in the permeability of the sub-lake system, and/or (ii) a thickening of the CBL and a decrease in infiltration velocity, and/or (iii) a reduction in the surface area of the magma source or area of high heat flow within the 2PZ.

7.5 General implications for heat and gas transfer in active, but non-erupting volcanoes

This study, and in particular the generalised models of heat transfer developed in chapters 5 and 6, has revealed many points generally applicable to active but not magmatically erupting volcanoes and geothermal systems.

Hydrothermal infiltration of magma provides a concentrated source of energy, and probably affects most intrusions emplaced within a hydrothermal environment (i.e. wet upper crust). The new model developed in chapter 5 predicts maximum infiltration rates of ~300 m a^{-1} for magma near the surface (a 100 °C 2PZ), and ~800 m a^{-1} for magma overlain by a 2PZ at 250 °C. These correspond to maximum heat fluxes of ~3 x 10^4 - 8 x 10^4 W m^{-2}. These values probably represent the maximum possible heat flux available from a crystallising intrusion. The theory predicts unlimited infiltration velocities (and hence heat fluxes) if no latent heat is released, i.e. if glass is formed. Magma cracking temperatures can span the range from that within the overlying hydrothermal system (at very low infiltration rates) to near magmatic (at very high infiltration rates). The opening of fractures at near magmatic temperatures could perhaps facilitate relatively passive magmatic degassing. In addition, the high fluid pressure gradient across the magma/country rock boundary could induce fracturing.

Voluminous magmatic degassing occurs at many volcanoes (see table 6.2), but is usually accompanied by evidence of only minor volumes of near surface intrusive activity. The model of magma recirculation developed in chapter 6 can explain this paradox, and recycling within minor intrusions probably occurs at many degassing volcanoes. The fact that magma increases in density with volatile loss also raises the possibility of convection induced by degassing within vesiculating magma chambers.

7.6 Suggestions for future work

The new cracking theory developed in chapter 5 needs to be more rigorously tested; one possibility would be to carry out a range of experiments on a lava flow, dome or lake, similar to the Heimaey example, to see if a maximum infiltration rate is reached, or glass formation occurs, and to measure created permeabilities and cracking temperatures.

Mechanisms of gas loss need further study; in particular the implications of large pressure gradients between gas bubbles within a magma and fluid within cracks exterior to the magma. Fracturing due to this pressure differential, and/or due to hydrothermal infiltration are possible methods of providing pathways for the exiting gas.

The model of internally circulating intrusions needs verification, with further determinations of the density decrease associated with the loss of dissolved volatiles from a magma. In addition, more laboratory experiments could be carried out to emulate the behaviour of the proposed intrusion using fluids of variable density and viscosity. Rapid overturn of the upper, vesicular region of an intrusion, compared to the overall flow rates should be considered as a mechanism that could lead to erratic degassing. The problem could also be approached theoretically, using equations to define the physical behaviour and interaction of the upflowing and downflowing fluids. The possibility of convection induced by degassing from larger magma bodies also deserves attention.

The cyclicity seen in the eruptive and degassing behaviour of Poás and Ruapehu suggests repeated emplacement of intrusions, possibly reflecting the release and build-up of pressure within a deep magma body (e.g. Tait et al., 1989). Further understanding of the trigger mechanisms for these intrusions could yield information on the size, depth, and composition of deep magma bodies.

References

Adams,E.E., Cosler, D.J., and Helfrich, K.R. (1990) Evaporation from heated water bodies: Combining forced plus free convection *Water Resources Research* **26** 425-435

Allard, P., Carbonelle, J., Dajilevic, D., Le Bronec, J., Morel, P., Robe, M.C., Maurenas, J.M., Faivre-Pierret, R., Martin, D., Sabroux, J.C., and Zetwoog, P. (1991) Eruptive and diffuse emissions of CO2 from Mount Etna *Nature* **351** 387-391

Andres, R.J., Rose, W.I., Kyle, P.R., deSilva, S., Francis, P.W., Gardeweg, M., and Moreno Roa, H. (1991) Excessive sulfur dioxide emissions from Chilean volcanoes *Journal of Volcanology and Geothermal Research* **46** 323-329

Barquero, J. (1983) Termometria de la fumarola del Volcán Poás *Boletin Vulcanologia* **13** 11-12

Bennett, F.D., and Raccichini, S.M. (1978) Subaqueous sulphur lake in Volcan Poas *Nature* **271** 342-344

Björnsson, H., Björnsson, S., and Sigurgeirsson, T. (1982) Penetration of water into hot rock boundaries of magma at Grímsvötn *Nature* **295** 580-581

Blake, S. (1984) Volatile oversaturation during the evolution of silicic magma chambers as an eruption trigger *Journal of Geophysical Research* **89** 8237-8244

Bottinga, Y., and Javoy, M. (1991) The degassing od Hawaiian tholeiite *Bulletin of Volcanology* **53** 73-85

Bottinga, Y., and Weill, D.F. (1972) The viscosity of magmatic silicate liquids: A model for calculation *American Journal of Science* **272** 438-475

Bowen, I.S. (1926) The Ratio of Heat Losses by Conduction and by Evaporation from Air Water Surfaces *Physical Review* **27** 779-787

Boza, M.A., and Mendoza, R. (1981) The National Parks of Costa Rica *Costa Rican Institute of Tourism, San José*

Brandeis, G., and Jaupart, C. (1986) On the interaction between convection and

crystallization in cooling magma chambers *Earth and Planetary Science Letters* 77 345-361

Brantley, S.L., Borgia, A., Rowe, G., Fernandez, J.F. and Reynolds, J.R. (1987) Poas volcano crater lake acts as a condenser for acid metal-rich brine *Nature* 330 470-472

Brown, G.C, Rymer, H., Dowden, J., Kapadia, P., Stevenson, D., Barquero, J., and Morales, L.D. (1989) Energy budget analysis for Poas crater lake: implications for predicting volcanic activity *Nature* 339 370-373

Brown, G.C., Rymer, H., and Stevenson, D. (1991) Volcano monitoring by microgravity and energy budget analysis *Journal of the Geological Society of London* 148 585-593

Brown, G.C., Rymer, H., and Thorpe, R.S. (1987) The evolution of andesite volcano structures: new evidence from gravity studies in Costa Rica *Earth and Planetary Science Letters* 82 323-334

Brutsaert, W.H. (1982) Evaporation into the Atmosphere: Theory, History and Applications *D. Riedel, Hingham, Mass.*

Brutsaert, W.H., and Yeh, G.T. (1970) A Power Wind Law for Turbulent Transfer Computations *Water Resources Research* 6 1389-1391

Burnham, C.W. (1985) Energy release in subvolcanic environments: implications for breccia formation *Economic Geology* 80 1515-1522

Burnham, C.W. (1979) The importance of volatile constituents *In: The evolution of igneous rocks, Ed. Yoder, H.S., Princeton University , New Jersey* 439-482

Burnham, C.W., and Davis, N.F. (1971) The role of H2O in silicate melts. I P-V-T relations in the system NaAlSi3O8-H2O to 10 kbars and 1000°C *American Journal of Science* 270 54-79

Cann, J.R., and Strens, M.R. (1989) Modeling periodic megaplume emissions by black smoker systems *Journal of Geophysical Research* 94 12227-12237

Cann, J.R., Strens, M.R., and Rice, A. (1985) A simple magma-driven thermal balance model for the formation of volcanogenic massive sulphides *Earth and Planetary Science Letters* 76 123-134

Carey, S., and Sigurdsson, H. (1985) The May 18, 1980 eruption of Mt. St. Helens 1. Melt composition and experimental phase equilibria *Journal of Geophysical Research* **90** 2948-2958

Carr, M.J. (1984) Symmetrical and segmented variation of physical and geochemical characteristics of the Central American volcanic front *Journal of Volcanology and Geothermal Research* **20** 231-252

Carrigan, C.R. (1986) A two-phase hydrothermal cooling model for shallow intrusions *Journal of Volcanology and Geothermal Research* **28** 175-192

Carrigan, C.R. (1983) A heat pipe model for vertical, magma filled conduits *Journal of Volcanology and Geothermal Research* **16** 279-298

Carslaw, H.S., and Jaeger, J.C. (1959) Conduction of heat in solids *Oxford University press, London*

Casadevall, T., Rose, W., Gerlach, T., Greenland, L.P., Ewert, J., Wunderman, R., and Symonds, R. (1983) Gas emissions and the eruptions of Mount St. Helens through 1982 *Science* **221** 1383-1385

Casadevall, T.J., De la Cruz-Reyna, S., Rose, W.I.Jr., Bagley, S., Finnegan, D.L., and Zoller, W.H. (1984) Crater lake and post-eruption hydrothermal activity, El Chichón volcano, Mexico *Journal of Volcanology and Geothermal Research* **23** 169-191

Casadevall, T.J., Rose, W.I.Jr, Fuller, W.H., Hart, M.A., Moyers, J.L., Woods, D.C., Chuan, R.L., and Friend, J.P. (1984) Sulfur dioxide and particles in quiescent volcanic plumes from Poás, Arenal and Colima volcanoes, Costa Rica and Mexico *Journal of Geophysical Research* **89** 9633-9641

Casadevall, T.J., Stokes, J.B., Greenland, L.P., Malinconico, L.L., Casadevall, J.R., and Furukawa, B.T. (1987) SO2 and CO2 emission rates at Kilauea volcano, 1979-1984 *In: U.S.G.S. Professional paper 1350 'Volcanism in Hawaii', Volume I, Editors: Decker, R.W., Wright, T.L., and Stauffer, P.H.* 771-780

Casertano, L., Borgia, A., Cigolini, C. (1983) El Volcan Poas, Costa Rica: Cronologia y caracterisiticas de la actividad *Geof. Int.* **22**(3) 215-236

Casertano, L., Borgia, A., Cigolini, C., Morales, L.D., Montero, W., Gomez, M., and Fernandez, J.F. (1987) An integrated dynamic model for the volcanic activity at

Poas volcano, Costa Rica *Bulletin of Volcanology* **49** 588-598

Casertano, L., Borgia, A., Cigolini, C., Morales, L.D., Montero, W., Gomez, M., and Fernandez, J.F. (1985) Investigaciones geofisicas y caracteristicas geoquimicas de las aguas hidrotermales: Volcan Poás, Costa Rica *Geof. Int.* **24** 315-332

Cole, J.W. (1990) Structural control and origin of volcanism in the Taupo Volcanic Zone, New Zealand *Bulletin of Volcanology* **52** 445-459

Cole, J.W., Graham, I.J., Hackett, W.R., and Houghton, B.F. (1986) Volcanology and Petrology of the Quaternary Composite Volcanoes of Tongariro Volcanic Centre, Taupo Volcanic Zone *In: 'Late Cenozoic Volcanism in New Zealand', Royal Society of New Zealand Bulletin (Editor: I.E.M. Smith)* **23** 224-250

Dalton, J. (1802) Experimental essays on the constitution of mixed gases; on the force of steam or water vapor from water and other liquids in different temperatures, both in a Torricellian vacuum and in air; on evaporation and on the expansion of gases by heat *Mem. Manchester Literary and Philosophy Society* **5** 535-602

Davies, J.A., Robinson, P.J. and Nuñez, M. (1971) Field determinations of surface emissivity and temperature for Lake Ontario *Journal of Applied Meteorology* **10** 811-819

Dawson, G.B., and Sorrell, G.K. (1985) Construction and operation of a remotely controlled catamaran for measuring the depth of Crater Lake, Mt. Ruapehu *DSIR Geophys. Div. Tech. note 96. Geophysics Division, Wellington*

Dibble, R.R. (1983) Recent volcanic activity and volcanological surveillance in New Zealand *In: Forecasting volcanic events, Eds. Tazieff, H., and Sabroux, J-C., Amsterdam, Elsevier.* 237-256

Dibble, R.R. (1972) Seismic and related phenomena at active volcanoes in New Zealand, Hawaii, and Italy *Unpublished Ph.D. thesis* **Victoria University of Wellington**

Dibble, R.R. (1974) Volcanic seismology and accompanying activity of Ruapehu volcano, New Zealand *In: Physical volcanology, Eds. Civetta, L., Gasparini, P., Luongo, G., and Rapolla, A., Elsevier*

Eichelberger, J.C., Carrigan, C.R., Westrich, H.R., and Proce, R.H. (1986) Non-explosive silicic volcanism *Nature* **323** 598-602

Eskinazi, S. (1975) Fluid Mechanics and Thermodynamics of our Environment *Academic*

Press, New York

Fernandez, M. (1990) The activity of Poás volcano: seismic analysis for the period 1980-1989 *Unpublished Ph.D. thesis* **University of Costa Rica, San José**

Francis, P.W., Thorpe, R.S., Brown, G.C., and Glasscock, J. (1980) Pyroclastic sulphur eruption at Poás volcano, Costa Rica *Nature* **283** 754-756

Gemmell, J.B. (1987) Geochemistry of metallic trace elements in fumarolic condensates from Nicaraguan and Costa Rican volcanoes *Journal of Volcanology and Geothermal Research* **33** 161-181

Gerlach, T.M. (1986) Exsolution of H2O, CO2, and S during eruptive episodes at Kilauea volcano, Hawaii *Journal of Geophysical Research* **91** 12177-12185

Gerlach, T.M., and Casadevall, T.J. (1986) Fumarole emissions at Mount St. Helens volcano, June 1980 to October 1981: degassing of a magma-hydrothermal system *Journal of Volcanology and Geothermal Research* **28** 141-160

Gerlach, T.M., and Graeber, E.J. (1985) Volatile budget of Kilauea volcano *Nature* **313** 273-277

Giberti, G., Jaupart, C., and Sartoris, G. (1992) Steady-state operation of Stromboli volcano, Italy: constraints on the feeding system *Submitted to Bulletin of Volcanology, May 1991*

Giggenbach, W. (1974) The chemistry of Crater Lake, Mt Ruapehu (New Zealand) during and after the 1971 active period *New Zealand Journal of Science* **17** 33-45

Giggenbach, W. (1987) Redox processes governing the chemistry of fumarolic gas discharges from White Island, New Zealand *Applied Geochemistry* **2** 143-161

Giggenbach, W., and Glover, R.B. (1975) The Use of Chemical Indicators in the Surveillance of Volcanic Activity Affecting the Crater Lake on Mt Ruapehu, New Zealand *Bulletin Volcanologique* **39** 70-81

Giggenbach, W.F., and Le Guern, F. (1976) The chemistry of magmatic gases from Erta'Ale, Ethiopia *Geochimica et Cosmochimica Acta* **40** 25-30

Giggenbach, W.F., and Le Guern, F. (1976) The chemistry of gases from Erta'Ale, Ethiopia *Geochimica et Cosmochimica Acta* **40** 25-30

Giggenbach, W.F., and Sheppard, D.S. (1989) Variations in the temperature and chemistry of White Island fumarole discharges 1972-85 *New Zealand Geological Survey Bulletin* **103** 119-126

Gregg, D.R. (1960) The geology of Tongariro subdivision *Geological survey bulletin* **40**

Hackett, W.R. (1985) Geology and petrology of Ruapehu volcano and related vents *Unpublished Ph.D. thesis, Victoria University of Wellington*

Hamilton, D.L., Burnham, C.W., and Osborn, E.F. (1964) The solubility of water and effects of oxygen fugacity and water content on crystallization in mafic magmas *Journal of Petrology* **5** 21-39

Harbeck, G.E. (1962) A Practical Field Technique for Measuring Reservoir Evaporation Utilizing Mass-Transfer Theory *U.S. Geological Survey Professional Paper* **272-E** 101-105

Hardee, H.C. (1980) Solidification of Kilauea Iki lava lake *Journal of Volcanology and Geothermal Research* **7** 211-223

Hardee, H.C. (1982) Permeable convection above magma bodies *Tectonophysics* **84** 179-195

Healy, J. (1954) Submission to the Tangiwai railway disaster board of inquiry *Report of the board of Inquiry, Government printer, Wellington*

Heiken, G., Wohletz, K., and Eichelberger, J. (1988) Fracture fillings and intrusive pyroclasts, Inyo Domes, California *Journal of Geophysical Research* **93** 4335-4350

Henderson-Sellers, B. (1986) Calculating the Surface Energy Balance for Lake and Reservoir Modeling: A Review *Reviews in Geophysics* **24** 625-649

Houghton, B.F., Latter, J.H., and Hackett, W.R. (1987) Volcanic hazard assessment for Ruapehu composite volcano, Taupo Volcanic Zone, New Zealand *Bulletin of Volcanology* **49** 737-751

Hurst, A.W. (1986) Monitoring volcanoes of Tongariro National Park. *In: 'Volcanic Hazards Assessment in New Zealand', Royal Society of New Zealand Bulletin (Eds. Gregory, J.G., and Watters, W.A.)* **10**, 23-34

Hurst, A.W., and Dibble, R.R. (1981) Bathymetry, Heat Output and Convection in Ruapehu Crater Lake, New Zealand *Journal of Volcanology and Geothermal Research* **9** 215-

Hurst, A.W., Bibby, H.M., Scott, B.J., and McGuinness, M.J. (1991) The heat source of Ruapehu Crater Lake; deductions from the energy and mass balances *Journal of Volcanology and Geothermal Research* **46** 1 - 11

Ingebritsen, S.E., and Sorey, M.L. (1988) Vapor-dominated zones within hydrothermal systems: evolution and natural state *Journal of Geophysical Research* **93** 13635-13655

Irwin, J. (1972) New Zealand lakes bathymetry surveys 1965-1970 *New Zealand Oceanographic Institute records* **1(6)** 107-126

Jaluria, A. (1987) Handbook of Convective Heat Transfer *Wiley*

Jaupart, C. (1991) Effects of compressibility on the flow of lava *Bulletin of Volcanology* **54** 1-9

Jaupart, C., and Allègre, C.J. (1991) Gas content, eruption rate and instabilities of eruption regime in silicic volcanoes *Earth and Planetary Science Letters* **102** 413-429

Jaupart, C., and Tait, S. (1990) Dynamics of eruptive phenomena *In: 'Modern methods of igneous petrology: understanding magmatic processes', Reviews in Mineralogy (Editors J. Nicholls and J.K. Russell)* **24** 213-238

Jessop, A.M. (1990) Thermal Geophysics *Elsevier, Amsterdam*

Jirka, G.H., Watanabe, M., Hurley-Octavio, H., Cerco, C.F., and Harleman, D.R.F (1978) Mathematical predictive models for cooling ponds and lakes; Part A: Model development and design considerations *Ralph M. Parsons Lab. report no. 238, Dept. Civil Eng., MIT, Cambridge, Mass.*

Juza, J. (1966) An equation of state for water and steam *Academia (Nakladateltvi Ceskoslovenské Akademic Ved) Praha*

Kakac, S. (1987) Handbook of single phase convective heat transfer *Wiley*

Kirkpatrick, R.J. (1974) Kinetics of crystal growth in the system CaMgSi2O6-CaAl2SiO6 *American Journal of Science* **274** 215-242

Kraichnan, R.H. (1962) Turbulent thermal convection at arbitrary Prandtl number *Physics of Fluids* **5** 1374-1380

Krushensky, R., and Escalante, G. (1967) Activity of Irazú and Poás Volcanoes, Costa Rica, November 1964-July 1965 *Bulletin Volcanologique* **31** 75-94

Lange, R.L., and Carmichael, I.S.E. (1990) Thermodynamic properties of silicate liquids with emphasis on density, thermal expansion and compressibility *In: 'Modern methods of igneous petrology: understanding magmatic processes', Reviews in Mineralogy (Editors J. Nicholls and J.K. Russell)* **24** 25-64

Latter, J.H. (1981) Volcanic Earthquakes, and their Relationship to Eruptions at Ruapehu and Ngauruhoe Volcanoes *Journal of Volcanology and Geothermal Research* **9** 293-309

Lister, C.R.B. (1983) The basic physics of water penetration into hot rock *In: Rona, P.A., Burtström, A., Lauber, L., and Smith, R.L. (Eds) 'Hydrothermal processes at seafloor spreading centres',* 141-168

Lister, C.R.B. (1974) On the penetration of water into hot rock *Geophysical Journal of the Royal Astronomical Society* **39** 465-509

Lowell, R.P. (1991) Modeling continental and submarine hydrothermal systems *Reviews of Geophysics* **29** 457-476

Marsh, B.D. (1989) On convective style and vigour in sheet-like magma chambers. *Journal of Petrology* **30** 479-530

Martin, D., and Nokes, R. (1988) Crystal settling in a vigourously convecting magma chamber *Nature* **332** 534-536

Martin, D.L., Griffiths, R.W., and Campbell, I.H. (1987) Compositional and thermal convection in magma chambers *Contributions to Mineralogy and Petrology* **96** 465-475

Martin, R.J., (1972) Time-dependant crack growth in quartz and its application to th ecreep in rocks *Journal of Geophysical Research* **77** 1406

Matsuo, S. (1991) Future aspects of volcanic gas studies *Presentation at IAVCEI, Naples 1991*

Mayrath, J.E., and Wood, R.H. (1982) Enthalpy of dilution of aqueous sodium chloride at 348.15 to 472.95 K measured with a flow calorimeter *Journal of Chemical Thermodynamics* **14** 15-26

McBirney, A.R., and Murase, T. (1984) Rheological properties of magmas *Annual*

Review of Earth and Planetary Science **12** 337-357

McLelland, L., Simkin, T., Summers, M., Nielsen, E., and Stein, T. (1989) Global Volcanism 1975-1985 *Smithsonian Institution, Washington*

McNutt, S.R., and Harlow, D.H. (1983) Seismicity at Fuego, Pacaya, Izalco and San Cristobal volcanoes, Central america *Bulletin of Volcanology* **46** 283-297

Menyailov, I.A., Nikitina, L.P., Shapar, V.N., and Pilipenko, V.P. (1986) Temperature increase and chemical change of fumarolic gases at Momotombo volcano, Nicaragua, in 1982-1985: are these indicators of a possible eruption ? *Journal of Geophysical Research* **91** 12199-12214

Minakami, T. (1969) Earthquakes originating from volcanoes *Atti. XVIII Conv. Ass. Geof. Ital., Napoli*

Monin, A.S., and Yaglom, A.M. (1971) Statistical Fluid Mechanics *MIT Press, Cambreidge, Mass.*

Moody, L.F. (1944) Friction factors for pipe flow *Trans. ASME, November*

Morales, L.D., Soley, J.F., Alvarado, G., Borgia, A., and Soto, G. (1988) Spectral analysis of some seismic signals of Arenal and Poas volcanoes, Costa Rica and their relation to eruptive activity *Boletin del Observatorio Vulcanologico del Arenal* **1(2)** 26-43

Murase, T., and McBirney, A.R. (1973) Properties of some common igneous rocks and their melts at high temperatures *Geological Society of America Bulletin* **84** 3563-3592

Nairn, I.A., Scott, B.J., Otway, P.M., and Cody, A.D. (1982) Depth measurement in Ruapehu Crater Lake *Volcano News* **12** 3

Nairn, I.A., Wood, C.P., and Hewson, C.A.Y. (1979) Phreatic eruptions of Ruapehu: April 1975 *New Zealand Journal of geology and geophysics* **22** 155-173

Newhall, C.G., and Dzurisn, D. (1988) Historical unrest at large calderas of the world *USGS Bulletin 1855* **2**

Norton, D.L. (1984) Theory of Hydrothermal Systems *Annual Reviews of Earth and Planetary Science* **12** 155-77

Oppenheimer, C. (1991) Sulphur eruptions at Volcán Poás, Costa Rica *Journal of Volcanology and Geothermal Research (in press)*

Oppenheimer, C., and Stevenson, D. (1989) Liquid sulphur lakes at Poás volcano *Nature* **342** 790-793

P.M. Otway (1979) In: Phreatic eruptions of Ruapehu: April 1975, Nairn et al., 1979

Prosser, J.T., and Carr, M.J. (1987) Poás Volcano, Costa Rica: Geology of the summit region and spatial and temporal variations among the most recent lavas *Journal of Volcanology and Geothermal Research* **33** 131-146

Robie, R.A., Hemingway, B.S., and Fisher, J.R. (1979) Thermodynamic properties of minerals and related substances at 298.15 K and 1 bar (100000 Pascals) pressure and at higher temperatures *U.S. Geological Survey Bulletin* **1452**

Roedder, E. (1965) Liquid CO2 inclusions in olivine bearing nodules and phenocrysts from basalts *American Mineralogist* **50** 1746-1781

Rogers, G.F.C., and Mayhew, Y.R. (1980) Thermodynamic and transport properties of fluids *Blackwell, London*

Rose, W.I., Chuan, R.L., Giggenbach, W., Kyle, P.R., and Symonds, R.B. (1986) Rates of sulfur dioxide and particle emissions from White Island volcano, New Zealand, and an estimate of the total flux of major gaseous species *Bulletin of Volcanology* **48** 181-188

Rowe, G.L., Brantley, S.L., Fernandez, M, Fernandez, J.F., Barquero, J., and Borgia, A. (1991a) Fluid-Volcano interaction in an active Stratovolcano: The Crater lake system of Poás Volcano, Costa Rica *Submitted to Journal of Volcanology and Geothermal Research*

Rowe, G.L., Ohsawa, S., Takano, B., Brantley, S.L., Fernandez, J.F., and Barquero, J. (1991b) Using Crater Lake chemistry to Predict Volcanic activity at Poás Volcano, Costa Rica *Submitted to Bulletin of Volcanology*

Roy, R.F., Beck, A.E., and Touloukian, Y.S. (1981) Thermophysical properties of rocks *In: Physical properties of rocks and minerals, Eds: Toulakian, Y.S., Judd, W.R., and Roy, R.F. McGraw-Hill* **2** 409-502

Rutherford, M.J., Sigurdsson, H., and Carey, S. (1985) The May 18, 1980 eruption of Mt. St. Helens 2. Modeling of dynamics of the plinian phase *Journal of Geophysical Research* **90** 2929-2948

Ryan, M.P. (1988) The mechanics and 3-D internal structure of active magma systems: Kilauea volcano, Hawaii *Journal of Geophysical Research* **93** 4213-4248

Ryan, P.J., Harleman, D.R.F., and Stolzenbach, K.D. (1974) Surface Heat Loss From Cooling Ponds *Water Resources Research* **10** 930-938

Rymer, H. (1985) Gravity studies of sub-surface structures and evolution of active volcanoes in Costa Rica *Unpublished Ph.D. thesis* **Open University, Milton Keynes**

Rymer, H., and Brown, G.C. (1984) Periodic gravity changes at Poás volcano, Costa Rica *Nature* **311** 243-245

Rymer, H., and Brown, G.C. (1986) Gravity fields and the interpretation of volcanic structures: geological discrimination and temporal evolution *Journal of Volcanology and Geothermal Research* **27** 229-254

Rymer, H., and Brown, G.C. (1987) Causes of Microgravity change at Poás volcano, Costa Rica: an active but non-erupting system *Bulletin of Volcanology* **49** 389-398

Rymer, H., and Brown, G.C. (1989) Gravity changes as a precursor to volcanic eruption at Poás volcano, Costa Rica *Nature* **342** 902-905

Sáenz, R. (1982) Edades radiometricas de algunas rocas de Costa Rica *Bol. Volcanol., Heredia, Costa Rica* **12** 9-30

Sapper, K. (1925) Los volcanes de la América Central *Max Niemayer, Halle*

Scandone, R., and Malone, S.D. (1985) Magma supply, magma discharge and readjustment of the feeding system of Mt. St. Helens during 1980 *Journal of Volcanology and Geothermal Research* **23** 239-262

Schneider, P.J. (1957) Conduction heat transfer *Addison-Weley, Reading, Mass.* 284-286

Schubert, G., and Straus, J.M., (1977) Two-phase convection in a porous medium *Journal of Geophysical Research* **82** 3411-3421

Schubert, G., and Straus, J.M. (1979) Steam-water counterflow in porous media *Journal of Geophysical Research* **84** 1621-1628

Schubert, G., and Straus, J.M. (1980) Gravitational stability of water over steam in vapor-dominated geothermal systems *Journal of Geophysical Research* **85** 6505-6512

Seyfried, H., Astorga, A., Amann, H., Calvo, C., Kolb, W., Schmidt, H., and Winsemann, J. (1991) Anatomy of an evolving island arc: tectonic and eustatic control in the south Central American fore-arc area *Spec. Publs. int. Ass. Sediment* **12**

Shaw, H.R. (1972) Viscosities of magmatic silicate liquids: An empirical method of prediction *American Journal of Science* **272** 870-893

Shepherd, J.B., and Sigurdsson, H. (1978) The Soufriére crater lake as a calorimeter *Nature* **271** 344-345

Sherburn, S., and Hurst, A.W. (1989) Two and Three Hertz Volcanic Tremor, Mt. Ruapehu, New Zealand

Sill, B.L. (1983) Free and Forced Convection Effects on Evaporation *Journal of Hydraulic Engineering* **109** 1216-1231

Smithsonian Institution (1969) Newsletter no.529

Smithsonian Institution (1969) Newsletter no.540

Smithsonian Institution (1969) Newsletter no.548

Smithsonian Institution (1969) Newsletter no.552

Smithsonian Institution (1969) Newsletter no.568

Smithsonian Institution (1976) Newsletter no.2477

Smithsonian Institution (1976) Scientific event alert network (1:10)

Smithsonian Institution (1977) Scientific event alert network (2:12)

Smithsonian Institution (1978) Scientific event alert network (3:11)

Smithsonian Institution (1979) Scientific event alert network (4:3)

Smithsonian Institution (1980) Scientific event alert network (5:1)

Smithsonian Institution (1981) Scientific event alert network (6:2)

Smithsonian Institution (1981) Scientific event alert network (6:5)

Smithsonian Institution (1981) Scientific event alert network (6:8)

Smithsonian Institution (1988) Scientific event alert network (13:6)

Smithsonian Institution (1989) Scientific event alert network (14:4)

Smithsonian Institution (1990) Scientific event alert network (15:4)

Smithsonian Institution (1990) Scientific event alert network (15:5)

Smithsonian Institution (1991) Scientific event alert network (16:2)

Sondergeld, C.H., and Turcotte, D.L. (1977) An experimental study of two-phase convection in a porous medium with applications to geological problems *Journal of Geophysical Research* **82** 2045-2053

Sparks, R.S.J. (1978) The dynamics of bubble formation and growth in magmas: a review and analysis *Journal of Volcanology and Geothermal Research* **3** 11-26

Stelling, E. (1882) Ueber die Abhangigkeit der Verdunstung des Wassers von seiner Temperatur und von der Feuchtigkeit und Bewegung der Luft. *Z. Oesterr. Ges. Meteor.* **17** 372-373

Stoiber, R.E., Malinconico, L.L., and Williams, S.N. (1983) Use of the correlation spectrometer at volcanoes *In: Tazieff, H., and Sabroux, J.C. (eds.) 'Forecasting volcanic events', Elsevier, New York* 425-444

Stolper, E., and Holloway, J.R. (1988) Experimental determinationof the solubility of carbon dioxide in molten basalt at low pressure *Earth and Planetary Science Letters* **87** 397-408

Streeter, V.L., and Wylie, E.B. (1975) Fluid Mechanics (6th edition) *McGraw-Hill Kogakusha, Tokyo*

Symonds, R.B., Rose, W.I., Gerlach, T.M., Briggs, P.H., and Harmon, R.S. (1990) Evaluation of gases, condensates, and SO2 emissions from Augustine volcano, Alaska: the degassing of a Cl-rich volcanic system *Bulletin of Volcanology* **52** 355-374

Tait, S., and Jaupart, C. (1990) Physical processes in the evolution of magmas *In: 'Modern methods of igneous petrology: understanding magmatic processes', Reviews in Mineralogy (Editors J. Nicholls and J.K. Russell)* **24** 125-152

Tait, S., Jaupart, C., and Vergniolle, S. (1989) Pressure, gas content and eruption periodicity of a shallow, crystallising magma chamber *Earth and Planetary Science Letters* **92**

107-123

Takano, B. (1987) Correlation of volcanic activity with sulfur oxyanion speciation in a crater lake *Science* **235** 1633-1635

Takano, B., and Watanuki, K. (1990) Monitoring of volcanic eruptions at Yugama crater lake by aqueous sulfur oxyanions *Journal of Volcanology and Geothermal Research* **40** 71-87

Thorpe, R.S., Locke, C.A, Brown, G.C., Francis, P.W. and Randal, M. (1981) Magma chamber below Poás volcano, Costa Rica *Journal of the Geological Society of London* **138** 367-373

Topping, J. (1972) Errors of Observation and Their Treatment *Chapman and Hall, London*

Vergniolle, S., and Jaupart, C. (1990) Dynamics of degassing at Kilauea volcano, Hawaii *Journal of Geophysical Research* **95** 2793-2809

Weisman, R.N. (1975) Comparison of Warm Water Evaporation Equations *Journal of the Hydraulics Division, Proceedings of the American Society of Civil Engineers* **101** 1303-1313

Weisman, R.N. and Brutsaert, W. (1973) Evaporation and Cooling of a Lake under Unstable Atmospheric Conditions *Water Resources Research* **9** 1242-1257

Westrich, H.R., Stockman, H.W., and Eichelberger, J.C. (1988) Degassing of rhyolitic magma during ascent and emplacement *Journal of Geophysical Research* **93** 6503-6511

White, D.E., Muffler, J.P., and Truesdell, A.H. (1971) Vapor-dominated hydrothermal systems compared with hot-water systems *Economic Geology* **66** 75-97

Williams, H. (1952) Volcanic history of the Meseta Central Occidental, Costa Rica *University of California Publications, Geological Sciences* **29** 145-180

Williams, S.N., Sturchio, N.C., Calvache V., M.L., Mendez F., R., Londoño C., A., García P., N. (1990) Sulfur dioxide from Nevado del Ruiz volcano, Colombia: total flux and isotopic constraints on its origin *Journal of Volcanology and Geothermal Research* **42** 53-68

Worster, M.G., Huppert, H.E., and Sparks, R.S.J. (1990) Convection and crystallization in magma cooled from above *Earth and Planetary Science Letters* **101** 78-89

Wunderlich, W.O. (1972) Heat and mass transfer between a water surface and the

atmosphere *Lab. Report 14, Eng. Lab., Tenn. Val. Auth., Norris*

Appendix A: Poás data

Crater lake data (*Small numbers in italics are interpolated*)

Date d m y	T_w / °C	Level / m	Area / 10^3 m^2	Mass / Gg	Mg / ppm	Cl / ppm	Total Mg / Gg	Total Cl / Gg
15 / 03 / 78	50	-5	73.11	1492.05				
15 / 06 / 78	52	*-6.5*	*70.13*	*1384.59*				
15 / 09 / 78	58	-8	67.22	1281.54				
15 / 10 / 78	70	*-10*	*63.43*	*1150.86*				
15 / 12 / 78	50	*-14*	*56.18*	*911.68*				
15 / 02 / 79	40	-18	49.37	700.62				
15 / 03 / 79	40	*-17.3*	*50.53*	*735.61*				
15 / 05 / 79	38	*-16*	*52.72*	*802.75*				
15 / 07 / 79	55	*-14.7*	*54.96*	*872.77*				
15 / 08 / 79	35	*-14*	*56.18*	*911.68*				
15 / 10 / 79	60	*-12.7*	*58.49*	*986.25*				
15 / 11 / 79	65	-12	59.75	1027.65				
15 / 12 / 79	58	*-11*	*61.58*	*1088.33*				
15 / 01 / 80	55	-10	63.43	1150.86				
15 / 02 / 80	50	*-10.3*	*62.87*	*1131.91*				
15 / 03 / 80	48	*-9.5*	*64.36*	*1182.82*				
15 / 05 / 80	44	*-7.8*	*67.60*	*1295.03*				
15 / 06 / 80	30	*-7*	*69.15*	*1349.75*				
15 / 08 / 80	40	*-5.4*	*72.31*	*1462.95*				
15 / 09 / 80	45	*-4.6*	*73.91*	*1521.46*				
15 / 10 / 80	45	*-3.7*	*75.73*	*1588.83*				
15 / 11 / 80	45	*-2.9*	*77.37*	*1650.09*				
15 / 12 / 80	45	*-2.1*	*79.03*	*1712.68*				
15 / 01 / 81	40	-1.3	80.71	1776.60				
15 / 02 / 81	50	*-1.6*	*80.08*	*1752.47*				
15 / 03 / 81	48	*-1.8*	*79.66*	*1736.49*				
15 / 04 / 81	45	*-2.1*	*79.03*	*1712.68*				
15 / 06 / 81	51	-2.6	77.99	1673.41				
15 / 07 / 81	48	*-2.7*	*77.79*	*1665.61*				
15 / 08 / 81	46	*-2.9*	*77.37*	*1650.09*				
15 / 09 / 81	48	*-3*	*77.17*	*1642.36*				
15 / 10 / 81	48	*-3.2*	*76.76*	*1626.96*				
15 / 11 / 81	42	*-3.3*	*76.55*	*1619.30*				
15 / 12 / 81	54	*-3.4*	*76.35*	*1611.65*				
15 / 01 / 82	47	*-3.6*	*75.94*	*1596.41*				
15 / 02 / 82	48	*-3.7*	*75.73*	*1588.83*				
15 / 03 / 82	47	*-3.9*	*75.33*	*1573.71*				
15 / 04 / 82	50	*-4*	*75.12*	*1566.19*				
15 / 05 / 82	50	*-4.1*	*74.92*	*1558.68*				
15 / 06 / 82	50	*-4.3*	*74.51*	*1543.73*				
15 / 07 / 82	49	*-4.4*	*74.31*	*1536.29*				
15 / 08 / 82	50	*-4.6*	*73.91*	*1521.46*				
15 / 09 / 82	56	*-4.7*	*73.71*	*1514.08*				

Appendix A: Poás data

Date d m y	T_w / °C	Level / m	Area / 10^3 m^2	Mass / Gg	Mg / ppm	Cl / ppm	Total Mg / Gg	Total Cl / Gg
15 / 10 / 82	54	*-4.8*	*73.51*	*1506.72*				
15 / 11 / 82	41	*-5*	*73.11*	*1492.05*				
15 / 12 / 82	40	*-5.1*	*72.90*	*1484.74*				
22 / 01 / 83	57	-5.3	72.51	1470.20		18000		26.46
14 / 02 / 83	54	*-7.1*	*68.96*	*1342.84*				
15 / 03 / 83	56	-9.6	64.18	1176.39				
07 / 04 / 83	60	-10.6	62.31	1113.12		18000		20.04
11 / 05 / 83	53	*-11.4*	*60.84*	*1063.84*		18000		19.15
15 / 06 / 83	57	*-12.3*	*59.21*	*1009.80*		21000		21.21
05 / 07 / 83	52	*-12.8*	*58.31*	*980.40*		22500		22.06
28 / 07 / 83	50	*-13.4*	*57.24*	*945.73*		22500		21.28
26 / 08 / 83	52	*-14.1*	*56.01*	*906.07*		28000		25.37
28 / 09 / 83	58	*-14.9*	*54.61*	*861.81*		18000		15.51
02 / 10 / 83	60	-15	54.44	856.35		21000		17.98
14 / 11 / 83	56	*-13.7*	*56.71*	*928.63*				
01 / 12 / 83	56	*-13.1*	*57.77*	*962.98*		29000		27.93
26 / 01 / 84	51	*-11.4*	*60.84*	*1063.84*		26000		27.66
14 / 02 / 84	51	*-10.8*	*61.94*	*1100.69*				
08 / 03 / 84	54	-10	63.43	1150.86		23000		26.47
05 / 04 / 84	50	*-9.2*	*64.93*	*1202.22*		20000		24.04
27 / 04 / 84	49	*-8.6*	*66.07*	*1241.54*		26000		32.28
14 / 05 / 84	49	*-8.1*	*67.02*	*1274.83*				
05 / 06 / 84	50	*-7.5*	*68.18*	*1315.41*		25000		32.89
01 / 08 / 84	48	*-6*	*71.11*	*1419.91*		24000		34.08
28 / 08 / 84	48	*-5.2*	*72.70*	*1477.46*		25000		36.94
15 / 09 / 84	50	*-4.7*	*73.71*	*1514.08*				
19 / 10 / 84	48	*-3.7*	*75.73*	*1588.83*		25000		39.72
27 / 11 / 84	48	*-2.7*	*77.79*	*1665.61*	780	23700	1.30	39.48
15 / 12 / 84	48	*-2.2*	*78.82*	*1704.78*				
23 / 01 / 85	44	*-1.1*	*81.13*	*1792.79*	790	25400	1.42	45.54
14 / 02 / 85	44	*-0.4*	*82.61*	*1850.12*				
01 / 03 / 85	43	0	83.47	1883.35				
19 / 03 / 85	44	*-0.2*	*83.04*	*1866.69*	710	24700	1.33	46.11
14 / 04 / 85	44	*-0.5*	*82.40*	*1841.86*				
06 / 05 / 85	44	*-0.7*	*81.98*	*1825.42*	690	22000	1.26	40.16
04 / 06 / 85	48	*-1*	*81.34*	*1800.91*				
25 / 07 / 85	46	*-1.5*	*80.29*	*1760.49*				
22 / 08 / 85	45	*-1.8*	*79.66*	*1736.49*	600	21100	1.04	36.64
09 / 09 / 85	45	*-2*	*79.24*	*1720.59*				
09 / 10 / 85	45	*-2.3*	*78.62*	*1696.91*	580	20700	0.98	35.13
28 / 11 / 85	45	*-2.8*	*77.58*	*1657.84*				
13 / 12 / 85	45	*-2.9*	*77.37*	*1650.09*				
14 / 01 / 86	45	*-3.3*	*76.55*	*1619.30*				
03 / 02 / 86	38	*-3.5*	*76.14*	*1604.02*	560	16500	0.90	26.47
14 / 02 / 86	39	*-3.6*	*75.94*	*1596.41*				
15 / 03 / 86	39	*-3.9*	*75.33*	*1573.71*				
03 / 04 / 86	38	*-4.1*	*74.92*	*1558.68*				

Date d m y	T_w / °C	Level / m	Area / 10^3 m^2	Mass / Gg	Mg / ppm	Cl / ppm	Total Mg / Gg	Total Cl / Gg
02 / 05 / 86	38	*-4.4*	*74.31*	*1536.29*	530	16500	0.81	25.35
15 / 06 / 86	48	*-4.8*	*73.51*	*1506.72*				
09 / 07 / 86	52	*-5.1*	*72.90*	*1484.74*				
22 / 08 / 86	52	*-5.5*	*72.11*	*1455.73*	550	18900	0.80	27.51
23 / 09 / 86	56	*-5.8*	*71.51*	*1434.18*				
0[/ 11 / 86	54	*-6.2*	*70.72*	*1405.72*	500	23200	0.70	32.61
14 / 11 / 86	54	*-6.4*	*70.33*	*1391.61*				
23 / 12 / 86	54	*-6.8*	*69.54*	*1363.63*				
09 / 01 / 87	61	*-6.9*	*69.35*	*1356.68*	550	30400	0.75	41.24
14 / 01 / 87	58	-7	69.15	1349.75				
26 / 02 / 87	62	*-8.9*	*65.50*	*1221.80*	620	33700	0.76	41.17
18 / 03 / 87	62	-10	63.43	1150.86	680	35900	0.78	41.32
14 / 04 / 87	64	*-11.4*	*60.84*	*1063.84*				
14 / 05 / 87	62	*-13*	*57.95*	*968.77*				
15 / 06 / 87	70	*-14.7*	*54.96*	*872.77*				
11 / 07 / 87	68	*-16.2*	*52.38*	*792.23*	560	28900	0.44	22.90
23 / 07 / 87	70	*-16.8*	*51.37*	*761.09*				
26 / 07 / 87	66	*-17*	*51.03*	*750.85*	830	44900	0.62	33.71
28 / 07 / 87	66	*-17.1*	*50.87*	*745.75*				
14 / 08 / 87	65	-18	49.37	700.62				
09 / 09 / 87	65	*-18.3*	*48.88*	*685.88*		43400		29.77
29 / 10 / 87	65	*-18.8*	*48.06*	*661.63*				
22 / 11 / 87	60	*-19*	*47.74*	*652.05*				
26 / 11 / 87	61	*-19*	*47.74*	*652.05*	500	48000	0.33	31.30
15 / 12 / 87	62	*-19.2*	*47.42*	*642.52*				
15 / 01 / 88	64	*-19.5*	*46.93*	*628.37*	840	59300	0.53	37.26
14 / 02 / 88	64	*-19.8*	*46.45*	*614.35*				
01 / 03 / 88	60	-20	46.13	605.09	740	51300	0.45	31.04
05 / 04 / 88	58	-21	44.56	559.72				
13 / 04 / 88	65	*-21*	*44.56*	*559.72*				
11 / 05 / 88	60	*-21*	*44.56*	*559.72*				
23 / 06 / 88	65	-21	44.56	559.72	1040	73100	0.58	40.92
05 / 07 / 88	65	-22.5	42.24	494.60				
03 / 08 / 88	65	*-24.3*	*39.54*	*420.97*				
01 / 09 / 88	75	-26	37.08	355.82	1520	44200	0.54	15.73
05 / 10 / 88	75	*-26.5*	*36.37*	*337.45*				
25 / 10 / 88	65	*-26.8*	*35.94*	*326.59*	1420	47400	0.46	15.48
10 / 11 / 88	75	-27	35.66	319.43				
15 / 12 / 88	75	-30	31.59	218.56				
13 / 01 / 89	82	*-31.4*	*29.77*	*175.59*				
21 / 01 / 89	79	*-31.8*	*29.26*	*163.77*				
07 / 02 / 89	87	*-32.6*	*28.26*	*140.75*	3590	28000	0.51	3.94
14 / 02 / 89	79	-33	27.76	129.54				
03 / 03 / 89	82	-35	20.39	81.58	3650	27200	0.30	2.22
14 / 04 / 89	82	-40	6.94	16.19				

Meteorological data: Windspeed

Date (all 1989)	Time (Costa Rican Time)	Average windspeed (m s^{-1}) at 1 m height on crater floor over previous period
27 / 2	11.40	-
27 / 2	14.15	1.56
27 / 2	16.36	1.33
1 / 3	09.02	1.63
1 / 3	13.18	2.41
1 / 3	15.02	2.16
1 / 3	17.48	1.11
2 / 3	10.12	1.66
2 / 3	13.13	2.20
2 / 3	15.34	1.55
3 / 3	09.38	1.81
3 / 3	13.21	1.48
4 / 3	09.49	1.61
4 / 3	11.31	2.25
4 / 3	12.27	1.77
4 / 3	14.36	1.76
6 / 3	10.41	2.14
6 / 3	15.45	2.14
7 / 3	13.11	1.72
16 / 3	14.17	2.97
16 / 3	16.18	1.56
18 / 3	15.45	2.39
Dismantled		
Dismantled		
18 / 3	17.28	-
20 / 3	12.54	2.61
20 / 3	13.56	2.04
21 / 3	10.10	2.12
21 / 3	10.16	2.78
Dismantled		
21 / 3	16.42	-
22 / 3	10.24	1.87
22 / 3	10.35	1.08
23 / 3	09.37	1.89
Dismantled		
23 / 3	11.30	-
30 / 3	11.42	2.14
30 / 3	14.02	2.81
31 / 3	13.15	1.65
Dismantled		
9 / 4	11.22	-
9 / 4	14.52	2.06
10 / 4	09.28	2.52
10 / 4	11.55	3.73
19 / 4	13.00	2.30
19 / 4	15.24	5.37
20 / 4	11.25	2.10

Average windspeed at 1 m height: 2.3 m s^{-1}

Rainfall data

Year	Month	Monthly rainfall at Poas visitor's centre / mm
1978	January	77.1
	February	196.4
	March	116.4
	April	50.4
	May	473.6
	June	335.8
	July	334.9
	August	343.9
	September	483.8
	October	397.9
	November	170.9
	December	333.7
1979	January	127.3
	February	30.1
	March	26.3
	April	355.0
	May	389.4
	June	490.8
	July	282.5
	August	534.6
	September	542.9
	October	425.7
	November	434.2
	December	346.0
1980	January	164.8
	February	178.6
	March	15.7
	April	120.5
	May	344.1
	June	482.5
	July	378.9
	August	356.6
	September	483.2
	October	389.5
	November	963.4
	December	352.0
1981	January	170.2
	February	296.9
	March	34.4
	April	113.6* *average of April rainfall, 72-86
	May	440.7
	June	483.1
	July	337.2
	August	645.3
	September	441.1
	October	566.3
	November	964.5
	December	353.9

Appendix A: Poás data

Year	Month	Monthly rainfall at Poas visitor's centre / mm
1982	January	162.7
	February	40.5
	March	17.6
	April	33.4
	May	568.5
	June	600.8
	July	652.2
	August	378.8
	September	531.9
	October	943.1
	November	240.0
	December	169.3
1983	January	159.7
	February	62.7
	March	138.8
	April	82.8
	May	379.2
	June	270.1
	July	330.9
	August	402.5
	September	402.4
	October	566.6
	November	237.6
	December	227.5
1984	January	427.2
	February	252.1
	March	52.9
	April	137.9
	May	373.6
	June	410
	July	549.2
	August	695.7
	September	563.0
	October	262.7
	November	375.8
	December	347.0
1985	January	76.9
	February	144.0
	March	17.1
	April	65.2
	May	143.9
	June	442.6
	July	228.0
	August	284.0
	September	304.9
	October	465.2
	November	363.1
	December	287.6

Year	Month	Monthly rainfall at Poas visitors centre / mm
1986	January	235.3
	February	31.2
	March	300.4
	April	60.0
	May	445.1
	June	498.5
	July	254.2
	August	216.2
	September	303.0
	October	397.7
	November	155.5
	December	106.2
1987	January	195.5
	February	24.3
	March	79.8
	April	120.7
	May	284.7
	June	366.3
	July	393.3
	August	470.4
	September	429.7
	October	541.8
	November	266.5
	December	255.6
1988	January	539.8
	February	124.0
	March	136.8
	April	53.4
	May	480.8
	June	411.5
	July	454.6
	August	714.8
	September	483.2
	October	706.6
	November	154.1
	December	424.3
1989	January	91.3
	February	157.5
	March	90.0
	April	75.0

Air temperature and humidity

Date (all 1989)	Average air temperature / °C	Average humidity / %
2 / 3	18	85
3 / 3	17	75
4 / 3	18	65
5 / 3	16	50
6 / 3	17	-
20 / 3	15	95
21 / 3	13	95
22 / 3	13	100
23 / 3	12	85
24 / 3	13	70
25 / 3	13	75
26 / 3	13	80
27 / 3	14	80
30 / 3	14	80
31 / 3	13	80
1 / 4	16	80

Average air temperature: 15 °C, Average humidity: 80 %

Survey of lake basin

Station	Horizontal angle	Horizontal distance / m	Vertical distance /m
From survey point 1 18 / 3 / 89	(Angle relative to BNL)		
BNL	0	255.912	-48.501
NE85	22° 10' 59"	201.282	-37.698
E89	11° 55' 33"	133.956	-63.918
SW85A	287° 32' 52"	213.383	-35.805
MUD1	320° 53' 24"	59.946	-51.698
MUD2A	339° 17' 35"	79.843	-63.777
From survey point 2 21 / 3 / 89	(Angle relative to SE85A)		
SE85A	0	41.832	-13.874
SE87A	36° 56' 52"	36.107	-29.024
SE87B	48° 52' 06"	29.597	-29.803
SSE87	49° 31' 49"	72.481	-31.273
MUD1	53° 26' 03"	94.407	-31.223
S85A	35° 27' 39"	96.444	-14.238
S87A	47° 59' 40"	132.888	-22.914
S87B	50° 16' 02"	140.357	-29.356
SW87A	51° 23' 30"	193.454	-29.453
SW85B	46° 19' 05"	215.935	-13.463
SW85C	65° 38' 06"	270.883	-13.381
SW87B	68° 19' 54"	253.053	-29.303
W85A	70° 39' 17"	298.220	-11.786
From survey point 2 22 / 3 / 89	(Angle relative to SE85A)		
NW85A	122° 59' 35"	286.178	-14.186
NW85B	125° 16' 40"	258.628	-18.612
N85B	133° 54' 52"	209.181	-25.478
E89	128° 53' 42"	62.654	-42.833
NE87A	140° 31' 30"	162.477	-26.459

Fumarole data

Year	Month	Maximum fumarole temperature /°C
1978	December	90
1979	February	90
	October	90
1980	January	95
	February	95
	September	90
	October	90
1981	January	700* *Estimate from incandescence
	February	700*
	March	871
	April	871
	May	960
	June	940
	July	940
	August	930
	September	930
	October	935
	November	898
	December	830
1982	January	860
	February	883
	March	887
	April	873
	May	852
	June	812
	July	760
	August	818
	September	830
	October	737
	November	642
	December	731
1983	January	753
	February	771
	March	805
	April	822
	May	832
	June	834
	July	822
	August	806
	September	802
	October	801
	November	750
	December	723

Appendix A: Poás data

Year	Month	Maximum fumarole temperature / °C
1984	January	709
	February	650
	March	568
	April	570
	May	586
	June	603
	July	602
	August	530
	September	500
	October	490
	November	510
	December	515
1985	January	550
	February	560
	March	584
	April	568
	May	490
	June	420
	July	316
	August	295
	September	294
	October	310
	November	289
	December	287
1986	January	300
	February	300
	March	300
	April	300
	May	300
	June	360
	July	367
	August	358
	September	338
	October	320
	November	360
	December	561
1987	January	540
	February	540
	March	502
	April	530
	May	540
	June	585
	July	540
	August	520
	September	520
	October	510
	November	486
	December	441

Appendix A: Poás data

Year	Month	Maximum fumarole temperature / °C
1988	January	392
	February	395
	March	665
	April	587
	May	506
	June	504
	July	450
	August	375
	October	275
1989	February	95
	March	95
	April	95

Appendix B: Ruapehu data

Crater lake data

Date d m y	T_w / °C	Level / m	Area / 10^3 m^2	Mass / Gg	Mg / ppm	Cl / ppm	Total Mg / Gg	Total Cl / Gg
09 / 01 / 66	33	0	196.3	7382.74	550	7600	4.06	56.11
10 / 02 / 66	40	0	196.3	7382.74				
14 / 02 / 66	49.5	0	196.3	7382.74	625	7890	4.61	58.25
08 / 03 / 66	46	0	196.3	7382.74	600	7965	4.43	58.80
24 / 03 / 66	47	0	196.3	7382.74	600	8060	4.43	59.50
01 / 04 / 66	42	0	196.3	7382.74	640	8050	4.72	59.43
13 / 04 / 66	37	0	196.3	7382.74	675	8240	4.98	60.83
04 / 05 / 66	33	0	196.3	7382.74	670	8092	4.95	59.74
19 / 05 / 66	33.5	0	196.3	7382.74				
19 / 06 / 66	31	0	196.3	7382.74	600	8310	4.43	61.35
24 / 07 / 66	53	0	196.3	7382.74	665	8485	4.91	62.64
27 / 07 / 66	54	0	196.3	7382.74				
29 / 07 / 66	53.8	0	196.3	7382.74				
03 / 08 / 66	53	0	196.3	7382.74	810	8850	5.98	65.34
18 / 08 / 66	50.5	0	196.3	7382.74	915	9240	6.76	68.22
20 / 08 / 66	49	0	196.3	7382.74				
01 / 09 / 66	49.5	0	196.3	7382.74	975	9488	7.20	70.05
12 / 09 / 66	44	0	196.3	7382.74	1000	9710	7.38	71.69
26 / 09 / 66	41	0	196.3	7382.74	970	9854	7.16	72.75
17 / 10 / 66	46	0	196.3	7382.74	1020	10190	7.53	75.23
10 / 11 / 66	44.3	0	196.3	7382.74	1050	10485	7.75	77.41
15 / 12 / 66	31.7	0	196.3	7382.74	1154	10590	8.52	78.18
10 / 01 / 67	39	0	196.3	7382.74				
23 / 01 / 67	39.5	0	196.3	7382.74	1050	10710	7.75	79.07
14 / 02 / 67	39	0	196.3	7382.74		10548		77.87
15 / 03 / 67	39.5	0	196.3	7382.74		10280		75.89
13 / 04 / 67	37.5	0	196.3	7382.74		10406		76.82
12 / 06 / 67	33	0	196.3	7382.74		10886		80.37
08 / 08 / 67	41.5	0	196.3	7382.74		11176		82.51
12 / 12 / 67	26.5	0	196.3	7382.74		11151		82.32
21 / 01 / 68	36	0	196.3	7382.74				
01 / 03 / 68	38	0	196.3	7382.74		11064		81.68
06 / 04 / 68	53.5	0	196.3	7382.74		11347		83.77
28 / 04 / 68	60	0	196.3	7382.74		11915		87.97
07 / 05 / 68	60	0	196.3	7382.74		12100		89.33
22 / 05 / 68	48.5	0	196.3	7382.74		12560		92.73
05 / 06 / 68	55	0	196.3	7382.74		13295		98.15
11 / 06 / 68	47.5	0	196.3	7382.74		13405		98.97
20 / 06 / 68	51.5	0	196.3	7382.74		13420		99.08
05 / 07 / 68	34	0	196.3	7382.74		13225		97.64
07 / 08 / 68	29.5	0	196.3	7382.74		13113		96.81
20 / 08 / 68	33.7	0	196.3	7382.74		13110		96.79

Date d m y	T_w / °C	Level / m	Area / 10^3 m^2	Mass / Gg	Mg / ppm	Cl / ppm	Total Mg / Gg	Total Cl / Gg
12 / 09 / 68	20.6	0	196.3	7382.74		13110		96.79
01 / 11 / 68	25.5	0	196.3	7382.74				
11 / 12 / 68	29	0	196.3	7382.74		12613		93.12
18 / 01 / 69	33	0	196.3	7382.74				
19 / 01 / 69	33	0	196.3	7382.74				
07 / 02 / 69	33	0	196.3	7382.74		12315		90.92
19 / 03 / 69	29.8	0	196.3	7382.74		12010		88.67
05 / 04 / 69	24	0	196.3	7382.74				
04 / 05 / 69	23	0	196.3	7382.74				
25 / 06 / 69	43	-2.7	185.9	6866.78	1430	11496	9.82	78.94
03 / 07 / 69	35.4	-2.7	185.9	6866.78				
11 / 07 / 69	38	-2.7	185.9	6866.78		11446		78.60
14 / 08 / 69	33	-2.7	185.9	6866.78		11446		78.60
24 / 08 / 69	36	-2.7	185.9	6866.78				
05 / 09 / 69	42	-2.7	185.9	6866.78		11600		79.65
22 / 09 / 69	36	-2.7	185.9	6866.78				
03 / 10 / 69	38	-2.7	185.9	6866.78	1580	11640	10.85	79.93
06 / 11 / 69	36.5	-2.7	185.9	6866.78	1560	11900	10.71	81.71
05 / 12 / 69	40	-2.7	185.9	6866.78				
22 / 12 / 69	39	-2.7	185.9	6866.78	1400	11300	9.61	77.59
05 / 01 / 70	40.5	-2.3	187.4	6941.44				
17 / 01 / 70	36	-1.8	189.3	7035.63	1430	11300	10.06	79.50
25 / 01 / 70	38	-1.8	189.3	7035.63				
11 / 04 / 70	35	-1.3	191.3	7130.79	1180	11400	8.41	81.29
24 / 06 / 70	34.4	-0.8	193.2	7226.91	1220	11400	8.82	82.39
10 / 08 / 70	28.5	-0.5	194.4	7285.05	1200	11700	8.74	85.24
21 / 09 / 70	34	-0.3	195.2	7324.01				
07 / 11 / 70	28	0	196.3	7382.74	1200	10800	8.86	79.73
08 / 12 / 70	25	-0.1	196.0	7363.12	1130	9990	8.32	73.56
23 / 03 / 71	27.5	-0.3	195.2	7324.01	1030	9450	7.54	69.21
01 / 04 / 71	35	-0.3	195.2	7324.01	1030	9470	7.54	69.36
02 / 04 / 71	37	-0.3	195.2	7324.01	1030	9540	7.54	69.87
06 / 04 / 71	38	-0.3	195.2	7324.01	1070	9590	7.84	70.24
11 / 04 / 71	41.5	-0.2	195.6	7343.55	1100	9620	8.08	70.64
21 / 04 / 71	47	0	196.3	7382.74	1130	9770	8.34	72.13
28 / 04 / 71	56	0	196.3	7382.74	1130	9840	8.34	72.65
07 / 05 / 71	55	0	196.3	7382.74	1190	9940	8.79	73.38
08 / 05 / 71	53	-0.3	195.2	7324.01	1260	10020	9.23	73.39
14 / 05 / 71	53	-1.9	189.0	7016.72	1320	10190	9.26	71.50
16 / 05 / 71	60	-2.5	186.7	6904.03	1420	10470	9.80	72.29
13 / 07 / 71	53	-1.5	190.5	7092.61	2290	11920	16.24	84.54
14 / 07 / 71	53	-1.5	190.5	7092.61	2380	12100	16.88	85.82
19 / 07 / 71	52	-1.5	190.5	7092.61	2350	12070	16.67	85.61
19 / 08 / 71	53	-1.5	190.5	7092.61	2350	12260	16.67	86.96
22 / 08 / 71	55	-1.5	190.5	7092.61	2290	12300	16.24	87.24
15 / 09 / 71	47.5	-1.5	190.5	7092.61	2320	12890	16.45	91.42
14 / 10 / 71	37.5	-0.2	195.6	7343.55	2420	13460	17.77	98.84

Date d	m	y	T_w / °C	Level / m	Area / 10^3 m^2	Mass / Gg	Mg / ppm	Cl / ppm	Total Mg / Gg	Total Cl / Gg
01	11	71	36	-0.1	196.0	7363.12	2380	13570	17.52	99.92
21	12	71	41	-0.1	196.0	7363.12	2320	13710	17.08	100.95
26	01	72	40.5	-0.1	196.0	7363.12	2000	12600	14.73	92.78
15	03	72	35	-0.1	196.0	7363.12	1930	12420	14.21	91.45
01	04	72	32	-0.1	196.0	7363.12	1970	12890	14.51	94.91
20	04	72	31.5	-0.1	196.0	7363.12	2000	13130	14.73	96.68
04	05	72	28	-0.1	196.0	7363.12	2030	13150	14.95	96.83
28	06	72	30.5	-0.1	196.0	7363.12	1950	13260	14.36	97.63
25	07	72	23	-0.1	196.0	7363.12	1890	13200	13.92	97.19
04	09	72	18.8	0	196.3	7382.74	1845	13120	13.62	96.86
01	10	72	22.5	0	196.3	7382.74	1810	12950	13.36	95.61
21	10	72	38	0	196.3	7382.74	1800	13200	13.29	97.45
10	11	72	38	0	196.3	7382.74	1750	13240	12.92	97.75
09	01	73	41	0	196.3	7382.74	1660	12990	12.26	95.90
06	02	73	40	0	196.3	7382.74	1590	12650	11.74	93.39
26	02	73	41	0	196.3	7382.74	1580	12240	11.66	90.36
28	03	73	35	0	196.3	7382.74	1518	12370	11.21	91.32
22	05	73	34	0	196.3	7382.74	1446	12350	10.68	91.18
17	06	73	30	0	196.3	7382.74	1412	12440	10.42	91.84
05	07	73	31	0	196.3	7382.74	1409	12400	10.40	91.55
24	08	73	28	0	196.3	7382.74	1380	12650	10.19	93.39
01	11	73	37	0	196.3	7382.74	1305	12680	9.63	93.61
10	11	73	44	0	196.3	7382.74	1275	12480	9.41	92.14
22	11	73	35	0	196.3	7382.74	1255	12375	9.27	91.36
25	01	74	38	0	196.3	7382.74	1175	12100	8.67	89.33
12	03	74	41	0	196.3	7382.74	1165	12200	8.60	90.07
21	03	74	36	0	196.3	7382.74	1160	12300	8.56	90.81
28	03	74	38	-0.2	195.6	7343.55	1160	12190	8.52	89.52
11	04	74	38	-0.1	196.0	7363.12				
13	04	74	38	-0.1	196.0	7363.12				
11	05	74	33.5	0	196.3	7382.74	1185	12424	8.75	91.72
01	07	74	27	0	196.3	7382.74	1192	12452	8.80	91.93
07	08	74	27	0	196.3	7382.74				
08	08	74	29	0	196.3	7382.74	1192	12459	8.80	91.98
12	09	74	33	-0.3	195.2	7324.01	1270	12500	9.30	91.55
24	10	74	28.5	0	196.3	7382.74	1290	12370	9.52	91.32
12	12	74	30.5	0	196.3	7382.74	1240	12520	9.15	92.43
22	02	75	25.5	0	196.3	7382.74	1090	11290	8.05	83.35
18	03	75	28.8	0	196.3	7382.74	1080	11100	7.97	81.95
07	04	75	24.8	0	196.3	7382.74	1040	10680	7.68	78.85
28	04	75	46	-8	166.2	5934.25	1430	11150	8.49	66.17
07	05	75	43	-8	166.2	5934.25	1540	11280	9.14	66.94
17	06	75	34	-6.1	173.1	6256.58	1550	10370	9.70	64.88
24	07	75	28.3	-6	173.5	6273.91	1560	10810	9.79	67.82
20	10	75	29	-6	173.5	6273.91	1440	10180	9.03	63.87
10	11	75	29	-5	177.2	6449.26	1450	10140	9.35	65.40
22	12	75	26	-3	184.7	6811.18	1460	9680	9.94	65.93

Date d	m	y	T_w / °C	Level / m	Area / 10^3 m^2	Mass / Gg	Mg / ppm	Cl / ppm	Total Mg / Gg	Total Cl / Gg
03	01	76	27.2	-1.9	189.0	7016.72	1480	9640	10.38	67.64
18	01	76	24.5	-0.4	194.8	7304.51	1330	8860	9.71	64.72
20	01	76	23	-0.5	194.4	7285.05	1330	8900	9.69	64.84
03	02	76	22.5	0	196.3	7382.74	1290	8540	9.52	63.05
01	03	76	25.3	0	196.3	7382.74	1260	8330	9.30	61.50
05	04	76	30.5	0	196.3	7382.74	1230	8140	9.08	60.10
04	05	76	27.5	0	196.3	7382.74	1210	7850	8.93	57.95
07	06	76	21.2	0	196.3	7382.74	1230	7780	9.08	57.44
05	07	76	21	0	196.3	7382.74	1210	7670	8.93	56.63
18	08	76	21	0	196.3	7382.74	1260	7730	9.30	57.07
20	09	76	28.2	0	196.3	7382.74	1270	7620	9.38	56.26
16	11	76	22	0	196.3	7382.74	1250	7490	9.23	55.30
22	11	76	24.5	-0.2	195.6	7343.55	1290	7660	9.47	56.25
15	01	77	18.8	0	196.3	7382.74	1180	7320	8.71	54.04
15	03	77	25.5	0	196.3	7382.74	1090	7161	8.05	52.87
10	05	77	23.5	0	196.3	7382.74	1010	7242	7.46	53.47
19	06	77	21.5	0	196.3	7382.74	920	7170	6.79	52.93
05	07	77	18	0	196.3	7382.74	930	7110	6.87	52.49
11	08	77	31	-0.3	195.2	7324.01	1115	7440	8.17	54.49
22	09	77	30.5	0	196.3	7382.74	1150	7520	8.49	55.52
26	10	77	31	0	196.3	7382.74	1195	7495	8.82	55.33
08	11	77	35	-0.2	195.6	7343.55	1320	7890	9.69	57.94
14	01	78	26	-0.2	195.6	7343.55	1220	7560	8.96	55.52
17	01	78	27	0	196.3	7382.74				
10	02	78	38.5	0	196.3	7382.74	1240	7870	9.15	58.10
20	02	78	32.5	0	196.3	7382.74	1215	7615	8.97	56.22
08	03	78	31.5	-0.4	194.8	7304.51	1190	7430	8.69	54.27
13	03	78	36	-0.1	196.0	7363.12	1235	7760	9.09	57.14
13	04	78	34.5	0	196.3	7382.74	1230	7790	9.08	57.51
29	05	78	43	0	196.3	7382.74	1169	8390	8.63	61.94
12	06	78	43	-0.3	195.2	7324.01	1185	8710	8.68	63.79
15	06	78	48.3	-0.3	195.2	7324.01				
17	07	78	30	-1	192.4	7188.34	1205	8920	8.66	64.12
01	09	78	24.5	0	196.3	7382.74	1180	8930	8.71	65.93
08	09	78	31	-0.5	194.4	7285.05	1175	8890	8.56	64.76
09	10	78	27.5	0	196.3	7382.74	1180	8990	8.71	66.37
28	11	78	32	0	196.3	7382.74	1150	9020	8.49	66.59
10	01	79	27	0	196.3	7382.74	1120	8590	8.27	63.42
02	02	79	32	0	196.3	7382.74	1180	8700	8.71	64.23
01	04	79	31.5	0	196.3	7382.74	1130	7920	8.34	58.47
05	06	79	18.5	0	196.3	7382.74	1095	7565	8.08	55.85
19	07	79	26.5	0	196.3	7382.74	1070	8050	7.90	59.43
16	08	79	24	0	196.3	7382.74	1055	8035	7.79	59.32
27	09	79	21.7	0	196.3	7382.74	1040	8320	7.68	61.42
25	10	79	21.5	0	196.3	7382.74	1010	8230	7.46	60.76
05	12	79	18	0	196.3	7382.74	920	7700	6.79	56.85

Date d m y	T_w / °C	Level / m	Area / 10^3 m^2	Mass / Gg	Mg / ppm	Cl / ppm	Total Mg / Gg	Total Cl / Gg
14 / 01 / 80	22	0	196.3	7382.74				
11 / 02 / 80	34	0	196.3	7382.74				
19 / 02 / 80	43	0	196.3	7382.74				
28 / 02 / 80	41	0	196.3	7382.74	875	7470	6.46	55.15
13 / 03 / 80	37	-0.5	194.4	7285.05	885	7380	6.45	53.76
26 / 03 / 80	40	-0.4	194.8	7304.51	885	7430	6.46	54.27
11 / 04 / 80	37	0	196.3	7382.74	890	7545	6.57	55.70
07 / 05 / 80	39	-0.5	194.4	7285.05	900	7625	6.56	55.55
29 / 05 / 80	31	-0.5	194.4	7285.05	895	7730	6.52	56.31
26 / 06 / 80	30	-1.4	190.9	7111.68	885	7740	6.29	55.04
28 / 07 / 80	27	-1	192.4	7188.34	860	7400	6.18	53.19
10 / 08 / 80	23	-0.9	192.8	7207.61	840	7450	6.05	53.70
01 / 09 / 80	18	-0.5	194.4	7285.05	820	7450	5.97	54.27
23 / 09 / 80	16	0	196.3	7382.74	800	7300	5.91	53.89
06 / 10 / 80	25	-0.2	195.6	7343.55	780	7150	5.73	52.51
18 / 11 / 80	35	-0.2	195.6	7343.55	770	7300	5.65	53.61
01 / 01 / 81	33	0	196.3	7382.74	745	7320	5.50	54.04
28 / 01 / 81	38	0	196.3	7382.74				
18 / 02 / 81	33.6	0	196.3	7382.74	715	7080	5.28	52.27
19 / 03 / 81	33.5	0	196.3	7382.74	700	7100	5.17	52.42
11 / 06 / 81	24	0	196.3	7382.74	710	6970	5.24	51.46
06 / 08 / 81	13.8	0	196.3	7382.74	680	6820	5.02	50.35
11 / 08 / 81	13	0	196.3	7382.74				
16 / 08 / 81	15	0	196.3	7382.74				
27 / 08 / 81	13.4	0	196.3	7382.74	655	6735	4.84	49.72
07 / 10 / 81	10.5	0	196.3	7382.74	620	6750	4.58	49.83
13 / 10 / 81	11.8	0	196.3	7382.74	630	6750	4.65	49.83
03 / 11 / 81	24	0	196.3	7382.74	615	6770	4.54	49.98
20 / 11 / 81	36.5	0	196.3	7382.74				
23 / 11 / 81	42	0	196.3	7382.74	625	6903	4.61	50.96
27 / 12 / 81	46.8	0	196.3	7382.74	663	6930	4.89	51.16
11 / 01 / 82	57.2	0	196.3	7382.74	765	7400	5.65	54.63
20 / 01 / 82	57	-0.2	195.6	7343.55	853	7730	6.26	56.77
04 / 02 / 82	49	-0.2	195.6	7343.55	1025	7884	7.53	57.90
10 / 02 / 82	50.5	-0.3	195.2	7324.01	990	7875	7.25	57.68
04 / 03 / 82	41	0	196.3	7382.74	953	7939	7.04	58.61
22 / 03 / 82	47	-0.5	194.4	7285.05	977	7875	7.12	57.37
14 / 04 / 82	39	-1.5	190.5	7092.61	1023	8168	7.26	57.93
20 / 04 / 82	42	-1.8	189.3	7035.63	998	8206	7.02	57.73
28 / 05 / 82	27	-3.5	182.8	6719.29	1018	8344	6.84	56.07
01 / 07 / 82	33	-2.1	188.2	6979.00	1025	8594	7.15	59.98
22 / 07 / 82	24.5	-1.9	189.0	7016.72	997	8690	7.00	60.98
19 / 08 / 82	23	-1.3	191.3	7130.79				
23 / 08 / 82	24	-1.3	191.3	7130.79	1005	8740	7.17	62.32
16 / 09 / 82	29	-1.2	191.7	7149.93	1010	8950	7.22	63.99
20 / 10 / 82	25	-1.2	191.7	7149.93	1022	8850	7.31	63.28
08 / 11 / 82	21	-0.5	194.4	7285.05	988	8725	7.20	63.56

Date d m y	T_w / °C	Level / m	Area / 10^3 m^2	Mass / Gg	Mg / ppm	Cl / ppm	Total Mg / Gg	Total Cl / Gg
15 / 12 / 82	13	0	196.3	7382.74	900	8240	6.64	60.83
02 / 01 / 83	22	0	196.3	7382.74	870	8390	6.42	61.94
10 / 02 / 83	19	0	196.3	7382.74	875	8165	6.46	60.28
27 / 02 / 83	27	0	196.3	7382.74	844	8015	6.23	59.17
16 / 03 / 83	23	0	196.3	7382.74	820	7880	6.05	58.18
23 / 04 / 83	20	0	196.3	7382.74				
14 / 05 / 83	16.5	0	196.3	7382.74	754	7465	5.57	55.11
21 / 06 / 83	16.5	0	196.3	7382.74	751	7455	5.54	55.04
17 / 07 / 83	18.7	0	196.3	7382.74	778	7310	5.74	53.97
15 / 08 / 83	18.3	0	196.3	7382.74	744	7470	5.49	55.15
28 / 09 / 83	18	0	196.3	7382.74	690	7320	5.09	54.04
28 / 11 / 83	28.5	0	196.3	7382.74	654	7290	4.83	53.82
01 / 01 / 84	29.5	-0.5	194.4	7285.05	652	7410	4.75	53.98
07 / 02 / 84	31	0	196.3	7382.74	648	7430	4.78	54.85
19 / 03 / 84	25	0	196.3	7382.74	604	7135	4.46	52.68
03 / 05 / 84	18.3	0	196.3	7382.74	597	7045	4.41	52.01
04 / 06 / 84	13.4	0	196.3	7382.74	574	7160	4.24	52.86
17 / 07 / 84	11.6	0	196.3	7382.74	552	6980	4.08	51.53
16 / 09 / 84	16.5	0	196.3	7382.74	537	6830	3.96	50.42
24 / 10 / 84	21	0	196.3	7382.74	538	7070	3.97	52.20
01 / 02 / 85	23	0	196.3	7382.74				
26 / 02 / 85	23	0	196.3	7382.74				
18 / 03 / 85	21.5	0	196.3	7382.74				
27 / 05 / 85	45	0	196.3	7382.74				
03 / 06 / 85	45	0	196.3	7382.74				
25 / 06 / 85	37	-0.2	195.6	7343.55	485	6565	3.56	48.21
10 / 07 / 85	31.5	-0.5	194.4	7285.05	496	6820	3.61	49.68
04 / 08 / 85	32	0	196.3	7382.74	493	6835	3.64	50.46
13 / 09 / 85	21	-0.4	194.8	7304.51	494	7025	3.61	51.31
17 / 10 / 85	20	-0.2	195.6	7343.55	501	7050	3.68	51.77
01 / 11 / 85	26.5	0	196.3	7382.74	508	7270	3.75	53.67
14 / 11 / 85	36	0	196.3	7382.74	507	7360	3.74	54.34
04 / 12 / 85	36	0	196.3	7382.74	498	7720	3.68	56.99
12 / 12 / 85	35	0	196.3	7382.74	499	7690	3.68	56.77
10 / 02 / 86	46	0	196.3	7382.74	480	8020	3.54	59.21
14 / 02 / 86	46.5	0	196.3	7382.74	476	7980	3.51	58.91
26 / 02 / 86	34	0	196.3	7382.74	467	7630	3.45	56.33
07 / 03 / 86	35	-0.1	196.0	7363.12				
18 / 03 / 86	32	-0.1	196.0	7363.12	473	7380	3.48	54.34
07 / 05 / 86	22	0	196.3	7382.74	476	7825	3.51	57.77
01 / 08 / 86	10.8	0	196.3	7382.74	499	7810	3.68	57.66
26 / 08 / 86	14.5	0	196.3	7382.74	475	7580	3.51	55.96
01 / 09 / 86	17	0	196.3	7382.74				
13 / 09 / 86	18	-0.1	196.0	7363.12	464	7395	3.42	54.45
09 / 10 / 86	21	0	196.3	7382.74	457	8165	3.37	60.28
14 / 10 / 86	23	0	196.3	7382.74	471	8385	3.48	61.90
02 / 11 / 86	31.5	0	196.3	7382.74	468	8080	3.46	59.65

Date d	m	y	T_w / °C	Level / m	Area / 10^3 m^2	Mass / Gg	Mg / ppm	Cl / ppm	Total Mg / Gg	Total Cl / Gg
19	11	86	34	-0.4	194.8	7304.51	477	8025	3.48	58.62
24	02	87	21.5	0	196.3	7382.74	453	7220	3.34	53.30
14	04	87	19	0	196.3	7382.74	410	6720	3.03	49.61
03	05	87	12	0	196.3	7382.74	430	6720	3.17	49.61
26	05	87	14.2	0	196.3	7382.74	420	6720	3.10	49.61
02	07	87	11.5	0	196.3	7382.74	430	6520	3.17	48.14
12	08	87	24.5	0	196.3	7382.74	420	6590	3.10	48.65
01	09	87	40	0	196.3	7382.74	430	6880	3.17	50.79
09	09	87	38	0	196.3	7382.74	440	6880	3.25	50.79
27	09	87	30.5	-0.1	196.0	7363.12	440	7130	3.24	52.50
15	10	87	28.5	0	196.3	7382.74	440	6880	3.25	50.79
11	11	87	27	-0.1	196.0	7363.12	420	6970	3.09	51.32
13	01	88	20	0	196.3	7382.74	410	6610	3.03	48.80
17	01	88	23.5	0	196.3	7382.74	400	6940	2.95	51.24
02	02	88	23.5	0	196.3	7382.74				
01	03	88	18.5	0	196.3	7382.74				
21	03	88	31.8	0	196.3	7382.74	400	6610	2.95	48.80
11	04	88	38.8	0	196.3	7382.74	420	6790	3.10	50.13
03	05	88	36.5	-0.4	194.8	7304.51	460	7160	3.36	52.30
01	06	88	25.5	-0.1	196.0	7363.12	450	6888	3.31	50.72
20	06	88	22.5	0	196.3	7382.74	440	6714	3.25	49.57
03	08	88	14	0	196.3	7382.74	430	6737	3.17	49.74
15	09	88	10	0	196.3	7382.74	400	6440	2.95	47.54
17	10	88	10.5	0	196.3	7382.74	390	6270	2.88	46.29
14	11	88	9	0	196.3	7382.74				
08	12	88	13.7	0	196.3	7382.74				
15	12	88	14	0	196.3	7382.74				
23	01	89	32	0	196.3	7382.74	380	5727	2.81	42.28
10	02	89	39	0	196.3	7382.74	410	5804	3.03	42.85
26	02	89	42.5	0	196.3	7382.74	410	5812	3.03	42.91
20	03	89	32	-0.1	196.0	7363.12	430	6126	3.17	45.11
05	04	89	31.3	-0.1	196.0	7363.12	430	6164	3.17	45.39
10	05	89	25	0	196.3	7382.74	430	6168	3.17	45.54